Jagiellonian University in Kraków

Faculty of Physics, Astronomy and Applied Computer Science

Department of Advanced Materials Engineering

New type of organic memristive devices - principles of operation and possible application

Doctoral Thesis

submitted by

Agnieszka Pawłowska

supervised by

Prof. Jakub Rysz

Kraków 2023

Wydział Fizyki, Astronomii i Informatyki Stosowanej

Uniwersytet Jagielloński

Oświadczenie

Ja niżej podpisana Agnieszka Pawłowska (nr indeksu 1111305), doktorantka Wydziału Fizyki, Astronomii i Informatyki Stosowanej Uniwersytetu Jagiellońskiego oświadczam, że przedłożona przeze mnie rozprawa doktorska pt. „New type of organic memristive devices - principles of operation and possible application" jest oryginalna i przedstawia wyniki badań wykonanych przeze mnie osobiście, pod kierunkiem prof. Jakuba Rysza. Praca została napisana przeze mnie samodzielnie.

Oświadczam, że moja rozprawa doktorska została opracowana zgodnie z Ustawą oprawie autorskim i prawach pokrewnych z dnia 4 lutego 1994 r. (Dziennik Ustaw 1994nr 24 poz. 83 wraz z późniejszymi zmianami).

Jestem świadoma, że niezgodność niniejszego oświadczenia z prawdą ujawniona w dowolnym czasie, niezależnie od skutków prawnych wynikających z ww. ustawy, może spowodować unieważnienie stopnia nabytego na podstawie tej rozprawy.

....

Kraków, dnia   Podpis autora pracy

I

Acknowledgements

I would like to express my gratitude to anyone who has, in any way, contributed to the development of this thesis.

At first, I would like to thank my parents and my late grandmother Genowefa, for their support and deep faith in me and my abilities. Without them, I would not get to a place and be the person I am today.

I would also like to express my deepest gratitude to my supervisor, prof. Jakub Rysz, for his guidance and support throughout my PhD studies. Without his help and advice, this thesis could not be completed. Throughout all the years of our cooperation, he believed in my abilities and helped me to grow as a scientist and as a person for which I am profoundly thankful.

My sincere gratitude also goes to dr. Paweł Dąbczyński, who provided me with his constant support and advice throughout my PhD studies. I would like to thank him for our countless and invaluable knowledge and ideas exchanges. His belief in my abilities has been a great source of courage and motivation and helped me to complete this thesis.

I had the great pleasure of working and collaborating with dr. Sebastian Lalik, prof. Dante Chialvo, dr. Juan Pablo Carbajal, and dr. Melika Payvand. I want to thank them for their inspirational and fruitful conversations, which were of great value to me.

Special thanks are due to my colleagues from Jagiellonian University: dr. Dariusz Augustowski, Julia Chudzik, Maciej Gala, Natalia Janiszewska, Agata Kubisiak and Jakub Wilgocki-Ślęzak. Our countless discussions and their support helped me to get through many difficult situations. I could not think of better working environment and more precious friends.

The completion of this dissertation would not be possible without support of my closest friends: Kaja Sztuczka, Alicja and Kamil Warnełło and Roma Wirecka. They helped me to overcome numerous obstacles and brought a lot of joyful moments to my life.

I would also like to thank my whole family, especially my siblings and their families, for their encouragement and support.

At last, I would like to thank everyone I encountered, even briefly, during this adventure.

Podziękowania

W tym miejscu chciałbym wyrazić swoją wdzięczność wobec wszystkich, którzy w jakikolwiek sposób przyczynili się do rozwoju tej pracy.

Na początku pragnę podziękować moim rodzicom oraz mojej babci Genowefie za ich wsparcie i głęboką wiarę we mnie i moje zdolności.

Chciałbym również wyrazić moją głęboką wdzięczność dla mojego promotora, prof. Jakuba Rysza, który przez wszystkie lata naszej współpracy wierzył w moje zdolności i pomógł mi rozwijać się jako naukowiec. Ukończenie tej pracy nie byłoby możliwe bez jego pomocy, wsparcia oraz udzielonych rad.

Serdeczne podziękowania kieruję również do dr. Pawła Dąbczyńskiego, który w trakcie moich studiów był źródłem nieustającego wsparcia. Chciałbym mu podziękować za liczne i bezcenne wymiany pomysłów i wiedzy. Jego wiara w moje zdolności była dla mnie ogromnym źródłem odwagi i motywacji, które pomogły mi ukończyć tę pracę.

W trakcie przygotowania tej rozprawy miałam przyjemność współpracować z dr. Sebastianem Lalikiem, prof. Dante Chialvo, dr. Juanem Pablo Carbajalem oraz dr. Meliką Payvand. Chciałbym im podziękować za inspirujące i owocne rozmowy, które miały dla mnie ogromną wartość intelektualną.

Szczególne podziękowania kieruję do moich kolegów z Uniwersytetu Jagiellońskiego: dr. Dariusza Augustowskiego, Julii Chudzik, Macieja Gali, Natalii Janiszewskiej, Agaty Kubisiak i Jakuba Wilgockiego-Ślęzaka. Nasze liczne dyskusje oraz udzielone mi przez nich wsparcie pomogły mi przetrwać trudy związane z pracą doświadczalną. Nie mogłam liczyć na lepsze środowisko pracy oraz cenniejszych przyjaciół.

Ukończenie tej pracy doktorskiej nie byłoby możliwe bez moich najbliższych przyjaciół: Kai Sztuczki, Alicji i Kamila Warnełło oraz Romy Wireckiej. Ich wsparcie ułatwiło mi przetrwanie wielu trudności, za co jestem im niezmiernie wdzięczna.

Chciałbym również podziękować całej mojej rodzinie, zwłaszcza mojemu rodzeństwu i ich rodzinom, za ich wsparcie i wiarę w moje możliwości.

Academic Achievements

List of papers

1. Dąbczyński, P. et al. Extraordinary conduction increase in model conjugated/insulating polymer system induced by surface located electric dipoles. Appl Mater Today 21, 100880 (2020).

2. Bogdanowicz, K.A., Lalik, S., Ratajczyk, P. et al. A new look at imines and their mixture with PC 71 BM: high pressure UV-Vis spectroscopy, thermoelectric, dielectric and mechanical properties for organic, flexible photovoltaics. Scientific Reports 13, 13240 (2023).

3. Pawłowska, A. I. et al. Dynamically altered conductance in an Organic Thin Film Memristive Device. Preprint: https://doi.org/10.48550/arXiv.2305.13466.

4. Dąbczyński, P. et al. Contact and on-distant interactions influence on conductivity in organic semiconductor/insulator system. Preprint.

List of conference contributions

1. A. Pawłowska, P. Dąbczyński, J. Rysz, Memory effects in Organic Field Effect Transistors (OFETs): from OFETs to memristive devices, 18th International Conference on Nanosciences & Nanotechnologies, poster, July 2021, Thessaloniki.

2. A. Pawłowska, P. Dąbczyński, J. Rysz, A new type of an Organic Memristive Device based on interactions between polymer thin-films, 4th International Conference on Materials: Advanced and Emerging Materials, oral presentation, October 2022, Barcelona.

Other scientific activities

1. Student internship at the Photovoltaic Research and Development Center of ML System S.A., where part of this thesis has been prepared.

2. Participation in BigBrain Workshop and Young Researchers Meet organized by Human Brain Project, Croatia, Zadar, 2022.

3. Visiting Student in the Institute of Neuroinformatics at UZH Zurich and ETH Zurich, where part of this thesis has been prepared.

Symbols

- A – area
- c – concentration
- C – capacitance
- d – thickness
- ϵ – permittivity
- η – constant related to the voltage induced conductance increase in the phenomenological model
- f – frequency
- G – conductance
- I – current
- j – imaginary unit
- L – inductance or length
- M – memristance
- μ – mobility
- u – weighted sum of the input signals
- U – voltage
- q – charge
- r – distance
- R – resistance
- ρ – viscosity
- t – time
- T – temperature
- τ – constant related to the spontaneous relaxation in the phenomenological model
- w – synaptic weight
- ω – angular speed of rotation angular speed of rotation
- ϕ – flux-linkage
- Z – impedance

Abbreviations

- 2AFC – 2-Alternative Forced Choice
- 3M2R bridge – 3 Memristor 2 Resistor bridge
- Ag – silver
- Al_2O_3 – aluminium oxide
- ANN – Artificial Neural Network
- BSE – Backscattered Electrons
- $CoBr_2$ - cobalt (II) bromide
- ITO – indium tin oxide
- LTD – Long Term Depression
- LTP – Long Term Potentiation
- OFET – Organic Field Effect Transistor
- OPV – Organic Photovoltaic
- R-P3HT – Regio regular poly(3-hexyltiophene)
- P4VP – poly(4-vinylpyridine)
- PE – Primary Electrons
- PSS – poly (sodium 4-styrene sulfonate)
- PVD – Physical Vapour Deposition
- RMS - Root Mean Square
- R-P3HT – Regio regular poly(3-hexyltiophene)
- SE – Secondary Electrons
- SEM – Scanning Electron Microscopy
- SIMS – Secondary Ion Mass Spectrometry
- SiO_2 - Silicon dioxide
- SNN – Spiking Neural Network
- TiO_2 – Titanium dioxide
- TOF – Time of Flight
- Triflate - trifluoromethanesulfonate

Theses

The aim of this thesis is to investigate the principle of operation of a new type of an organic memristive device and characterize its response to different stimuli. Within the framework of this thesis the following research questions are addressed:

1. How do the direct interactions between R-P3HT and P4VP influence the device's conductance?
2. What is the principle of operation of the studied system?
3. How does the ion enrichment influence the operation of the device?
4. How does the device respond to various stimuli?
5. How the processes occurring in the device can be described mathematically?
6. What is the outcome of different connections between devices?
7. Is it possible to emulate some of the neuronal functions using the device or its model?

Abstract

The topic of this thesis, a memristive device, is a subject of a relatively new field of research. Before their first physical realisation, this class of devices was only theorised, however, since their discovery, the memristive devices received a lot of attention from scientists working in various research areas.

Due to their unique features, memristive devices are studied not only in terms of their physics, as new dynamic systems, but also in terms of their possible applications. One specific branch of research on memristive devices receives a lot of attention. Due to rapid technological progress observed in the past years, the CMOS architecture is getting inevitably closer to its physical limitations. Moreover, the von Neumann bottleneck remains a big obstacle limiting the data transfer rate between CPU and memory. To overcome this issue new computing paradigms emerged, among them neuromorphic computing, which aims to utilize memristive devices as building blocks of next-generation computing architectures.

This thesis focuses on an organic memristive device with a unique principle of operation, which was not reported in the literature until today. It is based on long-range interactions between mobile ions in a polymer matrix and a dipole-induced electric field originating from the insulating layer, which acts as a separator between ions and the conducting layer. Throughout the framework of this thesis, its' extraordinary principle of operation as well as its' features are explored to fully characterize the system. Moreover, the research was extended to different types of ions to study the systems' dynamics. Based on these findings, the systems phenomenological model was created and shown to exhibit the key features of the devices. This work is completed by the study of the device's utility in neuromorphic applications, showing that it is a promising candidate for a building block of future computation architectures.

Streszczenie

Tematem niniejszej pracy doktorskiej jest urządzenie memrystywne, będące obiektem stosunkowo nowej dziedziny badań. Przed pierwszym doniesieniem o doświadczalnej realizacji urządzeń należących do tej klasy istniały jedynie teoretyczne założenia o ich istnieniu, jednak od ich odkrycia, urządzenia memrystywne zdobyły zainteresowanie ze strony naukowców pracujących w różnych obszarach badawczych.

Z uwagi na ich unikalne cechy, urządzenia memrystywne są badane nie tylko pod kątem fizyki, jako nowych systemów dynamicznych, ale także pod względem ich możliwych zastosowań. W szczególności jedna konkretna gałąź badań nad urządzeniami memrystywnymi cieszy się dużym zainteresowaniem. Ze względu na szybki postęp technologiczny obserwowany w ostatnich latach, architektura CMOS zbliża się nieuchronnie do swoich ograniczeń fizycznych. Ponadto wąskie gardło w architekturze von Neumanna pozostaje dużą przeszkodą ograniczającą szybkość transferu danych między jednostką obliczeniową a pamięcią. Aby przezwyciężyć ten problem, pojawiły się nowe paradygmaty obliczeniowe, w tym rozwiązania inspirowane funkcjonalnością mózgu, które mają na celu wykorzystanie urządzeń memrystywnych jako podstawowych elementów architektury układów scalonych nowej generacji.

Niniejsza praca doktorska skupia się na organicznym urządzeniu memrystywnym o unikalnej zasadzie działania, która nie była dotychczas opisywana w literaturze. Opiera się ona na oddziaływaniach dalekiego zasięgu pomiędzy ruchomymi jonami umieszczonymi w matrycy polimerowej a polem elektrycznym indukowanym przez warstwę izolującą, która dodatkowo działa jako separator między jonami a warstwą przewodzącą.

W ramach tej pracy doktorskiej została zbadana zasada działania oraz cechy urządzeń w celu pełnej charakteryzacji układu. Ponadto badania zostały rozszerzone na różne rodzaje jonów w celu zbadania dynamiki procesów zachodzących w układzie. Na podstawie tych wyników stworzono model fenomenologiczny układu, który odzwierciedla wszystkie kluczowe cechy urządzeń. Praca zwieńczona została badaniami możliwości zastosowania urządzeń w układach neuromorficznych, pokazując, że są one obiecującymi kandydatami na elementy budulcowe jednostek obliczeniowych przyszłości.

x

Contents

CHAPTER One – Introduction

Like many great inventions, the memristive device, which is the subject of this dissertation, has been discovered by accident. The aim of this chapter is to provide an overview of the studied system and the observed phenomena, to explain the main idea behind this dissertation. Moreover, to provide insight into the motivation for this research, the chapter presents the current state of the art in the field of memristive devices. By doing so, I hope readers will gain a better understanding of the research context and significance.

1.1. Scientific context of the research

The study of memristive devices and their unique characteristics, such as their principle of operation and application in neuromorphic systems, is a relatively new field of research. Although the concept of a memristor, a device that combines features of a resistor and a memory cell, was introduced in 1971[1], the physical realization of a similar device, known as a memristive device, was only presented in 2008[2]. Since then, the rapid technological progress has sparked significant interest in these devices, as they have the potential to overcome the memory-processor bottleneck in von Neumann computer architecture and reduce high energy consumption related to information processing.

Memristive devices have many potential applications, including non-volatile memories that could replace flash memories in the future[3]. However, the primary focus of researchers is on combining the memory effect of memristors with their ability to perform information processing. The human brain is a natural example of such a unit due to its ability to learn and perform parallel processing. This has inspired the development of neuromorphic computing, which involves the use of memristive devices in crossbar arrays for brain-inspired computing[4].

The device must meet requirements related to scalability, performance, and reliability[5] to be an effective building block in a neuromorphic system. Additionally, the device must

be capable of emulating synaptic plasticity, which is responsible for the brain's ability to learn by modifying the strength of synapses. The strength of a synapse, known as synaptic weight, can be adjusted for varying periods of time. Short-term Plasticity (STP) is a significant synaptic plasticity function that involves a temporary strengthening of synaptic weight. STP can last for a few minutes before fading away and is thought to be crucial for information processing in the human brain[6,7].

Most of the memristive devices reported in literature rely on non-organic materials, which offer high electrical stability, repeatability, and endurance. However, in recent years many organic materials-based memristive devices have emerged, with the benefit of being both biocompatible and biodegradable, providing at the same time electrical properties comparable to non-organic devices. Despite different principles underlaying their memristive character, the devices share a common feature: a pinched hysteresis loop in their current-voltage characteristics.

1.2. Introduction and research motivation

The study of memristive device, which is the subject of this thesis, is a continuation of previous investigation conducted in our group[8]. The main idea behind this research originated from the study of polymeric matrix of poly(4-vinylpyridine) (P4VP) cross-linked by a cobalt (II) salt bound within it. According to the results of this study, cobalt (II) bromide ($CoBr_2$) forms complexes with the pyridine rings present on the surface of the P4VP film. The bonding between cobalt (II) bromide and the nitrogen atom in the pyridine ring leads to reordering of the surface located pyridine rings, due to the formation of these complexes. As pyridine rings have non-zero dipole moment, the findings of this research brought an idea to incorporate the crosslinked P4VP as an insulator in an Organic Field Effect Transistor (OFET) and learn, whether the dipole moment-induced electric field influences the operation of the device.

While investigating the OFET, which comprises of regio regular poly(3-hexyltiophene) (R-P3HT, a semiconductor), P4VP (an insulator), $CoBr_2$, and poly(3,4-ethylenedioxythiophene) polystyrene sulfonate (PEDOT:PSS, as a gate), the time evolution of the device's current-voltage characteristics has been measured, and the outcome has been observed in a form of the hysteresis loop. The observed effect is a trait characteristic for a another class of devices, called memristive devices, and the findings of the mentioned study have been the main idea behind this dissertation.

2

Given that the initial investigation of the evolution of the OFET's characteristics is a subject of my previous work[9], only the most relevant findings are presented herein.

In the early stage of the research, the device was prepared as an Organic Field Effect Transistor with a gate consisting of PEDOT:PSS. During the device testing, an abnormal feature, the conductance increase with each subsequent measurement, has been observed. As seen in **Figure 1.1**, measurements performed alternatively for 50 V and 0 V gate voltage revealed a consistent increase in the current flowing through the transistor with each subsequent measurement, regardless of the gate voltage value. This result implies that the device could operate as a two-terminal device without application of the gate potential, as the device operates under 0 V gate voltage. It also suggests the existence of phenomena responsible for the current increase in the system. Such behaviour is indirect evidence of the dynamically altered conductivity of the system.
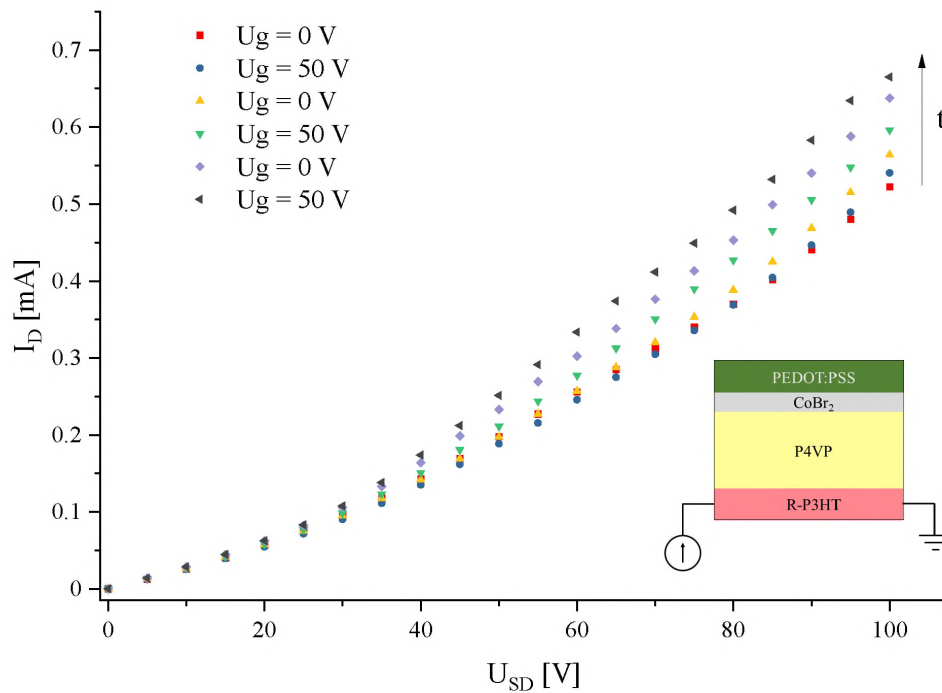
Figure 1.1. The drain current measured as a response to the gate voltage alternated between 0 V and 50 V, the inset in the bottom right corner illustrates the scheme of the device

On the other hand, the observed effect of conductance variation has been attributed to Na^+ ions stabilizing the PSS molecule in the gate material. The Na^+ ions are relatively small and mobile; therefore, we assumed that the external potential applied to drain and source electrodes forces the ion displacement, causing a change in the overall distribution of the electric field in the channel of the device. However, to be able to prove this hypothesis,

the existence of the dipole-induced electric field, which increases the conductance of R-R-P3HT, had to be proved.

To separate these two effects, the conduction increase and the time evolution of the system, the devices were prepared in a two-terminal geometry to study only the first effect. As it is a subject of our different work[10], only the most relevant findings, which are essential to understand the operation of the device, are presented herein.

The devices consisting of R-P3HT, P4VP and $CoBr_2$ have been investigated in terms of conduction increase related to the distance between the semiconductor and the dipole layer[10]. The results of this study demonstrated that the value of current in the modified devices increases by an order of magnitude compared to the reference samples. Both device types were fabricated with a consistent P4VP film thickness of 64 nm to preserve the distance between the dipole layer and the semiconductor. The plot, presented in **Figure 1.2**, shows the results of average current values with standard deviations calculated from five different device measurements. As depicted, the current increase in Co-modified devices is significant, up to an order of magnitude, compared to reference devices.
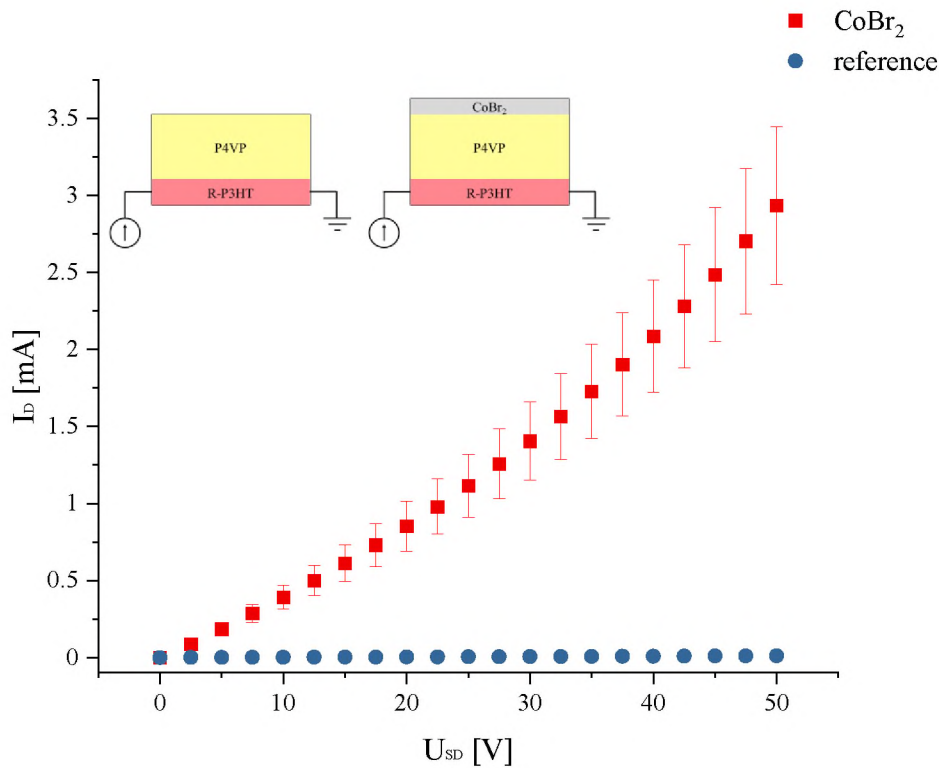

Figure 1.2. Current– voltage characteristics measured for reference (blue circles), and Co-modified devices (red squares), the inset illustrates the scheme of both systems

In theory the dipole moment-induced potential depends on the distance r as $\frac{1}{r^2}$. As depicted in **Figure 1.3**, the thickness of the P4VP layer, which is equivalent to the distance between the dipole layer and semiconductor, impacts the current flow through the device in a way, which is consistent with the theoretical prediction.
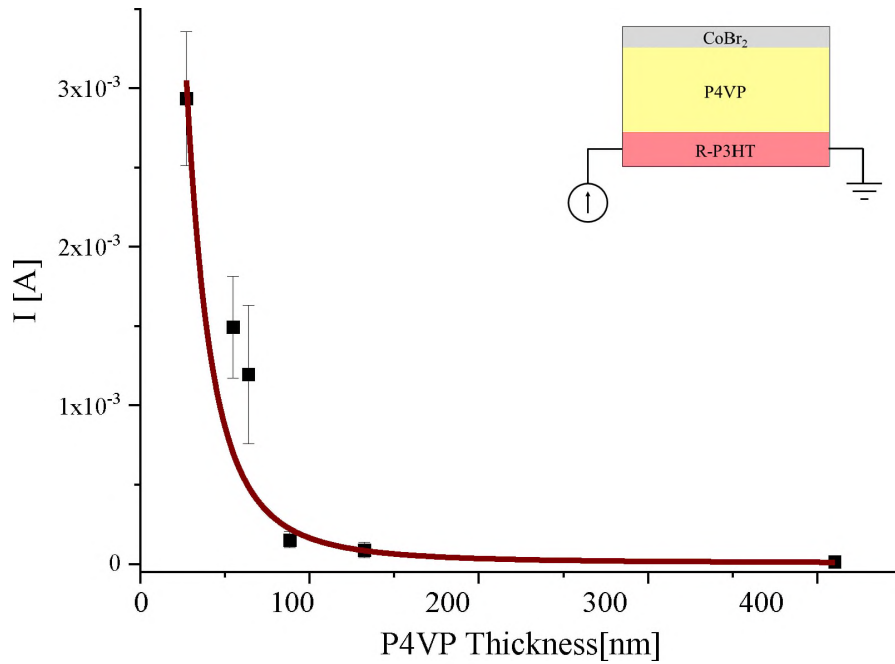
Figure 1.3. Current flow through the channel of Co-modified devices for a 50 V bias as a function of the P4VP film thickness, scheme of the device is depicted in inset. The brown line shows the experimental data fitted to the equation in which current flowing through the device depends on the P4VP thickness as $\frac{1}{r^2}$

Through these findings, the presence of a dipole-induced electric field, which introduces additional potential into the device channel and increases the conductance of R-P3HT, has been demonstrated. These findings are relevant to the hypothesis about the modulation of electric field intensity caused by ion mobility, which manifests itself in the form of a hysteresis loop.

To understand the second effect observed in the system, the time evolution of devices' current-voltage characteristics, the system was prepared in the initial architecture as a two-terminal device with PEDOT:PSS layer exchanged to PSS. The material change was dictated by the aim to simplify the system and gain more control over the hypothesized ion migration.

In the two-terminal system, the PSS serves as a polymer matrix, stabilized by sodium ions, which is further admixed with potassium ions (K^+). The addition of potassium ions is dictated by a larger ionic radius of K^+, which should manifest in the devices'

performance, and change the dynamics of relaxation processes. PSS, despite containing sodium ions, was selected as a matrix material as it produces consistent layers with precisely defined thickness, which was an issue with other materials considered for this purpose.

The current-voltage characteristics of a device measured in between each preparation step are presented in **Figure 1.4**. As depicted, the current measured for the R-P3HT increases after the deposition of the P4VP layer, and the next step, $CoBr_2$ modification, increases the values of the measured current even further. As mentioned earlier, the conduction increases with each consecutive preparation step, up to this point, is attributed to the dipole moment-induced electric field. However, the device behaviour is significantly altered by the deposition of a PSS layer enriched with 1% of K^+ ions. The introduction of a polymer matrix containing a reservoir of mobile ions leads to the appearance of a hysteresis loop in the device's current-voltage characteristic. The measured current values suggest dynamic conductance modulation in the system, which can be attributed to the interactions between ions in the PSS layer and the P4VP layer. It is also noteworthy to notice the direction of conductance changes, as indicated by arrows, which is very uncommon.
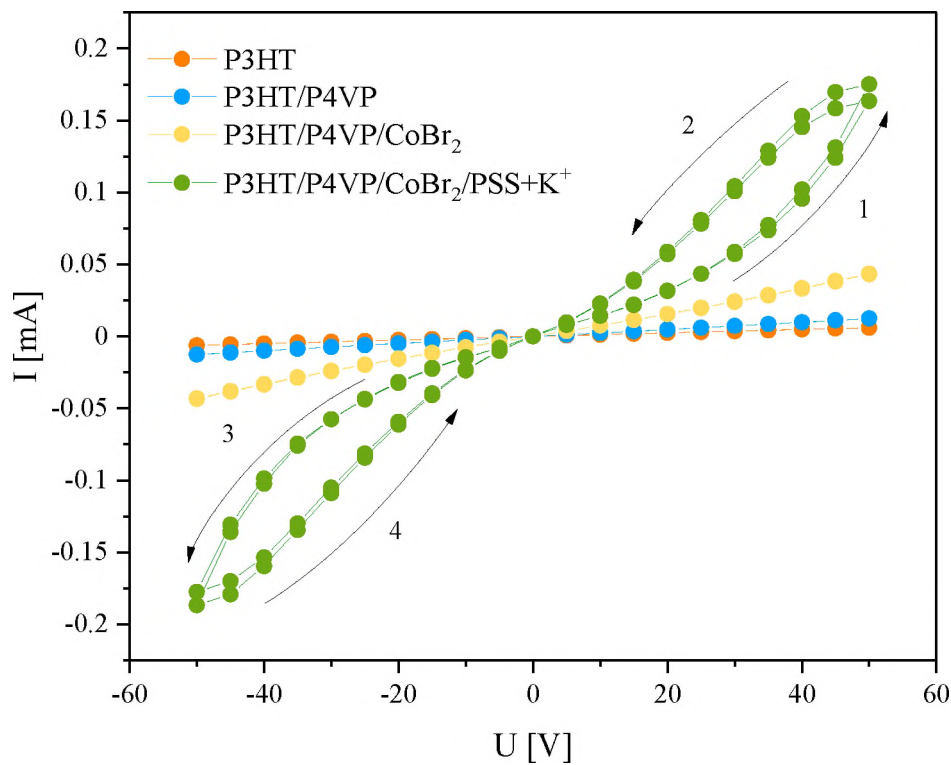
Figure 1.4. Current-voltage characteristics measured between consecutive preparation steps

The appearance of a pinched hysteresis loop in the current-voltage characteristic of the device classifies it as a memristive device with, up to this day, a new principle of operation. This dissertation aims to study this novel type of organic memristive device and explore its suitability for integration into neuromorphic systems. The investigation includes the study of the device's unique principle of operation, its response to various stimuli, and its ability to mimic synaptic plasticity, which is a critical feature for mimicking the learning processes occurring in the human brain. The aim of this work is to contribute to the development of field of organic memristive devices as a promising alternative to non-organic materials. The goal of this research is to identify the potential of these devices as a building block for next-generation neuromorphic computing systems.

CHAPTER Two   – Theoretical background

The aim of this Chapter is to introduce the most important concepts necessary to understand the topics covered in this thesis. At first, this theoretical background provides a short introduction to memristor and memristive devices based on symmetry between the four passive elements. It is followed by a review of memristive devices based on phenomena underlying their memristive character and the choice of the materials. At last, the concept of neuromorphic computing and Spiking Neural Networks is briefly introduced in the context of possible applications of memristive devices and the direction of trends in future research.

2.1. Memristive devices

The concept of a memristor, a fourth passive circuit element, was introduced by Leon Chua in 1971[1] long before its' physical realization. The name of the element combines its two features *mem*ory and resi*stance*, meaning that the devices' resistance depends on the past events[11]. Its existence was predicted based on conceptual symmetry between the capacitor, resistor and inductor, shown in **Figure 2.1**. The equations describing this symmetry are given by:

$$dq = C\,dv \ \text{ for capacitor,} \tag{2.1}$$

$$dv = R\,di \ \text{ for resistor,} \tag{2.2}$$

$$d\phi = L\,di \ \text{ for inductor,} \tag{2.3}$$

where: q – charge, C – capacitance, v – voltage, R – resistance, ϕ - flux-linkage, L – inductance. Two relationships – $dq = idt$ and $d\phi = v\,dt$ – combine Equations 2.1-2.3 and were used to formulate the equation describing memristor as:

$$d\phi = Mdq, \tag{2.4}$$

where M relates to memristance.

Theoretically, the memristor combines a relationship between charge q and ϕ flux-linkage, however, up to this day there were no reports in literature of devices, which satisfy this requirement[12]. Therefore, the devices reported so far can be classified as a more general group called memristive devices.
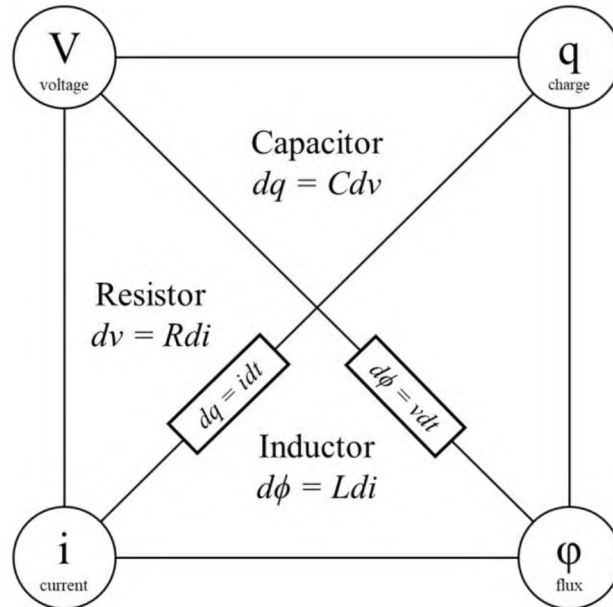
Figure 2.1. Conceptual symmetry of passive circuit elements

Memristive devices are believed to be a promising candidate for artificial synapses, which can be further integrated with crossbar arrays[13]. However, due to their unique features, they are believed to find different applications, for example as sensors[14]. Another interesting application is to use memristors in multi-level memory devices[15], due to multiple resistance states of some of the reported systems.

There are many reports of different realizations of memristive devices, varying in utilized materials or origin of memristive character, however, they all have one common feature, which is a pinched hysteresis loop[16].

Based on this feature, the first reports of memristive-like devices date back to the 19th century to arc lamp[17], followed by coherer[18] and hydraulic computers[11].

The first experimental realization of a memristive device was reported in 2008 by Strukov et. al.[2] in a TiO_2-based device. Since then, it has been a heavily investigated field of research, not only in the field of physics and materials science. What is interesting, memristive character can also be found in nature, for example, it was reported in Venus flytrap[19], aloe vera film[20], skin[21], and many more[22–24] showing the diversity of the field of memristive devices research.

2.2. Classification – materials and origin of hysteresis

Since the discovery of the first memristive device, there have been various reports of dynamic systems with parameters evolving in time. The memristive character was reported in devices utilizing both inorganic as well as organic materials.

Most of the reported inorganic memristive devices are based on transition metal oxides[2,25,26]. An interesting example of a memristive system is a resistance-switching device consisting of layers of co-sputtered Ag and Si active layer[25]. The gradient of Ag/Si mixture ratio results in Ag-rich (high conductivity) and Ag-poor (low conductivity) regions in the device. The Ag particles incorporated in the Si layer are responsible for conducting front formation in the system, which under the applied bias stays in continuous motion and changes the resistance of the whole device.

New memristive systems utilizing polymers, organic molecules, perovskites, or nanoparticles have emerged only recently[3,27–29]. The memristive nature of a device can vary depending on the characteristics of the materials involved in the process, e.g., conductive filament formation [25,30], charge trapping/detrapping[31], reversible redox reactions[32], ion migration[33] or phase transitions[31,34]. An interesting example of an organic memristive device based on conducting filament formation has recently been reported in a system utilizing cross-linkable polymer[33]. Neuromorphic arrays based on this system are reported to operate with high electrical and mechanical endurance due to the predefined localized ion migration paths in the polymer medium.

Another example of the developed memristive device is an artificial synapse network based on the proton-doped nanogranular SiO_2 in the laterally coupled transistor geometry. In this system, memristive effects, measured as post-synapse current flow between drain and source electrodes, are caused by proton migration under presynaptic pulse, defined as pulse applied to gate[35].

In almost every reported memristive device there is a reversible switch between two conduction mechanisms resulting in on-resistance state and off-resistance state. In 2020 Lu et al[36]. showed an artificial synapse system based on reduced graphene oxide, where conductivity is continuously modified during the increase and decrease of voltage. To this day it is the only example of such a device reported in literature.

Memristive devices can be also based on their ability to store information. Volatile devices are characterized by limited information retention time after which time

their conductance decays to its initial state[37]. On the contrary, the non-volatile devices remain in their programmed state until they are reprogrammed to a different one[38].

2.3. Neuromorphic computing and synaptic plasticity

The idea of neuromorphic computing was inspired by the structure and behaviour of the human brain. The brain is capable of processing information using energy-efficient and high-density neural networks[39], which consist of neurons and synapses. The aim of neuromorphic computing is to mimic the brain's functionality by incorporating artificial neurons and synapses into neuromorphic chips. By doing so it is believed to be a promising solution to the von Neumann bottleneck[40].

In one of the first mathematical descriptions of neurons, they serve as processing units capable of input signals (x_1, x_2, x_3, …) summation[41]. On the other hand, the synapses, which are connections between neurons, inform us about the strength of these connections[42]. They are responsible for the storage of synaptic weights (w_1, w_2, w_3, …), which multiply the respective input signals. The input signals received by the neuron are weighed by the synaptic weight, also called synaptic strength, and summed:

$$u = \sum_{i=0}^{n} w_i x_i, \qquad (2.5)$$

where u stands for the weighted sum of the input signals. It is further subject to a non-linear activation function, for example, sigmoid function[41].

Artificial Neural Networks (ANNs) are based on this concept and consist of artificial neurons, also called nodes, which are interconnected by artificial synapses[43]. The networks consist of multiple layers, where we can distinguish an input layer, at least one hidden layer and an output layer, as shown in **Figure 2.2**.
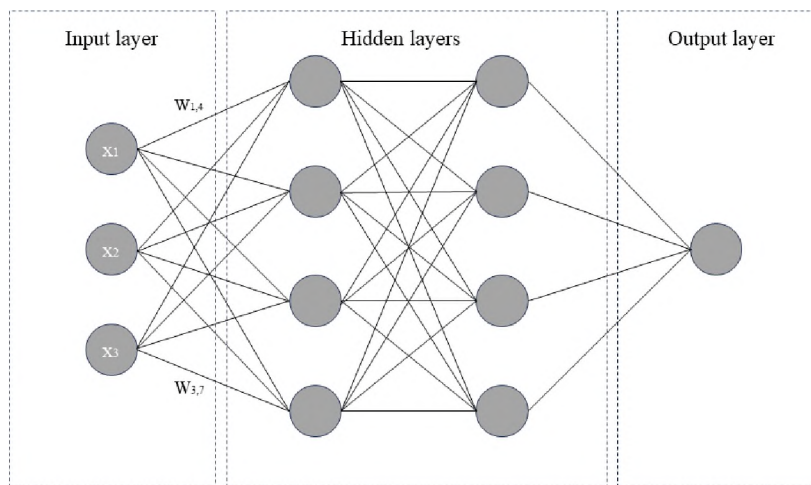

Figure 2.2. Schematic representation of an Artificial Neural Network

The input signal is fed into the input layer, which passes it through the network. The hidden layers transform the input data allowing the network to learn and return the output[39]. As the neurons in the hidden layer are connected to the input neurons with different weights, the algorithms used to train the network optimise the weights to obtain the desired output.

Looking at this problem from a device perspective, artificial neurons, which can successfully emulate the behaviour of biological neurons, can be achieved using CMOS technology[44]. However, to mimic the synaptic functions the devices must meet the criteria such as the ability to store and adjust the information. Therefore, volatile memristors are perfect candidates for artificial synapses, as they are dynamic systems with resistance spontaneously evolving in time. Based on this feature, memristive devices can emulate some of the basic synaptic functions. Among these is synaptic plasticity, a mechanism responsible for the brain's ability to learn by modifying the synapse strength based on the activity of the neurons connected to it.

One of the most prominent synaptic plasticity functions is Short-term Plasticity associated with a temporal strengthening or weakening of synaptic weight. Short-term Plasticity can last for a few minutes before it fades away and is believed to be responsible for the processing of information in the human brain[7,33].

The emulation of Short-term Plasticity has been reported in the literature as an incremental change of systems conductance caused by consecutive potentiating (Short Time Potentiation - STP) or depressing (Short Time Depression – STD) pulses[25,45,46]. If the synaptic strength is modified for a longer period it is considered as a Long-term Plasticity (LTP) which can last for weeks.

Another important synaptic plasticity modulation is Spike-timing Dependent Plasticity (STDP), which demonstrates the synaptic adaptation rule for Hebbian learning. The change of STDP depends on the timing of pre-synaptic (t_{pre}) and post-synaptic (t_{post}) spikes. Usually, the time difference between spikes is defined by:

$$\Delta t = \Delta t_{pre} - \Delta t_{post} \qquad (2.6)$$

If the pre-synaptic neuron spike precedes the spike of post-synaptic neuron ($\Delta t > 0$) it leads to Long-term Potentiation (LTP), otherwise, when $\Delta t < 0$, Long-term Depression (LTD) occurs.

The STDP measurements are performed by applying the pre-and post-synaptic signals to the device's terminals and measuring the system's conductivity change as a function of the time difference between both signals[25].

2.4. Spiking Neural Networks

Spiking Neural Networks (SNNs) are a different approach to brain-inspired computing. They are based on principles similar to ANNs, however, they employ learning rules and neuronal computations similar to the biological networks[47]. They operate in continuous time using discrete electrical signals to communicate within the network. Thanks to the short voltage spikes used in learning and inference, the SNNs are less power-consuming than ANNs[43].

Spiking Neural Networks' model incorporates the concept of time into its operation[43]. The spikes arrive at the neurons in so-called spike trains and the neuron fires only after reaching a certain threshold. Therefore, its' activity is based on the temporal correlation between the spike occurrences. This feature is believed to be applicable when dealing with dynamic information, for example, speech or visual gesture recognition[48].

Volatile memristors are believed to be good candidates for synapses in SNNs due to their volatility, meaning that after the spiking action the memristors' resistance, which changes as a response to the spike, will spontaneously go back to its initial state[42], just like in biological neurons. The timing between the spikes is essential in the SNNs information transfer, therefore the memristors for SNNs are required to emulate the STDP function.

Memristors were already reported to be successfully incorporated into neuromorphic systems as synapses integrated with CMOS technology[49,50]. They are believed to be a future building block of neuromorphic chips due to their high energy efficiency and high on-chip density. The neuromorphic architectures using memristors as synapses offer parallel computing, which is performed at the same location as data storage. This gives the advantage of a reduced data transfer rate and avoids the memory wall issue[51]. As the memristive device technology is still relatively new, there are many obstacles and limitations to overcome, therefore most of the reports refer to single devices or small-scale prototypes.

CHAPTER Three – Materials and methods

This chapter presents the materials and methods utilized within the scope of this thesis. The Materials section includes the main features of the materials and substrates used in the sample preparation process. The Methods section is divided into two parts. The first part covers the substrate cleaning and sample preparation procedures, emphasizing the importance of utilizing appropriate methods and tools to maintain the research quality and reproducibility. The second part of the Methods section concerns the techniques utilized to characterize the samples. It provides a brief description of the experimental methods utilized throughout this dissertation, allowing for an understanding of the methods' principles and the obtained results.
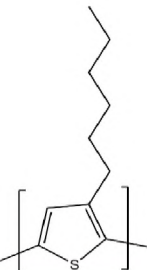
3.1. Materials

3.1.1. P3HT

Poly(3-hexyl thiophene) (**P3HT**) is one of the most commonly used p-type organic semiconductors. Because of its high carrier mobility, performance, and facile synthesis, it is often used in OFETs as a semiconductor or in OPVs as a donor[52,53]. Moreover, the crystallinity degree of P3HT, which plays a role in terms of its conductivity, can be increased by thermal annealing[54,55].

The P3HT chain consists of thiophene units and hexyl side chains. The side chain is responsible for the monomers' asymmetry and higher solubility, enabling material deposition from solution. However, the presence of a side chain is also responsible for the limitation of the backbone's conformation. Within the framework of this thesis, a Regio regular P3HT (**R-P3HT**) was utilized in the sample preparation process. The specification of the material is presented in **Table 3.1**.

Table 3.1. Specification of R-P3HT used within the framework of this thesis

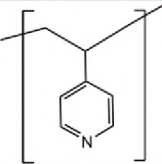|	
Full name	Poly(3-hexyltiophene)
Synonym	P3HT
Chemical structure	$(C_4H_2S)_n$
Chemical structure	
Regioregularity	95,2%
Molecular weight	36,600
Polydispersity index	2.0
HOMO/LUMO	HOMO = -5.2 eV, LUMO = -3.2 eV
Form and colour	Black powder
Solvents	Chlorobenzene, chloroform
Concentration	10 mg/ml in chlorobenzene
Supplier	Ossila Ltd

3.1.2. P4VP

Poly(4-vinyl pyridine) (**P4VP**) is an insulating polymer. Its monomer contains a pyridine ring and the vinyl functional group. Due to the presence of the pyridine rings, the monomer has a permanent dipole moment. P4VP has the capability of creating coordination bonds with other substances, which is another notable characteristic of this compound.

The nitrogen atom in the pyridine ring facilitates the formation of chemical bonds with other compounds, in particular with metal ions, forming strong complexes[56]. The specification of the material is presented in **Table 3.2**.
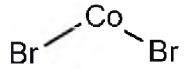
Table 3.2. Specification of P4VP used within the framework of this thesis

Full name	Poly(4-vinylpyridine)
Synonym	P4VP
Chemical structure	$(C_7H_7N)_n$
Chemical structure	
Molecular weight	Average 160,000
Form and colour	White flakes
Solvents	Ethanol, chloroform
Concentration	12,5 mg/ml in ethanol
Supplier	Sigma-Aldrich

3.1.3. Cobalt (II) bromide

Cobalt (II) bromide (**CoBr₂**) is an inorganic compound consisting of a d-block metal center – cobalt – and two bromide atoms. The complex possesses a high dipole moment, and the cobalt atom enables chemical bonding with other compounds. These two properties were utilized to crosslink the surface of a P4VP film with the CoBr₂, introducing an additional dipole moment to the system. Moreover, when the surface of P4VP is modified, the pyridine rings on the insulator's surface rearrange themselves, resulting in a greater overall dipole moment of the crosslinked system. The details of the material is presented in **Table 3.3**.

Table 3.3. Specification of CoBr₂ used within the framework of this thesis

Full name	Cobalt (II) bromide
Chemical structure	CoBr₂
Chemical structure	$\underset{Br}{\diagup} Co \underset{Br}{\diagdown}$
Molecular weight	218.74 g/mol
Form and colour	Blue powder
Solvents	Acetonitrile
Concentration	20 mg/ml in acetonitrile
Supplier	Sigma-Aldrich

3.1.4. Al₂O₃

Aluminium oxide (**Al₂O₃**) is an inorganic compound consisting of aluminium and oxygen atoms. Al₂O₃ is an electrical insulator with a wide bandgap, between 5.1 - 8.8 eV, depending on the synthesis method[57], and high breakdown reliability[58] making it suitable for various electronic applications. For instance, it can be used as a gate dielectric in transistors[59] or as a gas diffusion barrier[60,61]. The Al₂O₃ thin films can be deposited using Physical Vapor Deposition methods, which feature was exploited in this doctoral project.
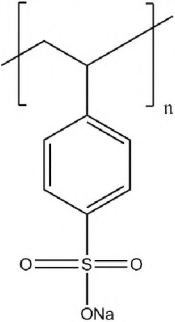
3.1.5. PSS

Poly (sodium 4-styrene sulfonate) (**PSS**) is a polyelectrolyte consisting of Na^+ cation and $C_8H_7NaSO_3^-$ anion. PSS is commonly used in a mixture with poly(3,4-ethylene dioxythiophene) (**PEDOT**) in order to stabilize the latter molecule. PEDOT:PSS is one

of the most commonly used organic materials in the field of organic electronics due to its' high conductivity, transparency, and stability[62].

In this thesis, PSS was employed both as a reservoir of sodium cations and as a matrix for materials containing other ions. The properties of PSS used in this work are listed in **Table 3.4**.
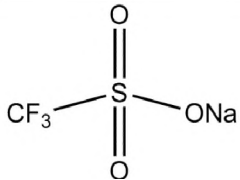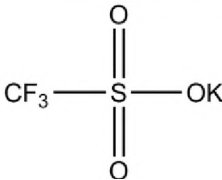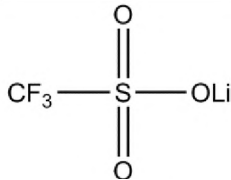
Table 3.4. Specification of PSS used within the framework of this thesis

Full name	Poly (sodium 4-styrenesulfonate)
Synonym	PSS
Chemical structure	$(C_8H_7NaO_3S)_n$
Chemical structure	
Molecular weight	Average 70,000
Form and color	Cream white powder
Solvents	Water, lower glycols
Concentration	20 mg/ml in distilled water
Supplier	Sigma-Aldrich

3.1.6. Trifluoromethanesulfonate

Trifluoromethanesulfonate (**$CF_3SO_3^-$**) is a functional group commonly known as triflate. The triflate anion exhibits weak coordination with the metallic cation. This property makes triflate salts a good reservoir of mobile ions and was utilized in this work to introduce sodium, potassium, and lithium ions into the polymer matrix. The properties of triflates are presented in **Table 3.5**. Triflates have found various industrial applications, from serving as reagents or catalysts in organic reactions to being used as electrolytes in lithium-ion batteries.

Table 3.5. Specification of triflate salts used within the framework of this thesis
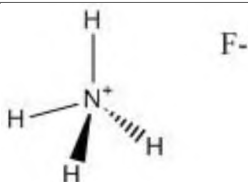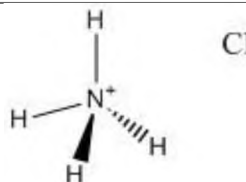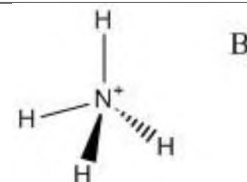
Full name	Sodium trifluoromethanesulfonate	Potassium trifluoromethanesulfonate	Lithium trifluoromethanesulfonate
Synonym	Sodium triflate	Potassium triflate	Lithium triflate
Chemical structure	CF_3SO_3Na	CF_3SO_3K	CF_3SO_3Li
Chemical structure	![CF3-S(=O)(=O)-ONa]	![CF3-S(=O)(=O)-OK]	![CF3-S(=O)(=O)-OLi]
Molecular weight	172.06 g/mol	188.17 g/mol	156.01 g/mol
Form and colour	White powder	White powder	White powder
Solvents	water		
Concentration	20 mg/ml in distilled water		
Supplier	Sigma-Aldrich		

3.1.7. Ammonium salts

Ammonium salts consist of an ammonium cation and an inorganic anion. They characterize high solubility in water and were utilized in this thesis as an agent introducing mobile anions to the polymer matrix. The ammonium salts utilized in this dissertation are ammonium fluoride, ammonium chloride, and ammonium bromide. Their properties are presented in **Table 3.6**.

Ammonium salts are commonly used in industry. Ammonium chloride and ammonium sulphate serve as fertilizers in agriculture and are considered to be the primary sources of nitrogen.

Table 3.6. Specification of ammonium salts used within the framework of this thesis

Full name	Ammonium fluoride	Ammonium chloride	Ammonium bromide
Chemical structure	NH_4F	NH_4Cl	NH_4Br
Chemical structure	![NH4+ F-]	![NH4+ Cl-]	![NH4+ Br-]
Molecular weight	37,04 g/mol	53,49 g/mol	97,94 g/mol
Form and colour	White, crystalline solid	White, crystaline solid	White, crystalline solid
Solvents		water	
Concentration		20 mg/ml in distilled water	
Supplier		Sigma-Aldrich	

3.1.8. S161 substrates for OFET

The Indium tin oxide (**ITO**) glass substrates for OFET were used as substrates in the process of sample preparation. The ITO finger electrodes are prepatterned on a glass substrate and act as the source-drain electrodes, enabling the preparation of 5 devices at once. The channel dimensions of 30 mm x 50 μm minimise the contact effects due to their relatively large size. The specification of substrates used in this work is presented in **Table 3.7**.

Table 3.7. Specification of OFET substrates used within the framework of this thesis

Substrate size	20 mm x 15 mm
Channel dimensions	$W \times L$: 30 mm × 50 μm
ITO thickness	100 nm
ITO resistance	20 Ω / square
Supplier	Ossila
Product code	S161

The scheme of substrates used in this thesis is shown in **Figure 3.1**. The yellow regions correspond to ITO electrodes deposited on glass substrate.
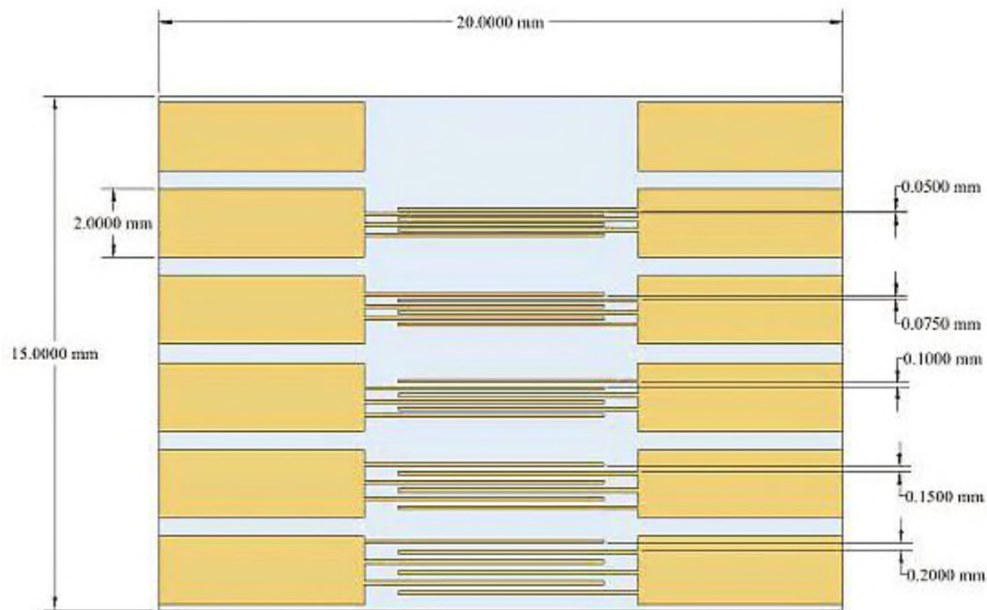

Figure 3.1. Scheme of the S161 OFET substrate[63]

3.2. Experimental methods

3.2.1 Atomic Force Microscopy (AFM)

Atomic Force Microscopy (AFM) is a non-destructive surface characterization technique providing information about the sample topography and mechanical properties in the nanoscale[64]. One of its advantages is the possibility to image both conductive and insulating samples with atomic and molecular resolution[65].

The technique utilizes a sharp tip attached to a cantilever, which when brought close to a surface, interacts with it. The information about the changes in the cantilever position corresponds to the change of force between the tip and the sample. It is collected by a quadrant photodiode, which detects a signal from a laser beam reflected by the cantilever, as shown in **Figure 3.2**. Therefore, the change in force between atoms at the tip and the atoms at the surface causes deflection of the cantilever, providing information about the sample topography[64]. The measured force depends on the distance between the tip and the surface as well as on their properties. The resolution of an AFM image is related to the geometry of the tip[66], as the sharper the tip the better the resolution can be achieved.

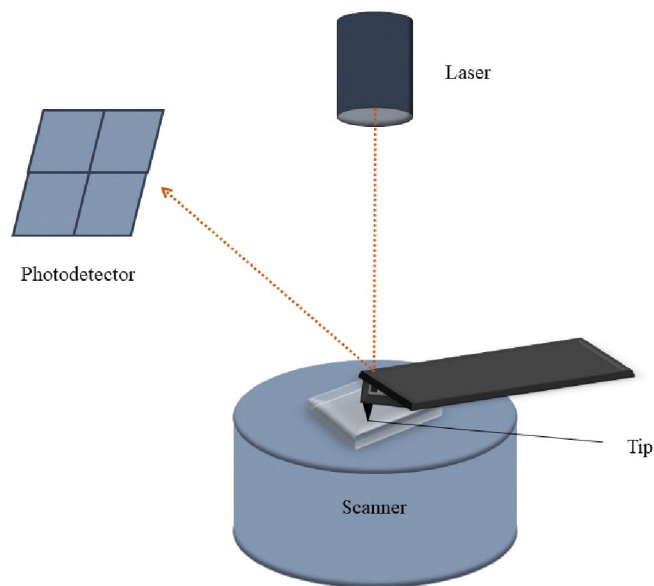*Figure 3.2. Schematic illustration of AFM working principle*

There are three main modes of operation in AFM measurements: contact mode, non-contact, and tapping mode. In the contact mode, the tip, and the surface stay in contact throughout the imaging, whereas in the non-contact mode, the cantilever is oscillating in close proximity to the surface and the changes of amplitude, caused by interaction with

the surface, is recorded[65,67]. In the tapping mode, the cantilever is oscillating vertically, making intermittent contact with the scanned surface. The mode provides higher resolution compared to contact mode by avoiding lateral-tip force[68].

The AFM can operate in various mediums, for example, air, vacuum, or liquid, which makes it a very useful and universal technique[65,67]. The technique has been employed throughout this dissertation to characterize the morphology of the prepared samples in air.

3.2.2. Electrical Characterization

The current-voltage measurements were performed under an argon atmosphere using a computer-controlled Keithley 2400 source meter unit.

The direct current-voltage characteristics were measured within the −50 V to 50 V range with a 2.5 V/s step.

The current-time measurements were performed using custom voltage sequencies with switching times below 125 ms for each measurement type, if not stated differently. *Temperature dependency measurements* were performed in a vacuum chamber using Keithley 2400 as a source meter unit and Eurotherm 2416 temperature controller. In order to cool down the sample to liquid nitrogen temperature it was brought in contact with a cold finger. Next, the contact between the sample and the cold finger was broken, and the current response of the sample was measured at eight chosen points, at temperature ranges: 1) −148.9∘C to −149.6∘C, 2) −123.5∘C to −122.5∘C, 3) −80.5∘C to −80.0∘C, −54.0∘C to −52.0∘C, 5) −20.9∘C to −20.0∘C, 6) −2.5∘C to 0∘C, 7) 8.0∘C to 9.0∘C, and 8) 22.4∘C to 22.5∘C. The current was measured as a response to voltage sequences of −50 V, -10 V, and 10 V. During the experiment the temperature of the sample was raised to room temperature at a slow rate without external heating.

3.2.3. Ellipsometry

Ellipsometry is a method providing information about thin films' refractive index and thickness, in some cases providing measurement accuracy within Å[69]. The technique measures changes in light polarization upon its' transmission or reflection on the surface of the sample. The method is suitable to characterize a wide range of samples, which reflect laser light.
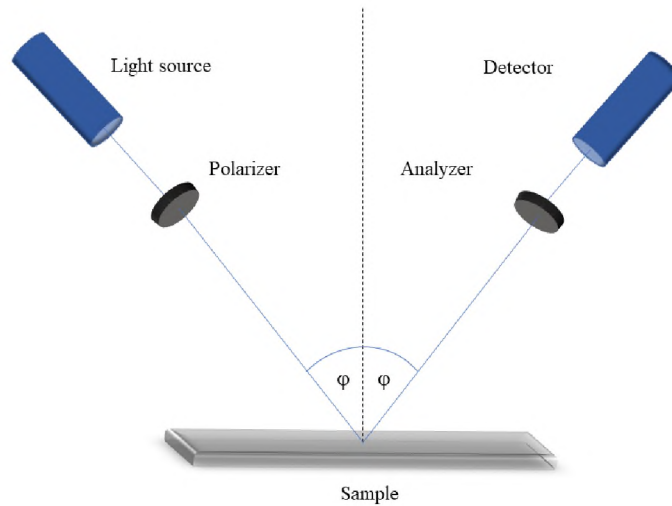
Figure 3.3. Schematic illustration of Ellipsometry measurement setup

In the experiment, as shown in **Figure 3.3**, a light with a well-defined polarization state is directed onto the sample. The light is reflected on the surface of the sample and changes in its polarization are measured and further analysed. The technique provides information about the layer thickness, surface roughness, electrical conductivity and many more. It was utilized throughout this dissertation to determine the thickness of individual layers.

3.2.4. Impedance Spectroscopy

Impedance Spectroscopy (IS) is a method, which allows characterisation of resistive and capacitive properties of materials. It is useful in studies of ionic and electrical conduction and can be performed in a wide range of frequencies[70]. During the impedance measurement mode, which is the equivalent of resistance in AC measurements, a response to the applied single-frequency voltage or current is measured. Usually, the impedance measurements are performed in the frequency domain, providing information about impedance vs. frequency dependency. As different conduction mechanisms have their own characteristic relaxation frequencies, impedance measurements performed in a wide range of frequencies can help to identify them.

The impedance measurements allow to measure its' two components: the real part Z' and the imaginary part Z''. The real part can be interpreted as an energy loss or resistance and the imaginary part can be interpreted as capacity. The impedance, as a complex function, can be given by:

$$Z = Z' + jZ'' \tag{3.2}$$

22

where j is the imaginary unit. The graphical representation of impedance can be accomplished using the Nyquist plot, which presents the dependence between the negative imaginary part (-Z'') and real part (Z') of impedance[71].

Additionally, impedance spectrometry allows us to determine the dielectric properties of materials in the frequency domain. It provides information about the permittivity of materials, and the relationship between the loss factor tanδ, the real part of permittivity ε' and the imaginary part of permittivity ε'' can be calculated as:

$$tan\delta = \frac{\epsilon''}{\epsilon'}.$$

(3.3)

The permittivity can be determined from materials' capacitance C and the samples' geometry – layer thickness d and electrode area[72] A – as follows:

$$\epsilon' = \frac{Cd}{\epsilon_0 A}$$

(3.4)

where ϵ_0 is vacuum permittivity. The relationship between the imaginary and real parts of the permittivity can be illustrated using Cole-Cole plot[73].

Impedance Spectroscopy has been utilized in this research to study the relaxation processes occurring in the sample. As ion mobility influences the operation of the device to a great extent, findings of the IS measurements played an important role in the development of this project.

3.2.5. Spin coating

Spin coating is a method of thin film deposition. It allows depositing a layer with a well-defined thickness on a flat surface. In this method the material is cast from solution, therefore, in the case of laterally arranged samples, the choice of appropriate solvent plays the key role in ensuring that the bottom layers are left intact. This technique is often used to deposit thin polymer films due to its' ease of use, low cost, and no need to provide vacuum conditions.

The process of film deposition can be divided into three consecutive steps. In the first step, a small amount of material solution is being casted on a still or slowly spinning substrate. Next, the substrate is set in rotational motion at high speed. Due to centrifugal force, the liquid is distributed on the surface and an excess of the solution drops down from the substrate. In the last part of the spin-coating process, the remaining solution drops off the substrate edges resulting in the formation of a thin film of material.

The film thickness d of the deposited material can be controlled by three factors: angular speed of rotation ω, concentration c, and the viscosity of the solution ρ [74]. The relationship between these parameters is given by:

$$d \sim \frac{c\rho}{\omega^{-\frac{1}{2}}} \qquad (3.5)$$

3.2.6. PVD

Physical Vapour Deposition (PVD) is a method of thin film deposition from a vapour phase. Throughout the process, the atomized or vaporized material is emitted from the source, also called the target. It can be carried out through plasma technology, sputtering, thermal evaporation, gas sources, and other methods[75].

After being extracted from the target, the deposited material condensates on a substrate atom by atom or molecule by molecule. The thickness of the resulting film can vary between angstroms and millimetres, depending on the PVD technique[76]. In order to reduce film contamination, the whole process takes place in a vacuum environment.

3.2.7. Magnetron Sputtering

Magnetron Sputtering is a type of Physical Vapor Deposition (PVD). It is a method of thin film deposition based on the sputtering of the deposited material in an inert gas environment.
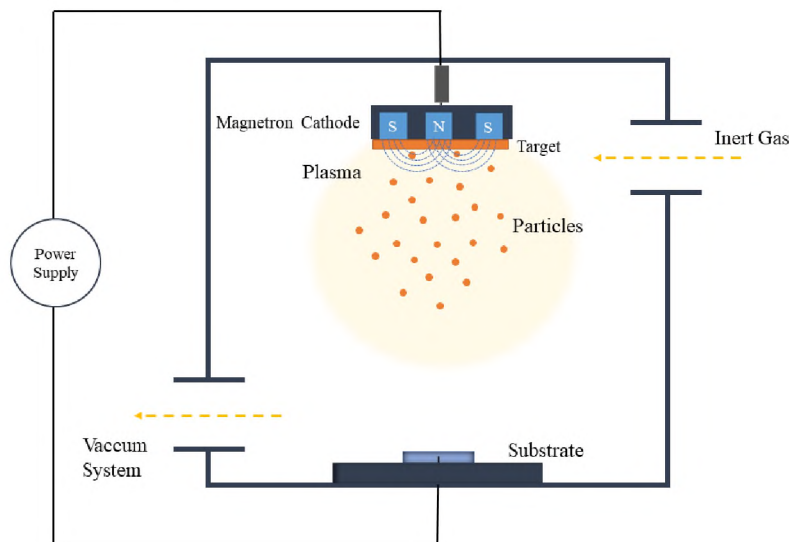

Figure 3.4. Scheme of Magnetron Sputtering Process

During the process, the deposited material, often referred to as the target or cathode undertakes a phase transition to vapour phase. In order to do so, the target is bombarded

with energetic ionic gas, which originates from magnetron[77]. As a result, the target is sputtered releasing atomic-sized particles which further condense on the substrate forming a film. **Figure 3.4** illustrates a schematic diagram of Magnetron Sputtering process.

Among PVD processes, Magnetron Sputtering allows for more control over grain size and stoichiometry of deposited films[78]. Therefore, the technique is widely used in industry to deposit high-quality films of a variety of materials[77]. These features have been employed in this dissertation to deposit a thin film of Al_2O_3 without any substantial damage to the inner layers of the sample.

3.2.8. Profilometry

Profilometry is a method of surface profile measurement. It enables to record 2-dimensional and 3-dimensional images of the surface provide information about the profile of the sample and its roughness. The technique utilises a stylus to scan the surface of a sample and generate its' image[79]. During the measurement, the stylus is in contact with the surface, which in certain conditions, for example, soft matter, can lead to sample deformation. During the measurement, the contact force, distance, and velocity of the stylus can be adapted. In the case of the 2D measurement the stylus is moved vertically, however in the 3D measurement, the stylus is moved both vertically and laterally at the set measurement step resulting in a 3D map of the surface. In this doctoral thesis, the profilometry technique was utilized as a complementary technique to determine the thickness of individual layers.

3.2.9. Scanning Electron Microscope (SEM)

Scanning Electron Microscopy (SEM) is an imaging technique which is based on the interaction between a focused electron beam and the sample. It provides information about the sample topography and chemical composition, which combined with high resolution, even up to 1 nm[80] for some SEMs, makes it a technique that is widely utilized in science and industry.

The first SEM was built in 1935 by Knoll and was limited in resolution to 100 μm. The theoretical explanation of the methods' principle was introduced in 1938 by von Ardenne and has remained unchanged up to this day[81]. The operating principle of SEM lies in the interactions between the focused electron beam and imaged sample and, in terms of working principle, is analogical to optical microscopy, where instead

of a focused electron beam, light is used as an illumination source[82]. The use of electrons rather than light is dictated by their shorter wavelength, which allows us to obtain higher imaging resolution by overcoming the diffraction limit of light. The scheme of the SEM experimental setup is shown in **Figure 3.4**.

In order to image the sample using SEM, a high-energy electron beam is focused on a sample causing the sample response in the form of electrons or X-rays which are further analysed.

The electron beam is emitted in the electron gun. Its energy can be adjusted according to the type of imaged sample. Accelerated electrons are further focused in a column consisting of electromagnetic lenses and apertures. To prevent the interactions between the electron beam and gas molecules the SEM operates in high vacuum environment. This allows to obtain high imaging resolution.
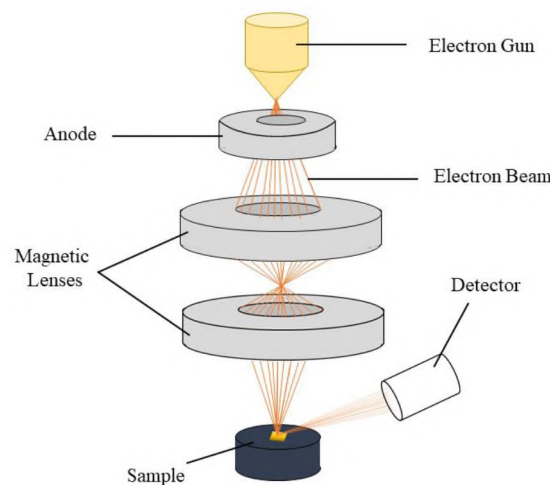
Figure 3.5. Scheme of Scanning Electron Microscope

When the high-energy electron beam, also known as Primary Electron (PE) Beam, reaches the imaged specimen, it interacts with it, and, as a result, electrons or X-rays are released from the sample. The Primary Electrons interact with atomic nuclei and electrons of the specimen, resulting in their scattering or absorption. As a result of such an interaction between PE and the specimen, signals such as Secondary Electrons (SE), Backscattered Electrons (BSE), X-rays or light (cathodoluminescence) can be generated. The PE Beam interacts with the specimen in the near-surface area, meaning that the PE interact not only with the surface but also with atoms within a certain depth of a sample. This teardrop-shaped interaction volume, as shown in **Figure 3.6**, depends on the atomic

number (Z) of the specimen, its' density, and the energy of the Primary Electron Beam. The interaction volume increases with the higher kinetic energy of the PE, however in terms of the atomic number and density of the sample, the higher these quantities the lower the interaction volume.
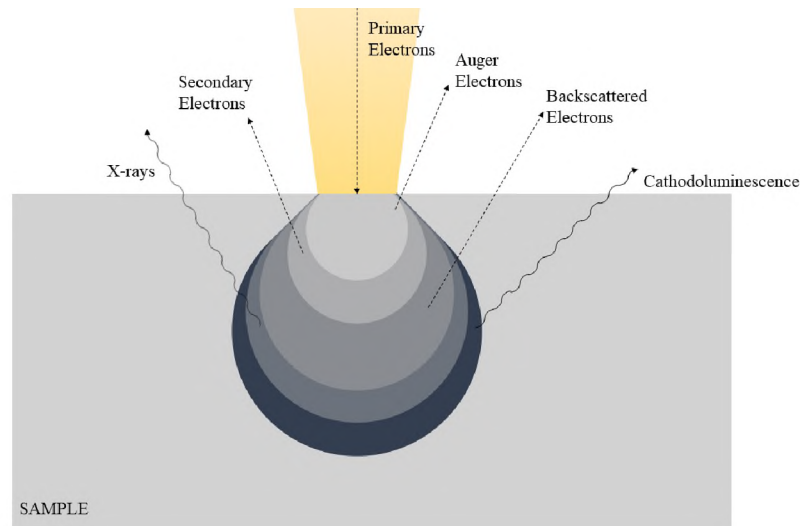

Figure 3.6. Illustration of interactions between the Primary Electron Beam and the imaged specimen and the resulting sample responses

Two of the most commonly used signals generated in SEM are SE, which inform about the topography and morphology of the specimen, and BSE which provide contrast between domains differing in chemical composition.

The SE are a result of inelastic interaction between PE and the sample. The PE, through energy transfer, eject the electrons from the valence or conduction bands of the specimen. The SE mean-free path is very short, which means that the information from the deeper parts of the specimen is absorbed by the specimen. This leads to highly localized information about the topography and morphology of the surface and regions in the near-surface, allowing for the high resolution of imaging.

On the contrary, BSE provide information from deeper regions of the sample and are a result of the elastic scattering of PE. The BSE are PE which are backscattered or reflected back by interacting with the specimen atoms. The contrast between different elements is related to their atomic number (Z). Because the electrons are backscattered stronger by elements with higher atomic numbers, the signal from these elements appears to be brighter compared to elements with lower atomic numbers.

The outcoming signal is further analysed providing qualitative information about the topography, morphology, chemical composition and many more.

3.2.10. Simulations

The simulations presented in this thesis were performed using Python programming language. The simulation parameters were selected to match the experimental parameters of the selected measurements. The model of the device and detailed description of simulations is the subject of Chapters Five, Six and Eight.

3.2.11. White Light Reflectance Spectroscopy (WLRS)

Spectroscopic Reflectometry is a method of determining a thin film's thickness. The method is non-destructive and utilizes a light beam, as shown in **Figure 3.7** in black. During the measurement part of the incoming light beam is reflected from the surface (orange), and part of it is transmitted inside the thin film (grey) being further reflected at its' bottom interface (green). Through the multiple reflections, the interference of the beams occurs (blue)[83]. The ratio of the intensity of the outgoing and incoming waves, called reflectance, is further detected, and analysed allowing us to calculate the layer thickness of the specimen[84,85].
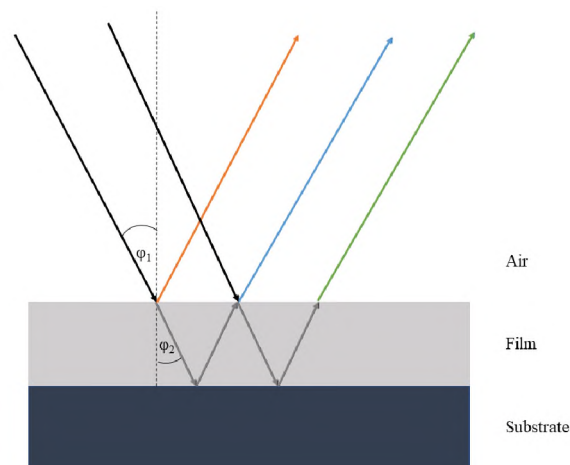
Figure 3.7. Scheme of Spectroscopic Reflectometry measurement. The orange beam is a beam reflected from the surface, the blue one is the beam which is a result of interference between the beams reflected from the surface (orange) and the one reflected at the interface film-substrate (green)

3.2.12. Time-Of-Flight Secondary Ion Mass Spectrometry (TOF SIMS)

Time-of-flight (TOF) Secondary Ion Mass Spectrometry (SIMS) is a technique used for a detailed analysis of chemical composition. It relies on an analysis of the mass spectrum of secondary ions emitted from a specimen's surface after it is bombarded by energetic primary ions or particles.

The secondary ions are only a small part of species emitted as a result of surface

bombarding. The majority of emitted species are neutral, therefore they cannot be detected and further analysed by the mass spectrometer.

As mentioned before, the method uses a beam of ionized particles, called a primary beam, to sputter the imaged surface and analyse the secondary particles emitted from the sample. The sputtered ions are analysed in terms of their mass based on their time of flight. Ions with different masses will differ in their time of flight to the analyser allowing to detection of a complete mass range in a single event[86]. The schematic illustration of the TOF-SIMS is shown in **Figure 3.8**.
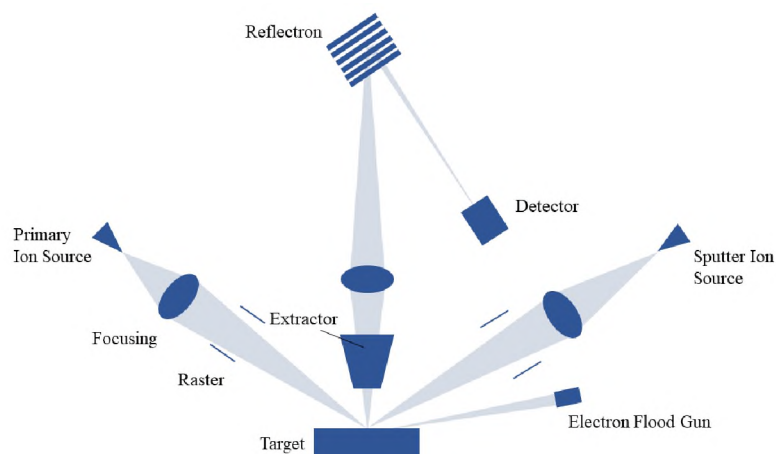

Figure 3.8. Schematic illustration of TOF-SIMS experimental setup

There are two basic modes of SIMS: static mode, which utilises a single ion gun to analyse the surface, and dynamic mode with two ion guns: a primary gun to analyse the surface, and a sputtering gun to reveal the inner layers of the sample for further analysis. Although the technique is regarded as a destructive one, one of the modes of the measurements, static mode, damages only the surface of the sample.

In the static mode, the technique provides information about the chemical composition of the surface. In this mode, an extremely low dose (less than 10^{13} ions per cm^{-2})[87] of primary ions, emitted from the primary gun, is used to bombard the surface. Such a low dose means that throughout the whole experiment, less than 1% of atoms or molecules on the top of the surface are impacted by the primary ions. As a result, statistically, no spot on the surface should be hit by primary ions more than once within the experiments' time scale. It also means that most of the specimens' surface remains unchanged or insensible to local effects of sputtering or removal of various species, leading to over 95% of the detected secondary particles originating from the top two layers of specimen[86]. Hence, the static mode of SIMS is, in some cases, regarded as a technique which does not lead to sample damage.

In contrast, the dynamic mode of SIMS gives us additional insight into samples' bulk properties, for example, it allows us to determine the depth distribution of compounds, by obtaining 3D profiles of the sample. This extra information is obtained through subsequent sputtering of the sample with the sputtering gun, to reveal the inner layers of the specimen without introducing too much damage to the revealed surface, followed by the primary ions from the analysing gun, which sputter the revealed surface to analyse its composition. As a result, the dynamic mode of the measurement causes irreversible damage to the sample, providing at the same time very precise information about the depth profile of the sample. The importance of using a proper sputtering gun for a specific sample type should be stressed, as it impacts the depth and yield of sputtering. For example, using polyatomic ion beams proves to be more appropriate while profiling organic samples, as they penetrate to lower depths causing less damage and enhancing sputter and secondary ion yields for molecular secondary ions[88].

3.3. Preparation methods

3.3.1. Material solutions preparation

The materials solutions were prepared in glass vials with Teflon-secured cups. To ensure cleanliness, they were weighed using spatulas, previously cleaned in an isopropanol ultrasound bath.

R-P3HT

The semiconductor solution was prepared in an inert gas atmosphere by weighting an adequate amount of the semiconductor and dissolving it in chlorobenzene to obtain a concentration of 10 mg/ml. It was then left on a hotplate at 50°C overnight to ensure that the material dissolves completely. Glass tools were exclusively used for the solution preparation process, as the chlorobenzene was shown to dissolve other tools.

P4VP

The insulator solution was prepared a day before the sample preparation to ensure that the polymer was well dissolved. The appropriate amount of insulator was weighted outside of the argon-filled glovebox. It was then transferred to the glovebox and dissolved in ethanol to obtain a concentration of 12,5 mg/ml and left on a hotplate at 50°C overnight.

CoBr$_2$

To prepare a 20 mg/ml solution of CoBr$_2$, the necessary amount of CoBr$_2$ powder was dissolved in acetonitrile within an argon-filled glovebox. The solution could be used immediately after the preparation or stored in the glovebox at room temperature.

Triflate and Ammonium salts

Triflates with K$^+$, Na$^+$, Li$^+$ cations and Ammonium salts containing Br$^-$, Cl$^-$, and F$^-$ anions were prepared outside of glovebox a day before mixing them with the PSS matrix. The 20 mg/ml solution was made by dissolving the salts in a proper volume of distilled water. It was then left overnight to ensure that the material dissolves completely.

PSS

The PSS solution was prepared a day prior the sample preparation to ensure that the polymer was well dissolved. The appropriate amount of PSS was weighted outside of an argon-filled glovebox and dissolved in distilled water to obtain a concentration of 20 mg/ml. It was then left overnight to fully dissolve and transferred to the glovebox before use.

To prepare PSS solutions containing ions (K$^+$, Na$^+$, Li$^+$, Br$^-$, Cl$^-$, F$^-$), the same method was employed. It involved dissolving the PSS solution in a smaller volume of deionized water, followed by adding the corresponding salt solution to achieve a final concentration of 20 mg/ml with the desired weight percentage of added salt.

3.3.2. Substrate cleaning

3.3.2.1. Establishing the substrate cleaning procedure

The device preparation process always starts with a thorough substrate cleaning procedure. To prevent material contamination and ensure accurate and reliable experimental results it is essential to ensure that substrates are properly cleaned from any organic or non-organic remains. Even a minor residue left on a substrate can introduce impurities into semiconductor, potentially altering the performance of the entire device and leading to unreliable results.

To determine the optimal substrate cleaning procedure, several methods, which are summarized in Table 3.9, were employed.

Table 3.9. Details of methods employed in substrate cleaning procedures

Step	Method 1	Method 2	Method 3	Method 4	Method 5
1	15 minutes sonication in hot deionized water + 5% surfactant		30 minutes sonication in hot acetone		30 minutes sonication in hot deionized water
2	15 minutes sonication in hot chloroform	30 minutes sonication in hot deionized water	Nitrogen stream drying		Nitrogen stream drying
3	30 minutes sonication in hot isopropanol	Air drying	30 minutes sonication in hot isopropanol		30 minutes sonication in hot acetone
4	24 hours immersion in isopropanol	-	Nitrogen stream drying		
5	Nitrogen stream drying	-	60 seconds oxygen plasma cleaning	-	30 minutes sonication in hot isopropanol
6	60 seconds oxygen plasma cleaning	-	-	-	Nitrogen stream drying
7	-	-	-	-	30 minutes sonication in hot deionized water
8	-	-	-	-	Nitrogen stream drying
9	-	-	-	-	60 seconds oxygen plasma cleaning

The effectiveness of the methods was determined based on the performance of R-P3HT layer, which was spin-coated on the substrates right after the cleaning. The current-voltage characteristics of the prepared samples are presented in **Figure 3.9.**
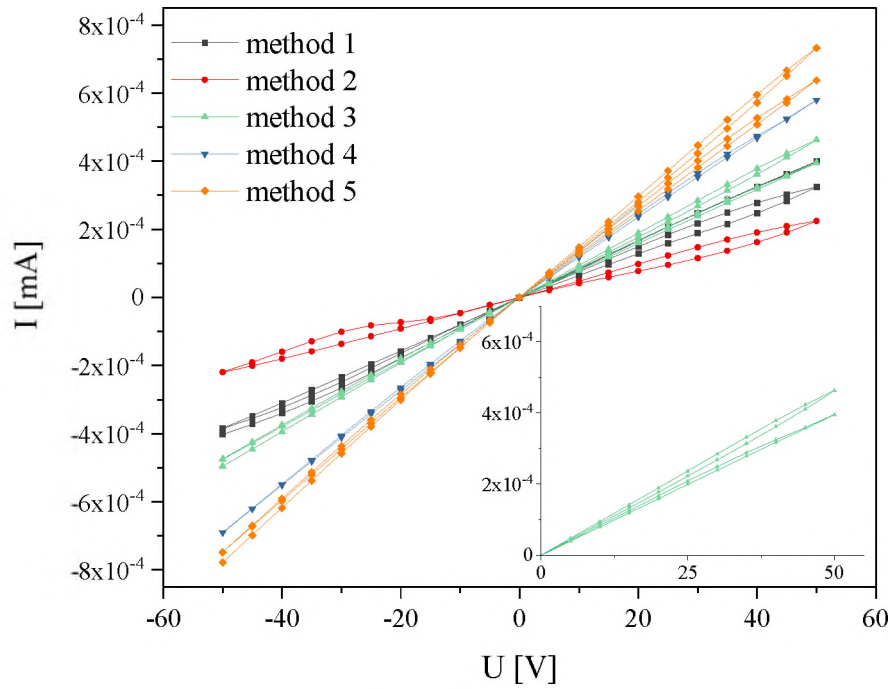
Figure 3.9. Current-voltage characteristics of R-P3HT measured on substrates which were cleaned using different procedures. The inset shows details of a sample prepared using third substrate cleaning method

As can be seen in Figure 3.9, methods 1, 3, and 5 leave an unknown residue on the surface of the substrate, leading to the R-P3HT contamination, which is seen as a change in the current response over time. The instability of R-P3HT is highly undesirable as it undermines device performance. The R-P3HT was originally chosen as a semiconductor due to its repeatability and high control over its performance, therefore purity of the material is crucial.

Due to high variability of the devices prepared on substrates cleaned with method 4, the devices prepared utilizing method 3 were selected to be further examined.

Figure 3.10 a) shows the current-voltage characteristic of R-P3HT prepared on substrate cleaned according to method 3. The procedure is described in detail below. As it can be seen in Figure 3.9 a), the R-P3HT instability remains at a level of hundreds of nano amperes, which in the case of the organic semiconductors is an acceptable performance. Moreover, after spin-coating of the P4VP layer the operation of the device remains stable without any significant changes, as seen in **Figure 3.10 b)**.
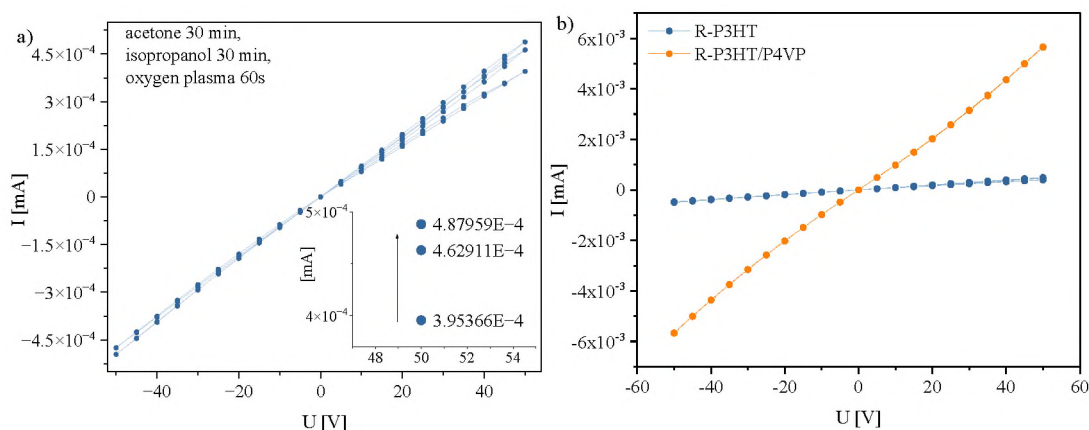
Figure 3.10. a) the current-voltage characteristic of R-P3HT prepared on a substrate cleaned with method number 3; the inset shows the difference between currents measured at +50 V in each consecutive measurement cycles; b) current-voltage characteristic of R-P3HT (blue) and R-P3HT/P4VP (orange) prepared on a substrate cleaned with method number 3

3.2.2.2. The cleaning procedure

Based on the results presented above method 3 has been selected as the substrate cleaning procedure and has been performed as follows.

The prepatterned ITO substrates were first cleaned in a hot acetone ultrasound bath for 30 minutes. Acetone tends to leave a small residue while evaporating, therefore the substrates were dried out using a stream of nitrogen. It was then followed by a 30-minute hot isopropanol ultrasound bath to remove the remaining non-polar compounds. The remaining solvent was rinsed from the substrate with a nitrogen stream. Lastly, the substrates were treated with oxygen plasma for 30 seconds, which not only removes the remaining organic residue but also improves the surface adhesion. In summary, the process was performed as follows:

1. Hot acetone ultrasound bath – 30 minutes.
2. Nitrogen stream rinsing.
3. Hot isopropanol ultrasound bath – 30 minutes.
4. Nitrogen stream rinsing.
5. Oxygen plasma treatment – 30 seconds.

3.3.3. Sample preparation

The sample preparation was performed in four consecutive steps in an inert gas-filled glovebox. First, the semiconducting layer was deposited by the spin-coating method on a previously cleaned substrate. The thin film was removed from the edges of the substrate to expose the ITO electrodes and ensure contact between the sample holder contact pins and electrodes. Then the insulating layer was deposited by spin-coating and the electrodes

were carefully exposed making sure to leave the semiconducting layer covered by an insulator. In the third step, the surface of the insulator was modified with a cobalt (II) bromide. Lastly, a thin film containing ions was deposited using spin-coating.

Detailed information about each preparation step is presented below. The details regarding the preparation and layer thickness of subsequent material layers are presented in Table 3.10.

Table 3.10. Layer thickness and preparation process details of materials used in the samples

Layer	R-P3HT	P4VP	CoBr$_2$	PSS/PSS+ions
Preparation method	Spin-coating		Immersion in CoBr$_2$ solution	Spin-coating
Spin-coating speed [rppm]	300 1000 3000	300 2000 3000	-	300 1500 3000
Thickness [nm]	70	135	Atomic layer	40

Semiconductor deposition

The R-P3HT solution was cast onto a rotating substrate at 300 rpm through a glass pipette. After 3 seconds, the speed of rotation was set to 1000 rpm for 60 seconds. In this step, the excess solution drops off from the substrate, and the thin film was formed through solvent evaporation. Lastly, the speed of rotation was set to 3000 rpm to assure that the remaining solvent evaporates from the edges of the substrate. After the spin-coating, the edges of the substrate were gently wiped with a chlorobenzene-soaked pad to enable contact between the holder pins and the ITO electrodes.

Within the framework of this thesis, it was crucial to maintain the quality of the semiconducting layer to ensure the proper functioning of the entire device. A significant aspect in addressing this issue was the preparation of the R-P3HT thin film. By utilizing appropriate glass tools, the purity of the semiconductor could be preserved, as depicted in **Figure 3.11**. The plot shows the current-voltage characteristics of samples prepared one after another using plastic tools. The only difference in the way the samples were prepared was the duration for which the R-P3HT solution was kept in a plastic syringe before being poured on a substrate. As can be seen, the performance of both devices is significantly different. The R-P3HT film prepared first, signal in black, exhibits a notable instability in regard to measured current. Its' current-voltage characteristic, instead of being linear, shows a current increase after each measurement cycle combined with a narrow hysteresis loop.

The performance of the R-P3HT layer changes even more drastically if the solution is stored in the plastic syringe longer e.g. 5 min, as shown in Figure 3.11 in red. The measured hysteresis loop, related to R-P3HT contamination, compromises the samples' utility as a part of the studied memristive device, due to its instability. What is also worth noting, is the reversed direction of the change of the R-P3HT's conductance compared to the operation of the studied memristive device.
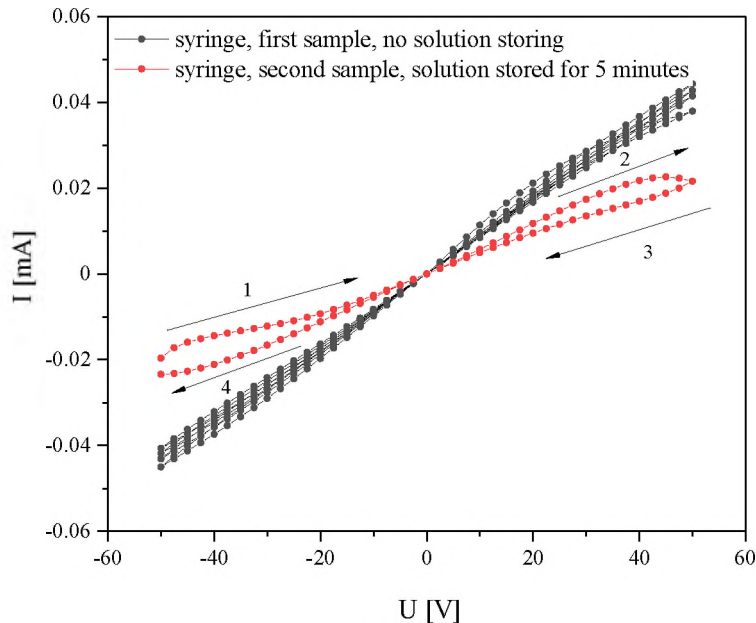

Figure 3.11. Current-voltage characteristics of samples a R-P3HT casted from a plastic syringe right after filling it in with solution (black), and after storing the solution in syringe for 5 minutes (red)

Considering the syringe-induced R-P3HT impurity, two additional samples were prepared utilizing only glass tools. The measured current-voltage characteristics for samples poured out of glass pipettes are presented in **Figure 3.12**. As can be seen from signals in blue, yellow, and green, the use of glass tools eliminates semiconductor contamination, resulting in the stable operation of R-P3HT. The second sample, signal in yellow and green, was measured twice, keeping a 15-minute interval between the measurements, to examine the R-P3HT stability. The results prove that there are no significant changes in the R-P3HT current response.
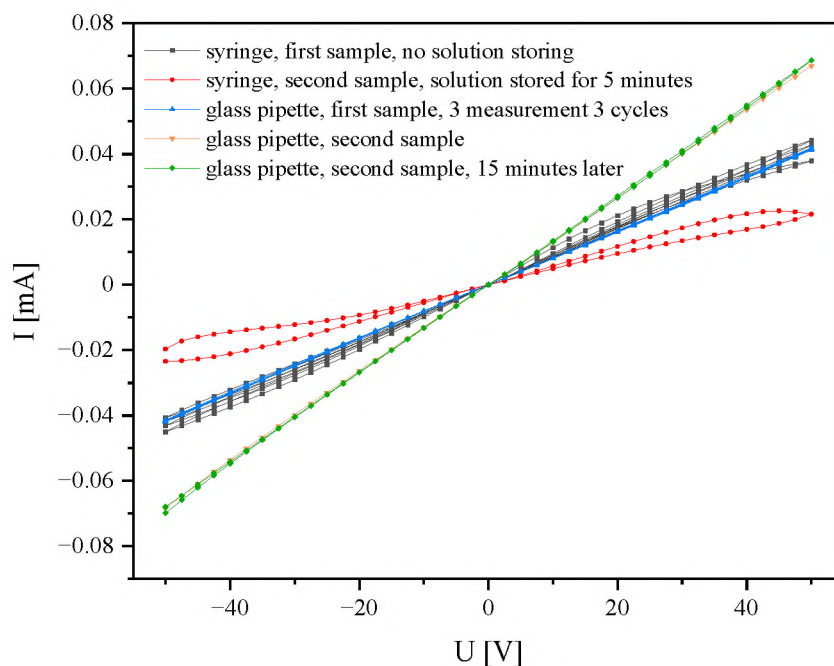
36

Figure 3.12. Current-voltage characteristics of samples containing R-P3HT casted from a plastic syringe right after filling it in with solution (black), and after storing the solution in syringe for 5 minutes (red) and of two different R-P3HT samples casted from a glass pipette (blue, yellow) with additional measurement of second sample after 15 minutes (green)

To check the device variability, four devices from sample number 2 were measured. Their average current response and standard deviation were calculated and are shown in **Figure 3.13**. As can be seen, there is a slight variability in device performance, which stays below 5%, and it can be linked to the border effects on the substrate.
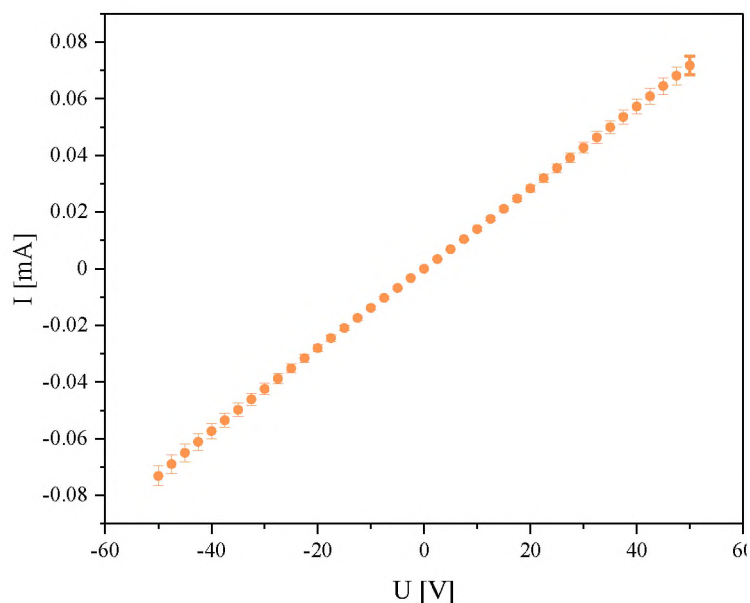

Figure 3.13. The average current response obtained by analysing four separate devices from sample 2 casted from glass pipette

To further highlight the importance of R-P3HT purity, the current responses to voltage sequences of -10 V, -50 V, 10 V, and 50 V has been measured for R-P3HT film prepared using glass and plastic tools. The results presented in **Figure 3.14** show the different character of current responses to voltage sequences of both samples.
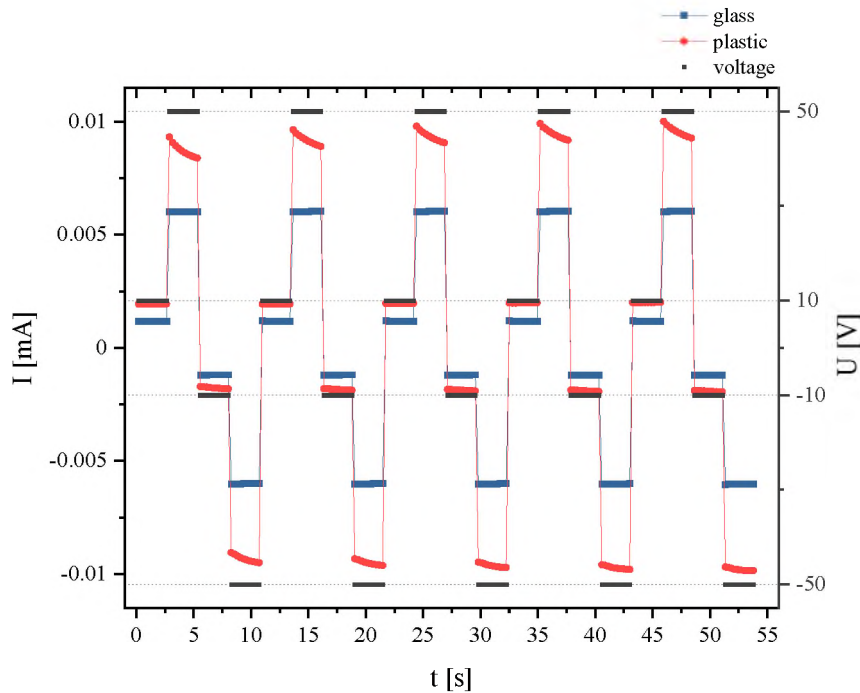

Figure 3.14. Current response to voltage sequences of -10 V, -50 V, 10 V, and 50 V measured for R-P3HT film prepared using glass (blue) and plastic (red) tools

The sample prepared using glass tools (blue signal) exhibits constant response to applied voltages. In contrast, the sample poured from the plastic syringe (red signal) displays changes in the conductance of R-P3HT throughout the measurement. This finding implies that the R-P3HT prepared with the use of plastic tools is of no use in the research, which utilizes this polymer's stability to study its conductance changes related to external stimuli.

Based on these results, throughout this thesis, the R-P3HT solution was poured on the substrate using glass pipettes.

P4VP deposition

The insulator solution was cast without filtering on a substrate rotating at 300 rpm. After 3 seconds the substrate was set to rotate at 2000 rpm for 60 seconds forming a layer of a well-defined thickness (Table 3.10). Finally, the substrate was set to rotate at 3000 rpm for 5 seconds.

The thickness of the P4VP layer casted at 2000 rpm was measured for several

38

concentrations of material solution. The measurements were performed with the use of a profilometer, and the obtained calibration formula of layer thickness can be determined from equation 3.1 given by:

$$d = 5.3c + 1.80, \tag{3.1}$$

where d is the layer thickness and c is the P4VP solution concentration.

Following the spin-coating of the P4VP layer, it is crucial to remove the insulator from the edges of the substrate to reveal the electrodes in a manner that ensures that the semiconducting R-P3HT layer was fully covered by the insulator. This way the insulator guarantees no physical contact between the semiconductor and the mobile ions from the top layer.

Surface modification of insulator

The surface of the insulator was modified with $CoBr_2$ by immersion of the substrate in $CoBr_2$ acetonitrile solution for 60 seconds. Then the sample was removed from the solution and the remaining unbound salt was generously rinsed with acetonitrile. The sample was left to dry, to let the solvent evaporate before casting the top layer.

Ion-reservoir layer deposition

The solution containing the mobile ions, PSS or PSS admixed with salts, was cast without filtering on a substrate rotating at 300 rpm. Then the substrate was set to rotate at a speed of 1500 rpm for 60 seconds and then for another 3 seconds at 3000 rpm. To ensure that the layer had no contact with the electrodes, the edges of the substrate were carefully wiped with distilled water, as shown in **Figure 3.15**. Otherwise, the ion-reservoir layer would partake in the samples' conduction, changing the response of the device.

Figure 3.15. Schematic representation of prepared sample

Study of R-P3HT surface morphology after ethanol treatment

To rule out any potential solvent-induced damage, which might result from the deposition of the P4VP layer, the surface properties of the R-P3HT layer were evaluated using AFM. The samples were prepared on the S161 substrates and were imaged before and after ethanol treatment. The ethanol treatment was performed using a spin-coating technique maintaining the same parameters as for the P4VP layer deposition.

The 10 μm x 10 μm and 2.5 μm x 2.5 μm AFM images were obtained through the non-contact mode of AFM at a few representative sample locations. **Figure 3.16.** presents the surface morphology of the samples before (Figure 3.16. a) and after ethanol treatment (Figure 3.16. b).

The morphology of the R-P3HT shown as 10 μm x 10 μm images in Figure 3.16 suggest that there is no significant solvent-induced damage of the R-P3HT surface. To evaluate the surface morphology of the samples quantitively, the mean Root Mean Square (RMS) roughness values were calculated from independent measurements taken at three different sample locations within the 2.5 μm x 2.5 μm image area. The RMS roughness of R-P3HT film before ethanol treatment has been estimated in Gwyddion software as 4.12(36) nm. After undergoing ethanol treatment, the RMS roughness of the R-P3HT film was estimated to be 4,17(31). These findings indicate that the semiconductor remains intact after the ethanol treatment, suggesting no significant changes in surface morphology.
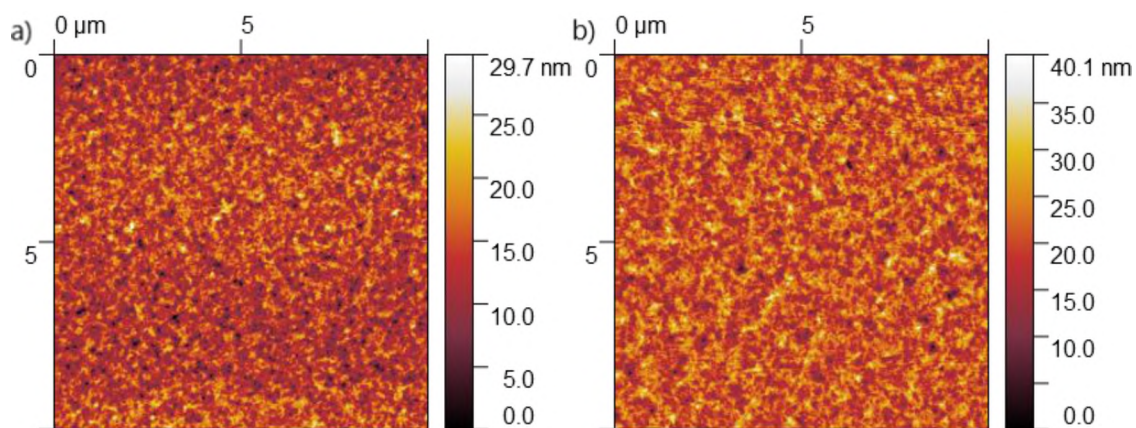

Figure 3.16. AFM images of R-P3HT surface performed a) before and b) after ethanol casting

CHAPTER Four - Investigation on the nature of interactions between R-P3HT and P4VP

The knowledge about interactions between semiconducting R-P3HT and insulating P4VP is a key factor to understand the mechanisms underlying the principle of operation of the studied system. In a work preceding my doctoral project, we assumed that the conduction increase in the system is related to the electric field induced in the P4VP film[10]. Moreover, we have shown, that the current increase in the system is inversely proportional to the square of P4VP layer thickness. We associated this effect with the distance between semiconducting R-P3HT and the P4VP-CoBr$_2$ complex at the surface of the P4VP layer, which has the highest contribution to the effective electric field induced in the system. However, the mentioned work does not tackle the nature of the interactions at the R-P3HT-P4VP interface, which might also be a factor altering the R-P3HTs' conductivity. In the aforementioned work, we stated, that the direct molecular interactions between R-P3HT-P4VP cannot be excluded and require further study. The aim of this chapter is to explore this problem and provide an explanation to the phenomena occurring at the materials interfaces.

This chapter presents the results of the investigation of whether the direct molecular interactions at the interface between the semiconductor and insulator are one of the factors influencing the conduction increase in the system. The results were obtained by separating the semiconducting and insulating layers with insulating aluminium oxide (Al_2O_3). The material was selected due to its' good electrical insulating properties and for the purpose of Al_2O_3 serving as a protection layer. In a different study, the R-P3HT/Al_2O_3 interface, with the Al_2O_3 layer deposited through the ALD process, was shown to be prone to materials intermixing and to have a rough interface[89]. The Al_2O_3 was used as a separator between R-P3HT and P4VP, and the material was deposited through Magnetron Sputtering at a low growth rate to avoid significant mixing of distinctive layers.

4.1. Sample preparation and characterisation

Al₂O₃ deposition. In order to prepare the samples varying in Al_2O_3 layer thickness, an initial calibration was performed based on three separate Magnetron Sputtering deposition processes.

The samples were prepared on silicon wafers, and the thickness of Al_2O_3 layers deposited in each process was determined by ellipsometry. The obtained results indicate that the layer thickness of deposited material is linear with deposition time in the selected time range. Therefore, to calculate the deposition times for the individual samples varying in layer thickness, the calibration was carried out via a linear fit, and the result is presented in **Figure 4.1**. The obtained calibration formula is given as:

$$d_{Al2O3} = \quad a \cdot t + b, \tag{4.1}$$

where d_{Al2O3} – Al_2O_3 layer thickness, t – deposition time, a = 0,0085(11) nm/s, b = 4,30(99) nm. In the formula, the *a* parameter corresponds to the layer thickness growth rate, and b is an independent parameter.
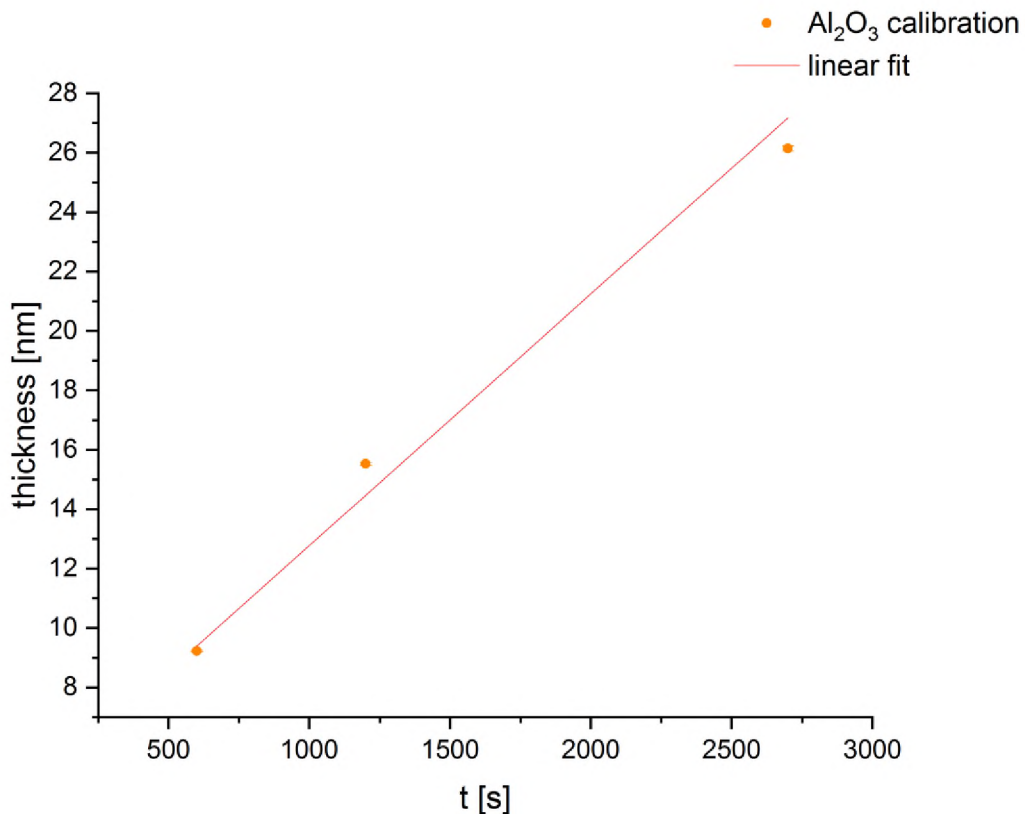

Figure 4.1. The Al_2O_3 layer thickness calibration plot determined based on results from ellipsometry measurements

42

Based on the calibration formula, three deposition times were selected 300 s (5 nm), 600 s (9 nm), and 1264 s (15 nm).

The samples in their final form were prepared on clean S161 transistor substrates in an inert gas atmosphere. First, the R-P3HT thin film was spin-casted on the substrate and the edges of the sample were wiped to assure contact between the holder contact pins and sample electrodes. Next, a layer of Al_2O_3 was deposited on the sample using the Magnetron Sputtering technique.

The Al_2O_3 layer was prepared in three separate processes, varying in deposition times, to prepare samples differing in Al_2O_3 layer thickness. The thickness of Al_2O_3 deposited in the distinctive Magnetron Sputtering processes was determined based on reflectometry and ellipsometry measurements, performed on an additional silicon wafer, and is presented in Table 4.1.

Table 4.1. The Al_2O_3 layer thickness measured for different deposition times using two techniques: ellipsometry and reflectometry

Measurement method	Al_2O_3 thickness deposited in time [nm]		
	300 s	**600 s**	**1264 s**
Ellipsometry	5.93(69)	8.77(72)	15.68(18)
Reflectometry	5.27(7)	8.51(3)	16.70(12)

Electrical characterization. The samples, prepared on S161 substrates, consisting of R-P3HT and Al_2O_3 layers were characterized by measuring the current-voltage characteristics. Next, the P4VP layer was spin-coated, and the current-voltage characteristics were measured again. Additionally, the sample with a 15 nm thick Al_2O_3 layer was modified with $CoBr_2$ and its' current-voltage characteristics were measured again. The reference sample, consisting of R-P3HT/P4VP was prepared without any alterations from the device preparation procedure described in Chapter 3.
The current-voltage characteristics were measured in voltage range from -50 V to 50 V with 5V/s step.

TOF-SIMS measurements. The samples with 5 and 9 nm Al_2O_3 layer thickness were imaged in the dynamic mode of the TOF-SIMS technique to determine the consistency/morphology of the Al_2O_3 film. Due to differences in the Al_2O_3 layer thickness, the sputtering parameters need to be adjusted for each measurement. The depth

profiles were acquired in positive polarity, in dual beam mode with Bi_3^+ as the analysis beam and Cs^+ (1 or 2 keV) as a sputtering beam. Each analysis was carried out in a 150 μm x 150 μm area concentric to the 300 μm x 300 μm sputtered area.

SEM imaging. Two additional samples, containing single Al_2O_3 and R-P3HT/Al_2O_3/P4VP/$CoBr_2$, were prepared in the same sputtering process on a silicon wafer with a SiO_2 native layer for SEM imaging purposes. The layer thickness was measured by stylus profilometry for a sample with a single Al_2O_3 and it was determined as 44(15) nm. The calculated layer thickness standard deviation is relatively high due to the sample roughness.

The cross-section profiles of the samples were obtained using the SEM technique. First, the sample was cut in half before measurement. One part of the sample was imaged as cut, and one part was polished before the measurement to eliminate the irregular structure caused by sample rupture. During the measurements, images of Secondary Electrons (SE) and Backscattered Electrons (BSE) were acquired.

4.2. Examination of sample integrity and structure

To properly interpret the results of the electrical characterization of the samples, it is important to assess their structure and integrity. To do so, the samples were characterized by SEM and TOF-SIMS techniques.

The TOF-SIMS measurements were performed in the dynamic mode on samples with 5 nm and 9 nm thickness of the Al_2O_3 layer. To investigate the interfaces between the consecutive layers, two versions of samples were imaged: one with the P4VP layer and one without it. Through obtaining the depth profiles of the subsequent layers, the samples were inspected in terms of possible discontinuities or mixing.

The depth profile of a sample consisting of Al_2O_3(5 nm)/R-P3HT/substrate is presented in **Figure 4.2 a)**. **Figure 4.2 b)** depicts the depth profile of the sample consisting of P4VP/Al_2O_3(5 nm)/R-P3HT/substrate. The distinctive materials signals are given as ITO glass substrate (SnO_2^-), R-P3HT ($^{34}S^-$), 5 nm Al_2O_3 (Al^-), and P4VP ($^{13}CN^-$).
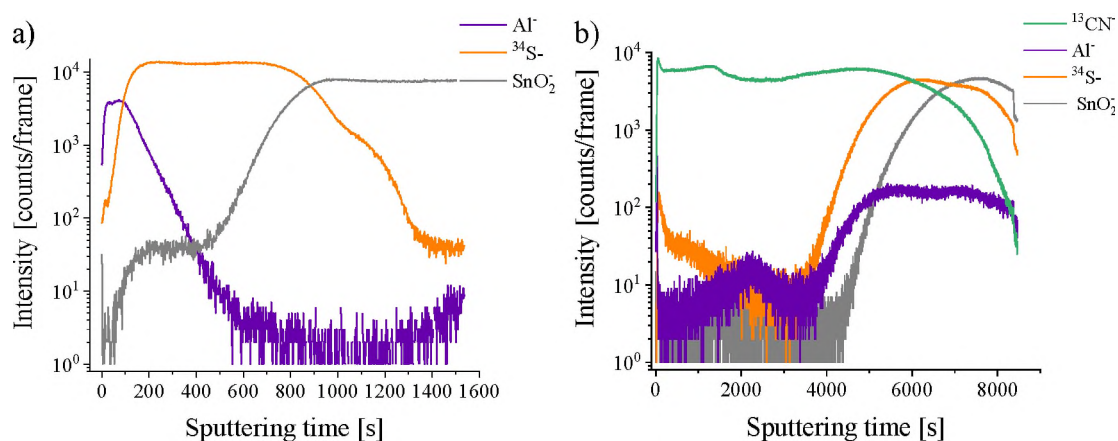
Figure 4.2. The depth profiles of samples with 5 nm Al$_2$O$_3$ layer thickness; a) sample containing ITO glass substrate (grey), R-P3HT (orange), and Al$_2$O$_3$ (purple), b) sample containing ITO glass substrate (grey), R-P3HT (orange), Al$_2$O$_3$ (purple), and P4VP (green). The distinctive signals for each subsequent layer includes SnO$_2^-$ (ITO glass substrate), ^{34}S$^-$ (R-P3HT), Al$^-$ (Al$_2$O$_3$), and ^{13}CN$^-$ (P4VP)

The samples were sputtered starting from the uppermost layer, which is visible in Figure 4.2 a) as a maximum signal intensity from Al$_2$O$_3$ in the first 100 seconds of sputtering time. During that time the signal characteristic for R-P3HT emerges and reaches maximum intensity around 200 seconds of sputtering time. As the Al$_2$O$_3$ layer thickness is around 5 nm, and the mean roughness of R-P3HT film was estimated by AFM measurements to be 4.12(36) nm, this result implies possible discontinuities in the insulating layer. The layer discontinuity may also explain the relatively high intensity of the ^{34}S$^-$ signal right from the measurement start. Broadening of the falling edge of the signal is related to ions being knocked in into deeper layers of the sample during the sputtering process.

The depth profile of the sample containing P4VP layer is presented in Figure 4.2 b). As depicted, at the beginning of sputtering the signal distinctive for the P4VP is the most prominent. Around 2000 seconds of sputtering, the signal characteristic for Al emerges, and not long after the trace of R-P3HT. The signals characteristic for Al$_2$O$_3$ and R-P3HT reach their maximum values almost simultaneously around 5000 seconds of sputtering time. This is attributed to the characteristic wrinkling of the P4VP. 3D reconstruction of the a well-defined interface between materials is shown in **Figure 4.3**. These profile reconstructions rule out any significant intermixing between the layers, which is demonstrated as a well-defined interfaces between the layers.
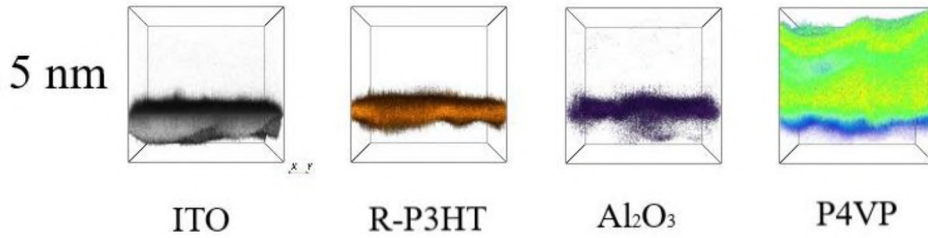
45

Figure 4.3. Profile reconstruction of a sample consisting of substrate (grey), R-P3HT (orange), 5 nm of Al$_2$O$_3$ (purple), and P4VP (green)

The profile reconstructions from Figure 4.3 was prepared with the assumption that the surface of the sample is flat. Regardless of it, the signals characteristic for subsequent layers imply layer folding, which is related to the P4VP roughness. The P4VP, which is the uppermost layer in the device, exhibits a characteristic folding, which is further projected into the inner layers. The P4VP roughness is also a cause of misleading display of materials interfaces in Figures 4.2 b) and 4.4 b).

Figure 4.4 presents depth profiles measured for samples consisting of **a)** Al$_2$O$_3$(9 nm)/ R-P3HT/substrate and **b)** P4VP/Al$_2$O$_3$(9 nm)/R-P3HT/substrate. Due to differences in the measurement parameters, the sputtering times are shorter compared to samples with 5 nm Al$_2$O$_3$ layer thickness.
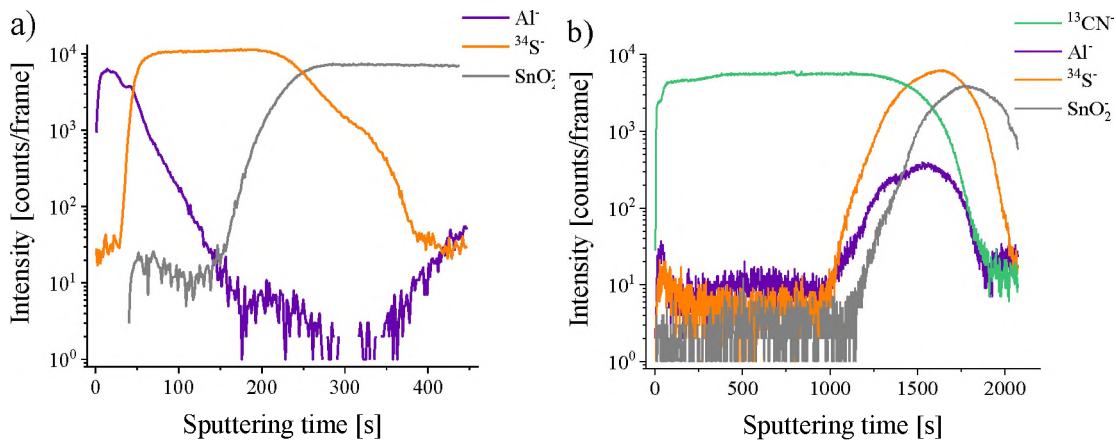

Figure 4.4. The depth profiles of samples with 9 nm Al$_2$O$_3$ layer; a) sample consisting of ITO (grey) glass, substrate, R-P3HT (orange), and Al$_2$O$_3$ (purple), b) sample containing of ITO (grey) glass substrate, R-P3HT (orange), Al$_2$O$_3$ (purple), and P4VP (green). The distinctive signals for each subsequent layer includes SnO$_2$⁻ (ITO glass substrate), ^{34}S⁻ (R-P3HT), Al⁻ (Al$_2$O$_3$), and ^{13}CN⁻ (P4VP)

As can be seen in **Figure 4.4 a)**, the distinctive signal of the Al$_2$O$_3$ layer reaches maximum value during the first 50 seconds of measurement and the signal characteristic for R-P3HT emerges only after the Al⁻ signal intensity starts to decrease. This result implies no intermixing or discontinuities in the sample with a 9 nm thickness of the Al$_2$O$_3$ layer.

46

The slow rate of Al⁻ signal intensity decrease is related to the material being knocked into the inner layers while the sample was sputtered.

Figure 4.5 depicts the reconstruction of the depth profile prepared for the sample with 9 nm of Al_2O_3. The profile reconstruction was prepared with the same assumption as reconstruction illustrated in Figure 4.3. The characteristic folding, which is further projected into the inner layers, is related to the roughness of P4VP. The Al_2O_3 layer depicted in Figure 4.3, appears to be thicker for the 5 nm layer, however, it is an artefact related to different scales of reconstruction boxes and a slower sputtering rate of the sample, which is linked to lower ion beam energy and current. Despite the wrinkling, the reconstructions provide solid proof that the interfaces between the distinctive layers are well-defined.
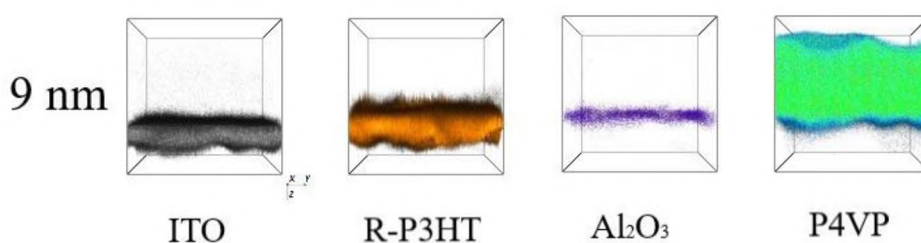

Figure 4.5. Profile reconstruction of a sample consisting of substrate (grey), R-P3HT (orange), 9 nm of Al_2O_3 (purple), and P4VP (green)

The main purpose of the Al_2O_3 layer was to prevent direct molecular interactions between the R-P3HT and P4VP layers by separating them. However, the TOF-SIMS results imply possible discontinuity of Al_2O_3 of 5 nm thickness. Based on these findings, the samples with 5 nm of Al_2O_3 were excluded from further analysis, as the R-P3HT/Al_2O_3/P4VP interface might further complicate the description of interactions.

To get complementary information about the structure of the samples, the cross-sections of the specimen with 44(15) nm Al_2O_3 layer were measured using the SEM technique. **Figure 4.6** shows the SEM cross-section of the sample at x200k magnification. The sample was imaged as cut, without polishing.

The individual layers were marked based on the contrast between each layer. As the SE signal provides higher contrast for the inorganic compounds within the sample, elements such as aluminium, or cobalt, it makes it easier to identify the subsequent layers.

The sample was imaged from a certain angle; therefore, the signal from the silicon wafer takes up most of the image and is visible as a smooth surface at the top of the image.

47

The R-P3HT layer is the uppermost layer in the imaged sample, and the Al_2O_3 underneath the semiconducting layer can be easily distinguished based on the difference between signal intensities. As can be seen, the insulating layer forms a thick and concise barrier between R-P3HT and P4VP. The P4VP layer is situated between Al_2O_3 and $CoBr_2$, which forms a very thin, but visible layer. The bottom part of the image is the signal from the measurement chamber.
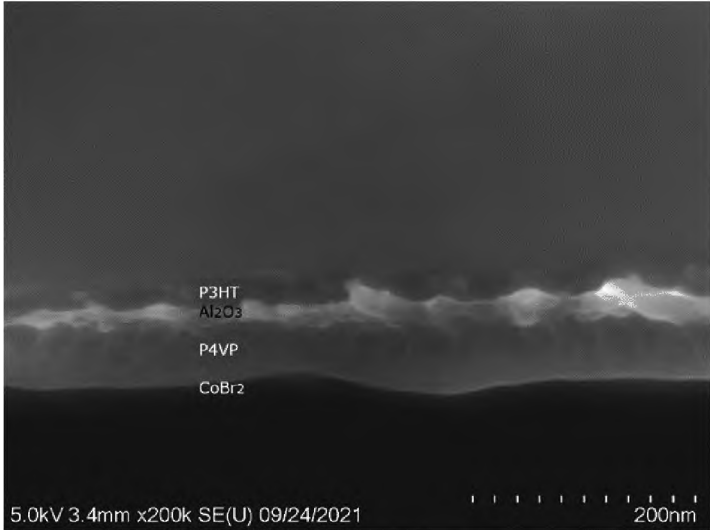

Figure 4.6. SEM image of a cross-section of a non-polished sample with individual layers marked. Detection of secondary electrons, magnification x200k

Figures 4.7 a) and **b)** show two images of a polished sample cross-section at magnification x100k. The figures show a noteworthy contrast between signals from secondary electrons in each layer in the sample.
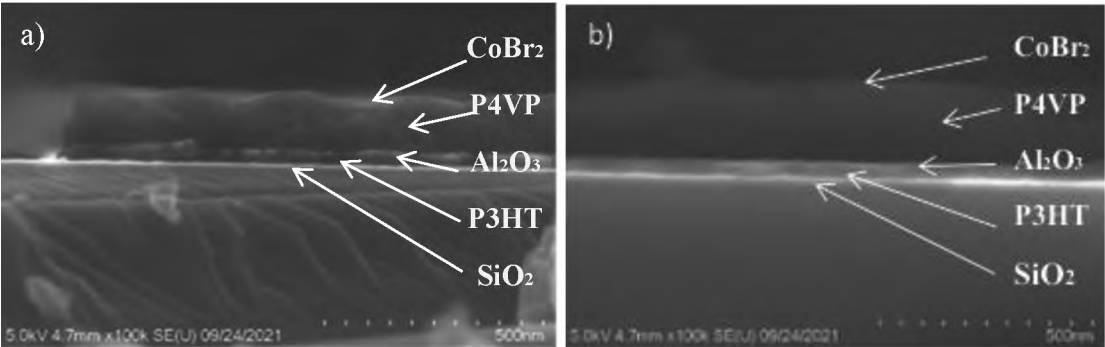
Figure 4.7. SEM image of a cross-section of a polished sample. Detection of secondary electrons, magnification x100k

Figures 4.7 a) and b) were imaged at a different angle than the sample in Figure 4.6. In this setup, the silicon wafer, with an intense signal from native silicon oxide, is seen at the bottom of the image. The R-P3HT layer provides a signal from in-between SiO_2 and Al_2O_3 layers, which are visible at/in high contrast. In Figure 4.7 a) the Al_2O_3 layer

appears to be disrupted in a few places, however, other images prove that it is not the case, and it might be an artefact related to sample polishing or P4VP roughness. Next, is the P4VP layer with a thin CoBr₂ film. Moreover, the P4VPs' characteristic wrinkled surface can be seen thanks to the signal from CoBr₂, which appears to be folded. This characteristic folding of the P4VP layer is even more apparent on **Figure 4.8**.

Figure 4.8. SEM image of a cross-section of a polished sample a) with wrinkles characteristic for P4VP layer; detection of secondary electrons, magnification x300; b) rotated at the 5-degree angle; detection of secondary electrons, magnification x50k

In order to have a better insight into the samples' structure it was rotated at a 5-degree angle and imaged detecting the secondary electrons at x50k magnification as shown in **Figure 4.8 a)**. The top of the image shows P4VPs' folded surface with CoBr₂ on top. The contrast at the bottom of the sample is linked to the native SiO₂ layer. Due to the sample rotation, and detection of an intense signal from Al₂O₃, the signal from R-P3HT is barely visible as a thin layer between SiO₂ and Al₂O₃.

The cross-section of a sample with the detection of Backscattered Electrons is shown in **Figure 4.9**. The sample was imaged at x40k magnification and provided more information about the chemical composition of the sample. The polymer films provide a signal with similar contrast, however, the Al₂O₃ layer is noticeable as a thin layer separating the top layer (P4VP) from the bottom layer (R-P3HT).
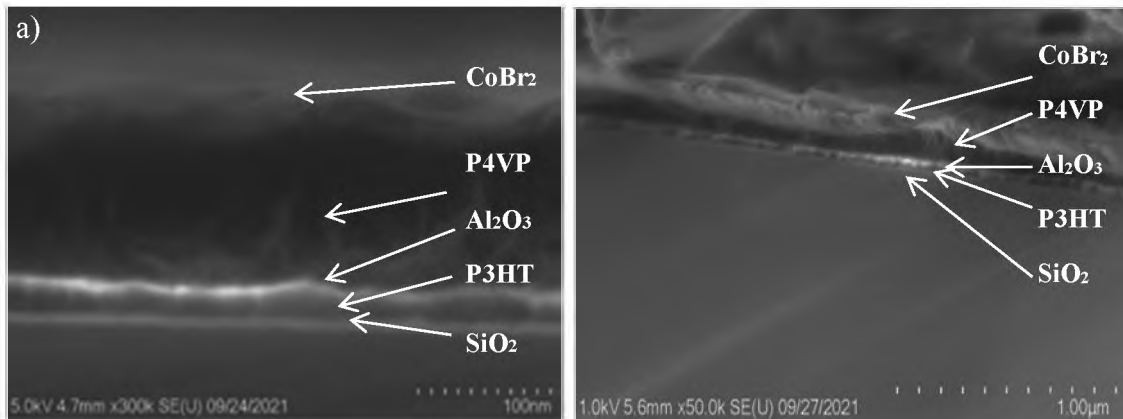
Figure 4.9. SEM image of a cross-section of a polished sample. Detection of backscattered electrons, magnification x40k

The results of SEM imaging on a sample consisting of R-P3HT/ Al_2O_3(44 nm)/P4VP/CoBr$_2$, prepared on a silicon wafer, confirms that the Al_2O_3 separates the R-P3HT and P4VP layers, forming a consistent layer without any visible intermixing. Compared to the results of TOF-SIMS imaging, the 44 nm layer of the Al_2O_3 layer proves to be a coating thick enough to prevent layer disruptions.

4.3. Electrical characterization of samples

In the next step the samples were characterized in terms of the conductivity change, based on measurements of current-voltage characteristics obtained in between the subsequent layer deposition steps. The results obtained for samples containing Al_2O_3 layers were compared to a reference sample without the Al_2O_3 layer between R-P3HT and P4VP.

The current-voltage characteristics measured before (black squares) and after (orange circles) P4VP layer deposition are presented in **Figure 4.10**.
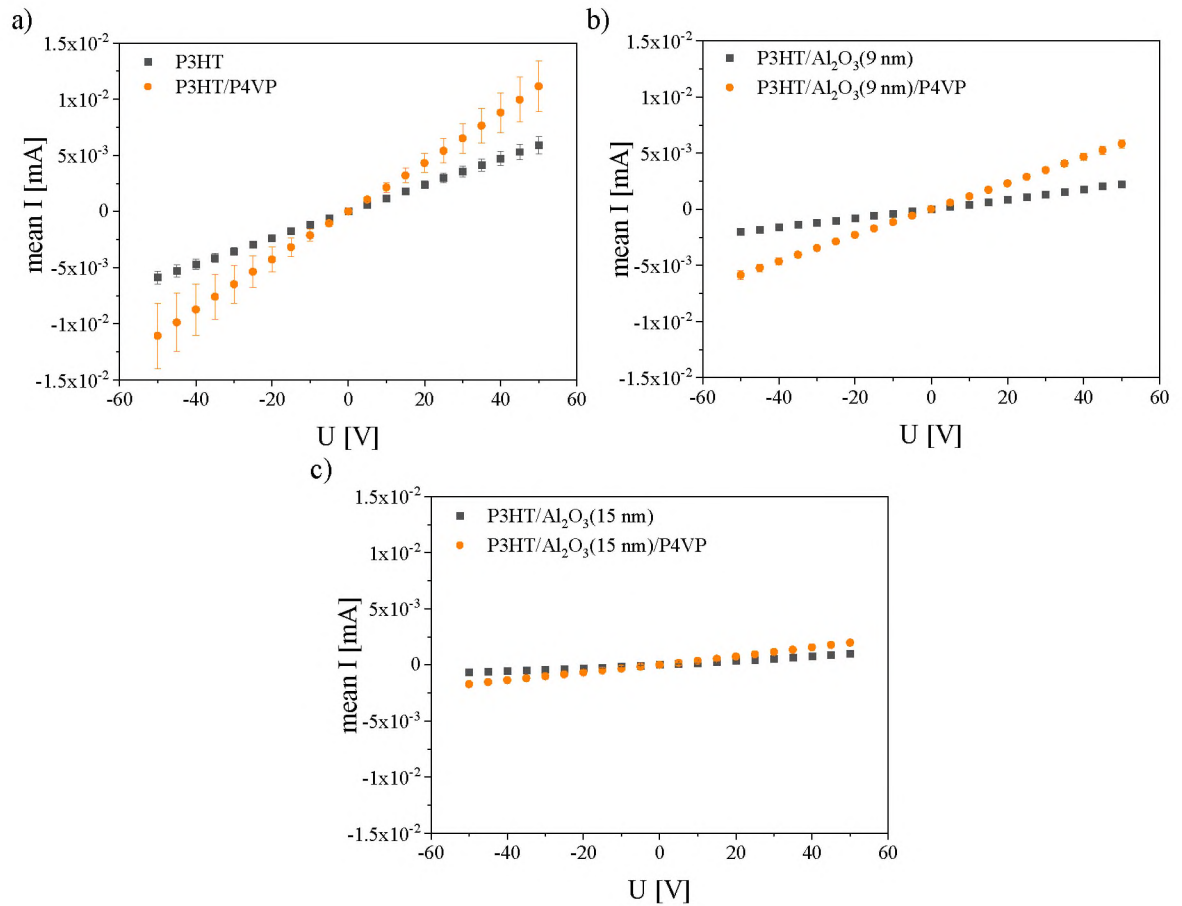
Figure 4.10. The mean current with maximum standard deviation calculated from 3 devices consisting of a) R-P3HT (black) and R-P3HT/P4VP (orange), b) R-P3HT/ Al_2O_3 (9 nm) (black) and R-P3HT/ Al_2O_3(9 nm)/P4VP (orange), and c) R-P3HT/ Al_2O_3 (15 nm) (black) and R-P3HT/ Al_2O_3 (15 nm)/P4VP (orange)

Before P4VP layer deposition samples consisted of a) R-P3HT (reference sample), b) R-P3HT/Al_2O_3(9 nm), and c) R-P3HT/Al_2O_3(15 nm). The measurement results were averaged over 3 devices and are presented in the same y-axis scale to showcase the differences in measured currents. As it was mentioned before, the devices from peripheral parts of the substrate, device number 1 and 5, tend to vary from the devices in the middle due to the boundary effects on the substrates. Therefore the final analysis was performed only on data from the 3 devices in the middle.

The plots show that the values of measured currents increase after the P4VP layer deposition for all three device types, which is consistent with the long-range interactions hypothesis. However, the initial mean current values, corresponding to the conductance of R-P3HT, vary between samples. It might be attributed to the Al_2O_3 layer screening the electric field or to interactions at the R-P3HT/Al_2O_3 interface. Moreover, mean current

values calculated for the reference sample (Figure 4.10 a) display significant variability after P4VP deposition, which can be seen as a high value of maximum standard deviation.

In order to compare the results quantitively, the mean value of conductivity was calculated. For the sake of consistency with our previous research[10], the conductivity values were determined as $\frac{dI}{dU}\big|_{25\,V}$ considering the electrode's geometric dimensions given as $A = 3 \cdot 10^{-5}$ cm and $l = 5 \cdot 10^{-3}$ cm. The method was employed in previous research given a slight deviation from the linear current response of devices, which is also shown in Figure 4.10. Calculated values of conductivity with maximum uncertainty (3σ). are summarised in **Table 4.2**.

Table 4.2. Calculated values of conductivity before and after P4VP deposition for reference devices and samples with 9 nm, and 15 nm Al_2O_3 layer thickness

Device type	Conductivity of devices with different Al_2O_3 layer thickness [µS/cm]		
	reference	9 nm	15 nm
before P4VP deposition	19.7 ± 2.5	7.8 ± 0.9	3.3 ± 0.5
after P4VP deposition	36.9 ± 7.5	19.5 ± 1.3	6.8 ± 0.1

The results confirm that the conductivity of all three types of devices increases after the deposition of P4VP. To get a better insight into the calculated values, they are illustrated in **Figure 4.11**.

The highest change in conductivity after P4VP layer deposition has been observed for samples with the 9 nm Al_2O_3 layer. In the case of the 15 nm Al_2O_3 layer thickness, the conductivity increase is lower compared to the 9 nm layer thickness. The observation aligns with the hypothesis of long-range interactions, which states that the shorter the distance between R-P3HT and the P4VPs' surface, where the dipole-induced electric field originates, the more prominent the current increase. According to this hypothesis, the system without an Al_2O_3 layer should display the largest conductance increase. However, due to different direct molecular interactions on the R-P3HT/P4VP and R-P3HT/Al_2O_3 interfaces these results cannot be compared directly, but can rather indicate trends.
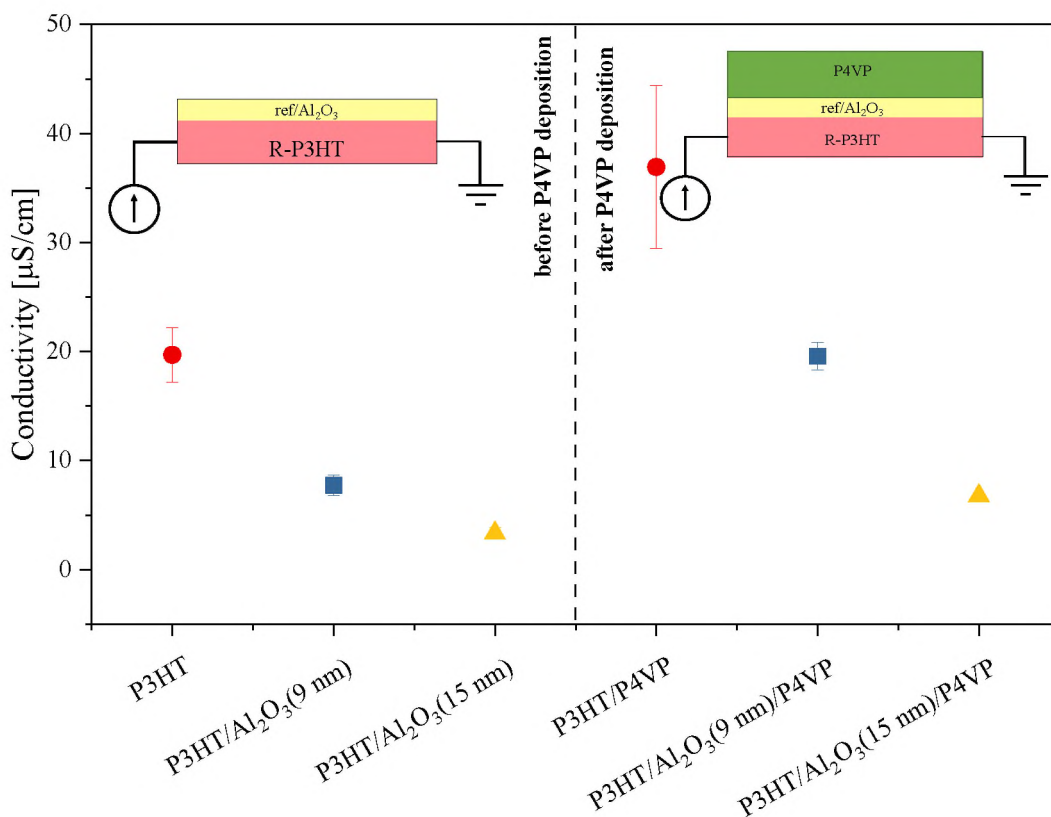
Figure 4.11. Mean conductivity calculated for potential set as +25 V for 3 devices with pure R-P3HT (red circle), P3HT/Al₂O₃(9 nm) (blue rectangle) and P3HT/Al₂O₃(15 nm) (yellow triangle) calculated before (left hand side) and after (right hand side) P4VP deposition

To further investigate the current increase in the system, the sample with 15 nm layer thickness was modified in $CoBr_2$ solution and its current-voltage characteristics were measured. This sample was selected to further examine the conduction increase based on the highest distance between R-P3HT and the modified P4VP. The Al_2O_3 is a dielectric and in theory, it should partly screen the induced electric field. Therefore, according to the hypothesis, further modification should intensify the induced electric field and, regardless of the screening, the conductance increase should be observed. The comparison between the current response measured for a sample at each preparation step is presented in **Figure 4.12**.
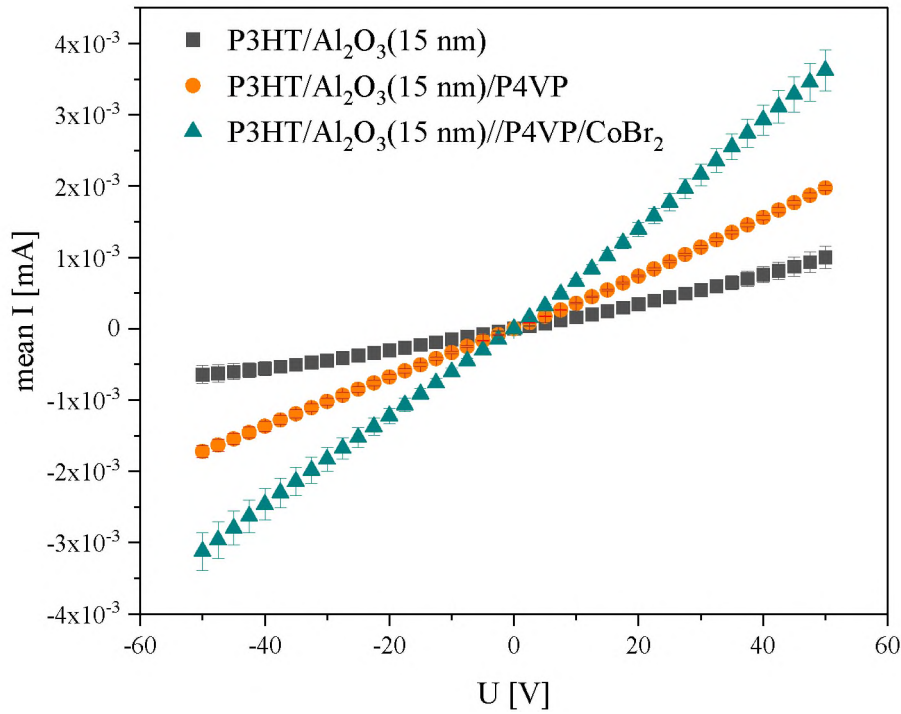
Figure 4.12. The mean value of current with maximum uncertainty calculated based on measurements performed on 3 devices in each of the preparation steps performed for a sample with 15 nm Al$_2$O$_3$ layer thickness

As depicted in Figure 4.12, the mean value of measured current increases with each preparation step. For consistency with the previous results, the values were determined based on data from 3 devices. As can be seen, the highest value of maximum uncertainty was calculated for the samples after CoBr$_2$ deposition. The increased variability of devices can be attributed to conductivity increase, which can vary in different regions of the sample. The irregular folding of the P4VP surface may contribute to this effect, as the folding increases the surface area available for the CoBr$_2$ to bond, changing the local distribution of the electric field.

Mean conductance values with maximum uncertainty were calculated as $(0.33 \pm 0.05) \cdot 10^{-5}$ S/cm for R-P3HT, $(0.68 \pm 0.01) \cdot 10^{-5}$ S/cm for R-P3HT/P4VP, and $(1.28 \pm 0.09) \cdot 10^{-5}$ S/cm for R-P3HT/P4VP/CoBr$_2$. The results are illustrated in **Figure 4.13**, and show the conductivity increase after each preparation step. Based on the calculated values, the highest conductivity increase occurs after the introduction of cobalt centres to the system. Therefore, these results further confirm that the dipole-induced electric field contributes to the conduction increase in the system, regardless of the electric field screening.
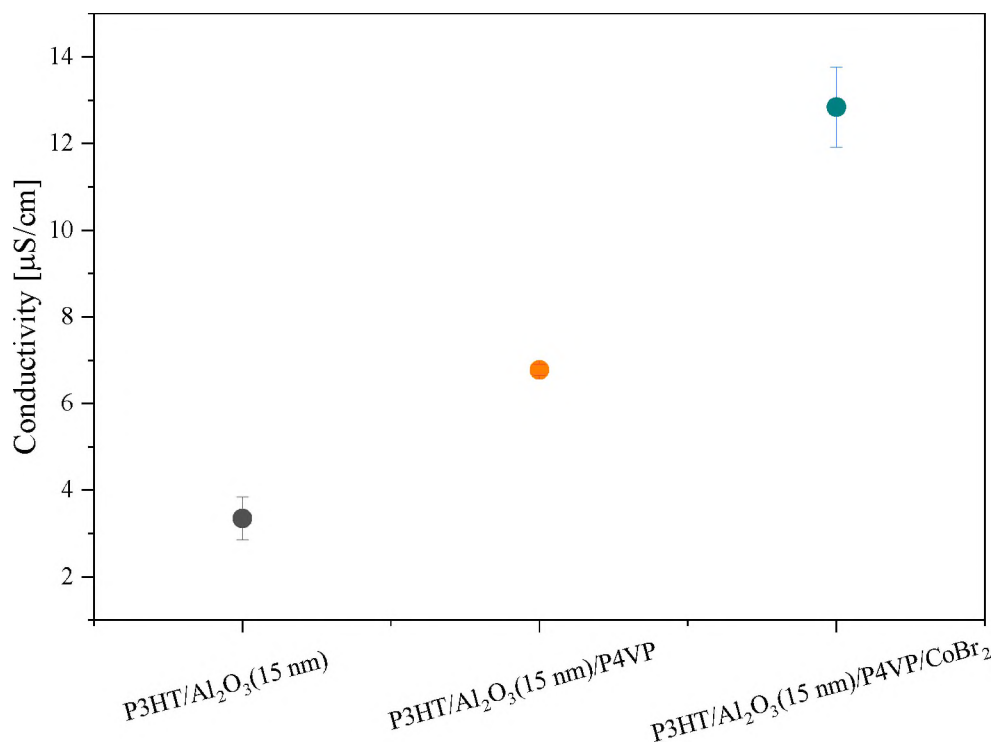
Figure 4.13. Mean conductivity of the devices with 16 nm Al_2O_3 layer thickness calculated for potential set as +25 V for devices consisting of R-P3HT/Al_2O_3 (grey), R-P3HT/Al_2O_3/P4VP (orange), and R-P3HT/Al_2O_3/P4VP/$CoBr_2$ (blue)

4.4. Conclusions

The samples consisting of R-P3HT and Al_2O_3 in three different layer thicknesses, with or without P4VP or $CoBr_2$ layers, were prepared and characterized by performing current-voltage measurements as well as TOF-SIMS profiling and SEM imaging.

The Al_2O_3 was used as a separating layer between R-P3HT and P4VP to prevent direct molecular interactions between the polymers. Through examining the TOF-SIMS profiles and SEM images, the Al_2O_3 layer was confirmed to be uniform for samples with layer thickness surpassing 9 nm. Moreover, the TOF-SIMS profiles prove no significant mixing between the subsequent layers for all of the prepared samples.

The current-voltage measurements were performed on samples consisting of R-P3HT (reference sample), R-P3HT/Al_2O_3(9 nm), and), R-P3HT/Al_2O_3(15 nm) before and after P4VP deposition. The sample with 5 nm Al_2O_3 thickness was excluded from analysis due to possible discontinuity of the separating layer.

The conductivity values calculated for all samples in between each preparation step display improved conductivity of R-P3HT. It was also demonstrated by measurements performed on samples consisting of 15 nm of Al_2O_3 thickness, which were additionally

modified with cobalt complexes. The obtained results confirm a further increase in systems' conductivity regardless of the separation between R-P3HT and P4VP.

The results mentioned above supports the hypothesis about the R-P3HT conduction increase due to the existence of long-range interactions between R-P3HT and the P4VP. Moreover, the aforementioned findings prove that direct molecular interactions at R-P3HT/P4VP interface, have a significant impact on the systems conductivity. Nevertheless, it was confirmed that the electric field induced in P4VP and Co-modified P4VP further increases the conductivity of R-P3HT.

In conclusion, the obtained results show that the previously observed conduction increase occurs in the studied system even when the R-P3HT and P4VP layers are separated by a thin insulating layer. This proves that the long-range interactions are an important factor causing the conduction increase in the system.

CHAPTER Five   –   Investigation on devices principle of operation

The aim of this chapter is to investigate the mechanism, which underlays the unique principle of operation of the studied device. According to the hypothesis, which was shortly discussed in Chapter One, the principle of operation of the studied memristive device is based on interactions between the electric field induced by surface-located dipoles and mobile ions present in the PSS matrix. The existence of a long-range dipole-induced electric field in the channel of the device has been confirmed in Chapter One and Chapter Four. Here, the investigation is extended to address the hypothesised relation between ion displacement, influenced by applied potential, and the observed hysteresis loop in the current-voltage characteristic, aiming to explore the relationship between electric field modulation and ion movement.

The chapter consists of four integral parts which together provide a complete explanation of the systems' principle of operation. At first, the ion migration hypothesis is examined utilizing methods such as TOF-SIMS profiling and imaging, Impedance Spectroscopy measurements, and electrical characterization. Next, the chapter explores the operation of devices with and without the $CoBr_2$ modification and the differences between these systems, explaining the final architecture of the device. Following, the relaxation processes and their time constants are investigated, to conclude all the findings with a phenomenological model of the device.

5.1.   Sample preparation and characterization

Electrical characterization. The devices were prepared, if not stated differently, on S161 substrates without any alterations from the device preparation process described in Chapter Three. The reference devices, samples without $CoBr_2$ modification, were prepared by omitting the substrate immersion in $CoBr_2$ solution and consisted of P3HT/P4VP/PSS+K^+(1%) only.

The sample consisting of PMMA thin film, instead of PSS matrix, was prepared utilizing the same spin casting parameters as for the PSS layer deposition.

The electrical characterization of devices was carried out by measuring the current-voltage characteristics. The measurements were performed in the voltage range from -50 V to +50 V with voltage step 2.5 V/s.

Current vs. time plots were measured for devices containing pure PSS and PSS+K$^+$(1%) as the uppermost layers. The current responses were collected for three different voltage sequences: 1) -10 V, -50 V, +10 V, and +50 V with 20 s potential step duration, 2) +10 V, +50 V, and 3) -10 V, - 50V with 6 s potential step duration. The switching time was set below 0.25 ms for all sequences.

TOF-SIMS characterization. The measurements were performed both in the static and dynamic modes of TOF-SIMS.

The sample consisting of R-P3HT/P4VP/PSS+K$^+$(1%) was characterized in dynamic mode to get an insight into the material interface structures. The depth profiles were acquired in positive polarity, in dual beam mode with Bi^{3+} as the analysis beam and Cs$^+$ 2 keV as a sputtering beam.

The sample consisting of R-P3HT/P4VP/CoBr$_2$/PSS+K$^+$(1%) was characterized in the static mode of TOF-SIMS to study the voltage-induced ion displacement on the surface of sample. The static imaging was performed utilizing the Bi^{3+} as the analysis beam. Each analysis was carried out in a 150 μm x 150 μm area concentric to the 300 μm x 300 μm sputtering beam area.

Impedance Spectroscopy measurements. The devices for SI characterization were prepared as a single layer of PSS or PSS admixed with 1% of K$^+$ on S161 substrates. The measurements were performed in an inert gas atmosphere and at ambient temperature, to preserve the electrical characterization parameters. The samples were characterized in a wide frequency range (0.5 – 3·10^6 Hz) with a measurement voltage of AC equal to 0.1 V.

The temperature dependency of conductance measurements. The measurements were performed for two samples: a device consisting of a single R-P3HT layer and a device consisting of R-P3HT/P4VP/CoBr$_2$/PSS+K$^+$(1%). The measurements were performed in a vacuum chamber using Keithley 2400 as a source meter unit and Eurotherm 2416 temperature controller.

Shortly before the measurements, the sample was cooled down to liquid nitrogen temperature by bringing it in contact with a cold finger. After breaking the contact between the sample and the cold finger the samples' current response was measured at eight selected points, at temperature ranges: 1) -148.9°C to -149.6°C, 2) -123.5°C to -122.5°C, 3) -80.5°C to -80.0°C, -54.0°C to -52.0°C, 5) -20.9°C to -20.0°C, 6) -2.5°C to 0°C, 7) 8.0°C to 9.0°C, and 8) 22.4°C to 22.5°C. The current was measured as a response to voltage sequences of -50 V, -10 V, and $+10$ V. During the experiment the temperature of the sample was raised to room temperature at a slow rate without external heating.

5.2. Results

5.2.1. Study of the origin of systems' memristive character

The system studied in this dissertation is a multilayer planar device in which each of its individual layers plays an important role in the device's operation. The systems' current response changes after deposition of successive layers, as illustrated in **Figure 5.1**.

The first layer of the device, the semiconducting R-P3HT corresponding to the characteristic plotted in red, exhibits a linear current response to the applied voltage. The P4VP deposition, characteristic in black, and $CoBr_2$ modification, depicted in blue, both increase the conductance of the R-P3HT due to the presence of dipole-moment induced electric field, nevertheless, the device's response remains linear. However, the character of the device's response changes from linear after the deposition of the layer containing the ion reservoir, which corresponds to the characteristic in orange.

The PSS, which serves as a polymer matrix, contains sodium ions and is further enriched with 1% of potassium cations. Assuming, that each mer of PSS is stabilised by one sodium cation, the sodium ions make up about 9% of the mass of the PSS layer. The exact amount of sodium ions in PSS is not disclosed, however it was reported[90], that the weight percentage of sodium in different compound, PEDOT:PSS, stays below 5%, which to some extent aligns with this assumption. As shown in Figure 5.1, the presence of the mobile ions further increases the systems' conductance and incorporates the hysteresis loop into the current-voltage characteristic of the device.

The voltage sweep direction in the I-U characteristics, indicated by the arrows in Figure 5.1, is described as forward and reverse to highlight the direction of changes in the current response.

Within one measurement cycle, the reverse current is measured during the voltage magnitude decrease (± 50 V $\rightarrow$ 0 V). On the contrary, the forward current refers to the voltage magnitude increase (0 V $\rightarrow$ ± 50 V).
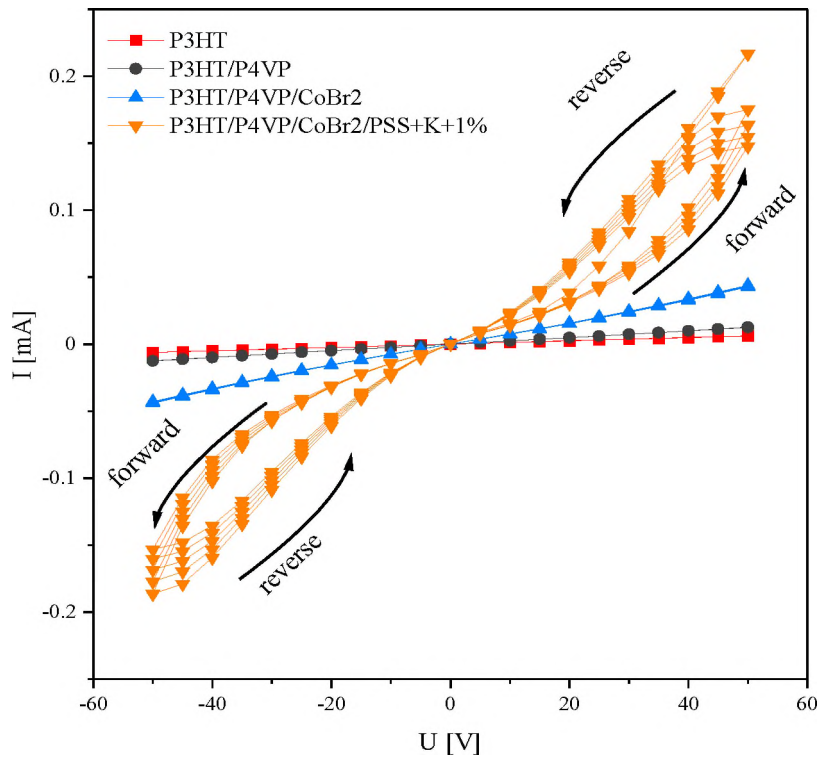

Figure 5.1. Current-voltage characteristic measured between successive preparation steps

In order to determine whether ion mobility is responsible for the hysteresis occurrence in the system, a number of tests have been conducted to validate the ion mobility hypothesis and to examine its influence on the operation of the devices.

At first, the structure and integrity of the device were examined by obtaining the depth profiles of samples containing R-P3HT/P4VP/PSS+K$^+$(1%). The devices were profiled in the dynamic mode of TOF-SIMS. The signals distinctive for each layer are given as K$^+$ for PSS+K$^+$(1%), C$_5$N$^+$ for P4VP, ^{34}S$^+$ for R-P3HT and PSS, and Si$^+$ for the substrate. The well-defined interfaces between subsequent layers are clearly demonstrated in **Figure 5.2**. Dashed lines indicate the time of particular layers' appearance. It is worth noting that the signal intensity measured for the P4VP layer decays slowly after the signal characteristic for R-P3HT emerges, and it is due to a significant wrinkling of the P4VP film. Based on these results, we can exclude substantial intermixing between the layers. Moreover, the data confirms the absence of potassium ions in the R-P3HT layer, which is proof of an effective separation of the PSS layer from the semiconductor. It also proves

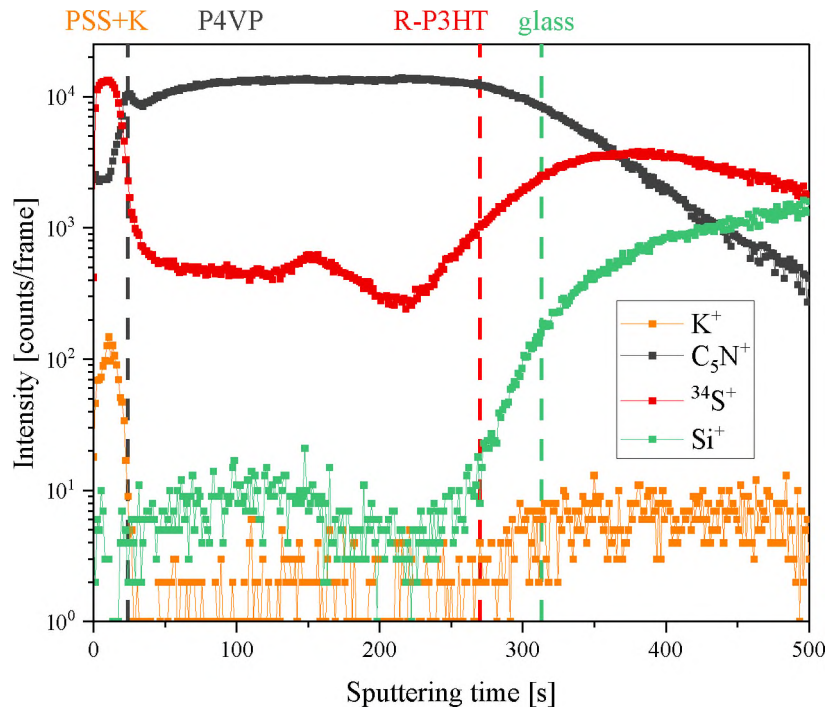that the R-P3HT layer remains undamaged and undoped by ions, which might alter the system's conductance.

Figure 5.2. Depth profile of a sample consisting of glass substrate, R-P3HT, P4VP, and PSS+K$^+$(1%). Distinctive signals measured for each consecutive layer: Si$^+$ for glass substrate (green), ^{34}S$^+$ for R-P3HT (red), C$_5$N$^+$ for P4VP (black), and K$^+$ for PSS+K$^+$ (orange)

Another factor, which has to be excluded is the ionic conductivity through the PSS layer contributing to the current response of the system. This scenario is possible if the sample preparation is performed improperly and the PSS layer is in contact with the holder electrodes. This can result in current flow through the PSS layer, apart from the conduction through R-P3HT.

To eliminate this possibility, the devices consisting of P4VP/CoBr$_2$/PSS+K$^+$(1%) were prepared with extra care to separate the PSS layer from direct contact with the electrodes. Their current-voltage characteristics were measured in between each following preparation step. The results presented in **Figure 5.3 a)** confirm that without the R-P3HT layer, the current response of the device is in the range of nA, which is within the limit of detection of the experimental setup. This is evidence that the ions present in the PSS matrix do not partake in the current conduction in the system if the preparation process is performed properly. Therefore, it is confirmed that the current flows in the system only through the R-P3HT layer.
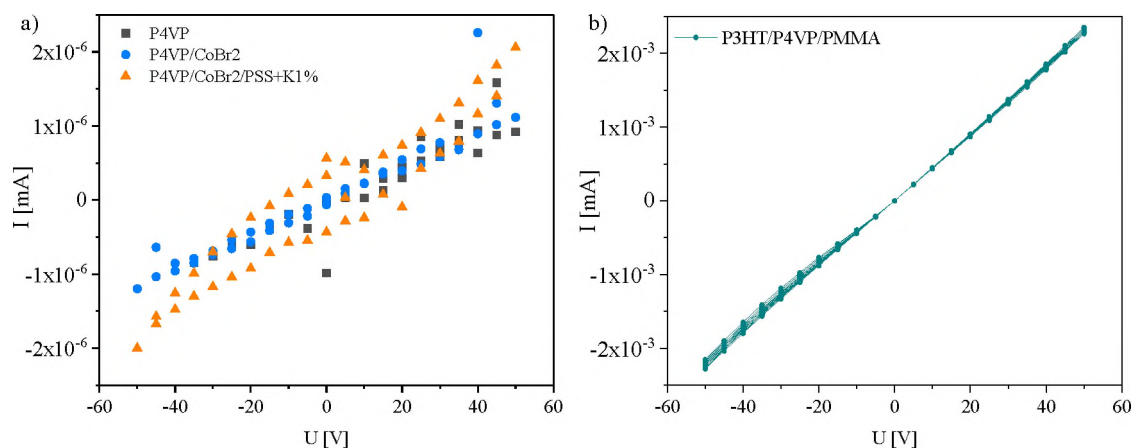
Figure 5.3. Current-voltage characteristics measured a) between consecutive preparation steps for devices consisting of P4VP/CoBr2/PSS+K+(1%), b) for devices consisting of P3HT/P4VP/PMMA

In order to investigate whether the ions present in a polymer matrix contribute to the appearance of the hysteresis loop, a device consisting of R-P3HT/P4VP/PMMA was fabricated. It is important to note that PMMA is an insulating polymer that does not contain any ions within it. Therefore, according to the aforementioned hypothesis, the presence of PMMA should not alter the character of the device's response. The measured current-voltage characteristic, as shown in **Figure 5.3 b)**, demonstrates the ohmic nature of conductivity in the device. This provides indirect evidence that the absence of an ion reservoir prevents the system from exhibiting a hysteresis loop in its I-U curves.

The research findings discussed above confirm that the PSS layer containing an ion reservoir does not take part in the conduction of the device but is responsible for incorporating the hysteresis loop into the current-voltage characteristic of the device. To determine whether the ions present in PSS+K$^+$(1%) can migrate in the layer under the applied electrical field, additional Impedance Spectroscopy measurements were performed. The samples for SI measurements consisted of a single PSS or PSS+K$^+$(1%) layer. All measurements were performed at ambient temperature in an inert gas atmosphere, and the sample geometry corresponds to the one employed in the measurements of current-voltage characteristics. The relaxation times related to sodium and potassium ions migration in PSS and PSS+K$^+$(1%) layers were determined by fitting data to the Cole-Cole model.

The results presented in the form of a Nyquist plot, **Figure 5.4**, reveal ionic relaxation processes both in a) PSS and b) PSS+ K$^+$(1%) films. Figure 5.4 b) shows that the resistance of a layer containing the addition of potassium ions is almost twice lower

compared to the resistance of pure PSS. Moreover, Figure 5.4 c) shows that the addition of 1% of K^+ ions alters the time constants of the processes that occur in the layer.
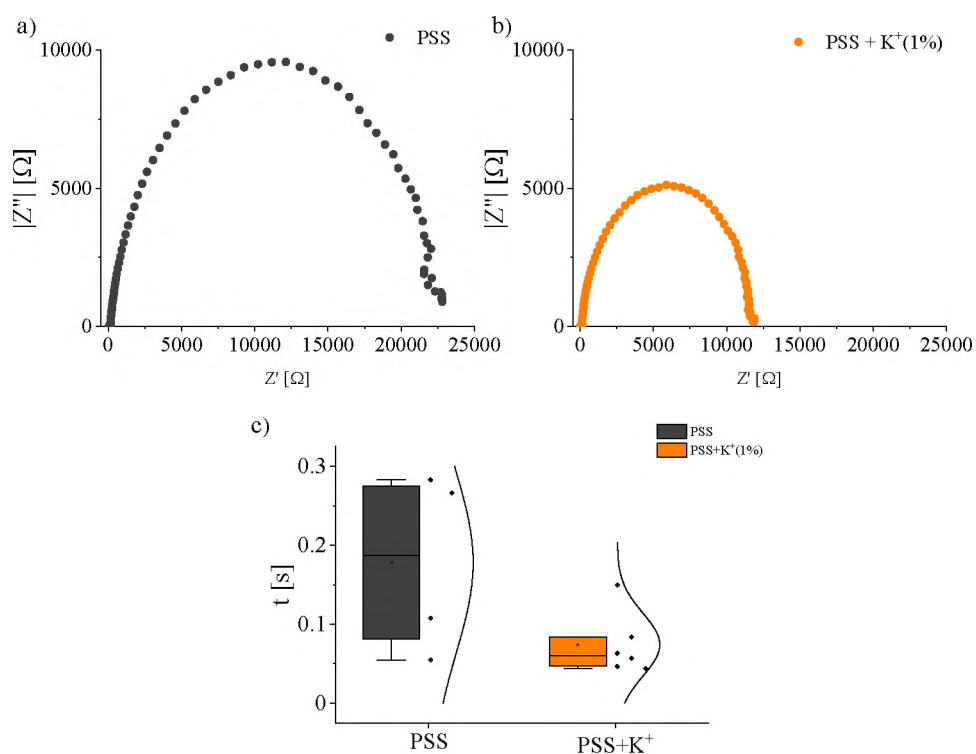

Figure 5.4. Nyquist plots for a) PSS and b) PSS+K^+(1%) thin film; c) comparison between relaxation times of PSS (black) and PSS+K^+(1%) (orange)

To demonstrate that the ion migration in the system is caused by applied external potential, we performed an in-situ experiment in static TOF-SIMS mode. The imaged sample prepared on S161 substrate consisted of R-P3HT/P4VP/CoBr$_2$/PSS+K^+(1%). During the measurement, the surface concentration of $^{41}K^+$ was measured, and at a certain stage, the measurement was temporarily stopped to apply potential +50 V to the sample. The voltage was applied for 120 s, and after that time the SIMS measurement was immediately resumed. The results of the surface imaging are shown in **Figure 5.5**. The red line indicates the time when the measurement was paused. The red, yellow, and blue boxes illustrate the signal distribution on the surface of the sample.

The results indicate that after applying the external voltage, the surface concentration of $^{41}K^+$ decays and then slowly returns to its initial value as the system gets back to its equilibrium state. Moreover, the $^{41}K^+$ signal distribution at the sample surface indicates that before and long after the external potential application the potassium ions are evenly distributed on the surface of the sample. However, right after the potential

application, some parts of the surface are depleted in $^{41}K^+$ signal (black area over the electrode), which is a direct prove of the ion migration under the applied electrical field.
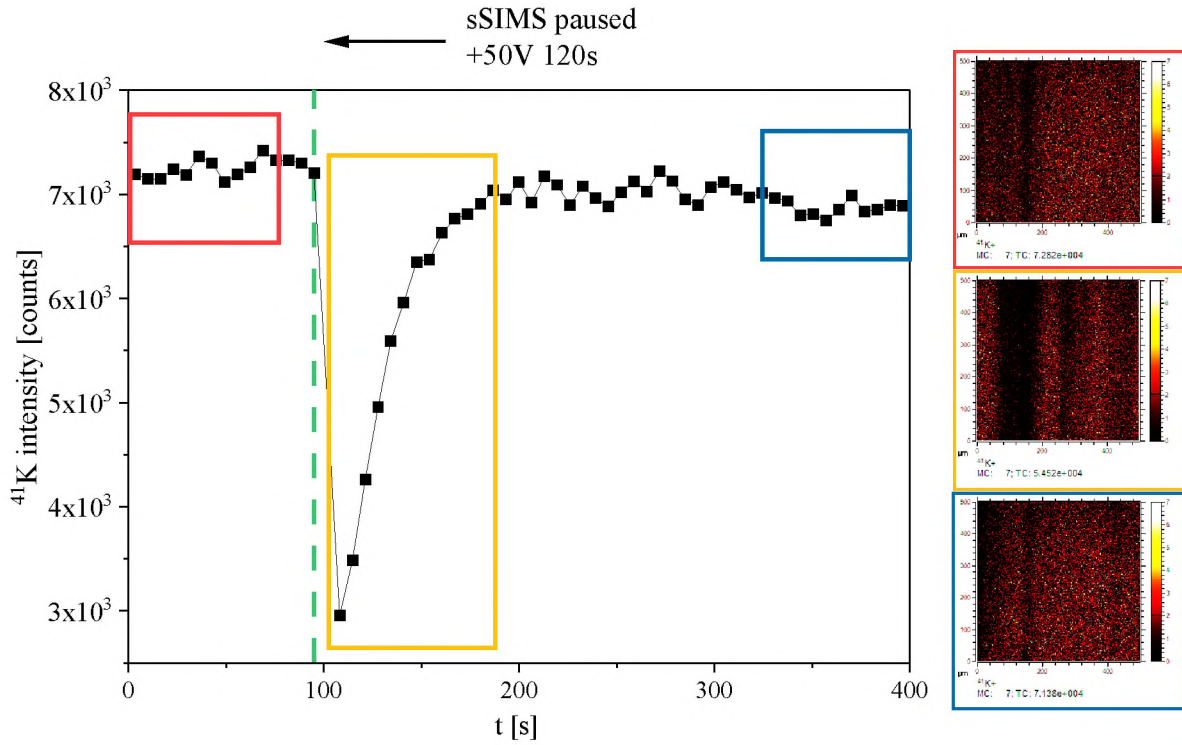

Figure 5.5. Intensity of $^{41}K^+$ secondary ion measured in time under static SIMS condition. Green line highlights the time, when the measurement was paused and external potential was applied to the device for 120 s, after which the measurement was resumed

Additionally, the devices consisting of R-P3HT and R-P3HT/P4VP/CoBr$_2$/PSS+K$^+$(1%) have been tested in regard to the device conductivity at different temperatures. The idea behind this experiment arises from the reduced ion mobility at low temperatures[91]. The temperature dependency of ion mobility in a polymer matrix can be described as follows:

$$\mu = \mu_\infty \exp\left(-\frac{B}{T-T_0}\right), \tag{5.1}$$

where μ is ion mobility, μ$_\infty$ is infinite temperature mobility, B is a constant, T is temperature, and T$_0$ is the temperature at which mobility goes to zero, also called Vogel temperature. This relationship between temperature and ion mobility has been utilized to slow down the ion migration process and to assess whether the decreased mobility of ions will influence the current response of devices.

The current responses to -10 V, -50 V, and +10 V voltage sequences have been measured in four selected temperatures and the results are presented in **Figure 5.6**.
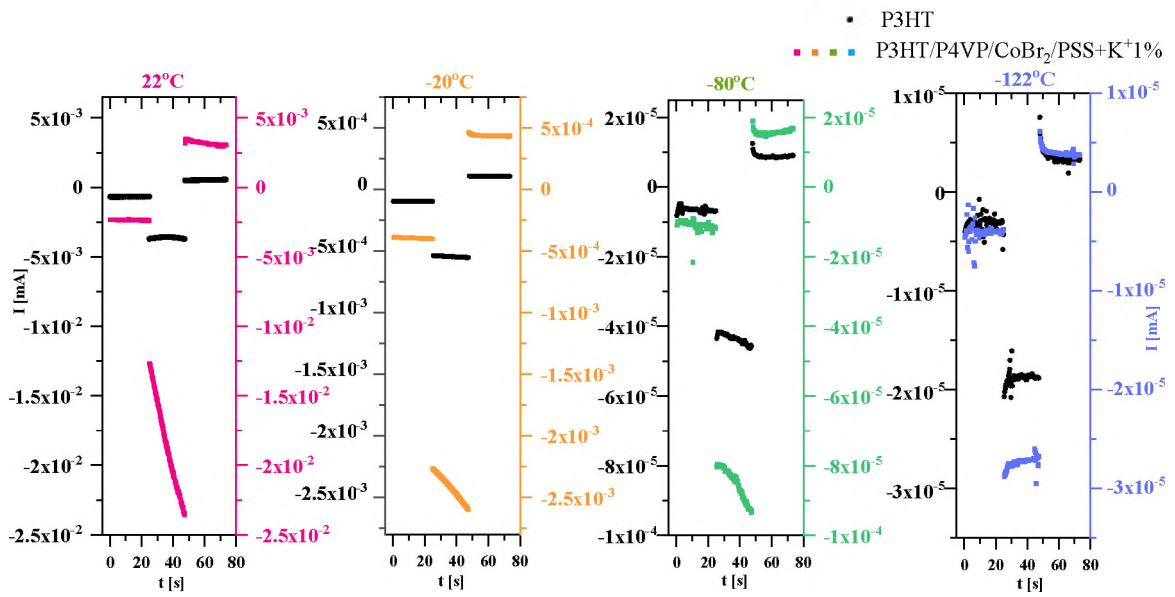
Figure 5.6. Measurements of the temperature dependency of conductance of R-P3HT (black) and of a device consisting of R-P3HT/P4VP/CoBr2/PSS+K+(1%) performed in 22°C (pink), -20°C (orange), -80°C (green), and -122°C (blue). Current responses were measured for voltage sequences: -10 V, -50 V, and +10 V with a 25 s potential step duration

Figure 5.6 illustrates the results of measurements performed at 22°C (pink), -20°C (orange), -80°C (green), and -122°C (blue). The right-hand side of the plot, signals in pink, orange, green, and blue, correspond to a current response of the whole system, and the left-hand side, in black, corresponds to the current response of R-P3HT in corresponding conditions.

As shown, at different temperatures the conductivity of the whole system differs in a significant way from the conductivity of the semiconductor. At room temperature, the conductivity of the system increases rapidly with time, while the measured current response of R-P3HT is rather constant. Similar responses are observed at -20°C with a decrease in measured current, which is related to the cooling of the semiconductor.

In -20°C and -80°C distortion of the current response, compared to the corresponding signal at room temperature, has been registered. This phenomenon could be attributed to a decrease in conductivity resulting from the reduced mobility of current carriers and ions, as these two factors are believed to be responsible for the overall increase in system conductivity.

At a temperature of -122°C, the device's performance is alike to that of the semiconductor. This observation indirectly supports the hypothesis that by reducing ion mobility it is possible to eliminate the electric field modulation caused by ions and to cancel the memristive character of the device.

The aforementioned findings confirm that ions in PSS+K$^+$(1%) can be moved by external potential and have significant mobility. The data implies that the current flows in the system exclusively through the R-P3HT layer, which shows variation in conductivity related to the applied potential. Moreover, the results prove that for the hysteresis effect to occur, the presence of the layer containing mobile ions is necessary, despite they do not directly engage in the charge transport in the system.

Considering the findings regarding ion diffusion being responsible for the conductance modulation, the following mechanism of systems operation can be postulated:

1. The presence of permanent dipole moments in P4VP/CoBr$_2$ complexes and ions within the PSS+K$^+$(1%) layer introduces an additional electric field in the R-P3HT layer. This electric field acts perpendicularly to the plane of the semiconducting layer.

2. In the absence of external potential, the ions are evenly distributed in the polymer matrix. However, they are attracted close to the P4VP/CoBr$_2$ interface due to the interaction with the dipole-induced electric field.

3. When an external potential is applied, it not only drives the current flow in the R-P3HT layer but also modifies the ion distribution within the PSS+K$^+$(1%) layer and at the interface between P4VP and PSS+K$^+$(1%), as shown in Figure 5.5.

4. Due to the finite mobility of ions, alterations in the component of the electric field, originating from ion mobility, exhibit a certain delay in response to changes in the voltage applied across the electrodes.

5. Modification in the ionic balance at the P4VP/PSS+K$^+$(1%) interface results in alterations of the perpendicular component of the electric field within the R-P3HT layer. In consequence, it affects the conductivity of R-P3HT and gives rise to the appearance of the hysteresis loop.

5.2.2. Investigation of device stability

The direction of conductance change in the studied memristive device is unique and relies on dynamic modulation of conductance of R-P3HT, which is realized through voltage sweeping. As confirmed above, the unique conductance change in the system is associated with interactions between the dipole moment-induced electric field and the mobile ions.

The findings of the investigation described in Chapter Four, as well as the current-voltage characteristics depicted in Figure 5.1, indicate that both P4VP and $CoBr_2$ increase the conductance in the system. The $CoBr_2$ is the only non-organic compound utilized in the device, and it is highly toxic, which is not a desirable feature. Therefore, to determine whether the electric field induced by P4VP is sufficient for the stable operation of the device the current-voltage characteristics of reference (P3HT/P4VP/PSS+K^+(1%)), and Co-modified (P3HT/P4VP/$CoBr_2$/PSS+K^+(1%)) devices were measured, and are illustrated in **Figure 5.7**. To examine the stability of both devices the measurements were registered for several operation cycles.
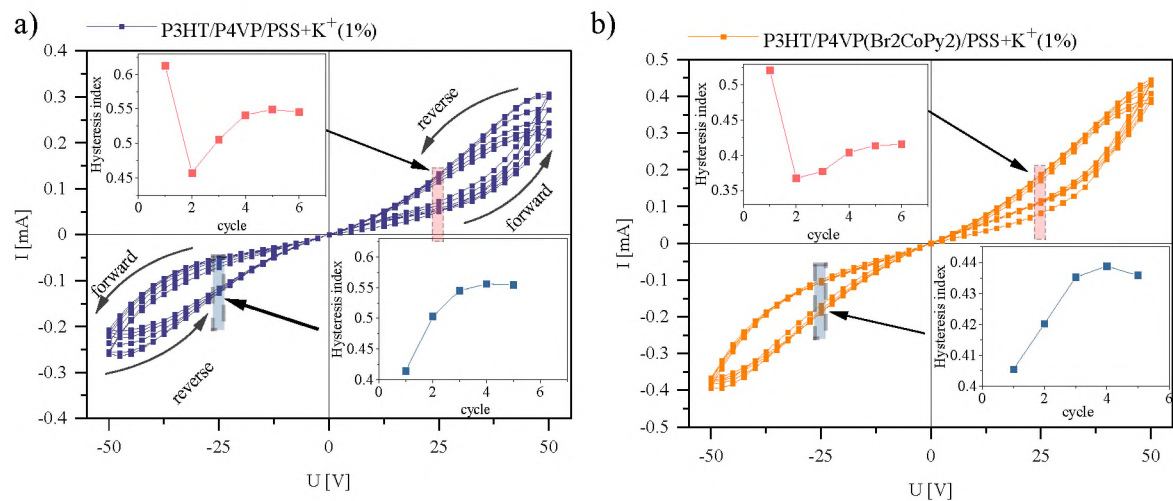

Figure 5.7 Current-voltage characteristic measured for a) reference sample (purple) and b) Co-modified sample (orange). The plots in insets illustrate Hysteresis Index calculated for ±27.5 V

The current-voltage characteristics in Figure 5.6 show that the conductivity of both device types undergoes dynamic changes in response to the applied voltage. In the Co-modified system, Figure 5.7 a), currents measured for respective voltages in the following cycles are slightly higher, and they reach a stable state after multiple measurement cycles. On the contrary, the currents measured for the reference system consistently decrease with each voltage sweep, as depicted in Figure 5.7 b).

The insets in the second and fourth quarter of the I-U plane illustrate the Hysteresis Index (HI)[92], calculated as follows:

$$HI = \left|\frac{I_2 - I_1}{I_1}\right|_{\pm 27.5\,V},\qquad (5.2)$$

where the I_1 is the current measured in the forward direction of the voltage sweep, and the I_2 is the current measured in the reverse direction of the voltage sweep. The Hysteresis Index was calculated for consecutive measurement cycles in positive and negative parts of the current-voltage characteristics for a voltage set as 27.5 V. This specific voltage is related to the maximum value of calculated HI, which appears to depend on voltage, as illustrated in **Figure 5.8** for a) reference and b) Co-modified devices. As depicted, the HI tends to stabilize around approximately 0.55 for the reference system and 0.40 for the Co-modified system.

The HI calculated for the Co-modified device exhibits a slight asymmetry in positive and negative parts (c.a. 0.42 in the positive part vs. 0.44 in the negative). However, the shape of the curves is similar regardless of the voltage polarity. The HI calculated for the first measurement cycle, red rectangles in the plot, shows a slight deviation in the positive voltages range and is related to the beginning of the measurement. However, after 3 cycles, the HI dependence on the voltage polarity disappears, as was seen in the insets in Figure 5.7.
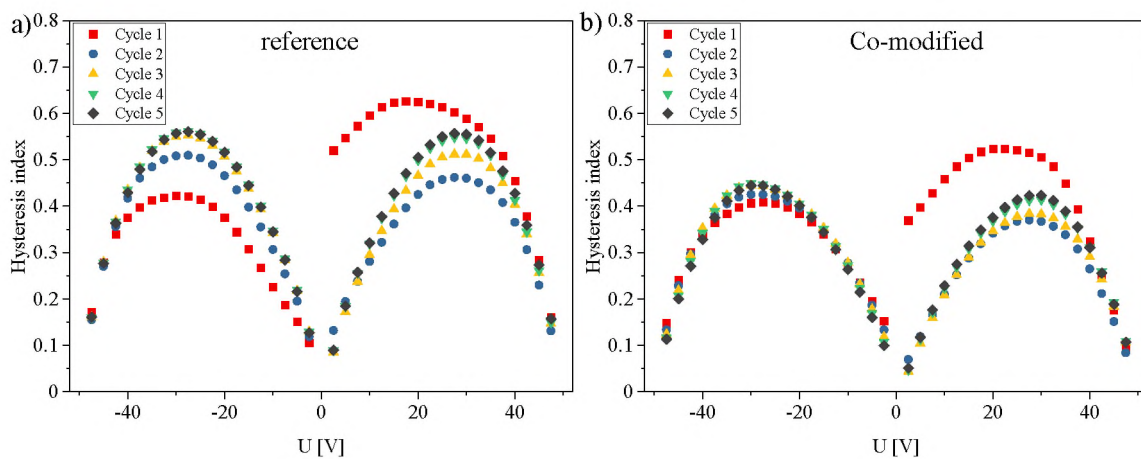

Figure 58. Hysteresis Index calculated in successive cycles for a) reference and b) Co-modified devices

To further examine the device's stability and performance the resistance of both systems has been calculated. The results are shown in **Figure 5.9** as a function of time during the voltage sweeps. The blue line in the plotted graph illustrates the voltage progression in time. As can be seen, the resistance calculated for both devices oscillates in time and

68

the resistance of Co-modified system is lower, compared to the reference sample.

After the first voltage sweep, where the change of the conductivity of the system is the highest, the performance of the Co-modified sample is more stable compared to the reference device. What is worth noting, for both Co-modified and reference systems, is the phase shift between the electric field variation and the resistance of the system. Moreover, a slight asymmetry of resistance amplitude between ± polarization has also been observed.
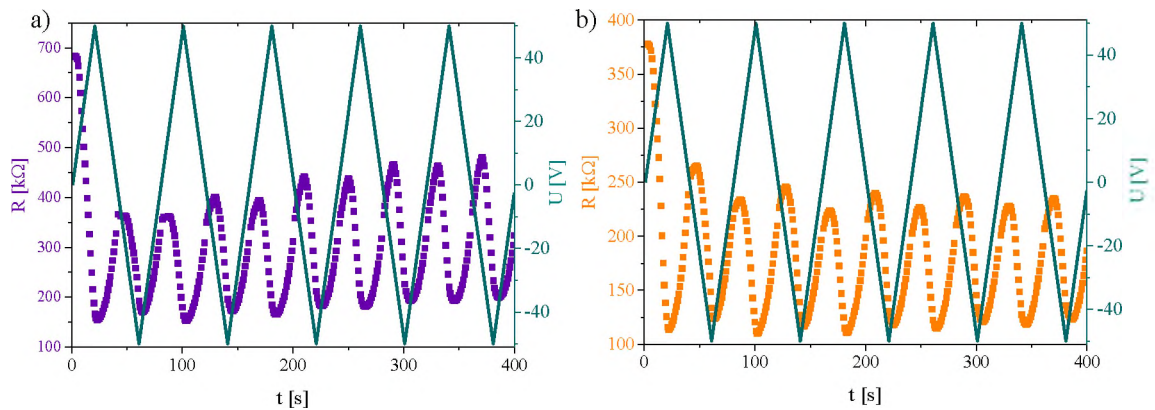

Figure 5.9. The systems' resistance calculated as a function of time for a) reference sample and b) Co-modified sample

Based on these findings the Co-modified system, due to its high performance and improved stability, has been selected to be further investigated.

5.3. Time constants of ion relaxation processes

As mentioned before, the devices have been tested with a PSS matrix enriched with 1% of potassium ions. To examine whether the admixed ions change the dynamic of processes occurring in the system, the devices with pure PSS (R-P3HT/P4VP/CoBr$_2$/PSS) and PSS enriched with 1% of K$^+$ ions (P3HT/P4VP/CoBr$_2$/PSS+K$^+$(1%)) were prepared, and their current vs. time curves were measured.

Figure 5.10 presents current vs. time curves registered for three different voltage sequences: 1) -10V, -50 V, +10 V, +50 V (Figure 5.10 a, b), 2) +10 V, +50 V (Figures 5.10 c, d), and 3) -10 V, -50 V (Figures 5.10 e, f). The duration of each potential step in voltage sequence 1) was set as 20 s and in voltage sequences 2) and 3) as 6 s. The switching time was fixed and shorter than 0.25 ms. To observe the relaxation processes occurring after ±50 V pulses stimulation, the "read" potential was selected

69

to be ±10 V. The value ±10 V was selected as it does not change the conductivity of the system in a significant way while ensuring a good signal-to-noise ratio in the current response of the device.
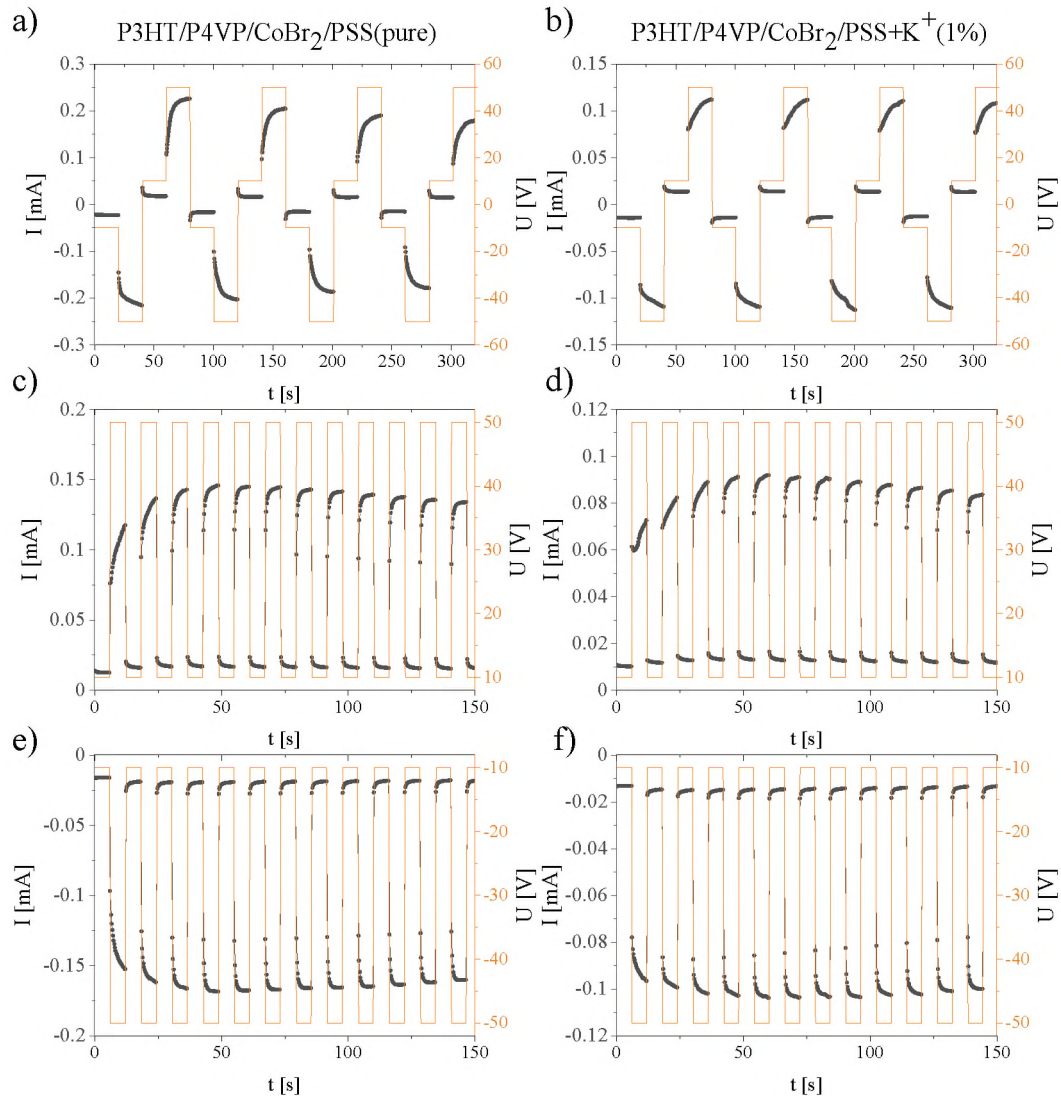

Figure 5.10. Current vs. time plots measured for devices with pure PSS (a, c, e) and PSS admixed with 1% of potassium (b, d, f) for three different voltage sequences: a), b) -10 V, -50 V, +10 V, and +50 V with 20 s potential step duration, c), d) +10 V, +50 V, and e), f) -10 V, - 50V with 6 s potential step duration. The switching time was set below 0.25 ms

Upon the application of a +50 V potential, the conductivity of both systems increases, with the corresponding currents approaching 0.23 mA for the PSS device and 0.12 mA for PSS+K+(1%) device. In contrast, when +10 V is applied the conductivity decreases as the respective currents drop by an order of magnitude, as shown in Figure 5.10 a) and b). Moreover, the current response of devices, illustrated in Figure 5.10, exhibits notable symmetry in relation to the polarity of the applied voltage.

The conductivity of the system with pure PSS matrix decreases globally in each following measurement cycle, as depicted in Figure 5.10 a). The respective currents registered for +50 V decreased approximately by 22% during the 4 cycles. The results of examination of the system admixed with 1% of K+ reveal the current decrease only by 8%, indicating more stable operation of the device.

Figure 5.10 c-f) shows, that through alternating between ±10 V and ±50 V the same symmetry is visible in case of both types of devices when a positive-only or negative-only voltage sequence is applied. Until the fourth cycle of applying the ±50 V sequences, the conductivity increases globally and then decreases with each following cycle.

Moreover, the devices demonstrate exponential current response increase upon application of ±50 V and exponential decrease as the voltage drops down to ±10 V pulses, indicating the systems' relaxation. To analyse the time dependence of the measured currents depicted in Figures 5.10 c-f) quantitively, the current values were described as a double exponential decay. The function, which describes two coexisting ion relaxation processes, is given by:

$$I(t) = A\left(\exp\left(\frac{t}{\tau_1}\right) + \exp\left(\frac{t}{\tau_2}\right)\right) + B, \qquad (5.3)$$

where I(t) is the current value in time t, A and B are signal amplitudes, and τ_1 and τ_2 are time constants of two independent relaxation processes.

The mean time constants for a device consisting of a pure PSS matrix were determined as follows: for the +10 V sequences $\tau_{1,+10V}$ = 0.26 s and $\tau_{2,+10V}$ = 1.89 s, for the -10 V sequences $\tau_{1,-10V}$ = 0.27 s and $\tau_{2,-10V}$ = 1.64 s.

The mean time constants calculated for a device consisting of PSS+K$^+$(1%) film equal to: for the +10 V sequences $\tau_{1,+10V}$ = 0.23 s and $\tau_{2,+10V}$ = 2.21 s, for the -10 V sequences $\tau_{1,-10V}$ = 0.20 s and $\tau_{2,-10V}$ = 1.99 s.

Figure 5.11 illustrates the total statistical distribution of the time constants for both device types. The plot implies that the addition of potassium ions alters the dynamics of relaxation processes in the PSS matrix. This result can be explained based on the values of the ionic radius of potassium and sodium. Sodium cation, native to the PSS layer, has a smaller ionic radius compared to potassium cation. The displacement of both types of ions is influenced by electric fields of the same magnitude and intensity, however, due to their differences in masses and ionic radius the sodium ions are expected to be less

inert in their reaction to the stimuli as well as migrate faster compared to potassium ions. Moreover, due to its large size, the K^+ will also encounter more resistance in its movement through the polymer matrix, what might be a factor contributing to higher values of τ_2 determined for the sample. The study of relaxation processes was further explored and is a subject of Chapter Six.
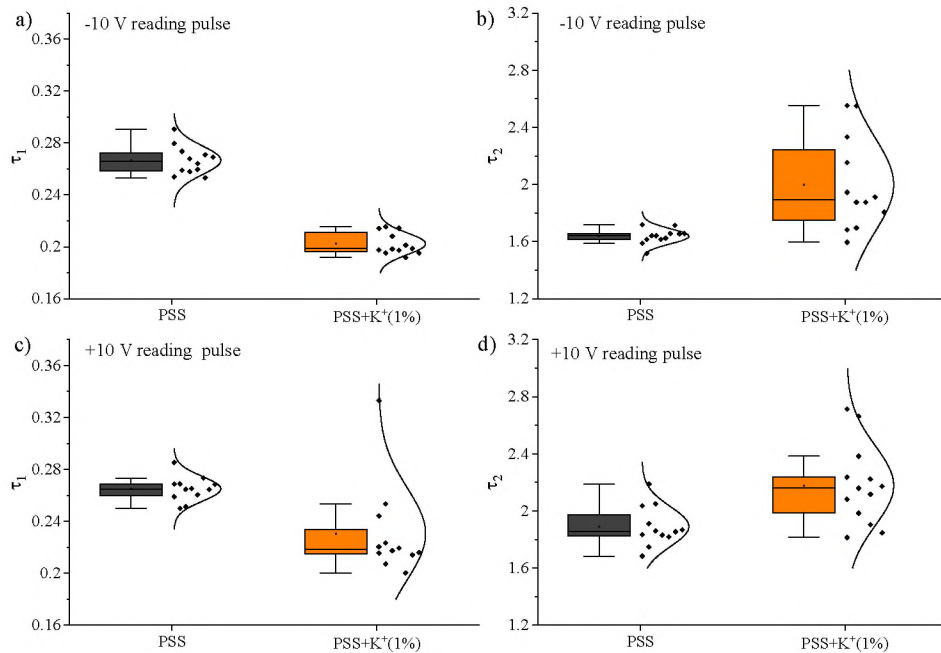

Figure 5.11. Time constants of relaxation processes determined from fitting Equation 5.3 to experimental data of devices consisting of pure PSS and PSS enriched with 1% of potassium ions. a) τ_1 determined for -10 V reading pulses, b) τ_2 determined for -10 V reading pulses, c) τ_1 determined for +10 V reading pulses, and d) τ_2 determined for +10 V reading pulses

5.4. Mimicking of the Short-Term Synaptic Plasticity

The results presented in the last section indicate that the devices exhibit one of the key properties desired in neuromorphic computing – the exponential relaxation of electric current. This feature can be elicited through applying electrical pulses which modify the device's conductivity for a certain time. In general, the conductivity can be increased by pulses of positive polarity, called potentiation (P), and it can be decreased by pulses of negative polarity, which corresponds to the depression (D) of a synapse.

The memristor which mimics such a behaviour can be classified as a biomimicking memristive device. In order to determine, whether the studied system can emulate the potentiation and depression of a synapse, the current response of a Co-modified device with the PSS matrix containing 1% of K^+ was measured to a series of pulses.

The current response of the device was measured under a +10 V bias between a series of potentiating (+50 V) pulses and depressing (-50 V) pulses, referred to as programming pulses. The state of the device was determined based on the response of the device measured under +10 V bias, referred to as reading pulses (R). The duration of each pulse was fixed as 100 ms and the time interval between pulses was set as 225 ms.
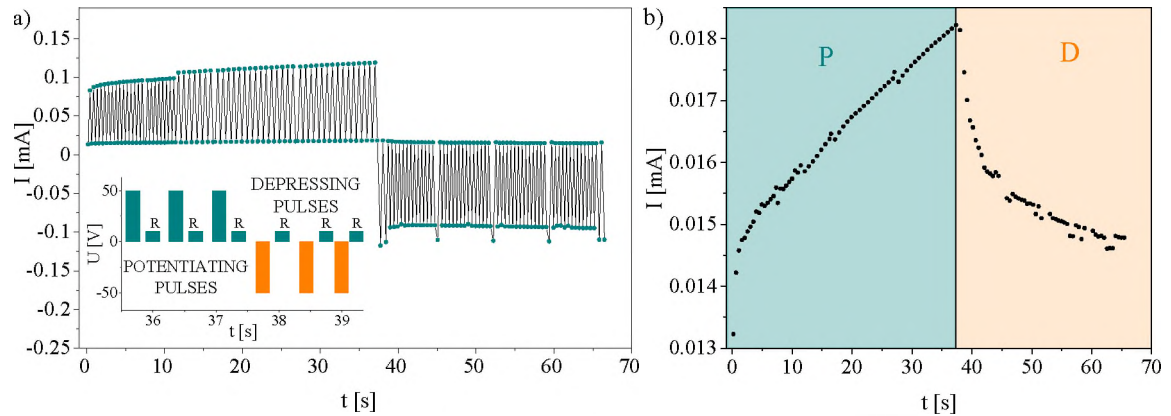

Figure 5.12. a) Current response measured at +10 V in between application of potentiating (+50 V) or depressing (-50 V) pulses. The sequence in which the pluses were applied is shown in the bottom left inset; b) the measured current response to reading pulses of +10 V magnitude divided into regions of potentiation (P in blue) and depression (D in orange)

Figure 5.12 a) shows the measured response of the device to potentiating and depressing pulses. As can be seen, during potentiating pulses global conductivity of the system increases with each step, regardless of the voltage magnitude, what is shown in Figure 5.12 b) as a current measured under +10V bias measured in between the programming pulses. What can also be seen, is that the application of depressing pulses decreases the device's conductance.

Previously, the systems' response to the voltage of +10 V magnitude has been shown to be not sufficient to increase devices' conductivity, as it was observed in Figure 5.10. Therefore, the current increase and decrease, measured as a response to the signal of lower magnitude in Figure 5.12 b), is related to the device programming with preceding pulses of higher magnitude. Due to the ionic relaxation processes, the state of the programmed device is temporal.

The dynamic alteration of device's conductance state mimics an important synaptic function, called Short-Term Plasticity, indicating possible implementation of the device in neuromorphic systems.

5.5. Device modelling attempt

5.5.1. Physical model

In the last part of the Chapter the attempt was made to describe the device mathematically. As the experiments are time and resources consuming, the equations which recreate the devices' response might be useful to utilize them in simulations and, based on their results, determine the best experiment parameters.

To explain the symmetry in the system's current response and it's unique direction of conductance changes we should consider the spatial electric field distribution from the two-electrode system of height 100 nm. In between the electrodes, in the area over the channel, the electric field is symmetric with respect to the line perpendicular to the channel center.

The field attracts the charges to the interface on one side of the channel, and is responsible for a repulsive force on its other side. The switch of polarity changes the direction of applied electric field to reversed, but the overall symmetry of the system remains unchanged. In order to get a better understanding a simplified field distribution is shown in **Figure 5.13**.
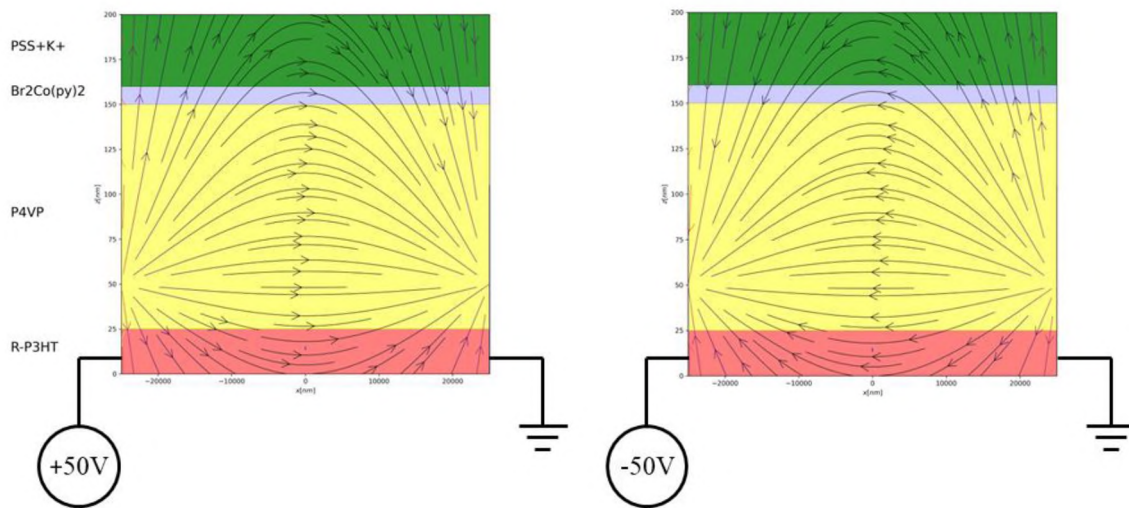

Figure 5.13. Simplified field distribution of a two-electrode system under a positive and negative external potential

By considering this aspect, together with the proposed model, it provides an explanation for the symmetrical conduction behaviour of the system under positive and negative bias.

In order to formulate the current flow equation of the system it is important to remember that the device is based in the architecture of OFET, which has to be further adapted based on the phenomena occurring in the system. The current flow in OFET in a linear regime,

which applies to the data presented in Figure 5.1, with the external gate potential U_G is given by[10]:

$$I_{DS} = C_i \mu \times \frac{W}{L} \times (U_G - U_T) \cdot U_{DS}, \tag{5.4}$$

where C_i is the gate capacitance per unit area, W is channel width, L is length, and μ is the carrier mobility of the semiconductor. If we take into account a homogeneous dipole layer the electric potential induced within it can be expressed at:

$$\phi_{dipole\ layer} (R) = \phi(0) \times \left(1 - \frac{R}{\sqrt{R^2 - r^2}}\right), \tag{5.5}$$

where R is distance from the dipole layer, $\phi(0) = \sigma/(2\varepsilon_r\varepsilon_0)$ and σ corresponds to the surface density of the dipole moments, and r is a radius of dipole layer approximated to a disc. The Equation 5.5, which can be used to describe the electric field induced in the P4VP-CoBr$_2$ complex, can substitute the gate potential in Equation 5.4. Therefore, the current flow in the Co-modified device can be expressed as follows:

$$I_{DS} = \frac{\varepsilon_0\varepsilon_r}{R} \cdot \frac{W}{L} \cdot U_{DS} \cdot \left(\frac{\sigma}{2\varepsilon_0\varepsilon_r} - U_T\right) - \mu \cdot \frac{W}{L} \cdot \frac{\sigma}{2} \cdot U_{DS} \cdot \left(\frac{1}{\sqrt{R^2 + r^2}}\right). \tag{5.6}$$

In Equation 5.6 the C_i has been expressed as $\varepsilon_0\varepsilon_r/R$ to further emphasize the relationship between the current and distance. To simplify the current modulation related to ion mobility, the Equation 5.6 can be reduced to:

$$I_{DS} = \mu \cdot C_i \cdot \frac{W}{L} \cdot U_{dip} \cdot U_{DS}, \tag{5.7}$$

where U_{dip} corresponds to the dipole-induced potential. If we add to this formula the electric field modulation related to ion migration the equation can be expressed as:

$$I_{DS} = \mu \cdot C_i \frac{W}{L} \cdot (U_{dip} * U_{ions}) \cdot U_{DS}, \tag{5.8}$$

where the $U_{dip}*U_{ions}$ part of the equation is the convolution of dipole-induced electric field and electric field related to presence of ions. This simplified equation is a function of the $U_{dip}*U_{ions}$ convolution and U_{SD}, as remaining factors such as C_i, μ, W, and L are constants. The convolution of the dipole-induced and ion-induced electric fields together with constants can be interpreted in terms of conductance G, and the resulting current flow can be expressed as:

$$I_{DS} = G \cdot U_{DS}. \tag{5.9}$$

Taking into account the assumption about the symmetry in devices current response we can consider two different resistance regions in the device: region containing ions (high resistance R_+) and region depleted in ions (low resistance R_-). The relationship between resistance and conductance is $R = 1/G$.

In case of absence of external electric field the ions are evenly distributed in the PSS layer, as confirmed by static TOF-SIMS measurements (Figure 5.5). It allows us to assume that in this condition the average resistance in both regions is even. However, if the electric field is applied to the system, it forces ion displacement, which results in formation of regions of high and low resistance. The ion migration through the polymer matrix is not an instant process, which was shown in Figure 5.10 as exponential current value increase over time. Therefore, the resistance of a system containing ion reservoir depends on two factors: magnitude of applied voltage U and time t. **Figure 5.14** illustrates in a simplified manner the regions of high and low resistance with distribution of potassium ions plotted in orange. Assuming that the two distinctive resistance regions in the sample can be approximated to series connection, the resistance of the system is a sum of resistances of both regions and is given by:

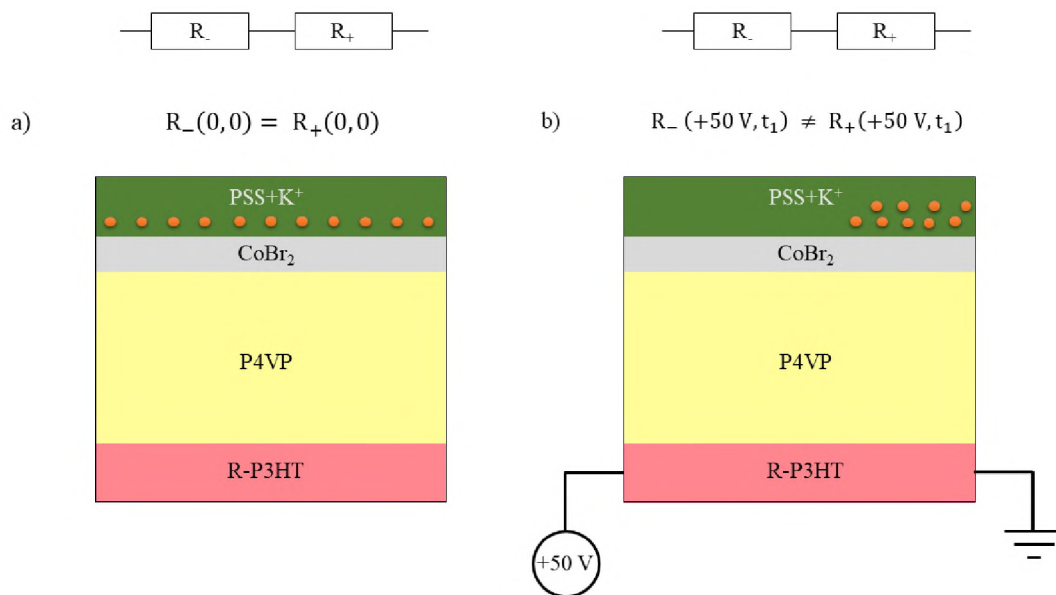$$R(U,t) = R_-(U,t) + R_+(U,t). \tag{5.9}$$

Figure 5.14. Simplified distribution of potassium ions of a) a device in the absence of external potential and b) device under +50 V bias

In the absence of external electric field the two components of resistance are equal and can be expressed as conductance:

$$R_- = R_+ = \frac{1}{\frac{1}{2}G_0} = \frac{1}{G_-} = \frac{1}{G_+}, \tag{5.10}$$

where G_0 is the initial value of conductance, and G_- and G_+ correspond to regions of low and high conductance. The equation can be rewritten as:

$$G_- = G_+ = \frac{1}{\frac{1}{2}R_0} = q_-(0) = q_+(0), \tag{5.11}$$

where $q_-(0)$ and $q_+(0)$ are initial conductance values of low and high conductance regions at $U = 0$. The conductance is a function depending on time and applied potential, and its change over time can be described as:

$$\frac{dG_+(U,t)}{dt} = -\alpha(G_+ - q_+), \tag{5.12}$$

$$\frac{dG_-(U,t)}{dt} = -\alpha(G_- - q_-), \tag{5.13}$$

where α corresponds to time constant of ion relaxation processes. The values of q_- and q_+ also change in relation to applied potential:

$$\Delta q_-(U) = \frac{\sigma}{1+exp\left(-\frac{U-U_0}{\epsilon}\right)}, \tag{5.14}$$

$$\Delta q_+(U) = \frac{\sigma}{1+exp\left(\frac{U+U_0}{\epsilon}\right)}. \tag{5.15}$$

The equations 5.11 - 5.15 take the systems symmetry into account, and by incorporating them into Equation (5.9) conductance changes and current flow can be expressed as:

$$G(U,t) = \frac{1}{R_-(U,t)} + \frac{1}{R_+(U,t)}, \tag{5.16}$$

$$I(U, t) = U \cdot G(U, t). \tag{5.17}$$

The simplified model presented above does not consider spatial distribution of ions, but separates the device into two regions of distinctive resistance. Therefore, further development of the model requires more complex study of the ion distribution in polymer matrix. Regardless of it, the simulation, performed by numerically solving the equations 5.11-5.17, replicates, to some extent, the unique shape and changes of conductivity in the hysteresis loop exhibited by the studied system, as illustrated in Figure 5.14.

The simulation model parameters were set as: $\alpha = 0.65$ $1/s$, $\epsilon = 1$ V, $U_0 = 1$ V, $\sigma = 5{\cdot}10^{-6}$ $1/\Omega$, and $G_0 = 1{\cdot}10^{-6}$ $1/\Omega$. The time step of simulation was fixed as 1 s to replicate the parameters of current-voltage characteristic measurements.
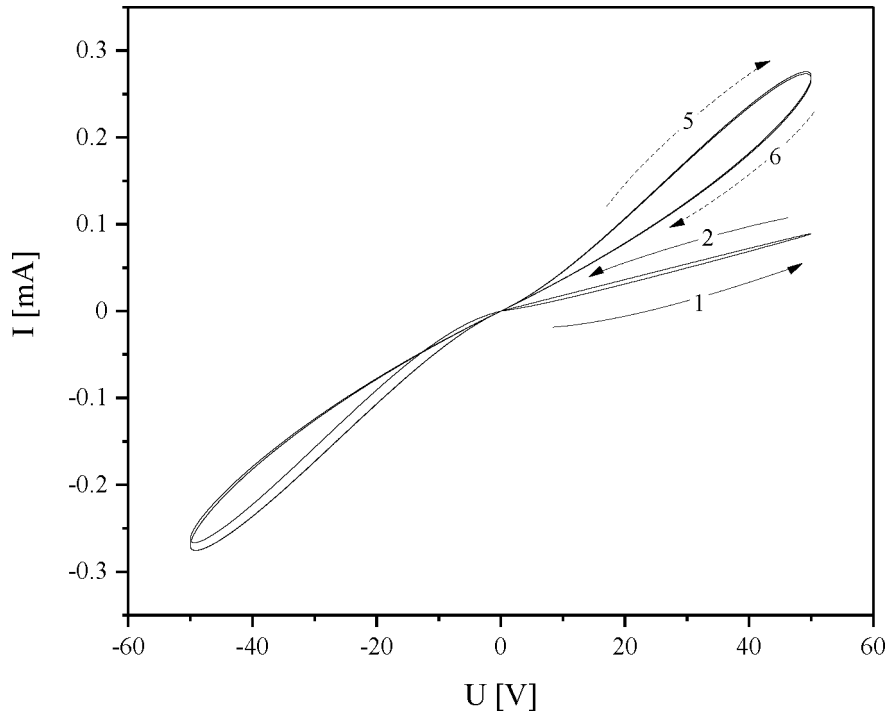

Figure 5.15. Result of numerical simulation of the simplified model performed for parameters set as: $\alpha = 0.65$ $1/s$, $\epsilon = 1$ V, $U_0 = 1$ V, $\sigma=5{\cdot}10^{-6}$ $1/\Omega$, and $G_0=1{\cdot}10^{-6}$ $1/\Omega$; solid lines indicate the direction of voltage sweep during the first operation cycle and dashed lines during following voltage sweeps

Unfortunately, the model performs well only during the first operation cycle, where it reproduces both current values and the direction of current increase. Starting from the second cycle the direction of conductance changes switches, therefore the model does not reproduce the systems' character correctly as shown with dashed lines on **Figure 5.15**. This issue demands further investigation and for the sake of simplicity the phenomenological model was developed, as described below.

5.5.2. Phenomenological model

In order to phenomenologically describe the device as a mathematical model it has to replicate it's features. The findings presented in this chapter indicate two unique features of the system: continuous modulation of conductance and the direction of those changes. However, the aforementioned mechanism of device operation implies a rather intricate form of equations describing the physical interactions within the system. As this matter requires to be further examined, a simplified difference-equation model has been proposed.

The model assumes time t to be a discrete value step and the current response I_t to be a function of voltage V_t and conductance C_t. The model equations are given as:

$$I_t = C_t \cdot V_t, \tag{5.4}$$

$$C_t = \tau \cdot C_{t-1} + \eta \cdot |V_t|, \tag{5.5}$$

where the coefficients τ and η represent the time and voltage dependence of the conductance change, respectively. The initial parameter values were estimated by fitting the model equations to experimental data obtained for a device containing 1% of potassium addition.
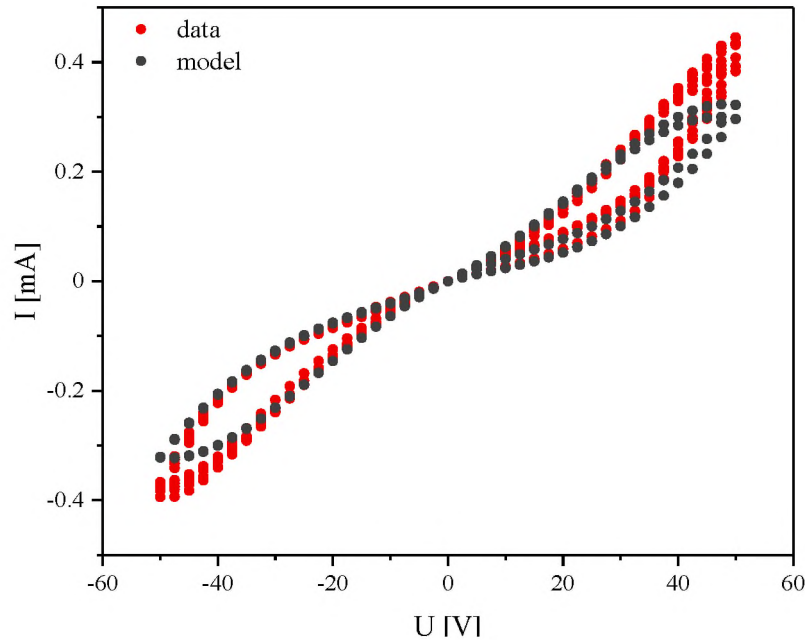

Figure 5.16. Current-voltage characteristic of experimental data (red) and reproduced by model equations (black); the models' initial parameters were set as $C_0 = 2.90 \cdot 10^{-6}$ mS, $\tau = 0.93$, and $\eta = 1.62 \cdot 10^{-8}$ mS/V

As can be seen in **Figure 5.16** the model equations (black points) replicate the continuous alteration of conductance and the direction of its changes (red points). The model parameters and the initial conductance value C_0 were estimated as $\tau = 0.93$, $\eta = 1.62 \cdot 10^{-8}$ mS/V and $C_0 = 2.90 \cdot 10^{-6}$ mS through fitting model equations to experimental data. As shown in **Figure 5.17** the changes of resistance in the system are also well replicated by the proposed model.
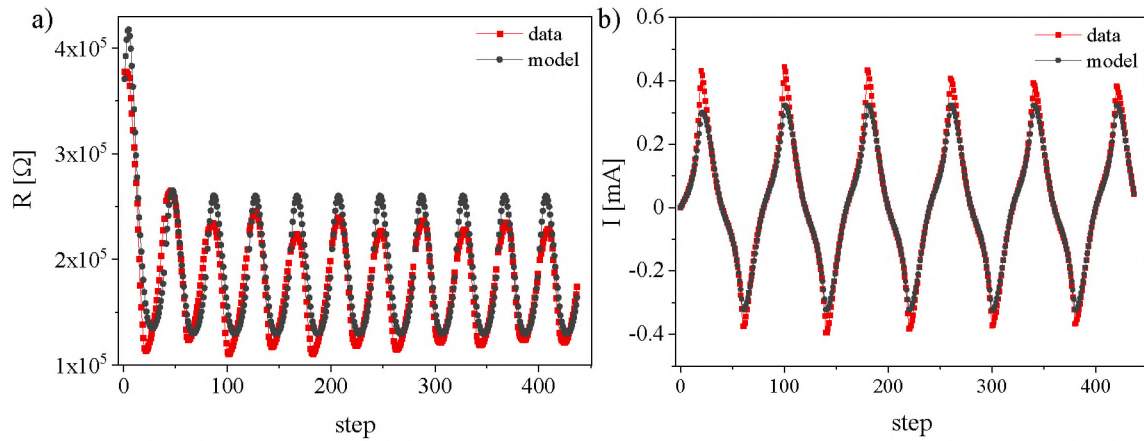
Figure 5.17. a) Current response and b) resistance changes for experimental (red) and modelled (black) data

In the proposed model the conductivity change depends on two factors, which dynamically alter the C_t value: τC_{t-1} and $\eta|V_t|$. In terms of physical interpretation, the first component relates to relaxation processes occurring in the system and the second component represents the conductance change caused by applied voltage. This interpretation aligns with the hypothesis, in which two processes alter the conductance in the system: the external electric field, which causes ion migration, and the spontaneous ionic relaxation responsible for device volatility.

The voltage dependency of conductance change is related to the parameter η. In the proposed model it is a constant, which represents the absolute value of the voltage-dependent conductivity. The competing process, corresponding to ion relaxation, depends on τ coefficient. For the model to replicate the key properties of the system the τ coefficient has to be set below 1, otherwise, the hysteresis loop will disappear from the current-voltage characteristic. Another feature of the system, its symmetry regardless of the polarity of the applied voltage, is reproduced by the absolute value of voltage $|V_t|$ in equation 5.5. Further analysis of the model in relation to its ability to reproduce other experimental data is a subject of Chapter Six.

5.6. Conclusions

The system, which is the objective of this dissertation, has been investigated in terms of the origin of its unique memristive character. At first, through the use of various methods, it has been confirmed that the external electric field causes ion migration within the PSS matrix. Moreover, the interactions occurring at the P4VP-CoBr$_2$/PSS interface have been confirmed to be responsible for the dynamic changes in conductivity in R-P3HT. This effect has been postulated to be caused by electric field modulation

caused by ion mobility. Additionally, by step-by-step measurements, it was verified that the memristive character of the device can be cancelled in the absence of a layer with an ion reservoir, which was illustrated in I-U curves of devices consisting of R-P3HT/P4VP/PMMA (accomplished by replacing PSS with PMMA). The possibility of cancelling the memristive character of the device was also validated by limiting the ion mobility at low temperatures. It was shown that through a significant reduction of the temperature, the ion movement can be inhibited.

It was shown that the devices display highly stable hysteresis loops, which have been obtained by smooth tuning of conductance caused by voltage sweeping. In addition, the study of constants of relaxation processes implies that, to some extent, the dynamics of the system can be controlled by changing the composition of the ionic reservoir. Based on these findings a simplified model of the device has been proposed and confirmed to mimic the shape and direction of changes in conductivity in the hysteresis loop.

CHAPTER Six – Response to different stimuli

In this chapter, the study of the system is extended to its response to different types of stimuli. The results of this study should provide more information on the dynamics of the processes occurring in the system while it operates, as the system's principle of operation is based on collective ion diffusion in a polymer matrix, which does not partake in the current conduction. Therefore, by forcing ion movement through different types of stimuli, the system should shift to non-equilibrium state and its' response should depend both on the type of stimuli and the past state of the device. Another factor, which should be included in the results analysis, is the systems' inertia related to the dynamics of collective ion movement, which should be apparent during fast voltage switching.

The Chapter consists of three parts. At first, the sampling frequency of the measurements is determined based on results from Impedance Spectroscopy. The selected measurement steps are further used to examine the device's responses to stimuli differing in signal shape, amplitude and duration. In the third part of the Chapter, the devices' phenomenological model is tested in terms of its ability to reproduce the experimental data, providing information about its' utility.

6.1. Sample preparation and characterization

Sample preparation. The samples, if not stated differently, were prepared following the device preparation process described in Chapter Three.

Electrical characterization. The samples consisting of R-P3HT/P4VP/CoBr$_2$/PSS+K$^+$(1%) were characterized in terms of current response to various voltage stimuli. The measurements were performed using computer controlled source-meter, Keithley 2400, at ambient temperature and in an inert gas atmosphere.

The voltage pulses were 225 ms or 400 ms long and the time step between the current

reading pulses was set as 0.125 s or 0.3 s. The samples were tested in the voltage range from -50 V to +50 V with different voltage steps.

Additionally, the current-voltage characteristics were measured in the voltage range from -50 V to +50 V with voltage step 5 V/2 s.

Simulations. The simulations were performed using the phenomenological model of the device described in Chapter Five. The model parameters obtained through fitting data to the model were determined as: $\tau = 0.946$, $\eta = 1.58 \cdot 10^{-8}$ mS/V, and $C_0 = 5.42 \cdot 10^{-6}$ mS. The simulations were performed by testing the models response to the stimuli matching the input signals from the experiments.

Impedance Spectroscopy. Samples for the Impedance Spectroscopy were prepared on S161 substrates, following the preparation process described in Chapter Three with one alteration: omitting the R-P3HT layer. The samples with pure PSS matrix and with 1% addition of K^+ were examined using the SI technique. The measurements were performed in an inert gas atmosphere at an ambient temperature, and in a wide range of frequencies (0.001 Hz – 1MHz) with a measurement voltage of AC equal to 0.1 V.

6.2. Results

6.2.1. Determining the sampling frequency

As shown in Chapter Five, the relaxation processes occurring in the system can be described as a combination of two coexisting processes. The time step of these processes should correspond to characteristic time constants of ion relaxations.

In order to determine the values of these time constants the samples consisting of P4VP/CoBr$_2$/PSS and P4VP/CoBr$_2$/PSS+K$^+$(1%) were examined using Impedance Spectroscopy in a wide range of frequencies. To obtain reliable results, the measurements were performed for four different devices.

The results, which are illustrated in **Figure 6.1 a)** for devices admixed with potassium and **c)** for reference samples, indicate the occurrence of relaxation processes in the frequency range below 1kHz. The data measured for consecutive devices, shown in red, blue, yellow, and green, overlaps, which proves the measurement's reliability.

To determine the frequencies of the relaxation processes the measurements were performed in the frequency range from 1 mHz to 1 kHz, and the results are illustrated in **Figures 6.1 b)** for PSS+K$^+$(1%) and **d)** pure PSS. What is worth noting, is that the results reveal a characteristic time constants' shift from higher frequencies, for

the sample with pure PSS, to slightly lower frequencies for the sample with a 1% addition of K^+, which is highlighted in circles. The characteristic time constants determined for the sample admixed with 1% of K^+ are c.a. 0.02 Hz and 10 Hz, which corresponds to relaxation time constants c.a. 50 s and 0.1 s respectively. In the case of the sample with pure PSS, the characteristic time constants occur at c.a. 0.04 Hz and 20 Hz, resulting in relaxation times c.a. 25 s and 0.05 s.
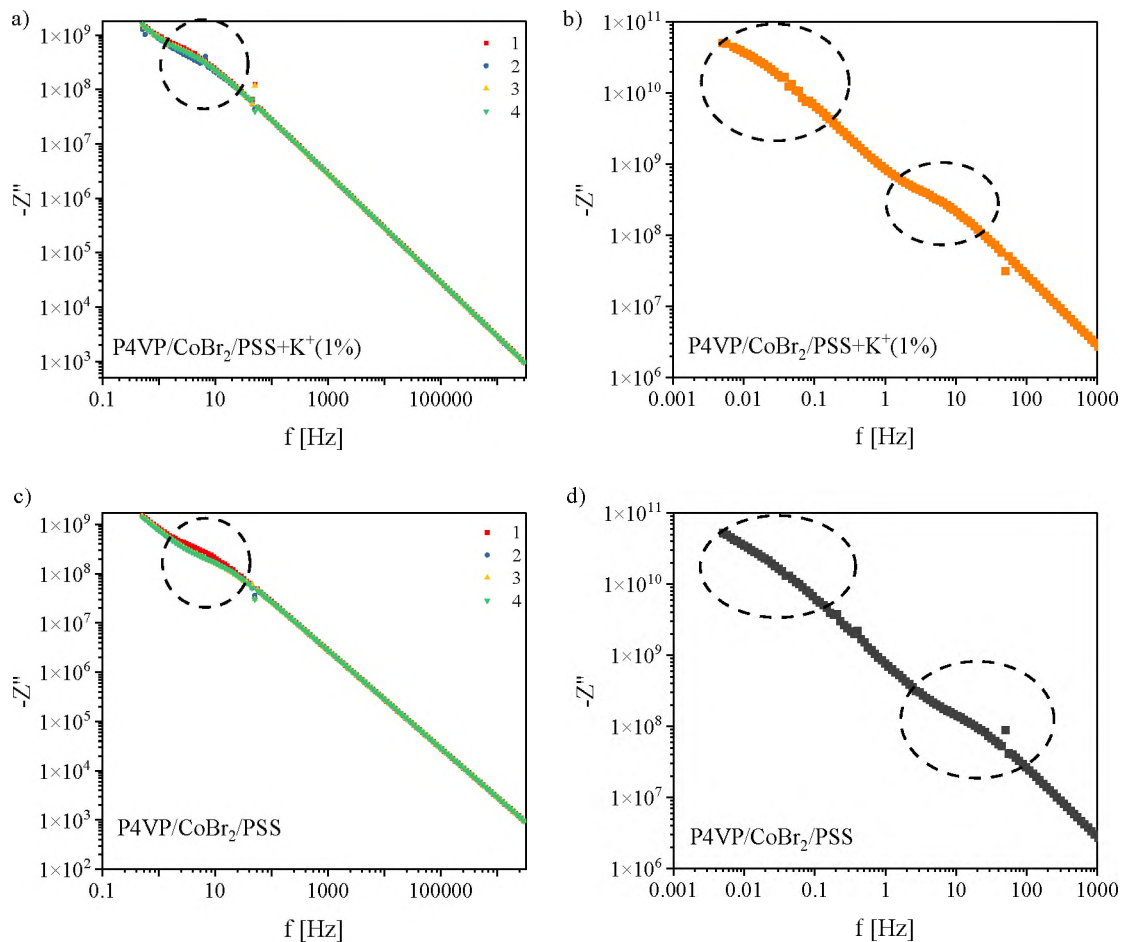

Figure 6.1. Results of Impedance Spectroscopy measurements performed for samples in frequency range a, c) 0.1 Hz to 1MHz and b, d) 0.001 Hz to 1000 Hz for samples consisting of a, b) P4VP/CoBr2/PSS+K+(1%) and c, d) P4VP/CoBr2/PSS

The 0.02 Hz and 0.04 Hz sampling frequencies are too low for their applicability, therefore the 10 Hz and 20 Hz frequencies were considered in further study. Unfortunately, due to equipment limitations, the highest sampling frequency, which can be used in the experimental setup is 8 Hz. Taking this into account, and the 8 Hz value being close to 10 Hz, the sampling frequencies for further examination were selected as 8 Hz (0.125 s) and 3.3 Hz (0.3 s). The 0.3 s time step of measurement was selected to differ significantly from 0.125 s but remain applicable.

6.2.2. Device response to various signals

To determine whether the time step of measurement alters the operation of the system, the device consisting of R-P3HT/P4VP/CoBr$_2$/PSS+K$^+$(1%) was examined at three fixed time steps of measurements: 2 s, 0.3 s, and 0.125 s. For consistency's sake, five devices were prepared and the most durable specimen was selected for further study.

At first, the current-voltage characteristics of the devices were measured in the voltage range from -50 V to 50 V with a 5 V per measurement step. The results, presented in **Figure 6.2**, correspond the first loop measured with **a)** 2 s (red), **b)** 0.3 s (blue), and **c)** 0.125 s (green) time step. What is interesting, is that the hysteresis loop gets narrow as the time step between the following measurement points decreases. It can be seen as a very narrow hysteresis loop measured for 0.125 s time step. This result implies that close to the characteristic time constant the hysteresis loop can be cancelled, showing that the device's response can be altered not only by temperature but also by adjusting measurement settings such as sampling frequency.

The aforementioned findings show that the sampling frequency alters the device's response – the more time ions have to migrate the more their influence on the conductance manifests itself.

What is also worth mentioning, is the lack of symmetry in the I-U curve measured with 0.3 s time step. As can be seen in Figure 6.2 b), the loop is wider in positive polarity, compared to negative one. This lack of symmetry is rather intriguing and requires extending the analysis to different types of stimuli, which was performed for time steps set as 0.125 s and 0.3 s. The 2 s time step, regardless of the symmetry and wide hysteresis loop, was excluded from the investigation due to its' low applicability. Therefore, further study was conducted using 0.125 s and 0.3 s time steps to determine possible differences in signal shapes measured as a response to various stimuli.
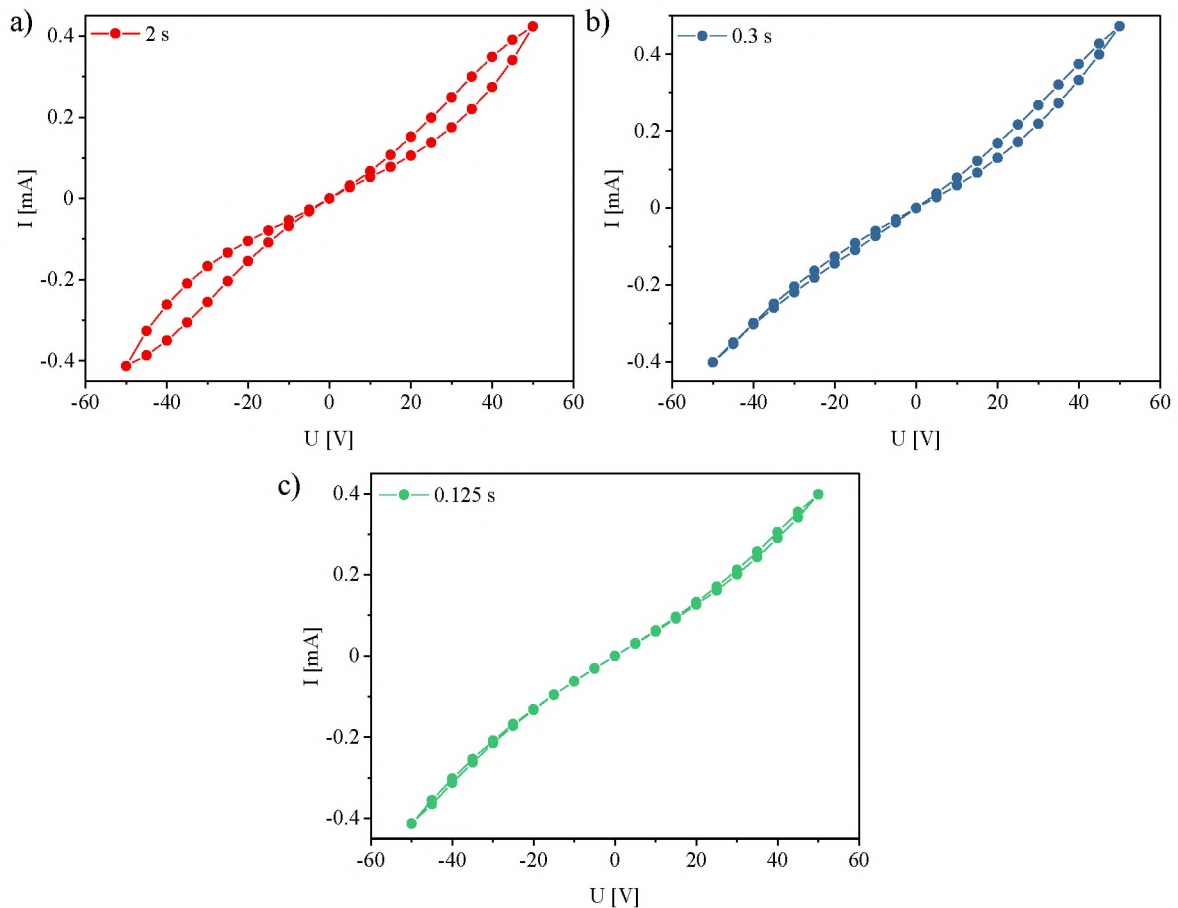
Figure 6.2. Current-voltage characteristics of device consisting of R-P3HT/P4VP/CoBr$_2$/PSS+K$^+$(1%) measured with a measurement time step a) 2 s, b) 0.3 s, and c) 0.125 s

In the next step of the investigation, the device was tested in terms of its response to the semi-rectangular signal, as shown in **Figure 6.3** (right axis).

The results, shown in Figure 6.3, prove that the character of the devices' response is similar for both measurement steps, however, both the maximum current and the slope of the current increase are different. What has to be stressed, is that the results are presented as a function of measurement step instead of time. This particular way of results presentation is related to transistor-like voltage dependency of current values. Therefore, to analyse the response measured with the 0.125 s measurement step, one has to take into account the shorter measurement time. This factor might be responsible for lower current values measured for the 0.125 s time step, as the ions have less time to migrate in between the consecutive voltage steps.
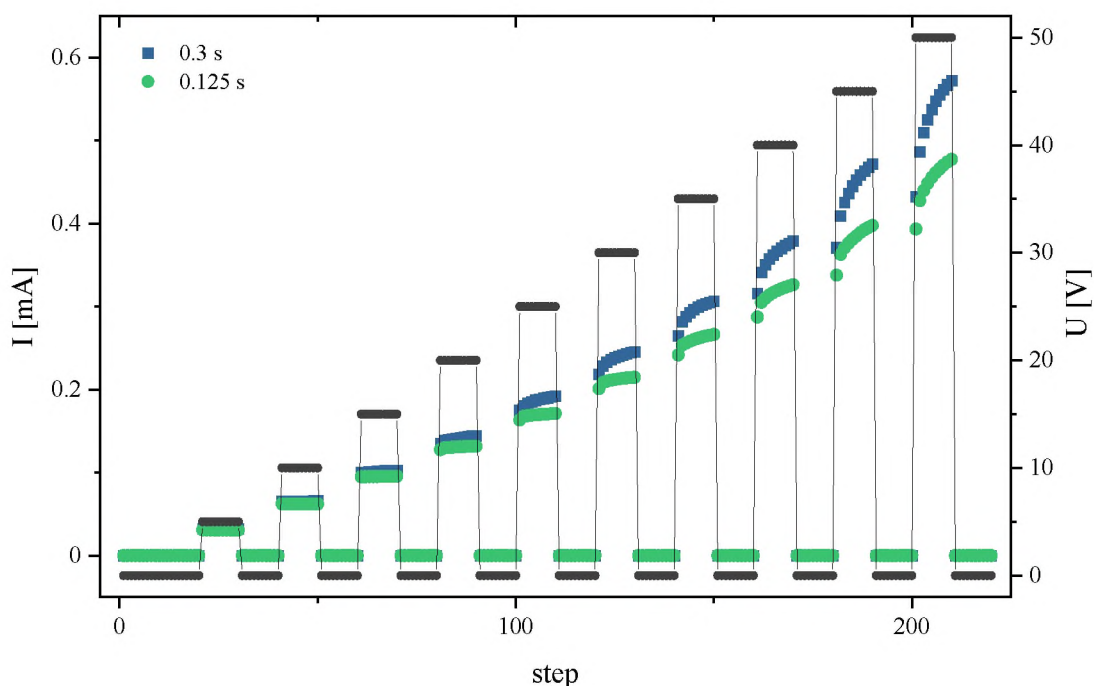
Figure 6.3. The current response of the device consisting of R-P3HT/P4VP/CoBr$_2$/PSS+K$^+$(1%) to rectangular signal with magnitude growth after each magnitude minimum; the response was measured for 0.125 s (green) and 0.3 s (blue) sampling rate and is presented as a function of measurement step

To further examine the device's response in different measurement time steps, the response, presented in **Figure 6.4**, to rectangular signal alternating between **a)** 10 V and 50 V, and **b)** -10 V and -50 V was measured.

The results show a lower current magnitude measured for time step 0.125 s, as it was reported earlier. As the slope of both signals measured for ± 50 V slightly differs, the signal measured for ± 10 V was fitted to Equation 5.3 to determine the time constants of relaxation processes for both time steps. The current response of the device to ± 10 V also exhibits a difference in signal magnitude and has a slightly altered slope for both time steps, which might result in altered time constants of relaxation processes and provide information about the dynamics of occurring processes.
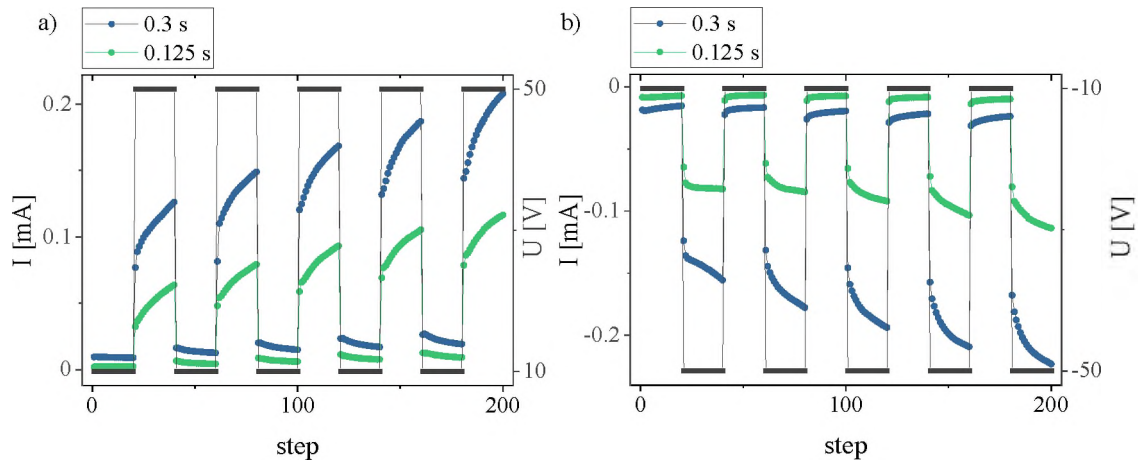
Figure 6.4. Current response of the device consisting of R-P3HT/P4VP/CoBr$_2$/PSS+K$^+$(1%) to rectangular signal alternating between a) 10 V and 50 V, b) -10 V and -50 V measured with the sampling rate 0.125 s (green) and 0.3 s (blue)

The calculated time constants of relaxation processes are presented in **Figure 6.5**. The boxes in green correspond to time constants determined for the 0.125 s time step, and in blue to the 0.3 s time step. The values of time constants determined under 10 V bias for 0.125 s time step equal $\tau_{1,+10\,V} = 1.16(23)$ s and $\tau_{2,+10\,V} = 7.7(2.7)$ s.

Corresponding values determined for 0.3 s time step equal to $\tau_{1,+10\,V} = 1.44(22)$ s, and $\tau_{2,+10\,V} = 8.4(2.2)$ s. As can be seen, the values of the first and the second time constants determined for 10 V for both time steps are similar and overlap in the range of measurement uncertainty. The standard deviation calculated for both of the τ_2 is rather high, however, the results of this study serve to indicate trends, therefore they were included in the analysis.

On the contrary, as illustrated in Figures 6.5 b) and d), the disproportion between the time constants in negative polarity is higher and might be related to the aforementioned lack of symmetry in negative polarity of the current-voltage characteristic from Figure 6.2 b). The time constants determined under -10 V bias for 0.125 s time step equal $\tau_{1,-10\,V} = 0.15(4)$ s and $\tau_{2,-10\,V} = 1.78(37)$ s.

As for the time constants for the 0.3 s time step, the values were determined as $\tau_{1,-10\,V} = 0.62(39)$ s and $\tau_{2,-10\,V} = 4.58(86)$ s. Moreover, the range of the determined time constants differs for the respective time constants, indicating that sampling frequency and polarity alter the system's response.
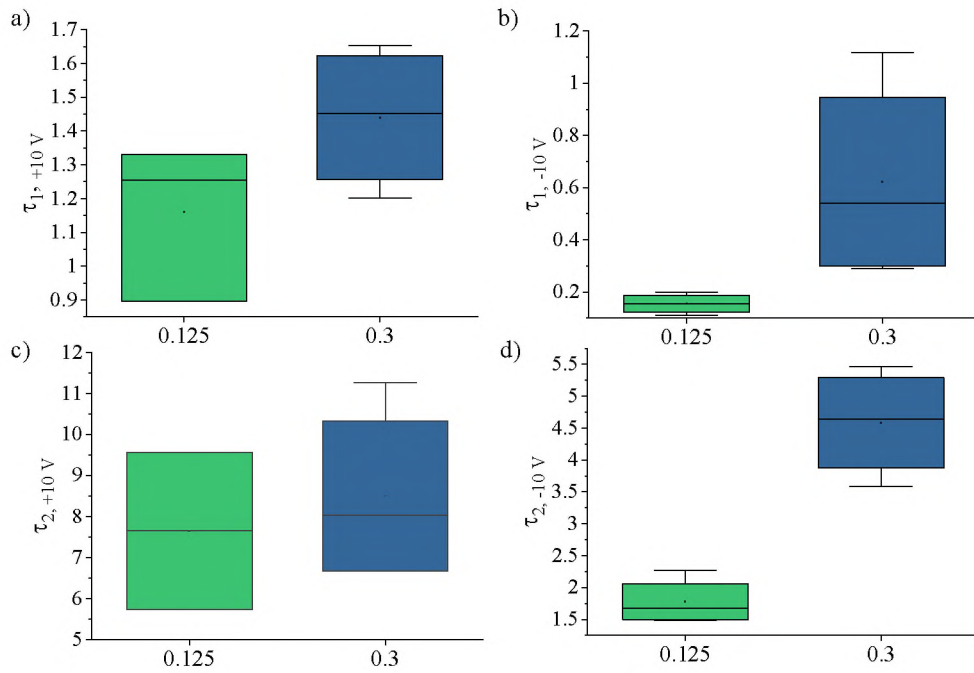
Figure 6.5. Time constants of relaxation processes determined from Equation 5.3 for device measured with 0.125 s (green) and 0.3 s (blue) time step

For more complementary insight into the device's operation, the device's endurance was illustrated in **Figure 6.6**. The endurance was determined based on the device's response to selected potentials, -50 V (red), -45 V (blue), -10 V (yellow), 10 V (green), 45 V (purple), and 50 V (grey), during first five cycles of current-voltage characteristic measurement. As potentials other than ±50 V and 0 V are measured twice in one cycle (forward and reverse direction) the presented values were selected to represent the reverse direction, as it holds information about the conductance increase in the cycle.
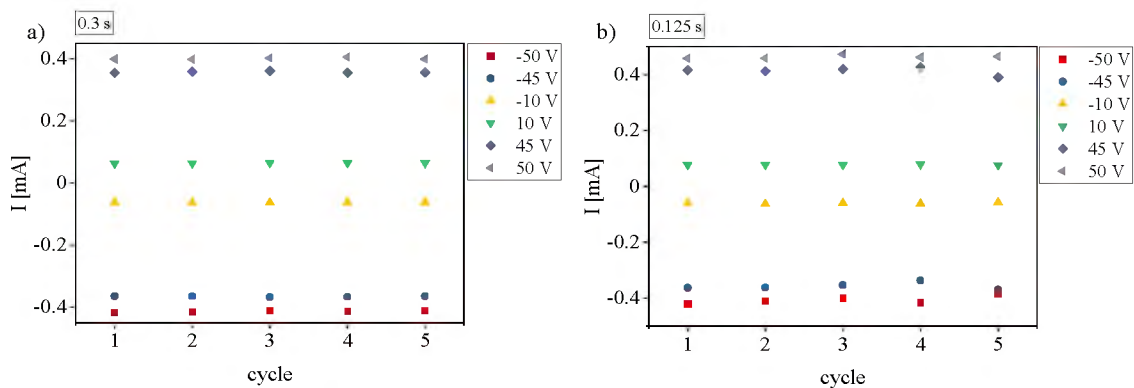

Figure 6.6. The endurance of the device determined based on its response to selected potentials in successive cycles of the current-voltage characteristic measurement with time step a) 0.3 s and b) 0.125 s

The results, shown in Figure 6.6 a), illustrate the high stability of the device in the measurement with 0.3 s time step. However, the measurements performed under -10 V imply slight asymmetry of the loop as the signal in yellow has a slight slope.

The measurements performed with 0.125 s time step, illustrated in Figure 6.6 b), indicate less stable operation of the device under faster sampling frequency. This result is in accordance with an earlier mentioned hypothesis about the sampling rate being close to the devices' characteristic time constant causing distortion in the ion diffusion processes. Nevertheless, the current changes cycle-to-cycle remain under 10%.

To further examine the differences between the responses to different sampling rates, the STP function was emulated and the results of the measurements are shown in **Figure 6.7 a)** for 0.3 s measurement time step, and **b)** for 0.125 s time step.
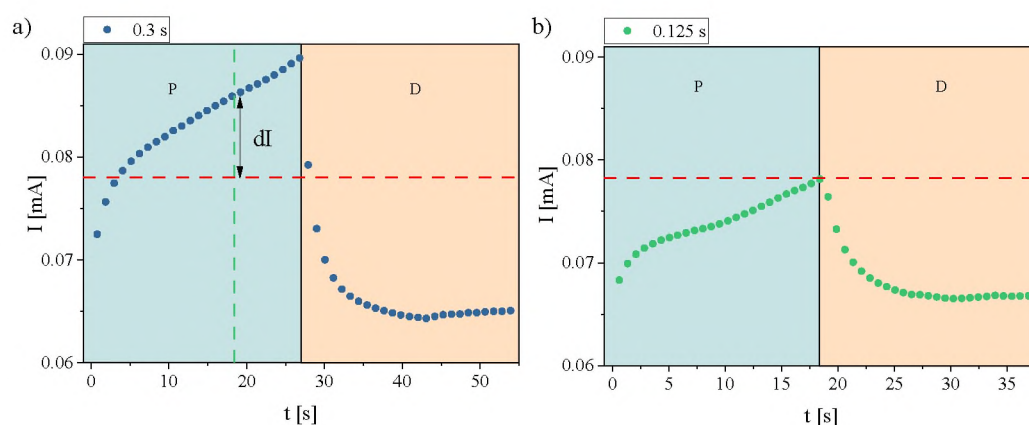

Figure 6.7. The STP function emulated for the device consisting of R-P3HT/P4VP/CoBr$_2$/PSS+K$^+$(1%) with a measurement step set as a) 0.3 s and b) 0.125 s

As can be seen, the device emulates the STP function in measurements with both time step. The device's current response to the 0.3 s time step has higher magnitude, compared to the 0.125 s time step. Moreover, the results are shown in the measurement time scale, which allows us to compare the current values at specific times. The time of the end of potentiation of the device in measurement with 0.125 s time step is indicated in Figure 6.6 a) with a green dashed line. The red dashed lines in Figure 6.6 a) and b) show the current value at that time measured in the experiment with 0.125 s time step.

As illustrated, the device with a longer time step reaches higher current values, which was previously suggested to be related to a longer time of ion diffusion in between subsequent voltage pulses. At the same time, the 0.125 s time step is closer to the characteristic time constant of the ion diffusion processes, which might also decrease the values of measured current, as in the resonance frequency the motion of ions is limited to their normal modes. What is also worth noting is the irregular shape of the curves, measured for 0.125 s time step during potentiation, and for both time steps in depression. The irregularity implies the occurrence of the competitive process, which at some point, decreases

the conductance during the potentiation and increases it during the depression. This observation requires further investigation, which will be a subject of different study, not included in this thesis.

So far, the STP function has been emulated including both device potentiation and depression. However, it was shown before that the system exhibits spontaneous relaxation. Having this in mind, the sample response at 10 V was tested for a series of potentiating pulses after which the device was left to relax spontaneously. The result of this experiment is shown in **Figure 6.8**.
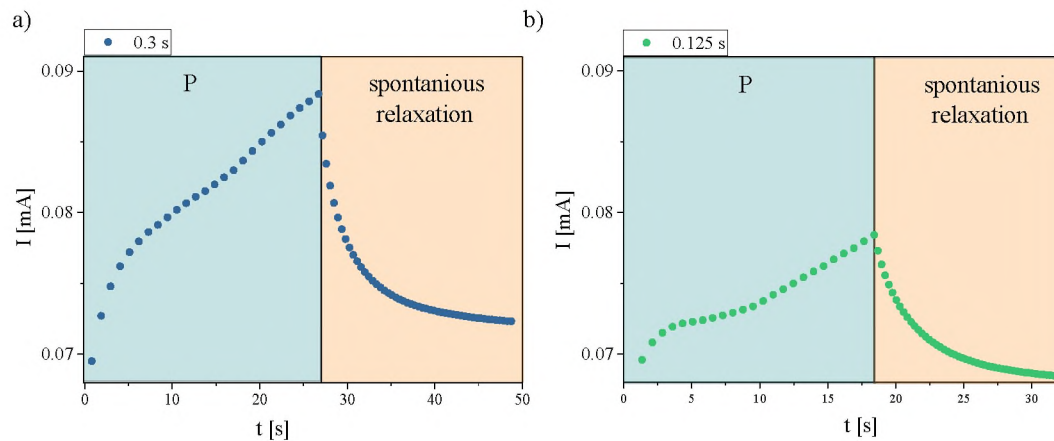

Figure 6.8. STP function, with spontaneous relaxation after the period of potentiation, emulated for the device consisting of R-P3HT/P4VP/CoBr$_2$/PSS+K$^+$(1%) with a measurement step set as a) 0.3 s and b) 0.125 s

The results of emulation of STP function with spontaneous relaxation illustrate a fast current decrease followed by signal saturation. The current value, after spontaneous relaxation, saturates at a higher value compared to the results shown in Figure 6.7. In contrast, during forced device depression, the slope of the current decrease is higher, and instead of saturating, the current starts to increase at some point during the measurement. This result is interesting, especially in terms of the device's applications, where the lack of device depression to decrease its conductance is an asset, allowing to decrease the power usage. Moreover, spontaneous relaxation allows omitting the current increase, which appears at some point of device depression.

6.2.3. Phenomenological model validation

Based on the findings presented earlier in this chapter, further study, regarding validation of the phenomenological model, was conducted for the 0.3 s sampling rate.

As devices from different samples differ slightly in terms of their parameters, the current-voltage characteristic of the device examined in this chapter was fitted to the model

equations to determine its parameters. As it was shown in Figure 6.2 b), the current-voltage characteristic measured with a 0.3 s time step lacks symmetry, therefore the model equations were fitted to data measured with a 2 s time step. This approach is valid due to the model's character, in which the conductance change depends on two factors: τC, which relates to relaxation processes and $\eta |V_t|$, which is responsible for the conductance increase related to voltage amplitude. The model assumes that the τ and η parameters are constant and their values should be independent of the sampling rate. The values specific for the studied device were estimated as $C_0 = 5.42 \cdot 10^{-6}$ mS, $\tau = 0.946$, and $\eta = 1.58 \cdot 10^{-8}$ mS/V. The current-voltage characteristics measured for the device, referred as data, and reproduced by the model are presented in **Figure 6.9**.
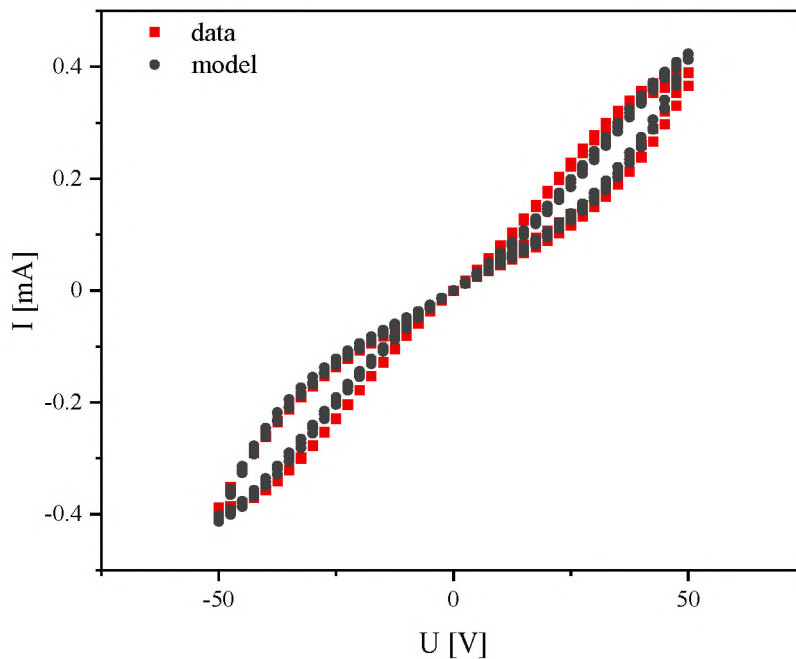

Figure 6.9. Current-voltage characteristic of experimental data (red) and reproduced by model equations (black); the models' initial parameters were set as $C_0 = 5.42 \cdot 10^{-6}$ mS, $\tau = 0.946$, and $\eta = 1.58 \cdot 10^{-8}$ mS/V

As can be seen, the model replicates the smooth tuning of conductance quite well in terms of the current values and shape of the hysteresis loop.

As shown in **Figure 6.10 a)** changes of resistance in the system are also well replicated by the model. However, there seems to be a phase shift between the model and the data. A similar feature, the phase shift between the current and voltage, has been reported in Chapter Five and was shown in Figure 5.9 for the experimental data. As it is shown in Figure 6.10, the model replicates this feature, however, modelled data is shifted around 1.8 s compared to the experimental data. These findings imply that the model is sufficient to replicate the key features of experimental data but requires further refinement.
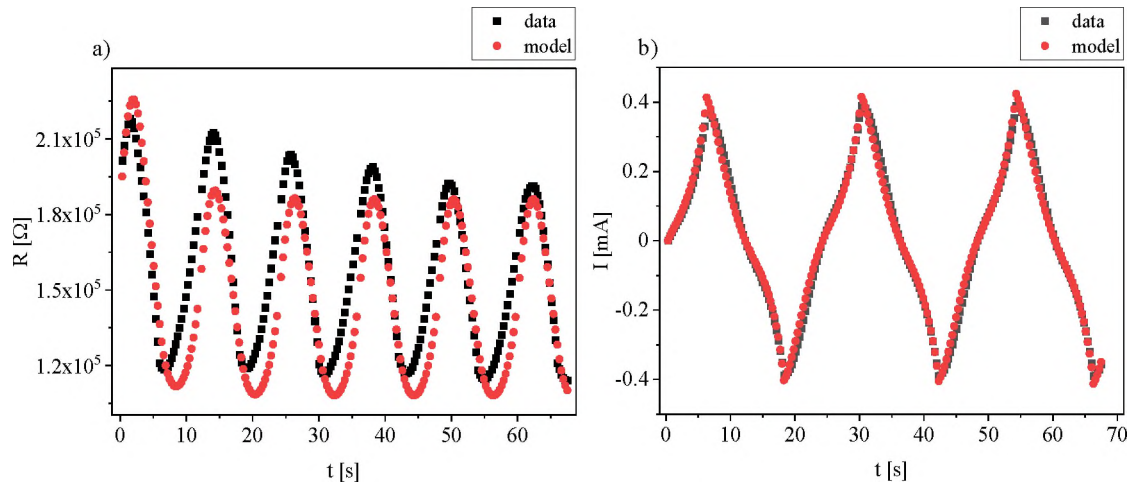
Figure 6.10. a) Resistance changes and b) current response for experimental (black) and modelled (red) data; the models' initial parameters were set as $C_0 = 5.42 \cdot 10^{-6}$ mS, $\tau = 0.946$, and $\eta = 1.58 \cdot 10^{-8}$ mS/V

Based on the aforementioned results, the model's ability to replicate key properties of the system can be concluded. These results were obtained for a triangular signal with a fixed voltage step equal to 5V. In such conditions, the model imitates the smooth tuning of the device's conductance with high accuracy.

In the next step, the investigation was extended to experimental and simulated responses to the sinusoidal signal. The results, illustrated in **Figure 6.11**, show that the hysteresis loop is more narrow in the case of experimental data, compared to the model. Moreover, the first loop simulated for the model deviates from the following loops, which replicate the forward direction of the loop in the experiment with good accuracy.

What is also worth mentioning is that the model assumes symmetry in the system and does not replicate the narrower loop in the negative polarity measured for the device. This finding implies that it is necessary to investigate the lack of symmetry of the device in order to include in the model a factor reflecting this behaviour. As this matter requires more attention it will be addressed in a different study, which will not be included in the framework of this thesis.
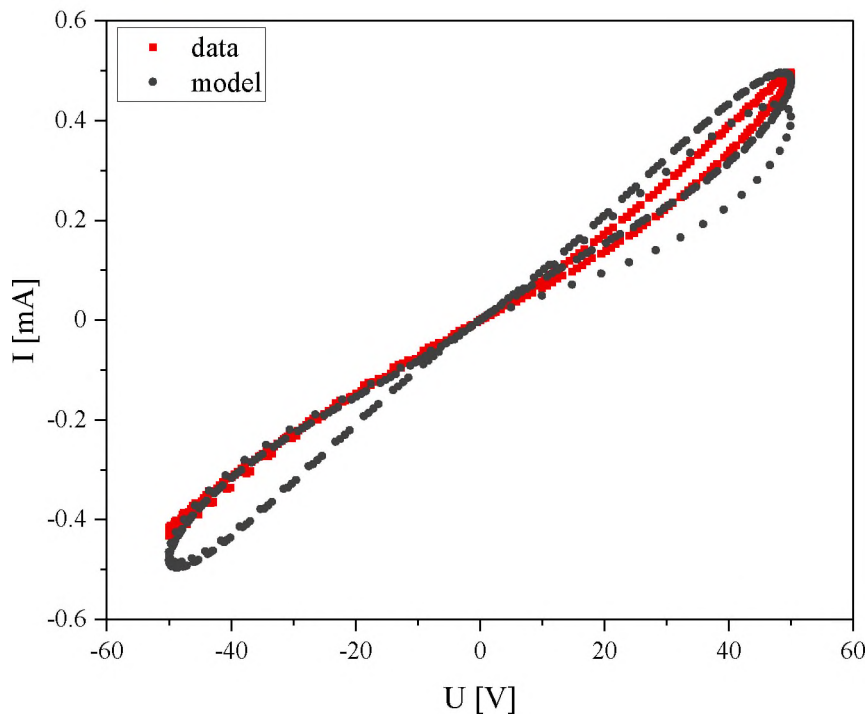
Figure 6.11. The current response to sinusoidal signal of experimental data (red) and reproduced by model equations (black); the models' initial parameters were set as $C_0 = 5.42 \cdot 10^{-6}$ mS, $\tau = 0.946$, and $\eta = 1.58 \cdot 10^{-8}$ mS/V

To examine this hypothesis the model was used to simulate current response to voltage sequences of 10 V, 50 V, -10 V, and -50 V. The calculated current values are presented as a function of time in **Figure 6.12** in black, together with the current response of the device illustrated as red rectangles.

What should be addressed at first is the difference in the slope of the current increase and decrease. It is also apparent, that the current values differ between the experimental results and the model. The values simulated for the model are lower compared to the current measured for the device, and the disproportion appears to be related to the switch between the value of applied voltage from lower to higher magnitude. Furthermore, when the voltage changes from high to low values, the simulated currents tend to be higher than the experimental values. This leads to the conclusion that the fast changes between potential values require additional simulation steps, which would address the breaking of symmetry caused by these events.
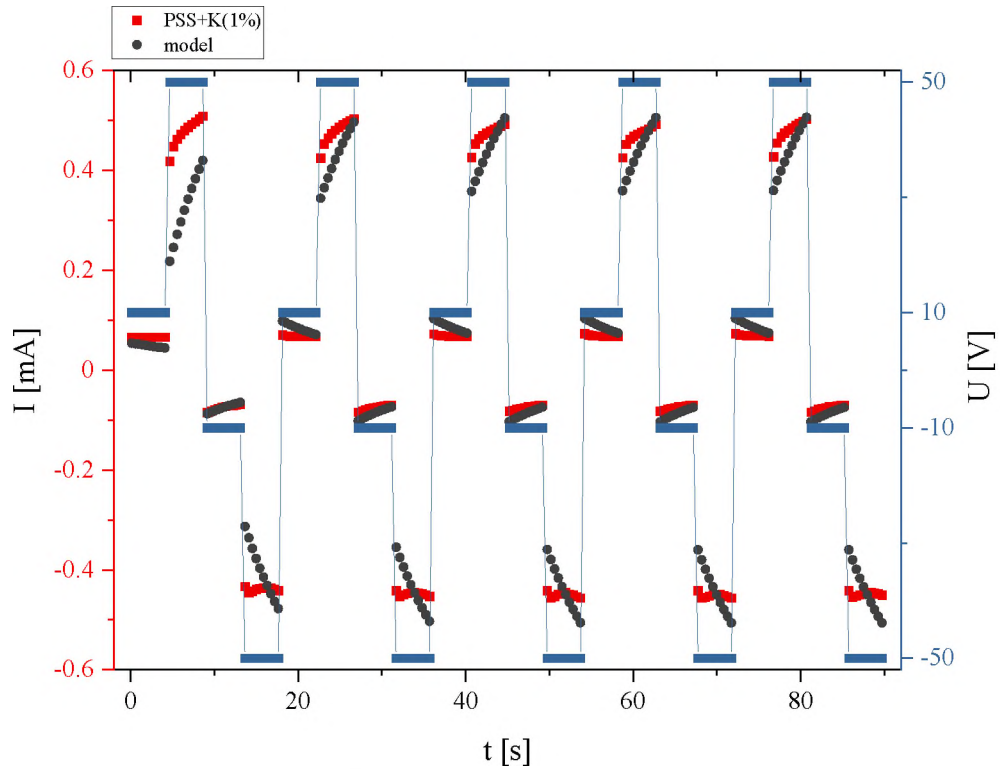
Figure 6.12. Current vs. time plots of device (red) and model (black) in response to voltage sequence of -10 V, -50 V, +10 V, and +50 V with 20 s potential step duration; the models' initial parameters were set as $C_0 = 5.42 \cdot 10^{-6}$ mS, $\tau = 0.946$, and $\eta = 1.58 \cdot 10^{-8}$ mS/V

To address this issue, the simulation was modified to include additional steps corresponding to the transition between abrupt voltage changes or different polarities. This operation can be justified by the execution of voltage switching in the experimental setup, which is performed in a similar manner. Such an approach also includes the changes of ion distribution throughout the layer caused by altered direction or magnitude of the electric field.

The simplified scheme of the simulation before and after including additional steps is presented in **Figure 6.13**. The additional voltage step was fixed as 2.5 V, as this was the value of the voltage step in between the following points in the current-voltage characteristic used to determine the model parameters. The number of additional steps depended on the value of the voltage change.
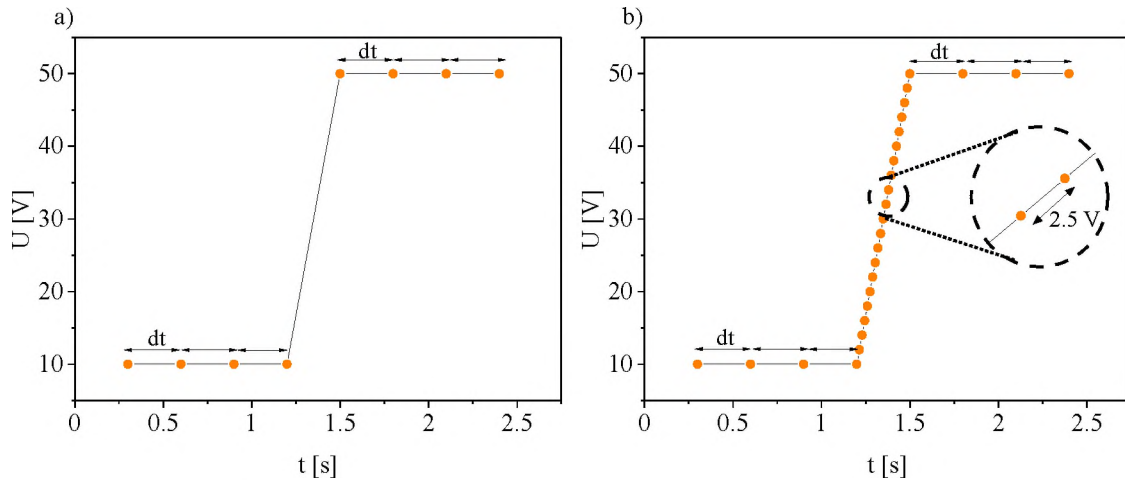
Figure 6.13. Scheme of the simulation voltage steps a) performed with rapid voltage changes, and b) after including additional steps

As can be seen in **Figure 6.14**, after incorporating the additional steps in between the voltage switching, the difference between the current measured for the device (red) and simulated using the model (black) is smaller, around 0.05 mA. Nevertheless, it appears that either the model parameters, fitted for the current-voltage characteristic with a fixed voltage step, or the model equations do not replicate the device's exact response in terms of the signal slope and magnitude.
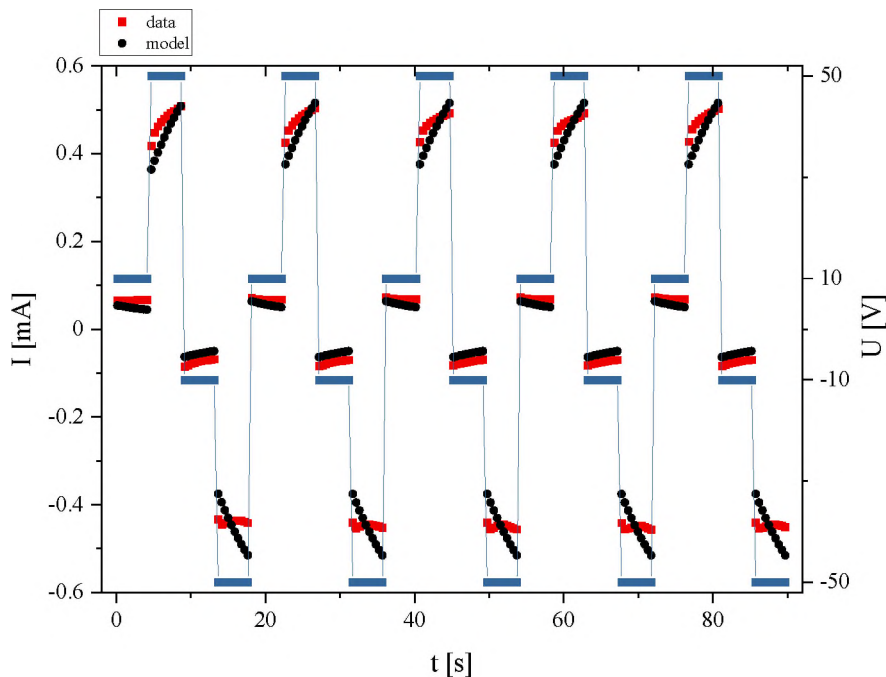

Figure 6.14. Current vs. time plots of device (red) and model (black) in response to voltage sequence of -10 V, -50 V, +10 V, and +50 V with 20 s potential step duration; the simulation performed with the additional steps in between rapid voltage changes; the models' initial parameters were set as $C_0 = 5.42 \cdot 10^{-6}$ mS, $\tau = 0.946$, and $\eta = 1.58 \cdot 10^{-8}$ mS/V

To extend the analysis to different types of signals, the device's response (red) and the response of the model (black) to a semi-rectangular signal with magnitude growth

96

after each minimum value, set as 0 V, are presented in **Figure 6.15**. As can be seen, the current calculated in the simulation is lower compared to the experimental data. The difference between the values in each voltage step is around 0.10 mA, meaning that the model successfully replicates the transistor-like current increase related to the applied voltage. This implies that the model parameter η related to the current increase in the system might be too low, as the slope of the current increase is too steep. However, the lack of signal saturation in the simulated data, which is related to the τ parameter, competing with the η and decreasing systems conductance, suggests that the model equations might require refinement. As the model relies on the recurrence function, including two previous terms, instead of one, might solve this issue. However, it requires further study and will not be a subject of this thesis.
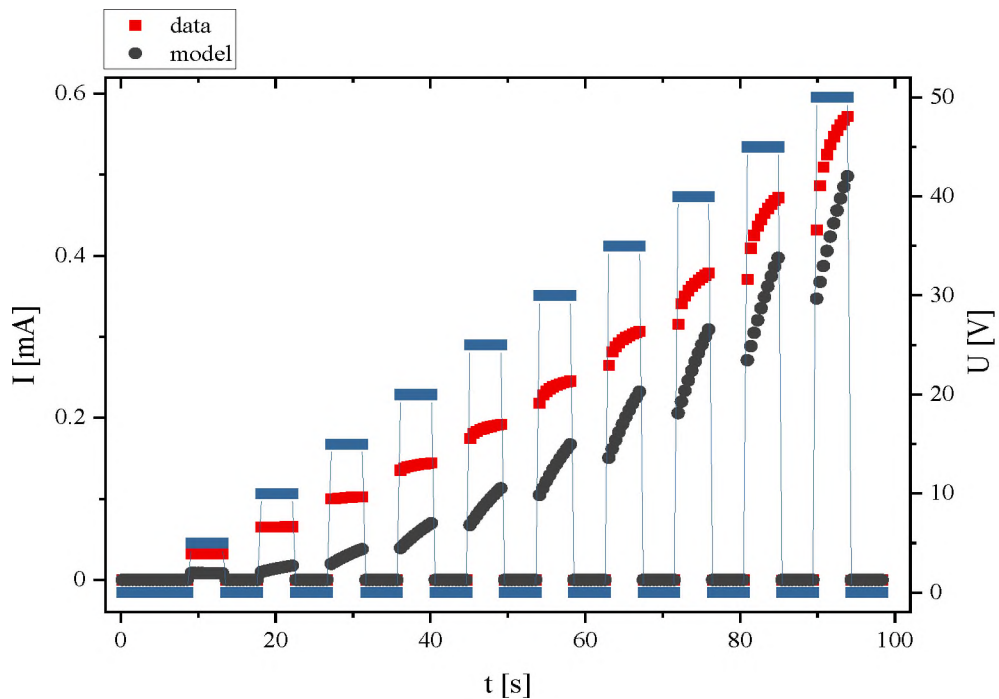

Figure 6.15. Figure 6.14. Current vs. time plots of the experimental data (red) and the model (black) in response to rectangular signal with magnitude growth after each magnitude minimum; the simulation was performed with the additional steps in between rapid voltage changes; the models' initial parameters were set as $C_0 = 5.42 \cdot 10^{-6}$ mS, $\tau = 0.946$, and $\eta = 1.58 \cdot 10^{-8}$ mS/V

Similar conclusions can be made based on results presented in **Figure 6.16**, where devices' and models' responses to rectangular signals alternating in between a) -10 V and -50 V, and b) 10 V and 50 V are illustrated. Comparing Figure 6.16 with Figure 6.14 it is apparent that the model performs better when polarization changes occur, as when it alternates between values of the same polarization the conductance value is updated too rapidly.
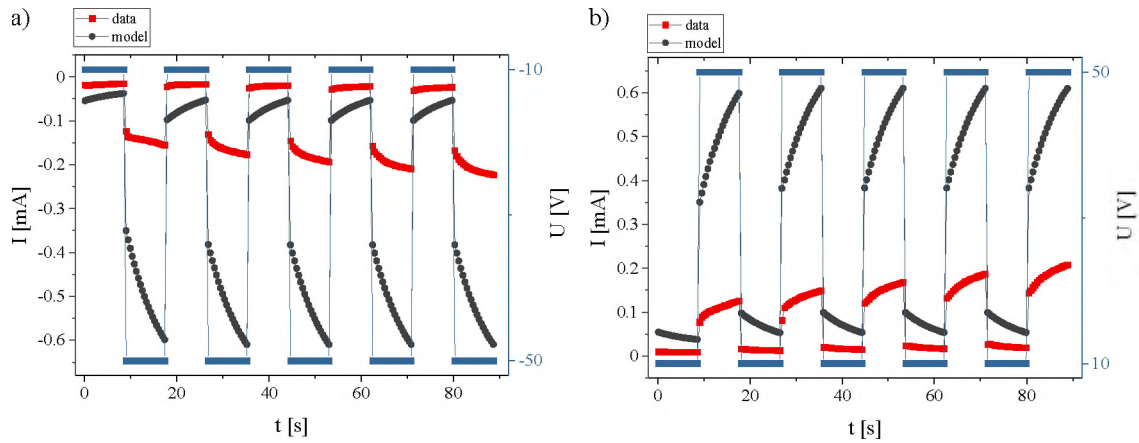
Figure 6.16. Current response of the device (red) and model (black) to rectangular signal alternating between a) -10 V and -50 V, and b) 10 V and 50 V; the simulation was performed with the additional steps in between rapid voltage changes;

To complete the analysis, the model was tested in terms of its ability to emulate the STP function. The simulations were performed including the additional steps in between the abrupt voltage changes and without it. **Figure 6.17 a)** shows the experimental data (red) and simulated response of the model (black) without the additional voltage steps.

As can be seen, the character of the response to voltage pulses of 10 V, differs from the experimental data both during the potentiation (50 V), and depression (-50 V). However, during the latter part, the conductance of the device does not decrease, as expected, but rather saturates. This behaviour might be related to too slow conductance changes or to the absolute value of voltage, which is hidden in $\eta|V_t|$ term of the equation during the conductance change.
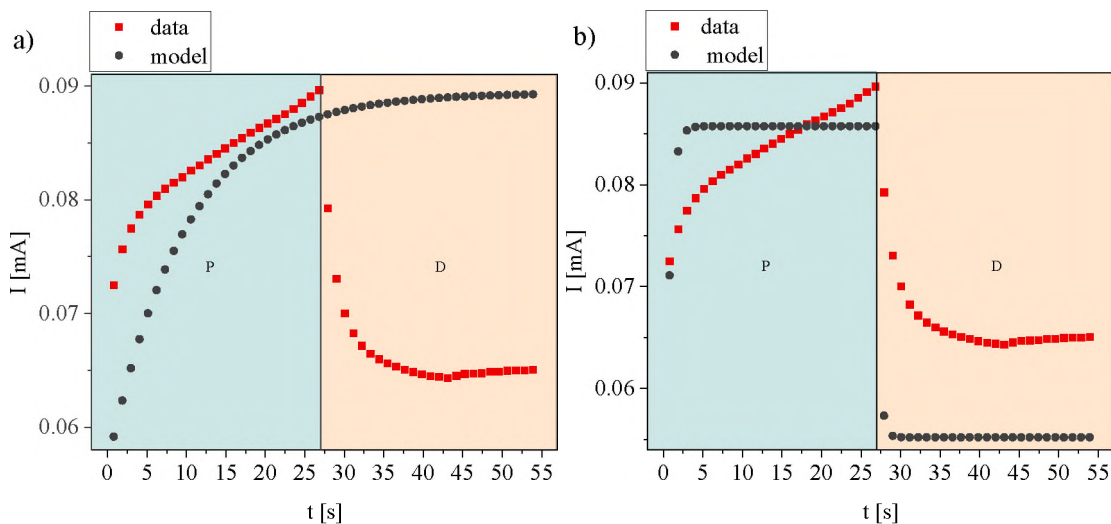

Figure 6.17. The STP function emulated experimentally (red) and simulated using model equations (black) a) without and b) with additional steps in between rapid voltage changes; the models' initial parameters were set as $C_0 = 5.42 \cdot 10^{-6}$ mS, $\tau = 0.946$, and $\eta = 1.58 \cdot 10^{-8}$ mS/V

If we include the additional steps in between the abrupt voltage changes, the simulated current response changes in terms of signal saturation.

As can be seen in **Figure 6.17 b)**, the potentiating pulses increase the conductance too rapidly, as well as the conductance decreases too fast when the depressing pulses are applied.

On contrary, in the STP function in, which the device is left to spontaneously relax, the model and the experimental data are similar in terms of the signal shape. Nevertheless, the current values at the beginning and end of the simulation differ from the experimental data, as shown in **Figure 6.18 a)**. What is interesting is that the model reaches similar current values at the end of the potentiation period. **Figure 18 b)** shows a comparison between the experimental and simulated data if we include additional steps in between potentiating and reading pulses.
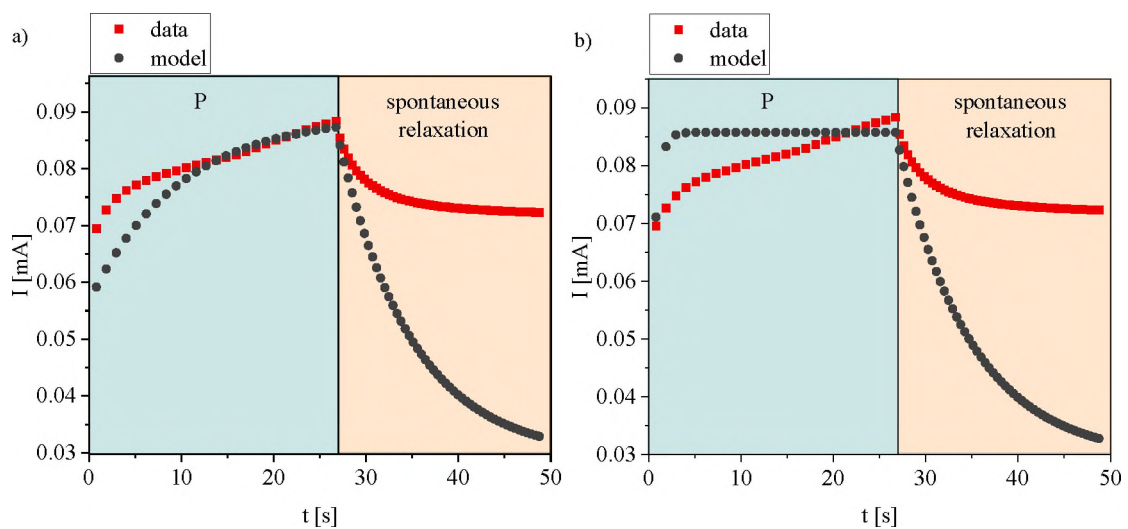

Figure 6.18. The STP function with spontaneous relaxation emulated experimentally (red) and simulated using model equations (black) a) without and b) with additional steps in between rapid voltage changes; the models' initial parameters were set as $C_0 = 5.42 \cdot 10^{-6}$ mS, $\tau = 0.946$, and $\eta = 1.58 \cdot 10^{-8}$ mS/V

Based on these findings the model is accurate in terms of replicating the character of the devices response. Moreover, the simulated currents are of the same order of magnitude as the experimental data. Therefore, the model equations require refinement but can be used to predict the device's response. Due to the model's better performance without the conductance adjustment in STP with spontaneous relaxation, this approach was utilized in simulations described in Chapter Eight.

6.3. Conclusions

In this Chapter, the device's response to signals differing in shape and sampling frequency was investigated. At first, based on findings from Impedance Spectroscopy measurements, the characteristic time constants of measurements were determined as 3.33 Hz and 8 Hz, which corresponds to 0.3 s and 0.125 s time steps. Next, the device's responses to different stimuli were analyzed in terms of alterations of current response in different sampling frequencies.

The study revealed that the faster the sampling frequency, the narrower the hysteresis loop in the current-voltage characteristic. This effect is associated with 8 Hz (0.125 s time step) being close to the characteristic time constant, in which the ions' movement is limited to their normal modes. Moreover, the devices' response measured to different types of stimuli revealed that the 8 Hz sampling frequency leads to slightly lower measurement stability.

Analysis of devices' response to different types of stimuli revealed that the currents measured with 0.3 s time step reach higher values in the same measurement times, compared to the 0.125 s time step. This feature is related to the time between the consecutive voltage steps and the ions' ability to migrate within the measurement time step. As the 0.125 s time step is closer to the characteristic time constant, which limits the ions' mobility, and the ion movement was shown to be inert, the measured currents have lower magnitude. The study revealed another important feature of the system, showing the system's ability to relax spontaneously after the series of potentiating pluses in the STP function. This feature is interesting, especially in terms of the device's applications in systems with spontaneous information decay.

In the second part of the Chapter the phenomenological model of the device, described in detail in Chapter Five, was tested in terms of its ability to reproduce systems response to various stimuli. The study shows that the model performs well in terms of smooth tuning of conductance, however, has problems reproducing the current response to rapid changes of resistance. An attempt to solve this issue was made by incorporating additional steps in between rapid voltage changes. This approach proved to be useful in terms of adjusting conductance values after an abrupt voltage switch, however, it does not solve the issue with conductance increase tempo.

These results imply the necessity to refine the model equations with additional terms, which would keep up with the conductance increase and allow the system to saturate

in the right time range. Nevertheless, the results of the simulations show that the model is able to mimic the experimental data in terms of character response. The values of simulated currents remain in the same order of magnitude as the experimental data, indicating that the model requires only minor adjustments.

CHAPTER Seven – Different types of ions

In this Chapter, the systems' investigation is further extended to study the devices, which contain different types of ions admixed to the PSS layer. The aim of this study is to determine whether the type of ion admixed to the polymer matrix changes the dynamics of processes occurring in the system allowing control over the systems' response. At first, the results of the investigation of devices containing pure PSS and PSS admixed with 1% potassium or bromide ions are presented. Both ions differ in ionic radius size and the sign of electric charge, which could potentially influence the operation of the device due to altered dynamics of processes occurring in the matrix. In order to characterize the devices and determine whether the type of ion addition alters the devices performance, their responses to different stimuli are shown and compared in terms of current response.

The second part of the chapter includes the preliminary results obtained for samples containing pure PSS matrix, and PSS admixed with 1% of lithium, sodium, potassium, bromide, chloride, or fluoride and their analysis. As these are only preliminary results their purpose is to show the trends and indicate the direction of further development of the system.

7.1. Sample preparation and characterization

Sample preparation. The samples, if not stated differently, were prepared following the device preparation process described in Chapter Three. The samples, consisting of R-P3HT/P4VP/CoBr$_2$/PSS differ in the type of the ion admixed to the PSS matrix.

Electrical characterization. The devices were characterized in terms of their current response to various voltage stimuli. The measurements were performed using computer controlled source-meter, Keithley 2400, at ambient temperature and in an inert gas atmosphere.

The current-voltage characteristics were measured in the voltage range from -50 V to +50 V with voltage step 2.5 V/s. The device's responses to different types of stimuli were tested using the reading intervals set as 0.3 s. During that time the voltage corresponding to the value of reading voltage was kept. The samples were tested in the voltage range from -50 V to +50 V with different voltage steps.

7.2. Results

7.2.1. Comparison between samples containing pure PSS and PSS admixed with potassium and bromide

The main goal of this investigation is to determine whether the device's response changes depending on the type of ion present in the PSS matrix. As it was mentioned before, the PSS contains sodium ions to stabilize the polymer, therefore there are two types of ions in the samples: sodium and admixed ions (K^+, Br^-).

At first, the devices' current-voltage characteristics were measured to compare the current values as well as the width of hysteresis loop. **Figure 7.1** illustrates the current-voltage characteristics of devices consisting of R-P3HT/P4VP/CoBr$_2$ and a) pure PSS (yellow), b) PSS with the addition of 1% of potassium ions (red), and c) 1% of addition of bromide ions (blue). As shown, the measured current values are similar for all three types of samples, and the maximum current values, measured at 50 V, equal to 0.45 mA for PSS, 0.45 mA for PSS+K^+(1%) and 0.53 mA for PSS+Br^-(1%).

The measurements were performed with a 2.5 V/s time step, meaning that the ions with similar ionic radius should migrate at a similar rate, resulting in similar current values. On the contrary, the bromide ion, which has the largest ionic radius reaches the highest current value, which might be attributed to its diffusion time. As the measurement time step is set as 1 second, smaller ions might relax faster and start returning to their initial position, which would result in lower current values.
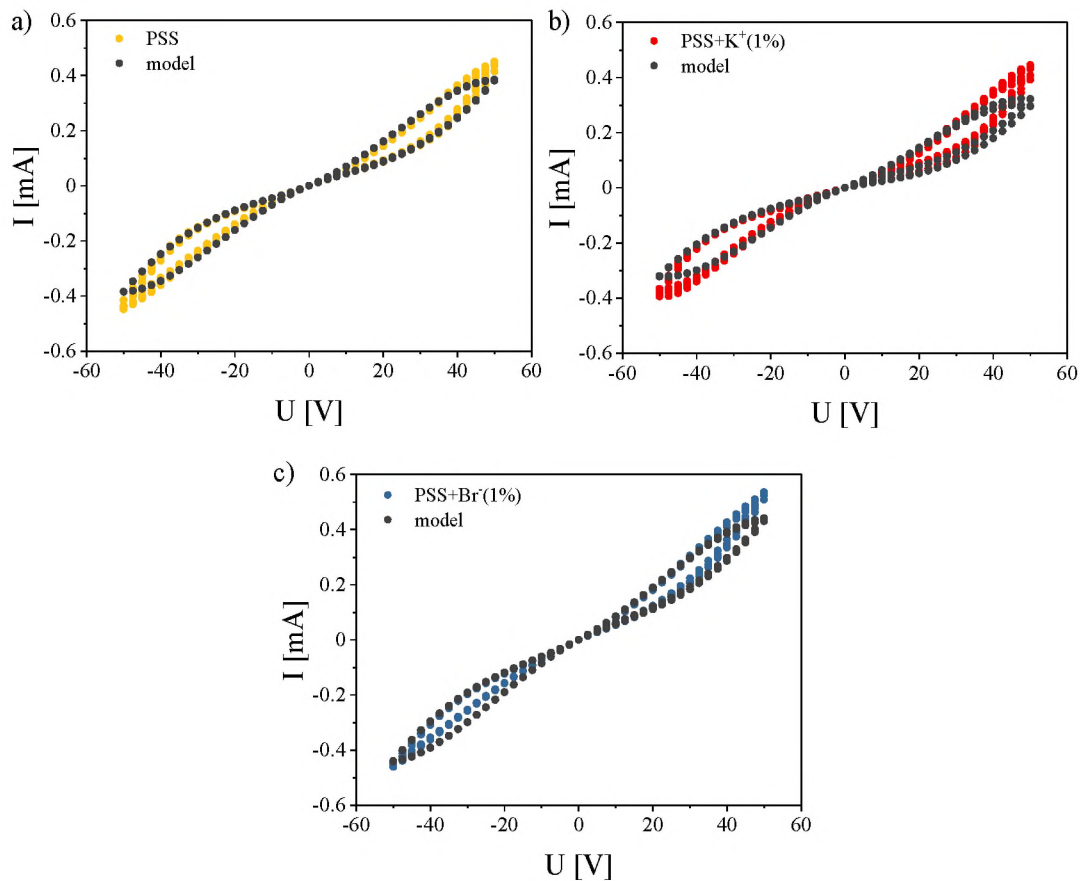
Figure 7.1. Current-voltage characteristics of devices consisting of R-P3HT/P4VP/CoBr₂ and a) pure PSS (yellow), b) PSS with addition of 1% of potassium ions (red), and c) 1% of addition of bromide ions (blue); the black circles correspond to the current-voltage characteristics simulated with model parameters determined as: a) $C_0 = 5.22 \cdot 10^{-6}$ mS, $\tau = 0.931$, and $\eta = 1.81 \cdot 10^{-8}$ mS/V, b) $C_0 = 5.42 \cdot 10^{-6}$ mS, $\tau = 0.946$, and $\eta = 1.58 \cdot 10^{-8}$ mS/V, and c) $C_0 = 6.49 \cdot 10^{-6}$ mS, $\tau = 0.949$, and $\eta = 1.64 \cdot 10^{-8}$ mS/V

Based on the measured currents, the devices' model parameters were determined by fitting the data to model equations, and are summarized in Table 7.1. The simulated current responses are marked as black circles in Figure 7.1, and as can be seen, reproduce the experimental data satisfactorily.

Table 7.1. Model parameters fitted for the devices containing pure PSS, PSS admixed with 1% of potassium and 1% of bromide

Parameter	PSS	PSS+K⁺(1%)	PSS+Br⁻(1%)
C_0 [mS]	$5.22 \cdot 10^{-6}$	$5.42 \cdot 10^{-6}$	$6.49 \cdot 10^{-6}$
τ	0.931	0.946	0.949
η [mS/V]	$1.81 \cdot 10^{-8}$	$1.58 \cdot 10^{-8}$	$1.64 \cdot 10^{-8}$

The parameters determined for each of the devices showcase similar initial conductance values for samples with PSS and PSS+K⁺(1%). The C_0 determined for a device with bromide addition is slightly higher, however in the same order of magnitude as for the other samples. The τ parameter is comparable for the devices with the extra ions,

but lower for the sample with pure matrix. On the contrary, the η parameter is the highest for the sample with pure PSS matrix and has similar values for samples admixed with potassium and bromide. These results suggest that the sample containing bromide addition has the highest conductance and saturates faster than other samples. On the contrary, a sample with a pure PSS matrix has the highest value of the η parameter, which suggests that the conductance changes, related to the $\eta|V_t|$ factor, should be more noticeable, compared to other devices.

In the next step of the investigation, the device's endurance during the first three cycles of operation was analysed in terms of device's stability. The illustrated values correspond to the reverse direction of the measurement. As can be seen in **Figure 7.2**, all three devices show slight instability during the second cycle, which is visible as an overlap of ±45 V and ±50 V signals. What is worth noting, is that the device with 1% of potassium addition exhibits the most stable operation, however, the results show a slight current asymmetry in positive and negative polarity.
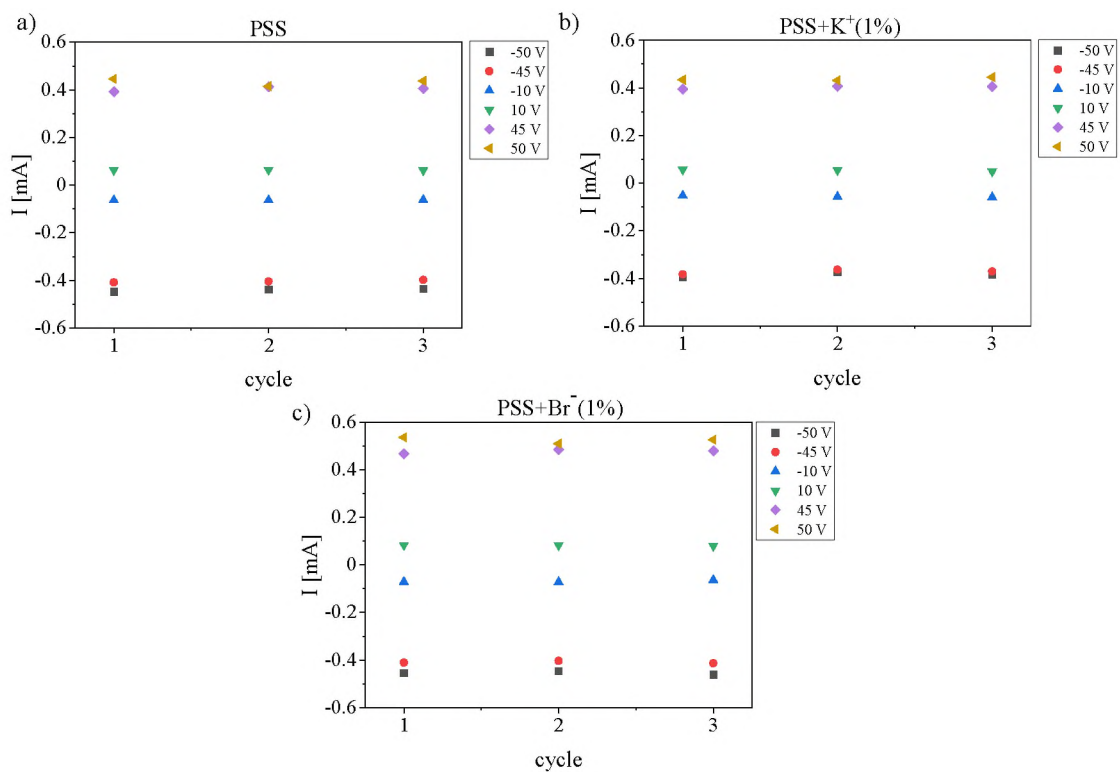

Figure 7.2. The endurance determined based on current response to selected potentials in successive cycles of the current-voltage characteristics measured for samples containing a) pure PSS, b) PSS admixed with 1% of potassium, and c) PSS admixed with 1% of bromide

In the next step, the devices' current responses to voltage sequences of -10 V, -50 V, +10 V, and +50 V, with a 4.5 s potential sequence duration, were tested. The results,

shown in **Figure 7.3**, show that the device with the addition of 1% of potassium (in red) reaches the highest current values. The lowest current values were measured for devices with 1% of bromide (in blue). These results suggest that the type of ion, cation or anion, or its' size influences the magnitude of the systems' response.

What is also worth mentioning, is that the sample containing bromide addition reached the highest current values in the current-voltage characteristic shown in Figure 7.1. This indicates that the signal shape and sampling frequency affect the dynamics of processes occurring in the system, and are related to ionic composition of PSS matrix. In terms of the character of the current response, the device admixed with potassium exhibits current distortion both in positive and negative polarities, however, the signal measured in positive polarities resembles the response of a device consisting of pure PSS matrix.

As for the signal measured for the device containing bromide in the PSS matrix, the current values saturate faster, compared to other devices. This result implies that the bromide ions, which have a bigger ionic radius than sodium and potassium ions, exhibit slower relaxation.
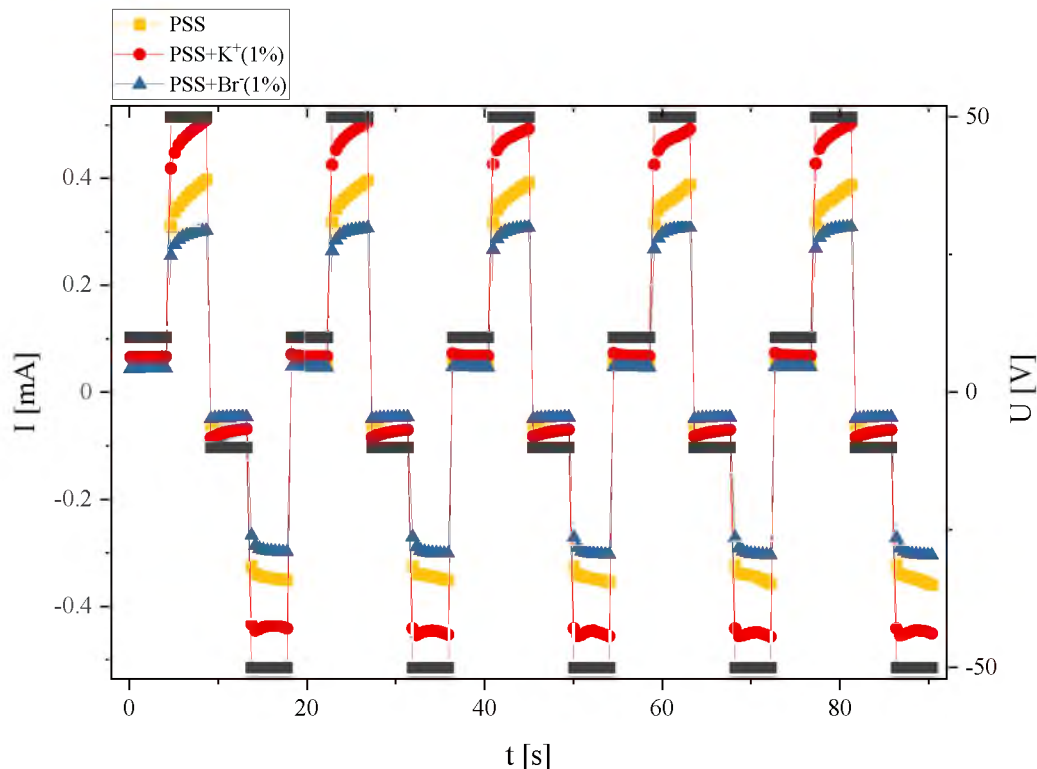

Figure 7.3. Current vs. time plots in response to voltage sequences of -10 V, -50 V, +10 V, and +50 V with 4.5 s potential sequence duration measured for samples containing pure PSS (yellow rectangles), PSS admixed with 1% of potassium (red circles), and PSS admixed with 1% of bromide (blue triangles)

On the contrary, the lower current values measured for devices with bromide addition might be related to Br^- anions being repulsed from the dipole layer, to which the sodium ions, also present in the PSS layer, are attracted. The influence of Na^+ cation, which initially decreases the conductance due to its attraction to the dipole layer, can be partially compensated by Br^- anions, which will be repelled by the dipole-induced electric field. Therefore the difference in the charge distribution in the P4VP-CoBr₂/PSS system might be the cause of the conductance decrease.

To extend the investigation of this phenomenon, the device's current responses to rectangular signals alternating between -10 V and -50 V, or 10 V and 50 V is illustrated in **Figure 7.4**. What is interesting, the magnitude of the measured current remains similar for the device admixed with 1% of bromide (blue triangles), compared to the results presented in Figure 7.3. However, the current values measured for samples with pure PSS (yellow rectangles) and PSS admixed with 1% potassium ions (red circles) are lower, compared to the values illustrated in Figure 7.3. This result indicates that the changes in the voltage polarity might cause symmetry breaking in the system, resulting in higher current values for samples containing only one type of mobile ions (cations).

In case of lack of polarity changes, the system admixed with bromide ions, which contains both Na^+ and Br^-, due to ions compensating each other to some extent, and due to longer relaxation of bromide ions, the symmetry in the system is preserved and its response remains similar regardless of the polarity changes. As for the devices containing only mobile cations, lack of polarity changes might result in different ion distributions throughout the PSS layer, compared to the distribution caused by the polarity switch, resulting in lower current values.
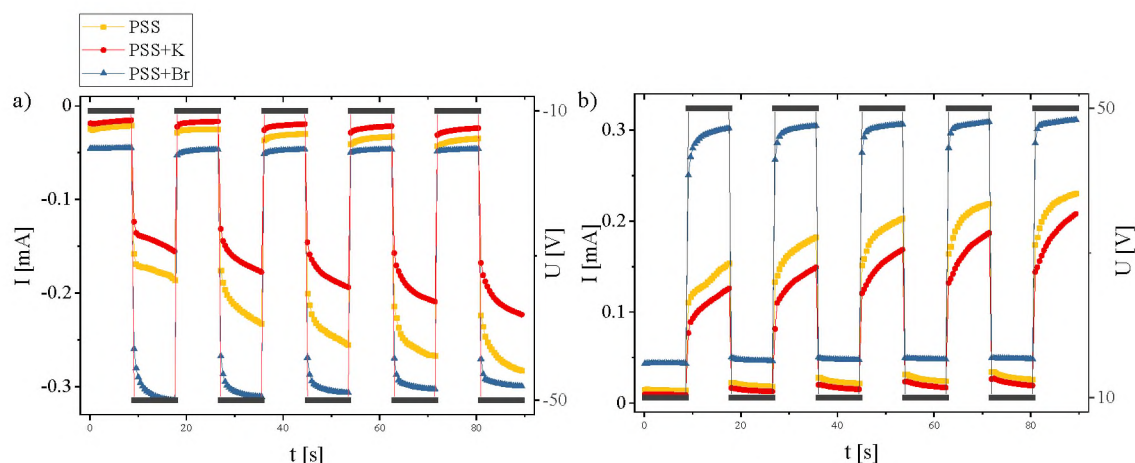
Figure 7.4. Current response to rectangular signal alternating between a) -10 V and -50 V, and b) 10 V and 50 V measured for devices containing pure PSS (yellow rectangles), PSS admixed with 1% of potassium (red circles), and PSS admixed with 1% of bromide (blue triangles)

To further examine the processes occurring in the samples, the time constants of the relaxation processes were fitted to the current values measured under ±10 V bias, illustrated in Figure 7.4. The data were fitted to Equation 5.3, and the distribution of calculated values is shown in **Figure 7.5**.

The results indicate that the time constants depend on the polarity of the measurement. In a positive polarity sample with 1% potassium addition tends to have the highest values of both relaxation constants. However, in negative polarity, it is the other way around, the values of relaxation constants are the lowest for the sample containing potassium ions. What is worth mentioning, is that both the first and second time constants are in the same value range in both polarities.

However, the results cannot be interpreted without considering over 9% of the mass of PSS being Na^+, which means, that these values should be considered in relation to time constants determined for pure PSS. In this context, in the positive polarity addition of both K^+ and Br^- increases the mean values of both time constants. In negative polarity, the sample containing bromide has a slightly higher value of τ_1 and a lower value of τ_2, compared to the PSS. However, the values determined for the sample admixed with potassium, indicate that the addition of a cation with a bigger ionic radius than sodium decreases the time constants in negative polarity and increases them in positive polarity.

As the values were determined based on data shown in Figure 7.4, they can only indicate trends, which are apparent in Figure 7.5. What is surprising, is that the time constants determined for a sample containing bromide ions have the highest value for the first time constant, however, it is not the case for the τ_2. Moreover, the mean values of time

constants in both polarities determined for samples containing bromide are similar. This result indicates that the dynamic processes occurring in the device containing both Na^+ and Br^- ions are symmetric in regard to voltage polarity.
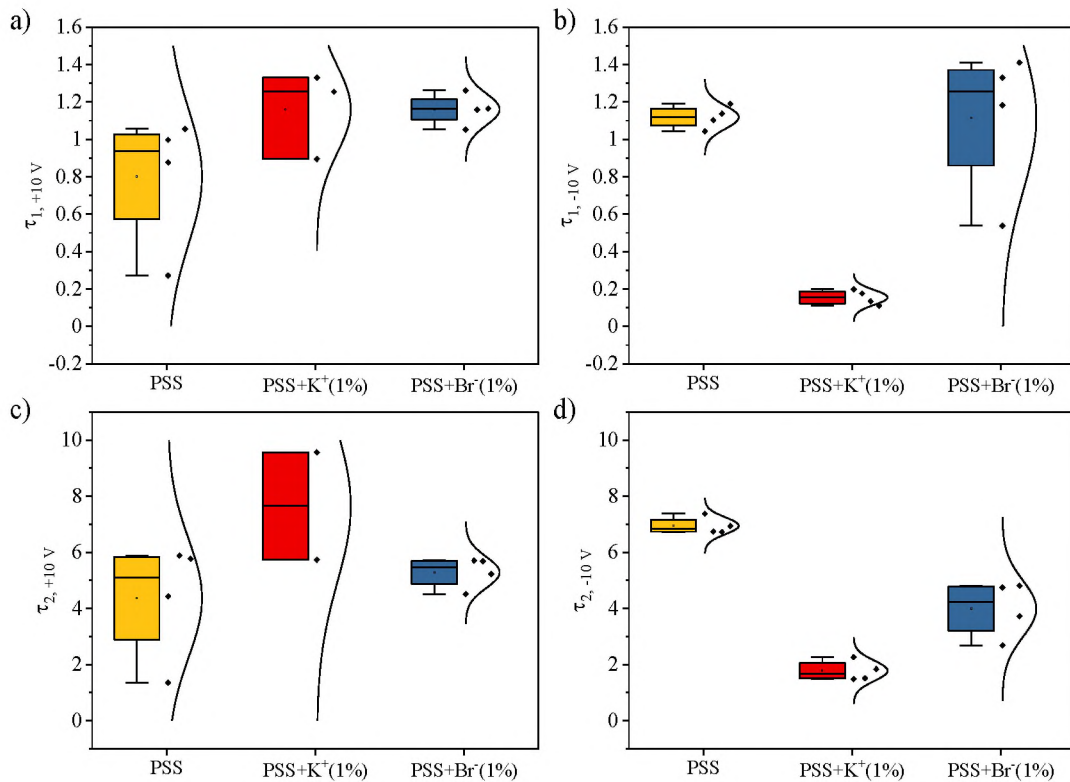

Figure 7.5. Time constants of relaxation processes determined from Equation 5.3 for devices containing pure PSS (yellow), PSS admixed with 1% of potassium (red), and PSS admixed with 1% of bromide (blue)

The changes between relaxation constants in between polarities might be also a cause of different current responses during the measurements performed while switching between polarities and within one polarity. This might serve as an explanation, as the values of time constants for both PSS and PSS+K^+ change in different polarities, but remain almost the same for the sample with bromide regardless of the polarity.

Additionally, the samples were tested in terms of their ability to emulate synaptic plasticity with spontaneous relaxation. The results, illustrated in **Figure 7.6**, show that all the examined samples are able to replicate the STP function. The measured currents are the highest for the sample containing potassium addition, and the lowest for the sample containing bromide. This further proves that by admixing different ions it is possible to change the conductance of the system without changing the character of its response.
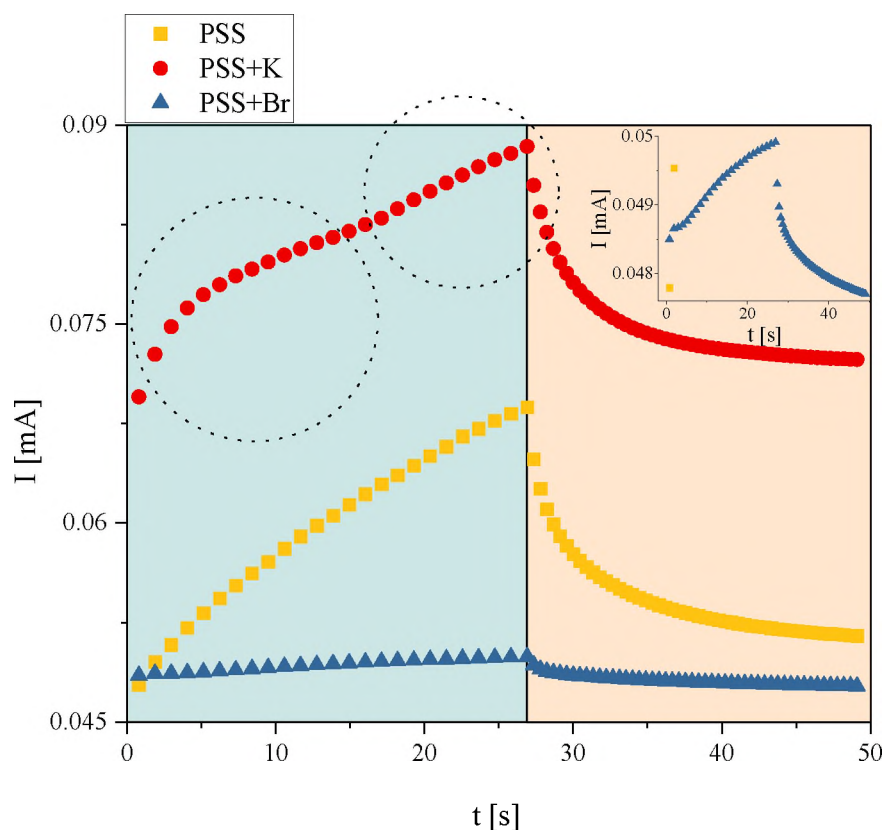
Figure 7.6. The STP function emulated experimentally for devices containing pure PSS (yellow rectangles), PSS admixed with 1% of potassium (red circles), and PSS admixed with 1% of bromide (blue triangles); the inset shown magnification of signal measured for sample containing bromide

What is also interesting, is the distortion of the signal visible for the sample admixed with potassium ions, which is not present in the signal measured for the sample with pure PSS. The distortion, registered at the beginning of the potentiation, as shown in the inset, is also visible for the sample containing bromide. This matter requires further investigation and will be addressed in a separate study, which will not be a part of this thesis.

The aforementioned results indicate that by admixing different ions to the PSS matrix it is possible to alter the systems' current response, in terms of its magnitude, as well as to change the time constants of the relaxation processes. Moreover, the results prove that the character of response is similar, however, differs in terms of the time required for the systems' saturation. The additional ions were also proved to cause distortions in the measured signals, compared to the response measured for samples with pure PSS.

7.2.2. Analysis extended to different types of ions

In the next part of the research, the analysis was extended to devices containing more types of ions: lithium (Li^+), sodium (Na^+), potassium (K^+), fluoride (F^-), chloride (Cl^-), and bromide (Br^-). All the samples consisted of R-P3HT/P4VP/CoBr$_2$ and PSS admixed with 1% of respective ion or left undoped for reference. All the samples were prepared in the same batch of samples in order to be able to compare them. For simplicity, the results are illustrated separately for anions and cations. This part of the Chapter presents the preliminary results, which will be expanded in the future. Nevertheless, the preliminary results showcase interesting trends and were included as part of this thesis.

At first, the current-voltage characteristics of the devices containing anion additions were measured with a 5 V/s time step and the results are presented in **Figure 7.7**. The plot shows only the first cycle of device operation, and the results for respective ions are compared to the signal measured for the reference sample with a pure PSS layer.

As can be seen, the sample containing the ion with the biggest ionic radius, potassium, reaches the highest current values. What is also interesting, is that the maximum value of current measured for this device is almost 4 times lower, compared to the same device prepared in a separate batch, which is illustrated in Figure 7.1.
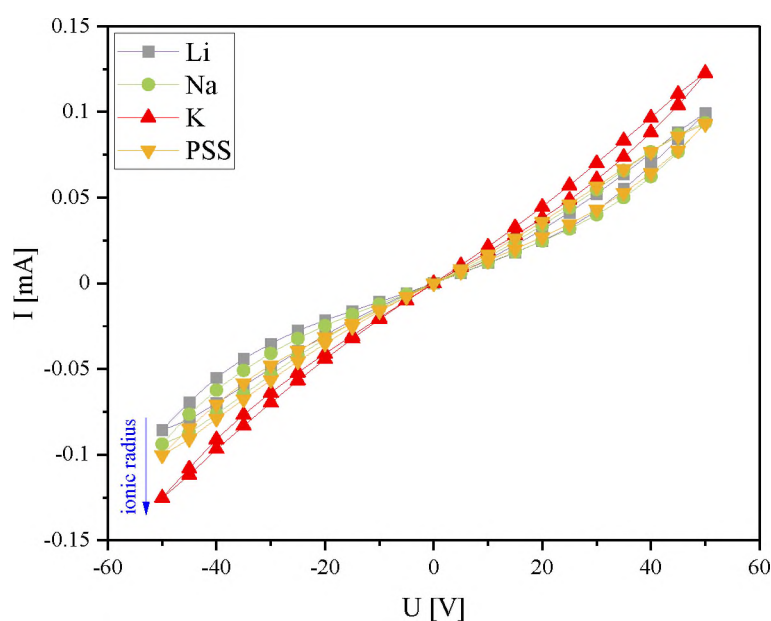

Figure 7.7. Current-voltage characteristic measured for devices containing addition of 1% of lithium (grey), 1% of sodium (green), 1% of potassium (red) and reference sample with pure matrix (yellow)

Samples containing only sodium ions in the matrix, samples with PSS and PSS+Na^+(1%), reach similar current values in positive polarity, however, the sample with pure PSS

matrix exhibits higher conductance in negative polarity, as the current values measured in 50 V reach 0.093 mA and in -50 V 0.100 mA. On the contrary, the sample with the addition of sodium ions is more symmetric in terms of current values measured in different polarities, which suggests that the addition of ions stabilizes the device's operation and introduces symmetry to the system.

Unfortunately, in the positive polarity, there is no apparent relation between the ionic radius size or electronegativity on the measured current values. Such a relation appears in the negative polarity of the current-voltage characteristic, as the bigger the ion the higher the current values flowing through the device.

Figure 7.8 shows the results of current-voltage characteristics measurements performed for devices with pure PSS or PSS with the addition of fluoride, chloride, or bromide ions. As can be seen, the results indicate that the addition of anions results in a lack of symmetry of the hysteresis loops measured for different polarities. Moreover, the width of the hysteresis loop differs between the polarities, and is bigger in positive polarities, with the exception measured for the device with the addition of chloride ions.
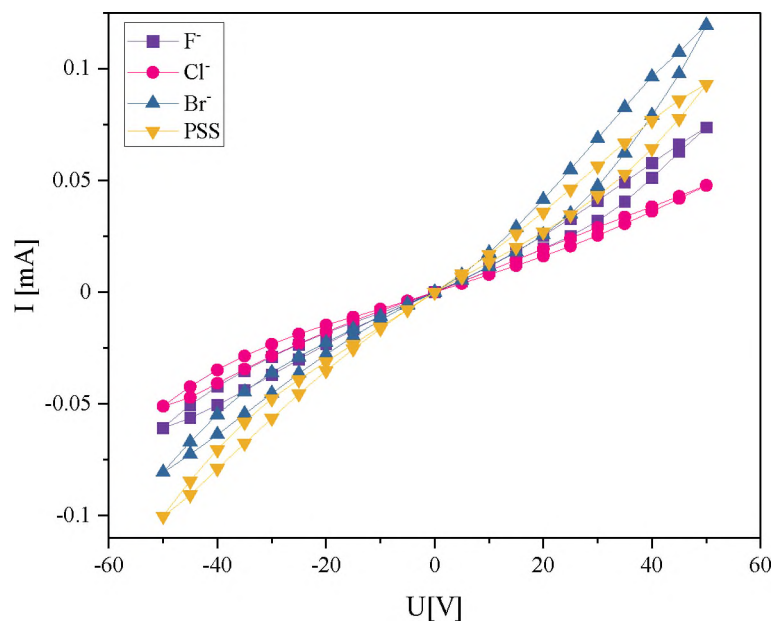

Figure 7.8. Current-voltage characteristic measured for devices containing addition of 1% of fluoride (purple), 1% of chloride (pink), 1% of bromide (blue) and reference sample with pure matrix (yellow)

As can be seen in Figure 7.8, there is no apparent relationship between the measured current and the size of the ion or the electronegativity. To determine whether the results are compromised in any way due to preparation issues, the devices' responses to voltage

sequences alternating between 10 V, 50 V, -10 V, and -50 V was measured. The results obtained for samples containing the addition of cations are presented in **Figure 7.9**.
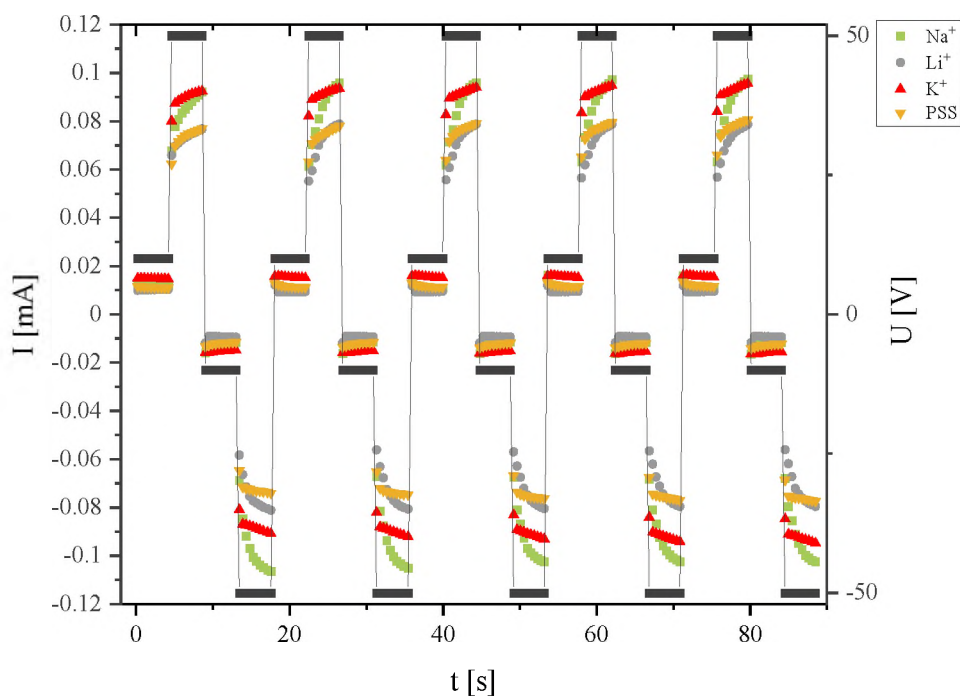

Figure 7.9. Current vs. time plots in response to voltage sequences of -10 V, -50 V, +10 V, and +50 V with 4.5 s potential step duration measured for devices containing addition of 1% of lithium (grey), 1% of sodium (green), 1% of potassium (red) and reference sample with pure matrix (yellow)

As can be seen, the current measured under ±50 V bias for devices with pure PSS and PSS admixed with potassium is slightly distorted at the beginning of the sequence. Moreover, the signal measured for these devices has a different slope and appears to saturate faster than devices with the addition of sodium or lithium. All the samples, excluding devices with the addition of sodium ions, exhibit decreased conductance in the negative polarity. The sample consisting of PSS with 1% of sodium ions enrichment reaches higher current values in this measurement, which has a 3.33 Hz sampling frequency, compared to the results from Figure 7.7.

Similarly, the devices containing PSS doped with anions showcase differences in signal slope, as shown in **Figure 7.10**. The highest current values were recorded for the device containing bromide addition. Samples containing fluoride or chloride exhibit lower conductance than the reference sample consisting of pure PSS.
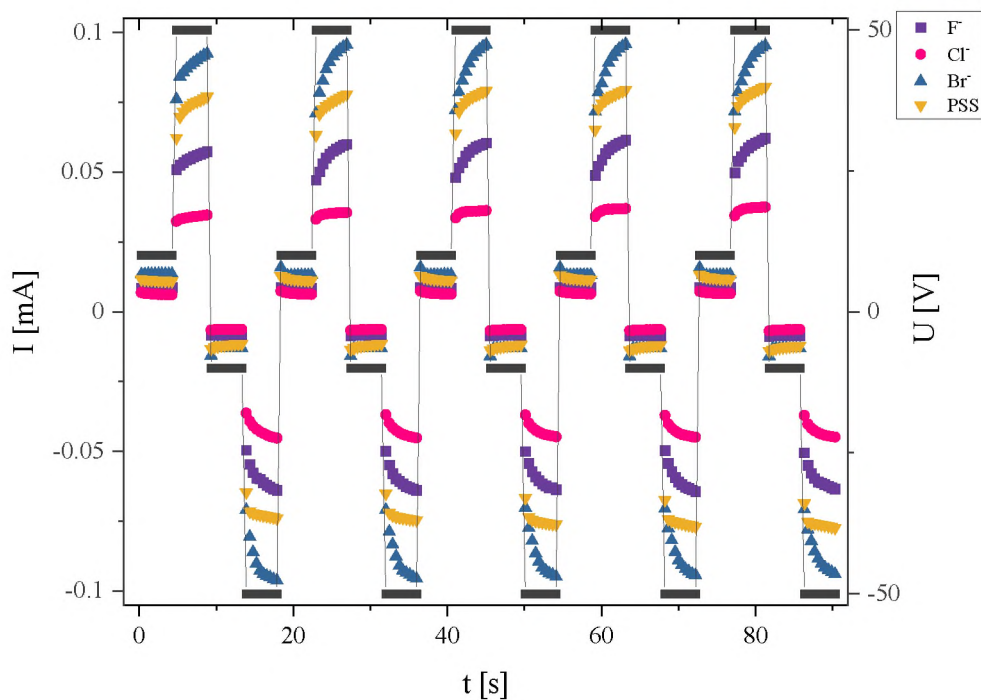
Figure 7.10. Current vs. time plots in response to voltage sequences of -10 V, -50 V, +10 V, and +50 V with 4.5 s potential step duration measured for devices containing addition of 1% of fluoride (purple), 1% of chloride (pink), 1% of bromide (blue) and reference sample with pure matrix (yellow)

The aforementioned results suggest differences in the dynamics of ion relaxation processes occurring in samples admixed with different ions. This result is consistent with the results presented and described in part 7.2.1. of this Chapter. However, due to differences in measured current values, the analysis can only be used to illustrate trends and requires to be extended to a larger sample population to come to reliable conclusions.

In order to compare the dynamics of processes occurring in the devices, the time constants of relaxation processes were determined by fitting the experimental data to equation 5.3. The results, presented in **Figure 7.11**, show that both the first and second time constants are in different value ranges in positive and negative polarities. Moreover, the results indicate that the relaxation processes occurring in negative polarity are slower, which corresponds to higher current values measured in Figures 7.9 and 7.10.

The first box in each of the panels corresponds to the time constants determined for the reference sample with pure PSS. The following boxes correspond to devices with different ions and are presented in the order of growing ionic radius size.
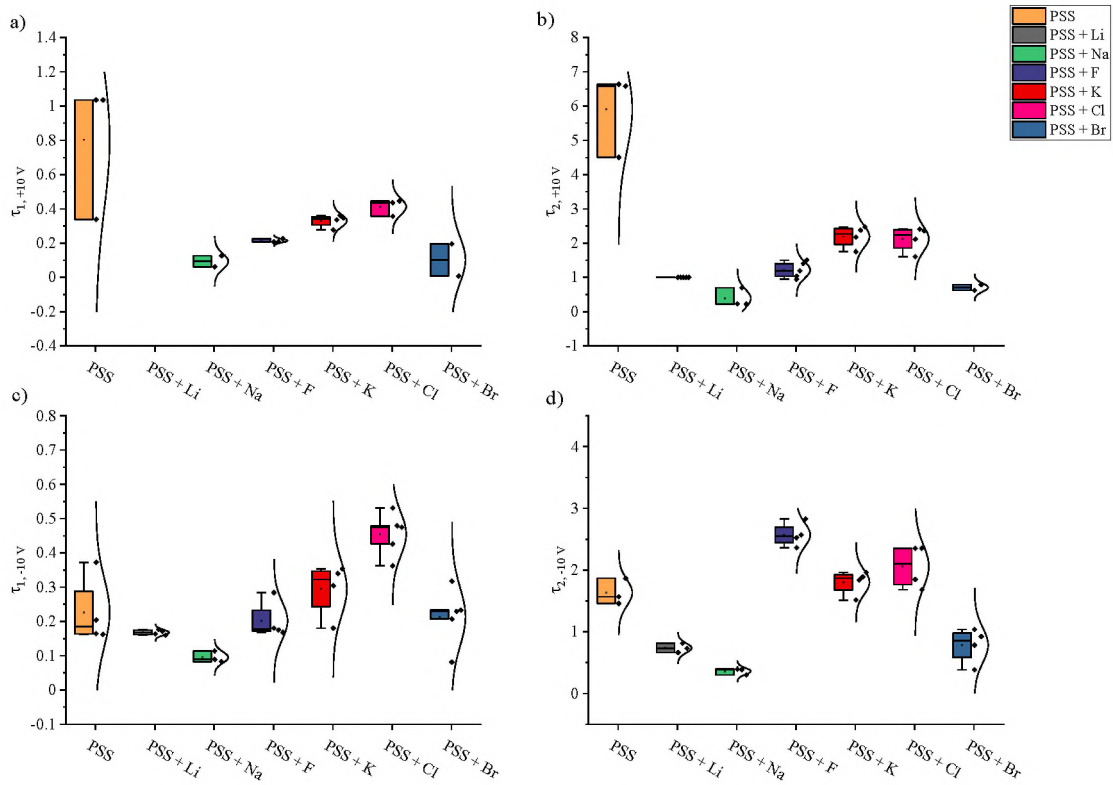
Figure 7.11. Time constants of relaxation processes determined from Equation 5.3 for devices containing pure PSS (orange) and PSS with addition of 1% of lithium (grey), 1% of sodium (green), 1% of fluoride (purple), 1% of potassium (red), 1% of chloride (pink) and 1% of bromide (blue)

Based on the results presented in Figure 7.11 it can be concluded that the results indicate the trend of higher relaxation times for samples admixed with ions of bigger size. However, the results obtained for the sample with the addition of bromide are not consistent with the results presented in Figure 7.5, which follow the suggested trend.

The differences between this preliminary study and the results shown earlier in this thesis suggest that this investigation requires to be extended to larger sample population to obtain more results. Nevertheless, the trends illustrated by the results of this study suggest that by admixing different ions into the PSS matrix it is possible to alter the time and character of response of the device. It is a promising result, which implies that by a simple change in the last step of device preparation process it is possible to alter the devices features.

7.3. Conclusions

The results discussed in this chapter, show that by admixing different ions to the PSS matrix it is possible to alter the systems' current response. It was shown, that this is

possible both in terms of the current magnitude, as well as in terms of the time constants of the relaxation processes. Based on the current vs. time plots it can be concluded that the character of the device's responses remains similar, however, differs in terms of the time required for the systems' saturation, which is visible as different signal slopes. The study, which compares samples containing pure PSS matrix and PSS enriched with 1% of potassium or bromide implies that the ion addition incorporates distortions in the measured current.

The preliminary results of the study extending the analysis to different ions suggest the existence of a relation between the size of the ionic radius and the time constants of relaxation processes. Unfortunately, due to too small sample population, the results can only indicate trends and further study is required to confirm this observation. Moreover, the interpretation of the results should include the difference in the counterions between anions and cations. The counterion for cations is triflate, and for anions, it is ammonium, and further study should include an analysis of the counterion's influence on the system's operation.

Nevertheless, the results shown in this Chapter show the system's utility as a volatile memristive device with possibility to easily adjust the device's information retention time by addition of a respective ion.

CHAPTER Eight   – Study of possible applications

The preceding Chapters explored the systems' features and provided information about its characteristics. This Chapter utilizes these findings to determine the devices' utility in two possible applications: as building blocks of composite memristive circuits and as artificial synapses in Spiking Neural Networks.

The first possible application, composite memristive circuits, is postulated based on memristors' stochastic nature in certain conditions. The studied system has been shown to be highly stable in a wide parameter range, however, it was only explored in one device scenario. Various memristive devices have been reported in the literature to behave in an unpredictable manner if connected in a certain way or operating in a specific parameter range. This feature has been utilized in particular in random numbers generator architectures[93;94]. Therefore, the first part of the Chapter aims to explore whether the studied system displays any fluctuations or distortions in its' current response when connected in certain ways. In particular, the devices were tested in linear and parallel connections and in a connection inspired by Wheatstone's bridge.

The second part of this Chapter explores the devices' applicability as an artificial synapse in Spiking Neural Networks. The investigation was performed for the 2-Alternative-Forced Choice (2AFC) Experiment[95], which is inspired by biological decision-making behaviour. At first, the device's model was tested in terms of its response to Spike Trains to establish whether the device is able to mimic synapse-like behaviour. Based on the results, the model was further used to determine the system's ability to reproduce the 2AFC Experiment. The success of simulations was further followed by experimental implementation of the experiment. The experimental data was further used to test the models' prediction accuracy utilising the voltage sequences from experiment as simulation inputs.

8.1. Sample preparation and characterization

Sample preparation. The samples, if not stated differently, were prepared following the device preparation process described in Chapter Three.

Electrical characterization in connections. The samples consisting of R-P3HT/ P4VP/CoBr$_2$/PSS+K$^+$(1%) were characterized in terms of their current response to long voltage sequences between 5 V and 50 V. The voltage sequence was held for 300 readings. The time step between the current reading pulses was set as 0.125 s or 0.3 s. The measurements were performed using a computer-controlled source meter, Keithley 2400, at ambient temperature and in an inert gas atmosphere on two devices connected in series as well as parallelly. Corresponding measurements were performed for connection based on Wheatstone's bridge.

Electrical characterization in 2-Alternative Forced Choice Experiment. Measurements were performed for four firing probabilities: 5%, 10%, 30% and 50% at each measurement step. The sampling rate was set as 250 ms, the reading potential as +10 V and the spike potential as +50 V. The responses of the device were tested for three numbers of points set as 15, 20, and 25, which translates to measurement times: 3.75 s, 5 s and 6,25 s. The measurements were performed for a number of trials fixed as 20.

Simulations of 2AFC. The simulations were performed using the phenomenological model of the device described in Chapter Five. The model parameters obtained through fitting experimental data to the model were determined as $\tau = 0.93$, $\eta = 2.62 \cdot 10^{-8}$ S/V, and $C_0 = 2.90 \cdot 10^{-6}$ mS. The simulations were performed by testing the models' response to the stimuli matching the input signals from the experiments.

8.2. Results

8.2.1. Connections between devices

So far, the system has been tested in a single-device scenario. However, various device implementations require different connections between devices and other circuit elements[96,97]. Therefore, the devices' responses were tested in two basic connections: in series and in parallel, as shown in **Figure 8.1**.

The behaviour of memristor connections might be non-trivial and depend on the initial state of the devices. However, linear and parallel connections for voltage-dependent memristors should obey the same rules as connections between resistors[98].
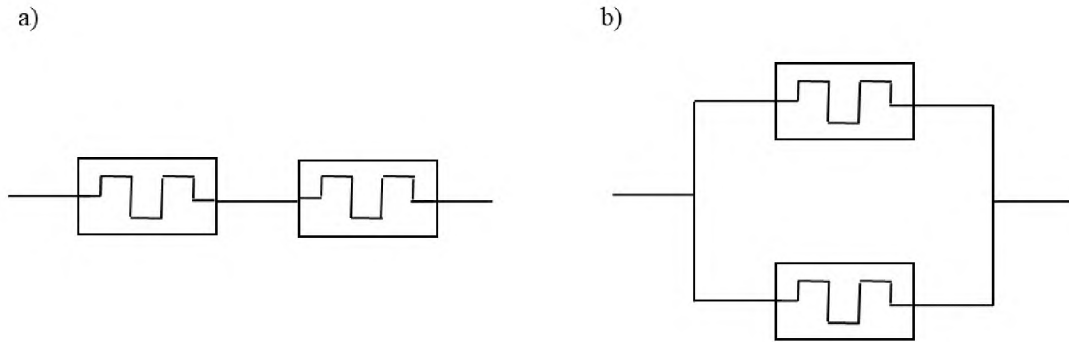
118

Figure 8.1. Scheme of composite memristive circuits in a) series and b) parallel connection

The current I at time t for two ideal voltage controlled memristors with resistances $R_1(U,t)$ and $R_2(U,t)$ connected in series can be described by:

$$I\ (t) = \frac{U}{R_1(U,t) + R_2(U,t)},$$ (8.1)

whereas for two ideal voltage controlled memristors in parallel connection it is given by:

$$I\ (t) = U \cdot \left(\frac{R_1 + R_2}{R_1 R_2}\right).$$ (8.2)

The tests were performed using two measurement time steps: 0.125 s and 0.3 s. It was shown before that the system is less stable close to its characteristic time constants, therefore the 0.125 s sampling rate is expected to provide valuable information on the system's response close to the edge of its stable operation.

At first, two out of five devices with the closest conductance values were selected based on their current-voltage characteristics. The devices were connected in series and tested for their response to voltage sequences in the range from 5 V to 50 V with a sampling rate set as 0.125 s. Each of the respective voltages was held for 300 measurement steps. The results of the measurements are shown in **Figure 8.2**.

As can be seen, the operation of two devices connected in series is stable when it operates at 20 V and above this value. However, under 10 V and 15 V bias signal fluctuations were observed for devices connected in series, as shown in insets. It is also worth mentioning that the current drop at the beginning of each of the measurements is not a valid result, but rather an anomaly caused by the circuit capacitance.

In previous Chapters, the +10 V potential was used as a reading voltage, as it is not strong enough to cause a significant ion movement in the PSS matrix. As the electric

field is too weak to cause ion migration, the mechanisms previously connected to devices' stable operation might be too weak to influence the system operation, allowing for temporal signal distortions.
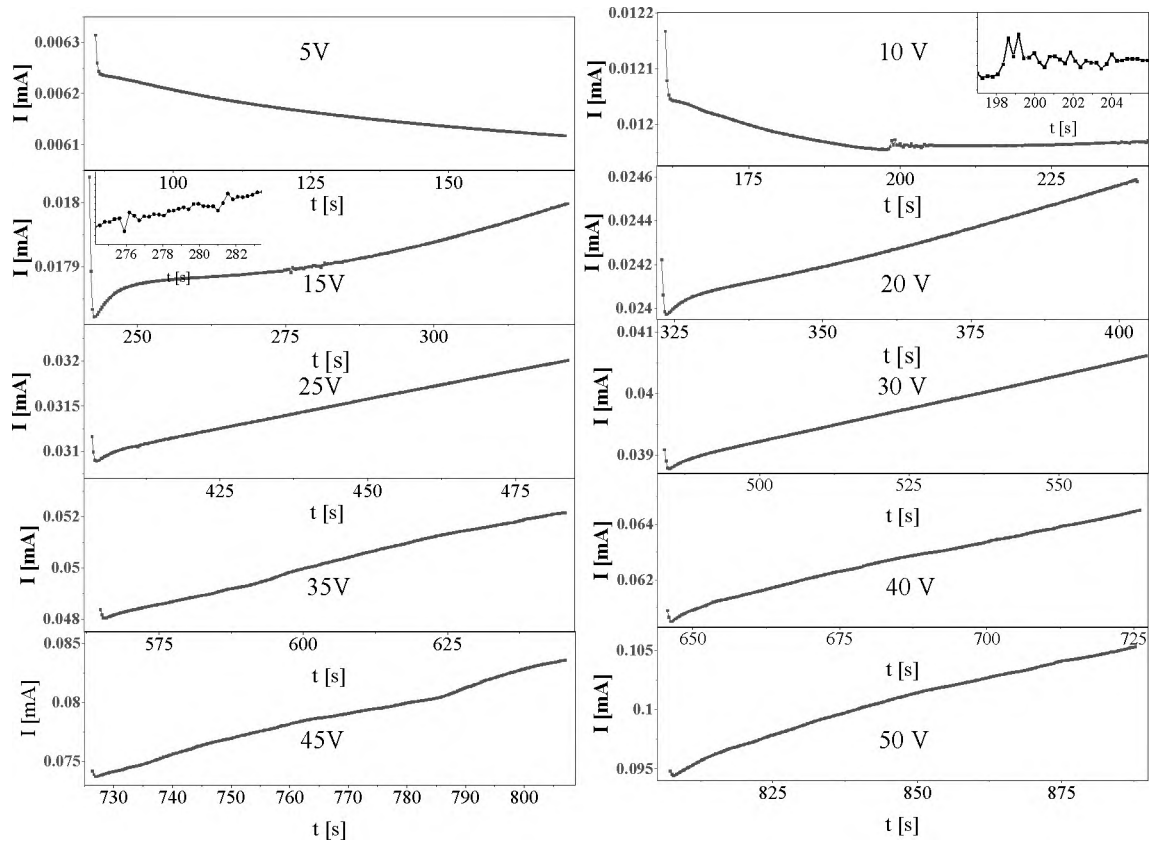

Figure 8.2 Current response of two devices connected in series measured in voltage range from 5 V to 50 V with 0.125 s sampling rate

The insets in Figure 8.2 show the signal distortions registered for device connection operating under 10 V and 15 V bias. In order to describe the observed fluctuations an autocorrelation function was calculated using Python statsmodels library[99]. Specifically, the plot_afc() function was used to illustrate the autocorrelation of time series by lag, which corresponds to a fixed amount of passing time. They provide information on temporal dependency in the data.

The output plot, often called a correlogram, informs us about the relationship between a variable's past values and its current value. The Pearson correlation coefficient equal to 1 corresponds to a positive correlation, a value of -1 corresponds to a negative correlation and a value close to 0 indicates no correlation. What is worth noting is that the lag = 0 is the correlation of the time series with itself and it is always equal to 1[100]. The blue area on the plot depicts the 95% confidence interval, meaning that the lags outside of it are statistically non-zero and the lags within it are statistically close to zero.

In order to calculate the autocorrelation function it is essential to check whether the data is stationary, which requires to check whether the statistical properties of the data change over time. It is determined based on its p-value, which has to be less or equal to 0.05. The p-values of the data were calculated using the adfuller() function from statsmodels library. The results showed that the utilised data did not meet the criteria of being stationary, therefore to continue the analysis the data was differentiated to fulfil this requirement.

After meeting the criteria of being stationary, the signal measured under 10 V bias, shown in **Figure 8.3 a)**, was analysed and its autocorrelation function has been calculated, as shown in **Figure 8.3 b)**.
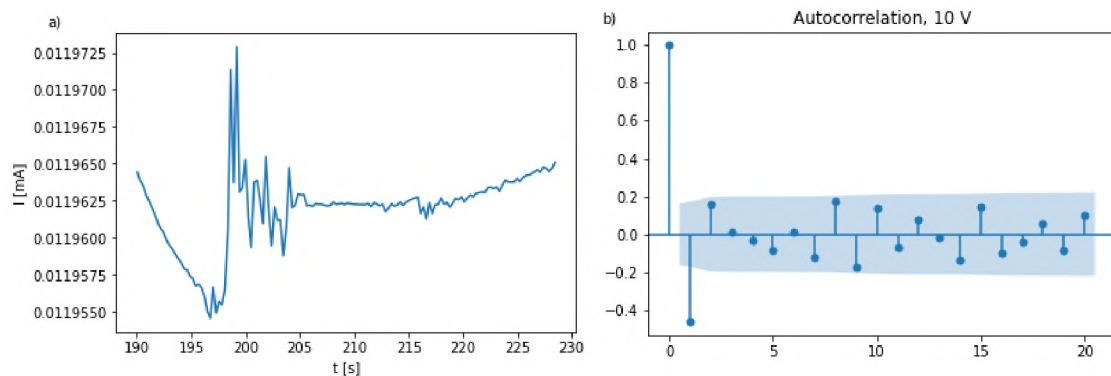

Figure 8.3. a) Signal fluctuation measured for two memristive devices connected in series under 10 V bias with 0.125 s measurement step and b) it's autocorrelation function calculated with 20 lags

The autocorrelation function was calculated with a number of lags equal to 20. This means that the autocorrelation function was calculated between the initial data and the data shifted in time up to 20 time periods. What can be seen is that there is no pattern in the autocorrelation function, meaning that there is no seasonality in the series. Moreover, it is apparent that there is a strong negative correlation at lag = 1, which lies above the blue area and therefore has statistical significance, meaning that at any given time t there is a correlation between I_t and I_{t-1}. This result leads to the conclusion that the observed process is not random. There are also several autocorrelations that are significantly non-zero within the blue area, however they were not included in the analysis.

Next, the signal distortions measured under 15 V bias with 0.125 s time step were analysed for two devices series connection. The analysed signal is illustrated in **Figure 8.4 a)** and its autocorrelation function is shown in **Figure 8.4 b)**.

The results show that there is a negative correlation at lag = 1, which vanishes with the following lags. Nevertheless, the significantly non-zero correlation at lag = 1 implies that the signal distortion is not random.
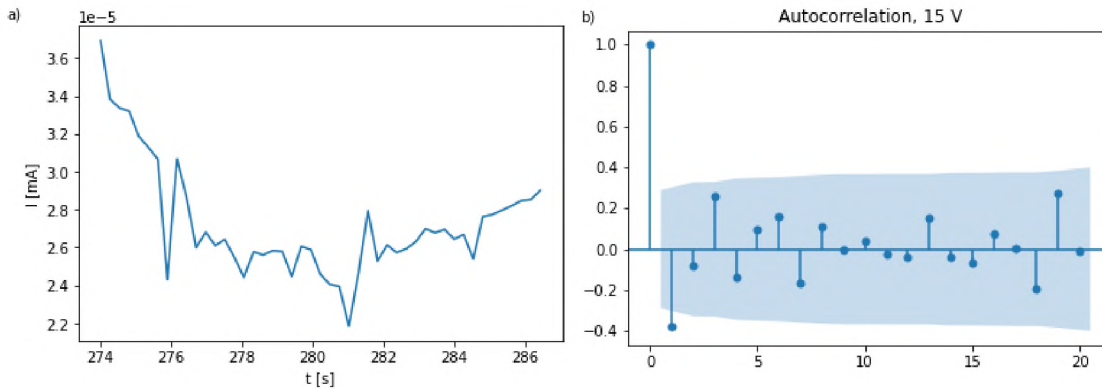

Figure 8.4. a) signal fluctuation measured for two memristive devices connected in series under 15 V bias with 0.125 s measurement step and b) it's autocorrelation function calculated with 20 lags

In the next part of the study, the devices in series connection were measured in voltage range from 5 V to 50 V with 0.3 s time step. The results presented in **Figure 8.5** imply that there are no significant signal fluctuations during the device operation. The only signal distortions were measured at 30 V and 45 V bias, however, they were excluded from further analysis in this thesis based on initial analysis results.
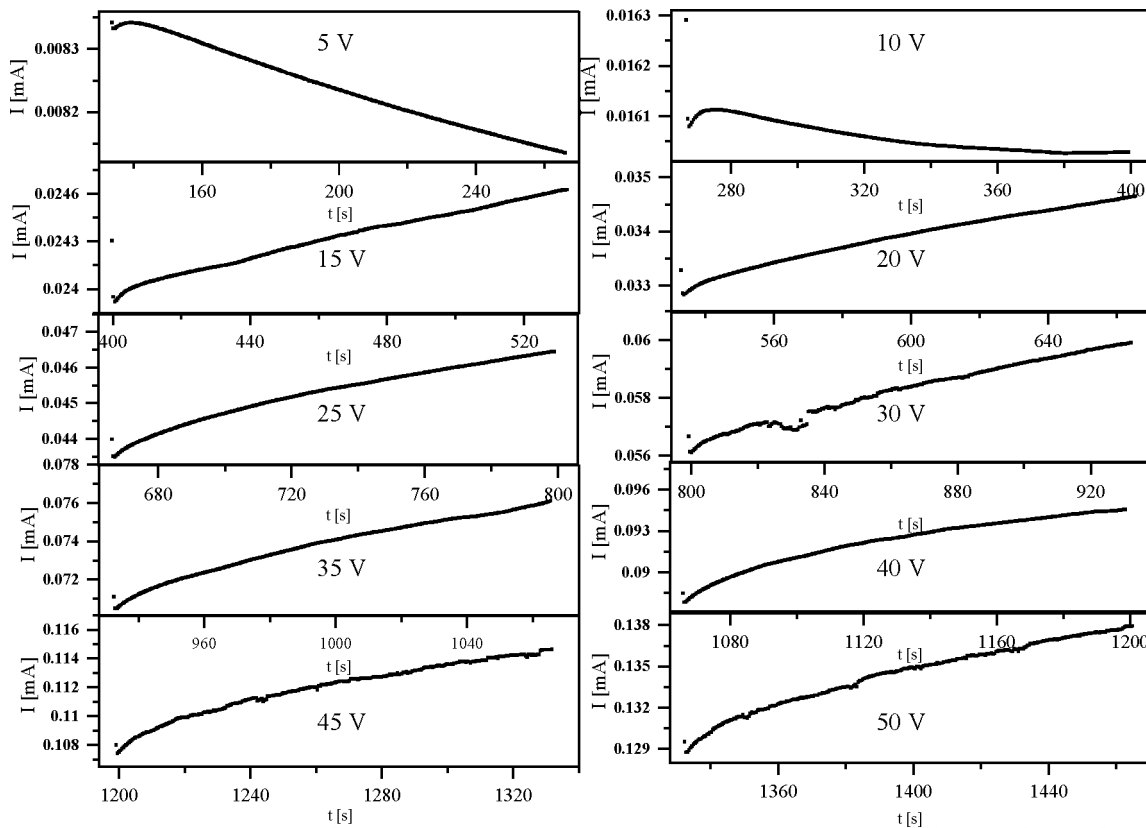

Figure 8.5. Current response of two devices connected in series measured in voltage range from 5 V to 50 V with 0.3 s sampling rate

122

The results show that the connections of devices in series exhibit fluctuations when operating under 10 V and 15 V bias and 0.125 s measurement step. It is in line with the previous assumption that the ion migration does not appear in the system when the electric field is too weak. In this scenario, the fluctuations can be connected to none of the described in Chapter Five mechanisms being strong enough to dominate the response of devices during their operation.

Moreover, using a 0.125 s sampling rate, due to it being close to the characteristic time constant, was shown in Chapter Six to cause less stable operation of devices, which further explains the observed distortions. Taking this and the analysis results into account, it is apparent that the observed fluctuations are autocorrelated and do not exhibit random behaviour. Therefore, the observed signal fluctuations might be related to the propagation of distortion from one device to another, causing them to be correlated.

In the next part of the study, the devices were connected in parallel and, at first, tested in voltage range from 5 V to 50 V with a time step set as 0.125 s. The results of the measurements are shown in **Figure 8.6**. As it can be seen, the measured signal is stable and in terms of signal shape, it does not differ in a significant way from the signal measured for a single device.
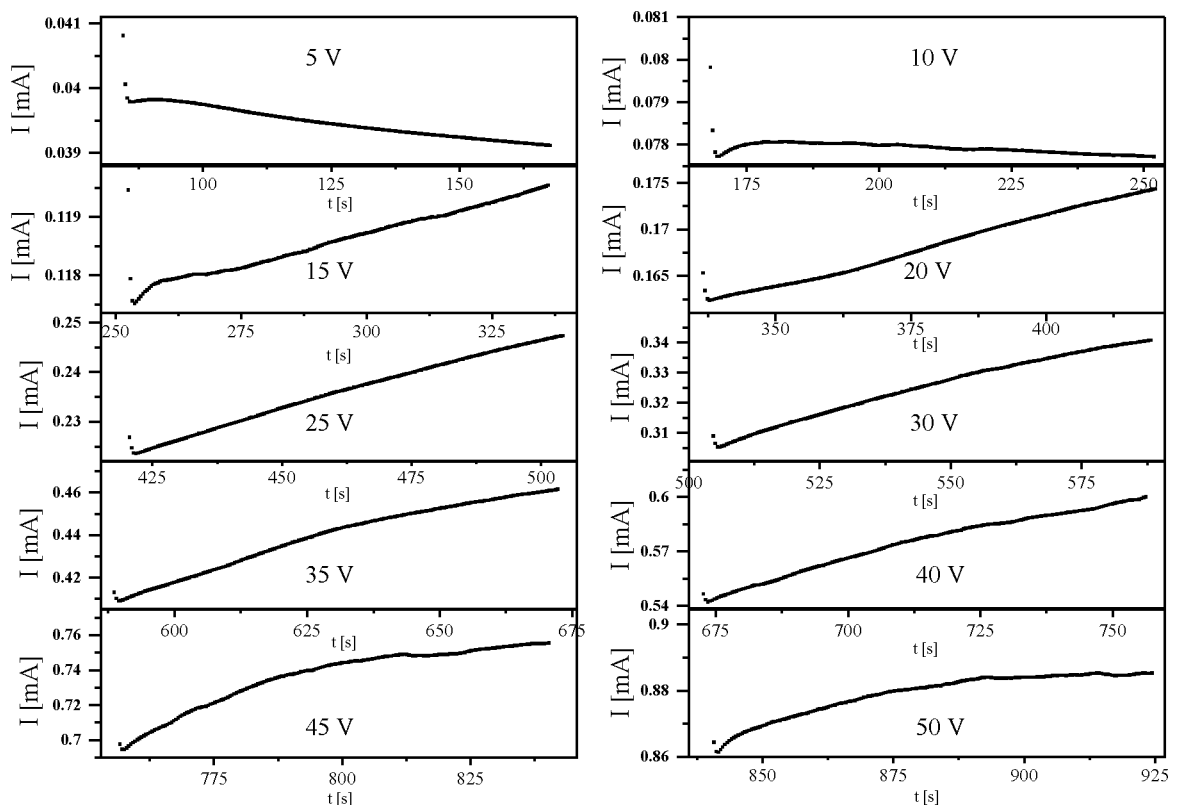

Figure 8.6. Current response of two devices connected parallelly measured in voltage range from 5 V to 50 V with 0.125 s sampling rate

The results obtained for devices connected in parallel and measured with a 0.3 s time step also indicate stable operation of the system, as shown in **Figure 8.7**. As a part of the preliminary analysis, the distortions measured for 50 V bias were excluded from the autocorrelation function calculation.
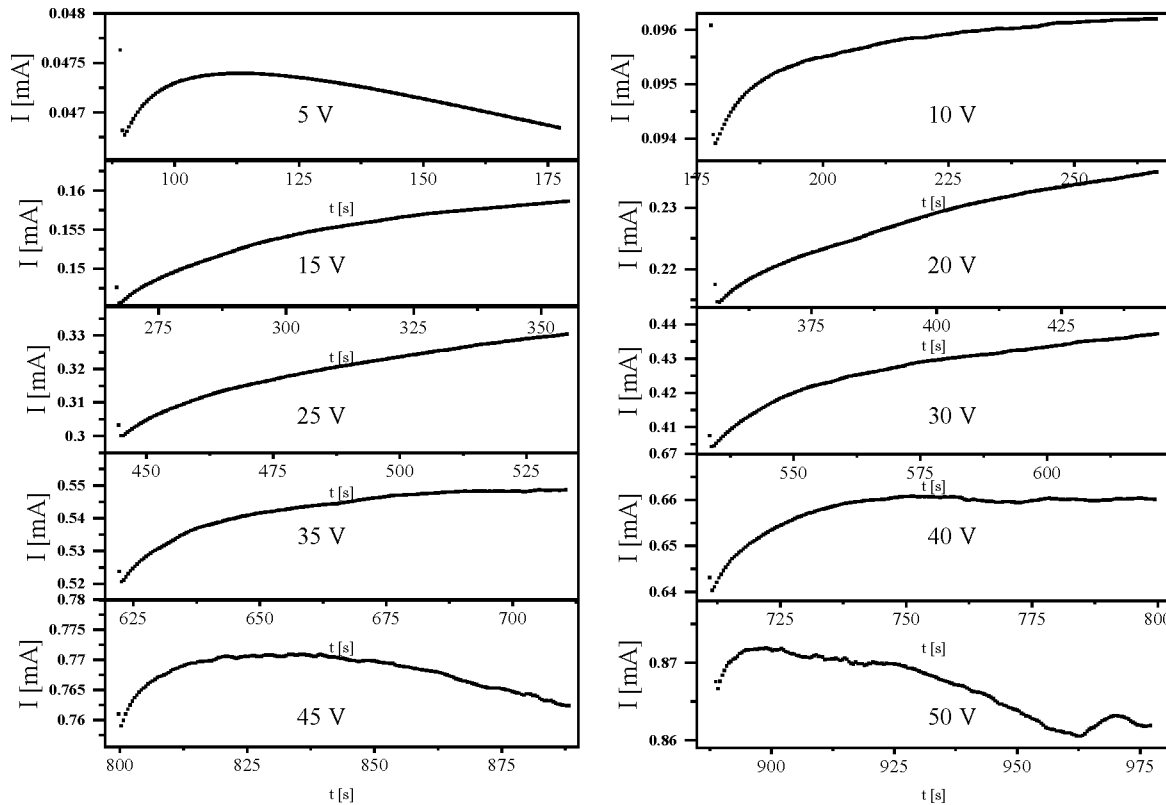

Figure 8.7. Current response of two devices connected parallelly measured in voltage range from 5 V to 50 V with 0.3 s sampling rate

The aforementioned results show that the devices' connections are stable while operating within the 15 V to 50 V range for both of the time steps. The signal distortions measured during the device's operation are most likely connected to local distortions being propagated within the systems, after which it returns to a semi-equilibrium state.

Moreover, the analysis performed for devices in series connection showed that the distortions are autocorrelated, which further supports this hypothesis. These results exclude the potential use of the devices as random generators. On the contrary, they show that the studied system might be utilised as a *reliable* building block of more complex circuits.

To support this thesis, in the next part of the study, the devices were connected into three memristor two resistor (3M2R) bridge. The idea behind this connection was inspired by Wheatstone's bridge, which is commonly used to test all sorts of signal distortions.

124

It is especially useful in detecting resistance changes, as it amplifies instabilities propagated in the bridge. A small signal anomaly in one of Wheatstone bridge's elements can be propagated through it and cause a significant change in response to a different component. The simplified diagram of the 3M2R connection is illustrated in **Figure 8.8**.

The resistors used in the bridge were selected as 2 MΩ to match half of the value of resistance of the memristive devices used in the experiment. The measurements were performed in voltage range from 5 V to 50 V with 0.125 s time step. As the results obtained for a 0.3 s time step were similar, they are not shown in this thesis.
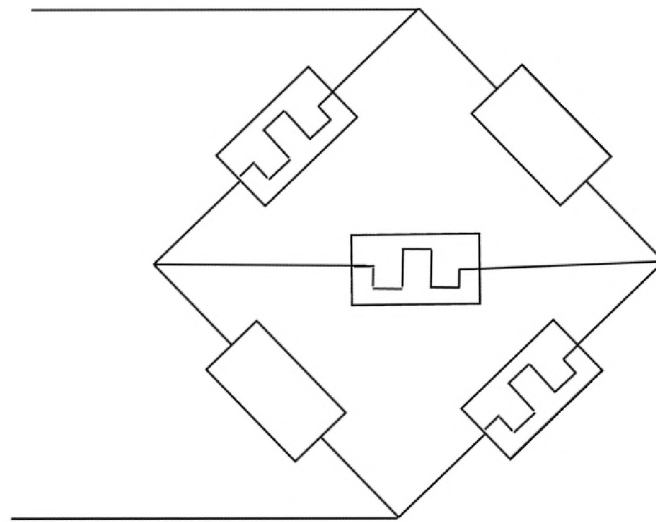

Figure 8.8. Scheme of three memristor two resistor bridge

The results of the measurements are illustrated in **Figure 8.9**, showing stable operation of the devices connection within the whole measurement parameters range. What is also worth mentioning is that under 5 V and 10 V bias, the bridges' response differs from the one measured under higher bias, which is also in line with the previous observations.

To conclude, within the measurement parameters, the two resistor three memristor bridge operation is highly stable and no signal distortions were detected. This supports the aforementioned claim that the devices might be used as elements of more complex circuits. In order to do so, the research should be extended to different operation frequencies, as memristor bridge frequency dependency has been previously shown in literature as an asset[101].
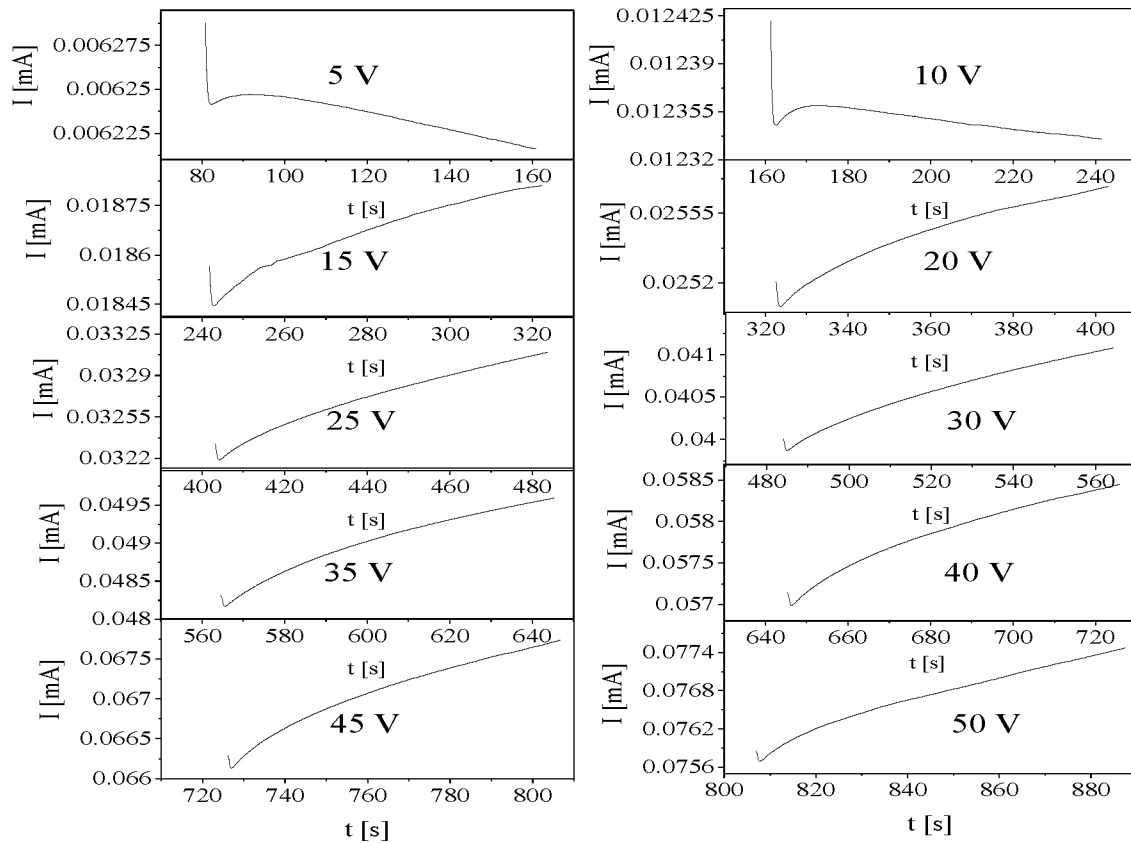
Figure 8.9. Current response of three memristor two resistor bridge measured in voltage range from 5 V to 50 V with 0.125 s sampling rate

However, in the early stage of this research, the same connection was tested on memristive devices with an R-P3HT layer containing impurities. As it was shown in Chapter Three, the R-P3HT contamination can cause the device's instability. This impurity was tested to determine whether it enhances the signal distortions in the system and is able to introduce a stochastic nature into three memristor two resistor connection.

The 3M2R connection utilizing memristive devices made with an R-P3HT layer containing impurities was tested in the voltage range from 10 V to 45 V with a 0.125 s time step. The measurements were performed in an extended time, for measurement steps number set as 4800.

As can be seen in **Figure 8.10**, there is a certain parameter range within the memristor bridge behaves in an unpredictable manner. The signal fluctuations are the most apparent for measurements performed under 10 V and 15 V bias. To describe these distortions the datasets were analyzed as described before, using the autocorrelation function.

126
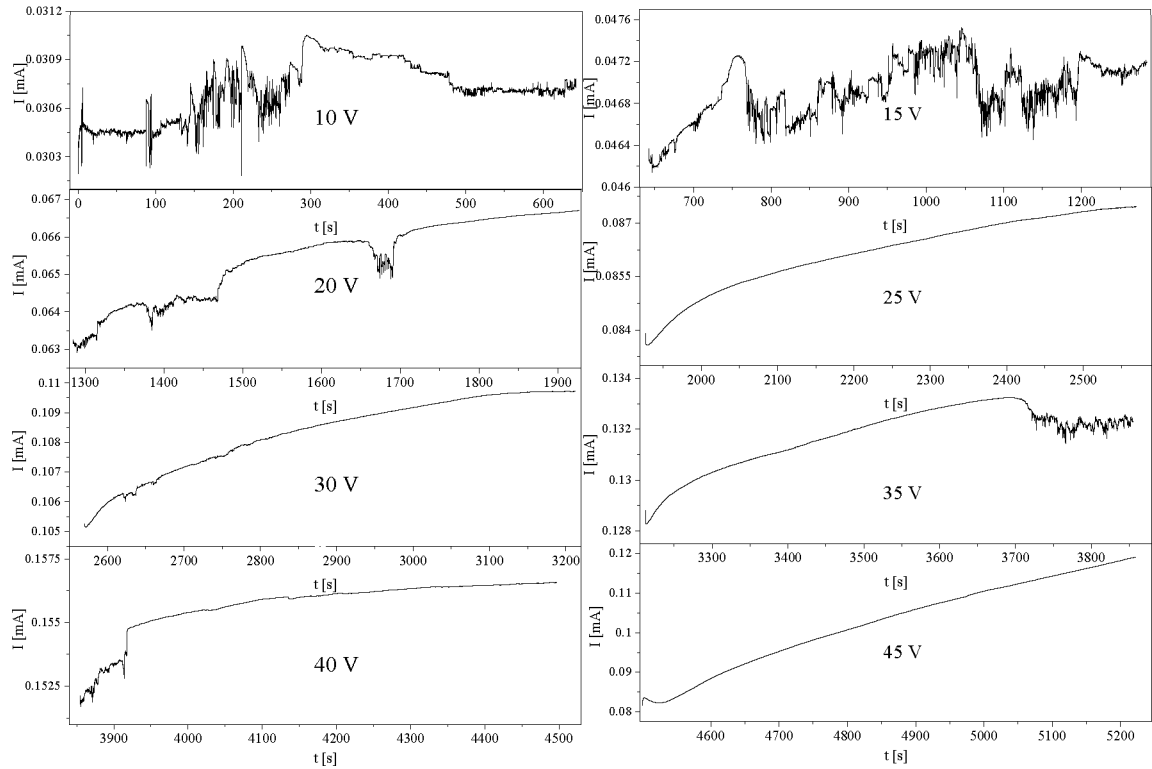
Figure 8.10. Current response of three memristor two resistor bridge measured in voltage range from 5 V to 50 V with 0.125 s sampling rate. The measurements were performed on devices with R-P3HT contamination

In the first part of the analysis, the signals were tested to find out whether they are stationary. The calculated p-values revealed that the data was non-stationary, therefore signals were differentiated before calculating the autocorrelation function. The data analyzed for measurement performed under 10 V bias with 0.125 s measurement step and it's autocorrelation function are illustrated in **Figure 8.11 a)** and **b)**.

Figure 8.11. a) signal fluctuation measured for three memristor two resistor bridge under 10 V bias with 0.125 s measurement step and b) its autocorrelation function calculated with 20 lags

127

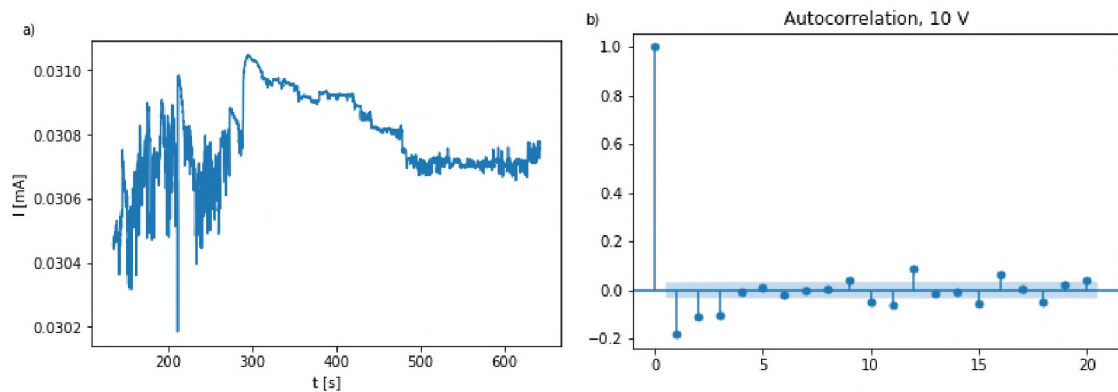The autocorrelation function illustrated in Figure 8.11 b) implies negative autocorrelation at lags 1, 2, and 3, as well as positive autocorrelation at lags 12 and 16. The points lay outside of the blue area, which implies strong statistical significance.

Based on these results, it is apparent that the signal fluctuations are non-random and the current measured at time t_n depends on the current measured in t_{n-1}, t_{n-2}, etc.

The data measured under 15 V bias with 0.125 s time step was analysed using the same method. The results presented in **Figure 8.12** show that despite major signal distortions, the measured current is correlated at lag = 1 and lag =2.
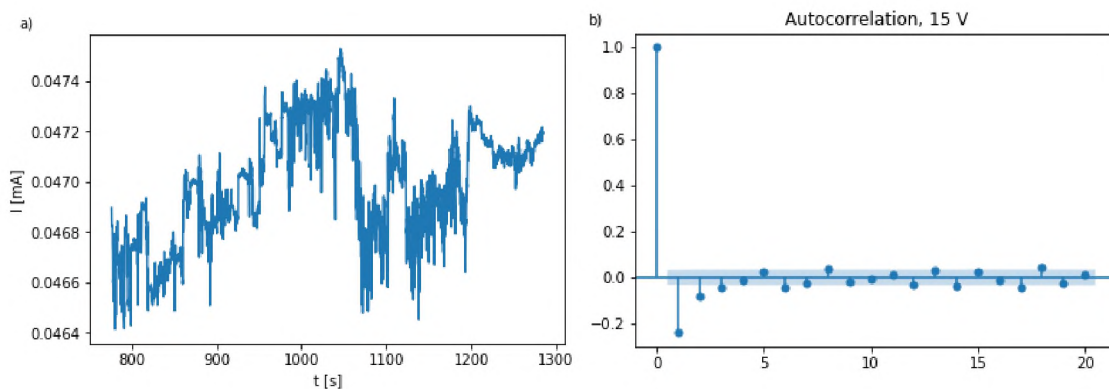

Figure 8.12. a) signal fluctuation measured for three memristor two resistor bridge under 15 V bias with 0.125 s measurement step and b) its autocorrelation function calculated with 20 lags

Based on these results it is apparent that in devices connection, similarly to single devices, the current response is determined on their previous state. The calculated autocorrelation functions prove that the data carries history of the past events, which can be easily explained based on the device model proposed in Chapter Four.

The model describing the device uses differential equations, which couple the relationship between the current and conductance change, allowing to reproduce the smooth tuning of the devices' conductance. As the state of the device is described by the differential equations, it is unlikely to observe a stochastic behavior of the system.

8.2.2. Generation of neuronal spikes

The second part of the Chapter explores the devices' utility as synapses in Spiking Neural Networks. As it was mentioned before, among features of memristive devices, the ability to store information for a limited time is particularly interesting in terms of mimicking the activity of synapses. For example, volatile memristors have found applications in

spiking neural networks (SNN) to store the weights of synapses in the form of conductance.

To emulate the behaviour characteristic for neurons, the output signal (current) is calculated as the dot product of the inputs (voltage) and weights (conductance), and further integrated to return the output as their sum. In the case of multiple devices connected parallelly, such operation is possible because of Kirchhoff's' law – the current of memristors connected parallelly to the same output neuron sums up[95]. However, for the sake of simplicity, the simulations, and experiments, described further, were performed for one device.

To assess the studied systems' utility as synapses in SNNs, a series of simulations were performed, including an investigation of the device model's ability to emulate spike-like signals.

Experimentally, the weights, corresponding to memristor's conductance, can be adjusted by mimicking Short Term Plasticity (STP) function by potentiating (increasing the weight by applying a high voltage) or depressing a synapse (applying low voltage or voltage of negative polarity to decrease the conductance), as it was shown in previous chapters. The slow decrease of conductance after potentiation is shown in **Figure 8.13**, in the red circle, as a current decrease in following simulation time steps.

As the simulations are less time and resources consuming, the device's model was tested instead of real devices. The simulation was performed using the model and parameters described in Chapter Five. The simulation time step was set as 0.4 s, the reading voltage as +10 V, and the potentiating pulse as +50 V. The voltage spike was simulated as a triangular signal and is shown in the upper panel in Figure 8.13. The times of spike occurrences were generated randomly.

The STP decays in time, therefore, to maintain the information the weight has to be updated throughout the simulation. It can be accomplished by applying pulses of higher magnitude in a short period of time. In this scenario, the conductance of the device increases with each pulse, what manifests as higher currents, as highlighted with an arrow in Figure 8.13. If the programming pulses do not occur frequently, the conductance decreases, and the device loses information about past events.
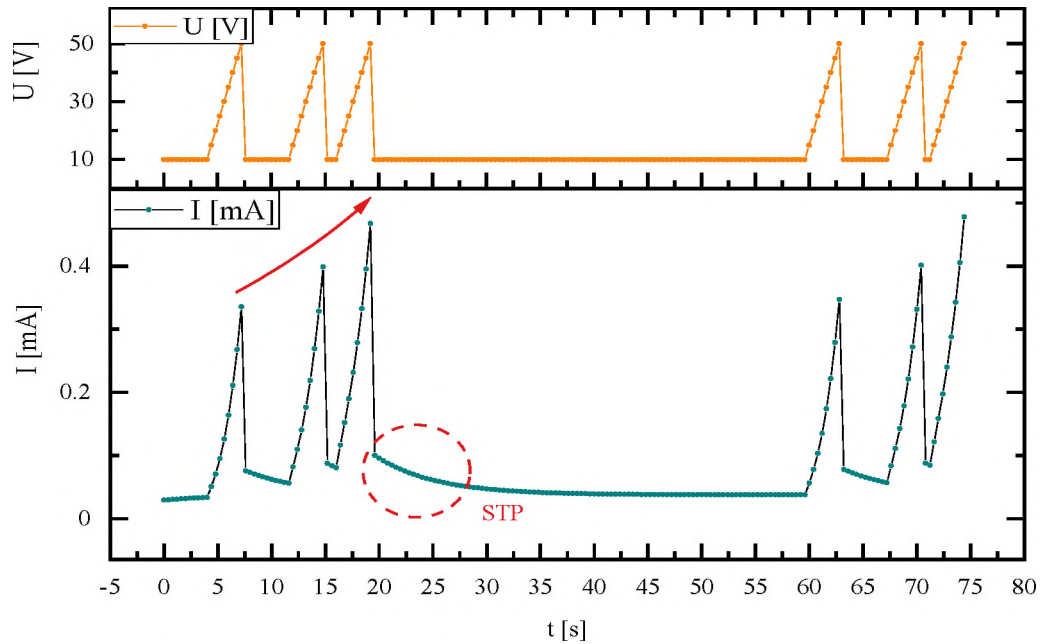
Figure 8.13. Simulation of current response (bottom panel) to a stimulation with voltage pulses with a +10 V reading pulses and +50 V programming pulses (upper panel) performed for a single device. The pulses were generated at random times

The significance of the frequent arrival of spikes, in terms of information retention, is even more visible in extended simulation time, as shown in **Figure 8.14**. After the 410th second of simulation, as highlighted in the blue box, there are 4 spikes occurring one after another within 30 seconds. This event results in a significant conductance increase and longer conductance retention time.

As can be seen, the current response depends on the temporal spacing between the programming spikes. Moreover, the device's volatility allows it to store information about past events for a limited time, which complies with device requirements for SNNs.
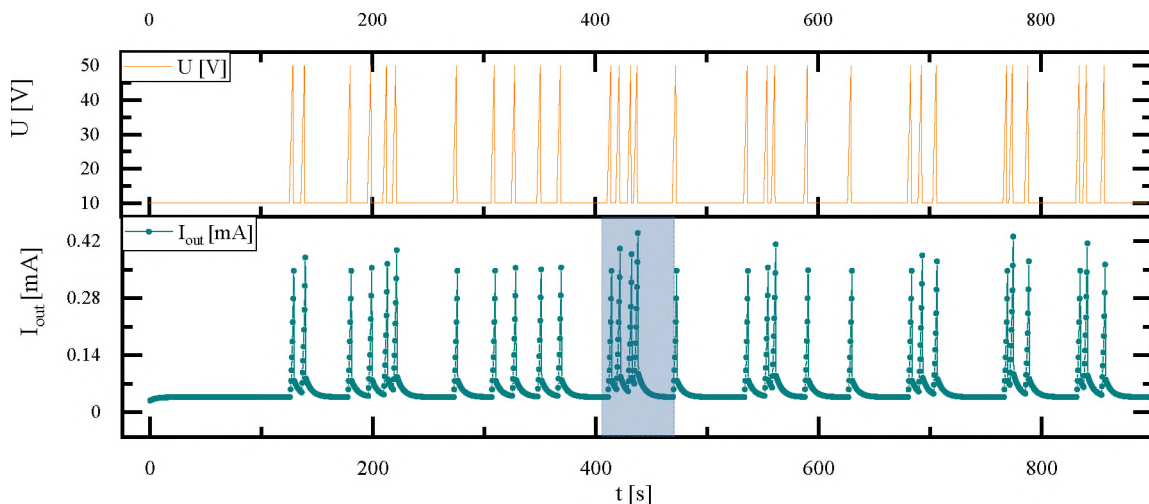

Fig. 8.14. Simulation of current response to a stimulation with a +10 V reading pulses and +50 V programming pulses performed for a single device in extended simulation time

130

Based on these results let us consider two synapses, each of them with its' own adjustable weight. In this scenario, both output neurons fire in response to the same external stimuli (input), which is generated as a train of spikes. However, there is a delay between both input spikes. One of them is called excitatory Neuron A (increases weight) and the second one is called inhibitory Neuron B (decreases weight). The memristors A and B serve as a synapse, which is fed with the input signals generated in neurons A and B. This reasoning will allow us to understand further experiments.

Based on the temporal spacing between the spike occurrences in the spike train, we compare the output currents by calculating the difference between i_A and i_B. If the first input neuron spikes first then, for a short period of time, the resulting current is positive, otherwise, when the resulting current is negative then Neuron B fires.

To determine the impact of spike delay, two neurons were simulated: Neuron A (excitatory) and Neuron B (inhibitory). Both neurons were fed with the exact same train of spikes with 3 pulses delay between times of pulses arrival for devices A and B, as shown in **Figure 8.14** in orange. The programming voltage was set as +30 V and increased in a form of a triangular shape.
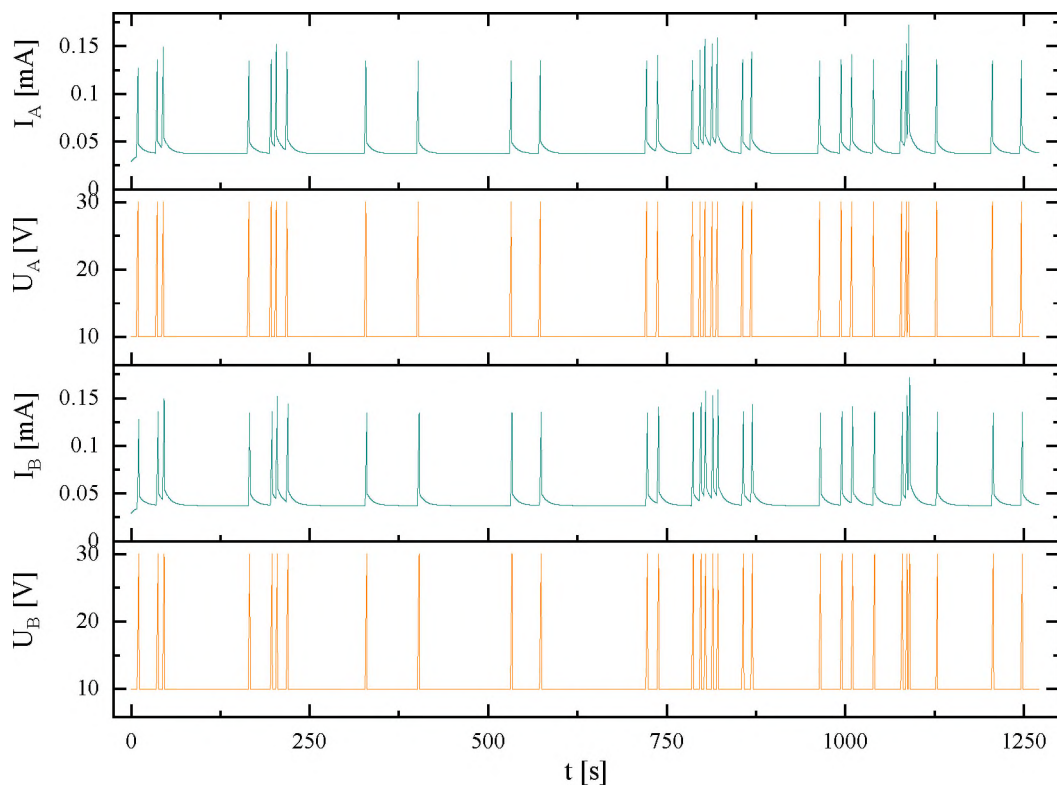

Fig. 8.14. Simulated current responses (blue) to the stimulations (orange) for neurons A (top) and B (bottom); the delay between the pulses occurrence between devices was set as 3 pulses (iteration steps)

131

As can be seen in **Figure 8.15**, the current difference calculated between neurons A and B depends on the temporal spacing between the pulses. Due to the delay, the calculated difference has a higher magnitude in negative current values. Therefore, in further experiments, the current responses are integrated at first and then the difference is calculated. This specific example does not possess a great experimental value, as both train spikes are the same, however, it shows the significance of the delay between the spike occurrences.

Moreover, the results of this study show the utility of the devices in SNNs.
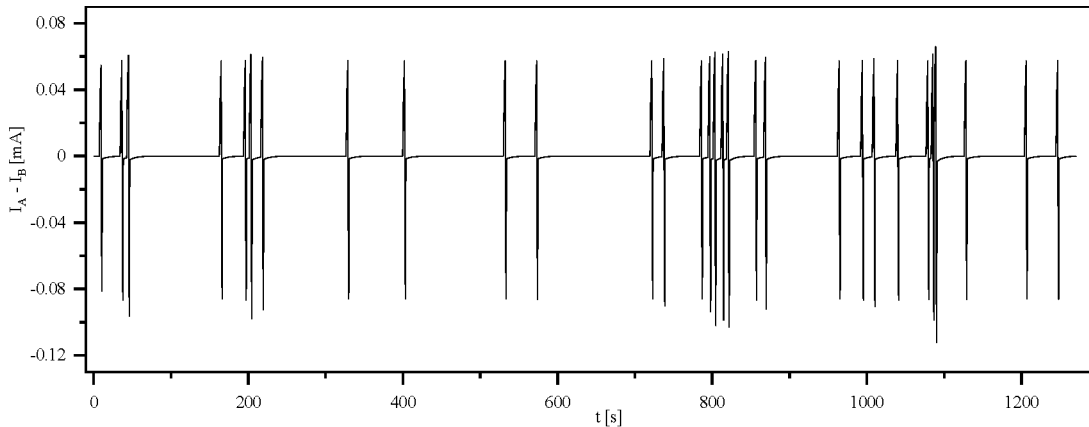
Fig. 8.15. The calculated difference between excitatory (A) and inhibitory (B) neurons

8.2.3. Simulation of 2 Alternative-Forced Choice Experiment

The 2-Alternative-Forced Choice (2AFC) Experiment[95] is inspired by the biological decision-making behaviour. In the experiment a decision has to be made between two alternative spike trains, based on noisy observations made in time[95]. In the experiment, the spike trains are generated in input neurons A and B and are fed to two synapses – memristors M_A and M_B. Both spike trains differ in the number of spikes as well as the times of their occurrence. To simplify the simulation, the spikes are in a form of a single +50 V pulse, instead of a triangular one as in the tests.

For a reminder, the current response I_t of both memristors at a given time t depends on the time of occurrence of consecutive spikes and the devices conductance C_t is updated in each iteration step as follows:

$$I_t = C_t \cdot V_t, \tag{8.1}$$

$$C_t = \tau C_{t-1} + \eta |V_t|, \tag{8.2}$$

where $\tau = 0.93$, $\eta = 2.62 \cdot 10^{-8}$ S/V, and $C_0 = 2.90 \cdot 10^{-6}$ mS.

In the experiment, if two spikes arrive in a short time one after another, the memristors'

conductance increases after each spike resulting in increased current response (as shown in **Figure 8.12** in red circle). Otherwise, when the time between two spikes is long, the memristors' conductance value decays to some extent after the first spike.
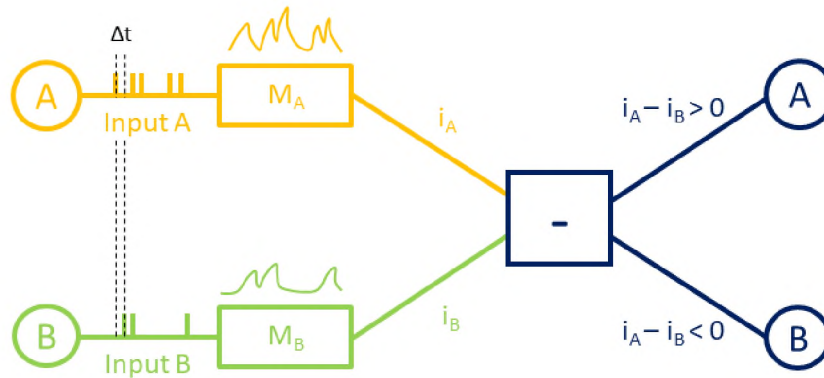

Figure 8.16. The scheme of the 2 Alternative-Forced Choice experiment. Neuron A (orange) fires to the memristor M_A and Neuron B fires to memristor M_B. Both spike trains differ in the number of spikes and times of their occurrence. The current response is integrated for both memristors and the difference between i_A and i_B is calculated. Based on the value of the difference of the currents, whether it is positive or negative Neuron A or B fires

As mentioned before, one of the input neurons is called an excitatory neuron, Neuron A, which increases the weight, and the second one is called an inhibitory neuron, Neuron B, which decreases the weight. In this simulation, the weight of a biological neuron is associated with the memristors' conductance value.

During the simulation, the parameters of both memristors are calculated for reading voltage +10 V and spike value set as +50 V. The current response to +50 V is not calculated, only the conductance change is updated. The time between reading pulses is set as 0.4 s. Simulations for each pair of spike trains, differing in times of spikes appearance in each trial number, were performed for 10000 trials for statistics.

During the simulation, the memristors' current responses to spikes are calculated and saved. Next, the currents for both memristors are integrated and the difference between i_A and i_B, which corresponds to the integrated current response of memristors M_A and M_B, is calculated. If the resulting current difference is positive then the output Neuron A fires and we associate it with success, otherwise, when the resulting current is negative, Neuron B fires. Scheme of the experiment is illustrated in **Figure 8.16**.

The simulations were performed for different numbers of inputs for Neurons A and B, in simulation times in the range from 4 seconds to 100 seconds (10 to 400 iteration steps). A fixed number of train spikes for each of the 10,000 trials were generated at random simulation times for statistical purposes. Therefore, one trial corresponds to one

simulation run performed for one variable, in this experiment spike times, with other parameters such as simulation time and numbers of inputs, fixed.

The simulations were performed with two different initial conditions: assuming devices have no memory of past events (conductance is set to its initial value at the beginning of each trial), and with the assumption that the devices store information about past events (the value of conductance at the beginning of each trial is set as the conductance value from last iteration step of the previous trial).

8.2.4. Simulation without the memory of the past events

The simulation in which the devices do not possess memory of the past events was performed on devices which are set in their initial conditions at the beginning of each trial. The results of this simulation inform us about the probability of making the right choice having no memory of past events. This setup corresponds to the case of a new device or to the case of the time in between trials being long enough for the conductance to decay to its initial value).

At first, the Neuronal Spike Times for both neurons are generated at random iteration steps. **Figure 8.17** shows an example of neuronal spike trains randomly generated in 10 trials. The excitatory Neuron A fires 10 times and the inhibitory Neuron B fires 7 times throughout the simulation time.
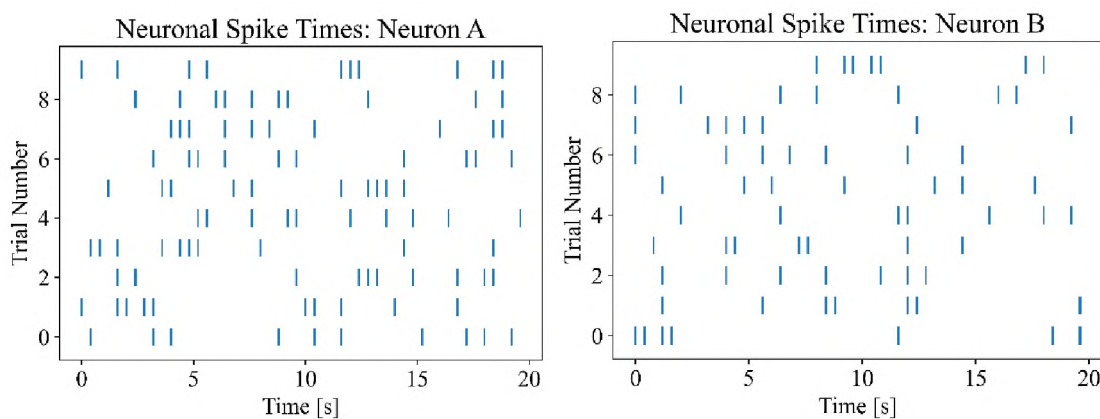
Figure 8.17. An example of randomly generated times of neuronal spike trains of 10 spikes for Neuron A and 7 spikes for Neuron B presented for 10 trials

Next, the input spikes are "fed" to the memristors, and the resulting current is calculated, as shown in **Figure 8.18**. The current simulated for device A is shown in red and for device B in blue. The calculated currents of both devices increase in time to reach a certain value, which is related to the $\epsilon |V_t|$ component of the updated conductance.
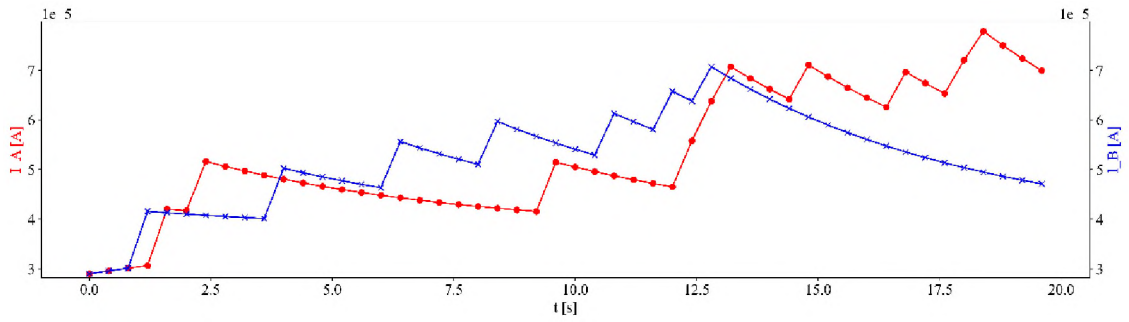
Figure 8.18. Current response of memristor M_A (in red) and memristor M_B (in blue) to a spike train of neuronal spikes from trial 2 presented in Figure 8.17

As the spike arrives, the value of the current increases for both devices and slowly decays until the arrival of the next spike. The time between the arrival of spikes determines whether the conductance will decay (sparse pulses) or further increase (frequent pulses). The conductance decay caused by the rare arrival of spikes is evident for Neuron B (in blue) between the 13th and 20th second, in which time, during 18 iteration steps, no spike arrives and the conductance decays. In contrast, the increase of conductance is noticeable between the 12th and 13th second of simulation in the case of Neuron A (red) after the arrival of a train of 3 spikes in a short period of time.

In the next step, the difference between integrated currents, i_A and i_B, and its value is calculated and analysed in terms of positive or negative value. The current value is negative in case of more frequent activity of the inhibitory neuron (Neuron B) and positive when the excitatory Neuron A fires more often in a short period of time. **Figure 8.19** shows the difference between currents at each simulation time step. It illustrates, that for the devices behaving like in the model – no noise or stochasticity – the calculated current difference differs from zero only if the spikes appear in a short period of time for both neurons or when there is a long period of time with no spike occurrences.
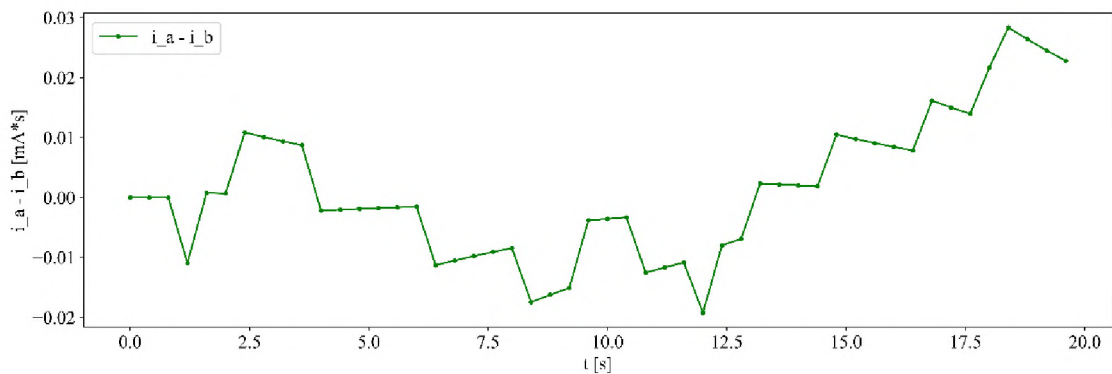

Figure 8.19. Difference between currents i_A and i_B calculated for each simulation step

During the simulation, both i_A and i_B are integrated and the difference between the currents, $i_A - i_B$, is compared in terms of positive or negative value. In case of a positive value, which in this experiment is a correct choice, the output Neuron A fires. Otherwise, when the value is negative the output Neuron B fires, which is an unexpected result and lowers the accuracy of the performed simulations.

After each trial, the parameters of the memristors are set to initial values. The accuracy of the simulations for different input ratios, different simulation times and fixed 10,000 trials were calculated as a number of correct choices divided by the number of trials[95].

The results of simulations performed for 10 000 trials, in simulation times in the range from 1 s to 20 s, with a number of input signals for Neuron A/Neuron B set as 4/3, 4/2, 4/1, 3/2, 3/1 and 2/1 are shown in **Figure 8.20**. The difference between the number of spikes for both neurons is set as 1, 2 or 3 to see how a slight change in the ratio between the number of spikes changes the accuracy of the experiment.
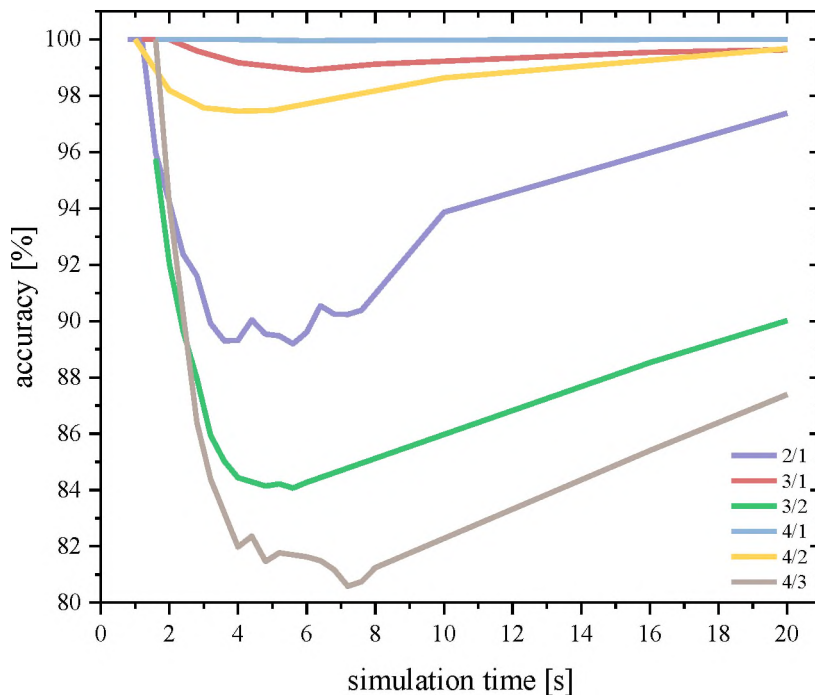
Figure 8.20. Results of simulation performed for number of spikes for Neuron A/Neuron B set as 2/1, 3/1, 3/2, 4/1, 4/2, and 4/3. The simulation was performed in time range from 4 to 160 seconds for 10 000 different trials

It is apparent that the accuracy of the experiment is lower both for the long simulation times as well as for the higher ratio between the number of input signals. The high accuracy in the case of the short simulation time is caused by a short time between the moments in which the spikes occur. The spikes arrive shortly one after another, therefore

the conductance value is increased but there is no time between the spikes for its' value to decay. For example, in a simulation with a 4/2 input signal ratio with 4 seconds of the simulation time, the spikes generated by Neuron A arrive at 4 of the 10 iteration steps of the simulation, whereas the spikes generated by Neuron B arrive only twice throughout the simulation. Therefore, the accuracy will always be 100%. When we compare this result to the simulation with a 3/2 input signal ratio and 1.6 seconds of the simulation time, there are 4 iterations in the simulation (0.4 seconds each), which means that the spikes in Neuron A are present during 3 of 4 iterations and in Neuron B in 2 of 4 iterations resulting in the 95,76% accuracy of the simulation.

In terms of the higher ratio between the number of spikes for Neurons A and B, the accuracy is higher, compared to experiments with a lower ratio. However, excluding the 4/1 ratio, it is not 100% due to many possible spike sequences for both inhibitory and excitatory neurons.

What is also noticeable is existence of the local minimum of experiment's accuracy, which will be analysed further in this chapter.

8.2.5. Results of simulations with memory of the past state

This simulation setup includes the devices, which at the beginning of the simulation, are set in the last conductance state from a previous simulation trial. This means that the devices have a memory of past events instead of being modelled as devices in their initial conductance state (resting state). This scenario corresponds to the real devices in the experimental setup in which the time between following trials is short.

At the beginning of the simulation the times of occurrences of neuronal spikes were generated at random times. An example of the Neuronal Spike Times for Neurons A and B generated randomly for 10 trials is presented in **Figure 8.21**.
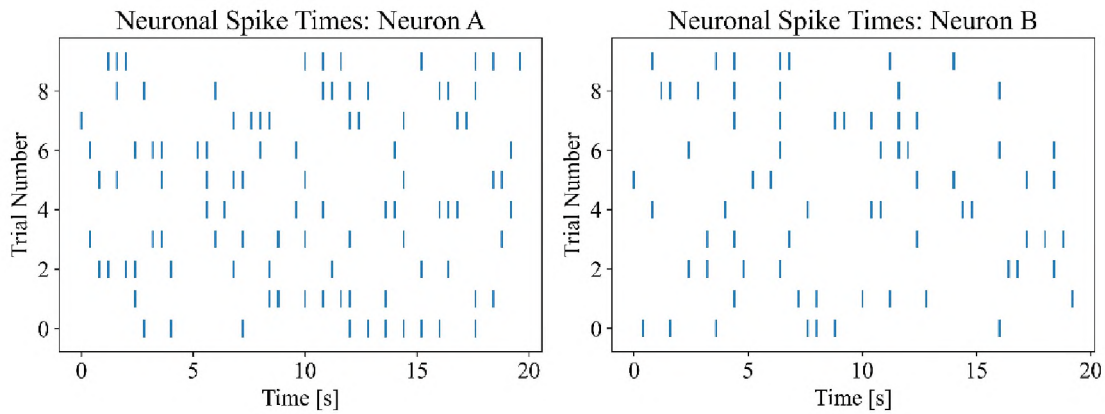
Figure 8.21. An example of randomly generated times of neuronal spike trains of 10 spikes for Neuron A and 7 spikes for Neuron B presented for 10 trials

Next, the current responses to each trial were calculated for both inhibitory and excitatory neurons. **Figure 8.22** shows current responses for memristor A (in red) and memristor B (in blue) calculated for the Neuronal Spike Times of trial 6 from **Figure 8.21**. Before the arrival of the first spike, as the devices have a memory of the past events and both are in conductance states higher than the initial one, the conductance of both devices decreases due to τC_{t-1} factor, which is responsible for the relaxation in the system.
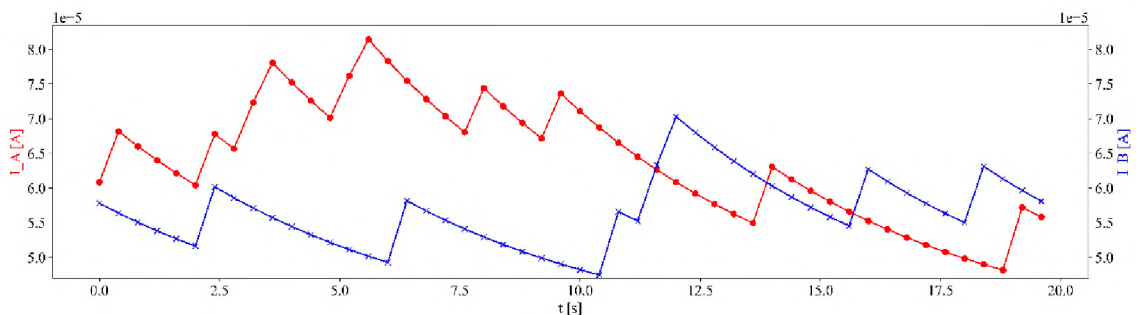
Figure 8.22. Current response of memristor M_A (in red) and memristor M_B (in blue) to a spike train of neuronal spikes from trial 6 presented in Figure 8.21

The difference between the current calculated for memristor A and memristor B at each time step is presented in **Figure 8.22**. As mentioned before, the currents' value is positive when the excitatory Neuron A fires more often and negative in case of more frequent activity of the inhibitory neuron (Neuron B).

138
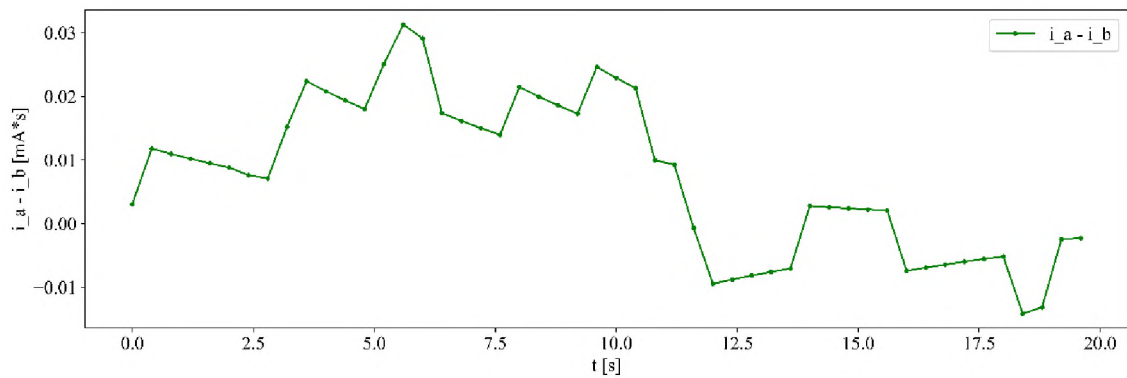
Figure 8.22. Difference between currents i_A and i_B calculated for each simulation step; the ratio of number of spikes for Neurons A and B are set as 7/10

The current values are further integrated and the i_A-i_B difference is calculated to determine the accuracy of the simulation.

Figure 8.23 shows the results of simulations performed for the number of spikes fixed as 10 for input Neuron A and the number of spikes varying between 5 and 9 for Neuron B. The simulations were performed at simulation times in the range from 4 to 100 seconds. The simulation was performed every 2 seconds from the 4th to the 20th second and for longer simulation times every 10 seconds.

As can be seen, the accuracy of the simulation is the highest for the highest ratio between the number of A and B inputs (10/5). As the ratio between the number of input signals becomes smaller the accuracy of the simulation decreases in the first 20 seconds of the experiment and increases after reaching a local minimum. What is interesting, the difference in accuracy between ratios 10/7 and 10/5 is less than 1%. Moreover, lower ratios of input spikes tend to give lower accuracy of the simulations due to a similar number of spikes, which leads to smaller differences in conductance states of memristors and therefore lower current differences. These results show that the system performs the best in the 2AFC Experiment for high signal ratios conditions, however its' accuracy remains above 75% even when the number of spikes in trial differs only in 1 spike.
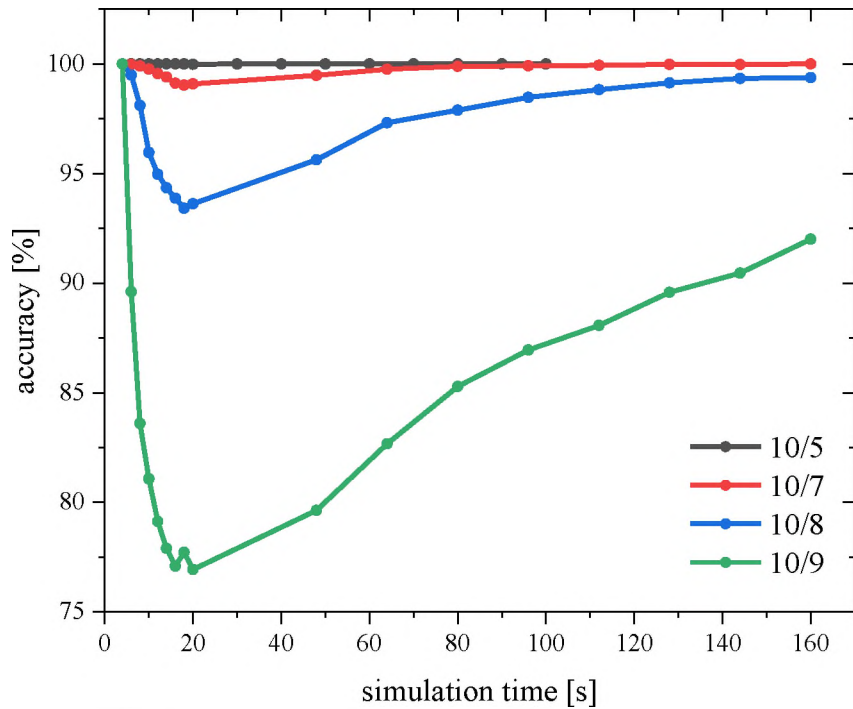
Figure 8.23. Results of simulation performed for number of Neuron A spikes fixed as 10 and various numbers of spikes for Neuron B. The simulation was performed in time range from 4 to 160 seconds for 10,000 different trials

Similarly, in **Figure 8.24**, the results of the simulation with a number of spikes for Neuron B fixed as 2 and a number of spikes for Neuron A between 3 and 5 shows that the accuracy decreases with simulation time for the first 20 seconds where it reaches a minimum value and further increases.
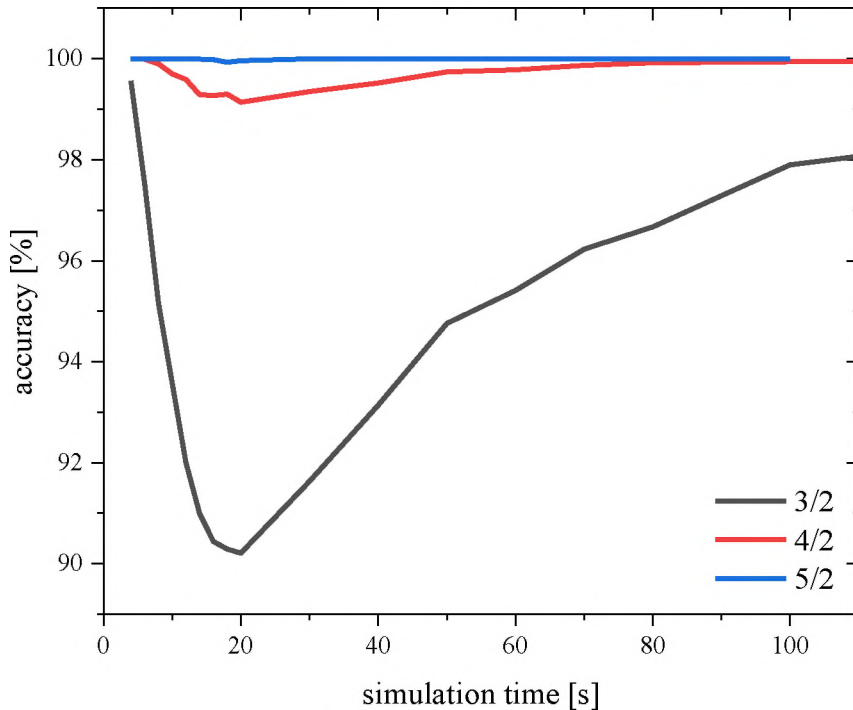
Figure 8.24. Results of simulation performed for number of A spikes varying between 3 and 5 and number of spikes for Neuron B fixed as 2. The simulation was performed in time range from 4 to 100 seconds for 10,000 different trials

140

As the results show, the system reaches the lowest accuracies when the difference between number of spikes is set as 1. To determine how does the accuracy change for different ratios in experiments where the number of spikes differs in 1 spike the simulations were performed for ratios 2/1, 3/2, 5/4 and 10/9.

Figure 8.25 shows that the accuracy of simulations performed for different ratios differing in the number of spikes by one spike is the higher the lower the number of spikes – accuracy above 95% for a 2/1 ratio. In contrast the accuracy of simulations with a higher number of spikes – for example, 10/9 – decreases very fast with the simulation time, reaches a minimum value of 76,94% at 20 seconds and slowly increases. The increase of accuracy above 20 seconds of simulation can be explained in terms of more possible combinations of spike time occurrences (more sparse spikes) and longer times for the devices' relaxation between spikes.

In longer simulation times the accuracy does not reach the initial value, which is close to 100% at 4 seconds, due to competition between excitatory and inhibitory signals, which differ by a single spike. It is due to less frequent spikes in longer simulation times, which causes that the probability of two spikes arriving before the high conductance value decreases is lower compared to shorter simulations.
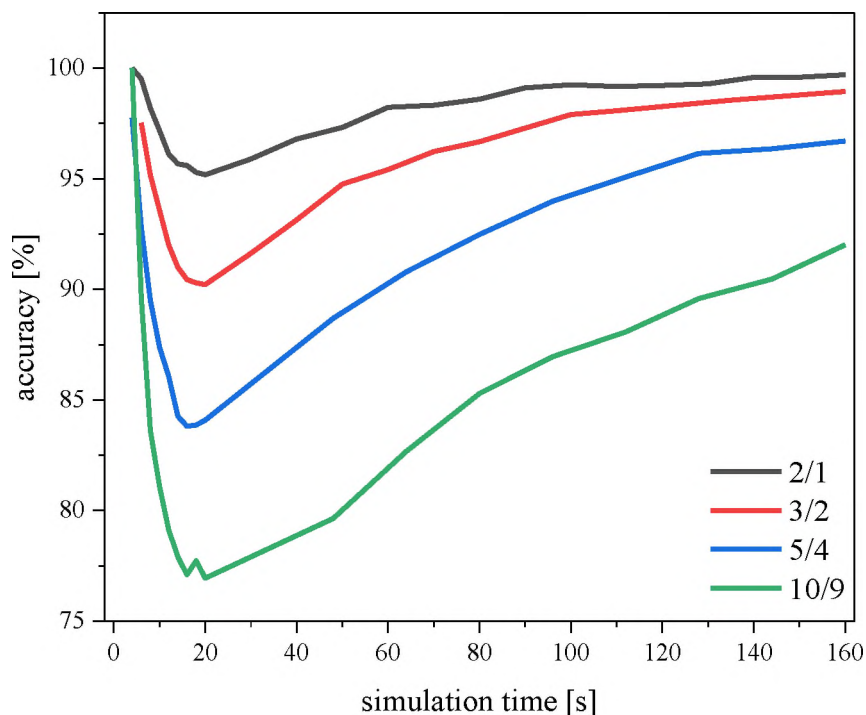

Figure 8.25. Results of simulation performed for ratios between number of spikes of Neuron A and B differing in numbers of spikes by one spike. The simulation was performed in time range from 4 to 180 seconds for 10 000 different trials

If we compare these results to the results of the simulation performed for the devices with no memory of past events, they differ both in terms of the time of occurrence as well as the value of the local minimum. The occurrence time of the minimum value of accuracy in the simulation for the devices with no memory is of the same order of magnitude as the decay time of the conductance value determined experimentally for STP. Due to setting the conductance value to an initial value at the beginning of each trial, the accuracy of the same ratios is lower compared to the simulation with the memory of the previous state of conductance. For example, in the experiment with 2/1 ratio the accuracy of simulation without the memory of past state was determined as 89.19%, the accuracy of the same simulation with memory of past events equals 95.18%. These results show that the systems' volatility, which seemed like disadvantage because of preceding trials having an impact on consecutive trials, in simulations increases the systems' utility in the 2AFC Experiment.

8.2.6. Assessment of device's utility in 2 Alternative Forced Choice Experiment

The results of simulations proved that the studied system is a good candidate for the 2AFC Experiment. This part of the chapter concerns an experimental attempt to this experiment.

The aforementioned simulations assume that both Neurons A and B are identical. Unfortunately, under experimental conditions, it is impossible to prepare two devices with identical parameters and history. Because of the limitations of the experimental setup, two devices cannot be measured at the same time under the same conditions. This would result in slight differences in devices' history. Moreover, even minor differences in device dynamics, for example, time constants of ion relaxation processes, could cause incorrect results in the experiment. Therefore, for the sake of comparability and simplicity, the measurements were performed for one device with different firing probabilities and the number of points, and the results between a series of measurements performed under different parameters were compared. The firing probability was introduced to the experiment to include the probabilistic nature of both neuronal activity and stimuli occurrences, and it informs us about how likely it is that the neuron will fire at each iteration step.

During data analysis, the results obtained for higher firing probability were taken as excitatory Neuron A, and the results obtained for lower firing probabilities were taken as inhibitory Neuron B.

Measurements were performed for four firing probabilities: 5%, 10%, 30% and 50%. The sampling rate was set as 250 ms, the reading potential as +10 V and the spike potential as +50 V. The responses of the device were tested for three numbers of points set as: 15, 20 and 25, which translates to measurement times: 3.75 s, 5 s and 6,25 s. The measurements were performed 20 times, and are further addressed as trials, with random times of spikes occurrences for each combination of parameters, further referred to as series.

Figure 8.26 shows an example of generated Neuronal spike times for the experiment consisting of 20 points in each trial in which the firing probability was set as a) 10% and b) 30%. As can be seen, the number of spikes is not set at a specific number, but rather differs in between trials, due to the probabilistic nature of spikes occurrences.
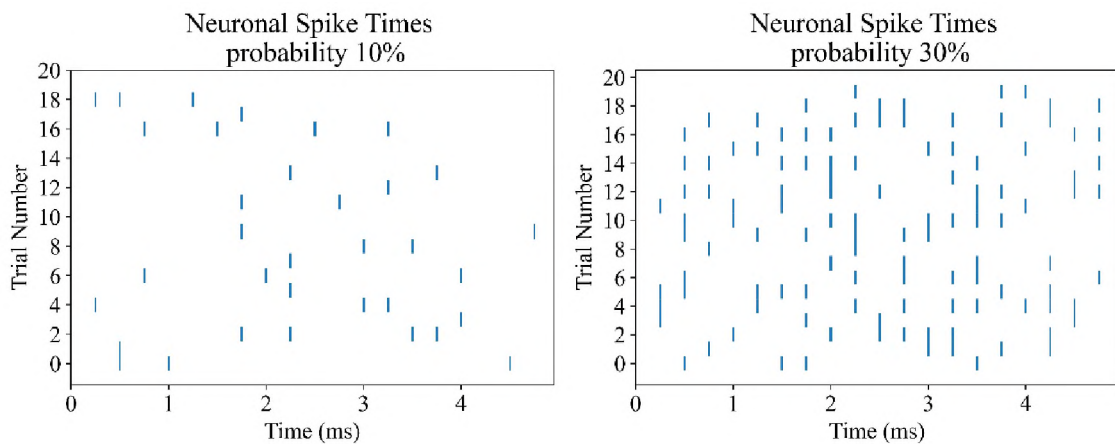
Figure 8.26. The times of occurrences of neural spikes (+50 V) from the experiment with 20 points for firing probabilities set as a) 10% and b) 30%

The current response to the spikes (+50 V) and reading voltages (+10 V) was measured and further analysed. Due to the increase in conductivity of the device, while it operates, the experimental data from the respective series were normalized to the first current value measured for +10 V in the first measured trial. This way the results of measurements performed for different sets of parameters could be compared based on conductance changes within each trial, excluding the global conductivity increase.

The experiment was further reproduced in simulations. To do so, the device's current-voltage characteristic, measured before the 2AFC experiment, was used to determine the parameters of the model. The model parameters, determined as $\tau = 0,978$, $\eta = 1,88 \cdot 10^{-9}$ S/V, and $C_0 = 1,64 \cdot 10^{-6}$ S, were further used in simulation.

The input voltage signals from the experiment were used as inputs in the simulations for

each of the respective sets of parameters. The simulations were performed with the assumption of memory of the past state, to reproduce the experiment, in which the time between the trials was set as 250 ms.

For the sake of consistency with the experiment, the simulated data were normalized to the first current value in the first trial.

Figure 8.27 shows the experimental and simulated current values before the normalization. The dashed lines indicate the spike appearance and the experimental data is shown only for the reading voltage to observe the conductance changes.
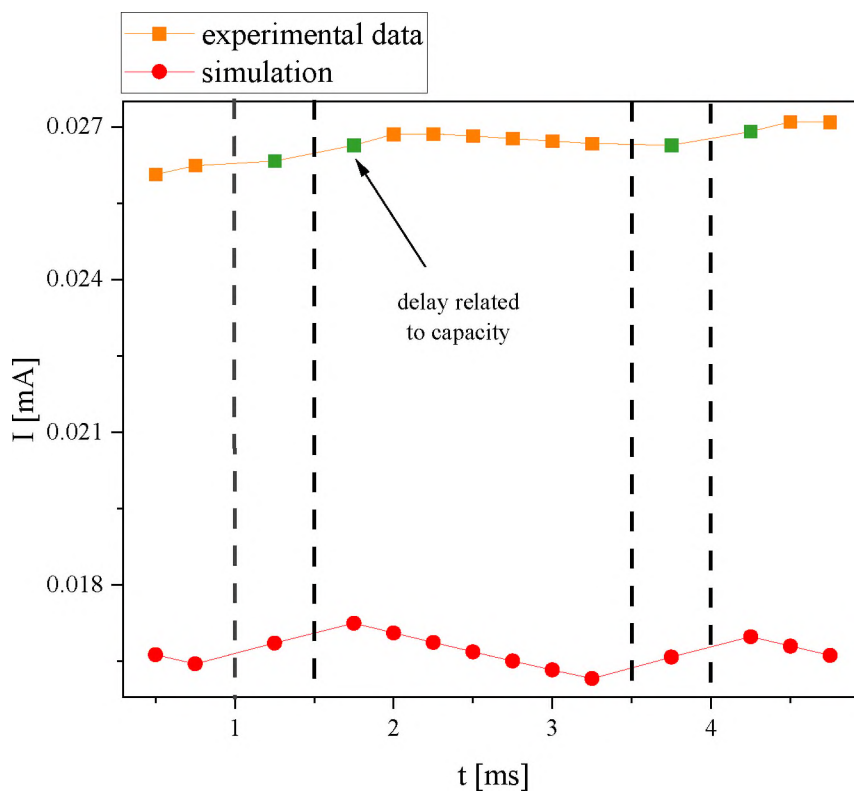
Figure 8.27. Current response to reading pulses measured experimentally (orange) and simulated with the model (red); the data corresponds to the 11th trial of experiment with 20 points in which firing probability equals 30%; the green points indicate the experimental data altered by capacitance effects

As can be seen, the experimental and simulated response of the device differs in terms of current values, which further justifies the current normalization. What is also visible is that the conductance increase after the spike occurrences followed by slow decay. In the case of the experimental data, the current increase after the spike is lower and its' decrease is slower, compared to the simulation. However, in the experimental setup, the capacity of the device lowers the current response of the system due to the voltage drop from +50 V to +10 V. Therefore, the first record after the spike occurrence is altered by parasite

effects and the conductance increase is delayed, as highlighted in green. Nevertheless, the increased conductance, and its' decay, are visible in the following measurement steps, indicating a successful alteration of conductance. What is also worth noting, is the character of the responses of the device and its model. Although the slope of the current decay differs slightly for real and simulated devices, the character of both datasets is similar allowing to compare the final results.

In the next step, the normalized data was integrated and the difference between values in each trial number was calculated and compared. Following, the accuracy of the experiment was calculated based on the 20 trials performed for each measurement parameter set.

The accuracy of the experimental setups' prediction is shown in **Figure 8.28**. The results of measurements performed for a) 15 points, b) 20 points, and c) 25 points are presented in the form of heat maps to indicate the trends. The results show that the accuracy is higher for experiments with more points. This result is reasonable, as the probability of spike occurrence corresponds to a single measurement point. Therefore, for longer experiments, the probability of a higher number of spikes within one trial is higher. Taking into consideration the 5% and 50% probability of spike occurrence, the disproportion between the number of actual spikes and the spike ratio within a trial will be higher the longer the experiment.

The calculated accuracy of the device's prediction complies with the expectations, in which the neuron with a higher firing probability succeeds. The only exception is the experiment performed for 15 points with the ratio of firing probability between Neurons A and B equal to 50/5. The accuracy of this probability ratio in other experiments (20 and 25 points) equals 1.0, meaning a 100% probability of Neuron A firing. This slight anomaly, 90% probability of success, might be related to lower experiment time or device stress.

In terms of the devices' prediction accuracy, the lowest accuracy, 70%, has been calculated for the series of 20 points with probability ratios 50/30 and 30/10. These results might be low due to the high probability of neurons firing. Also, the low number of trials, set as 20 due to the time required to perform all the measurements, might not reflect properly the real accuracy of the device, which might be different if the experiment was extended to a higher number of trials.

145
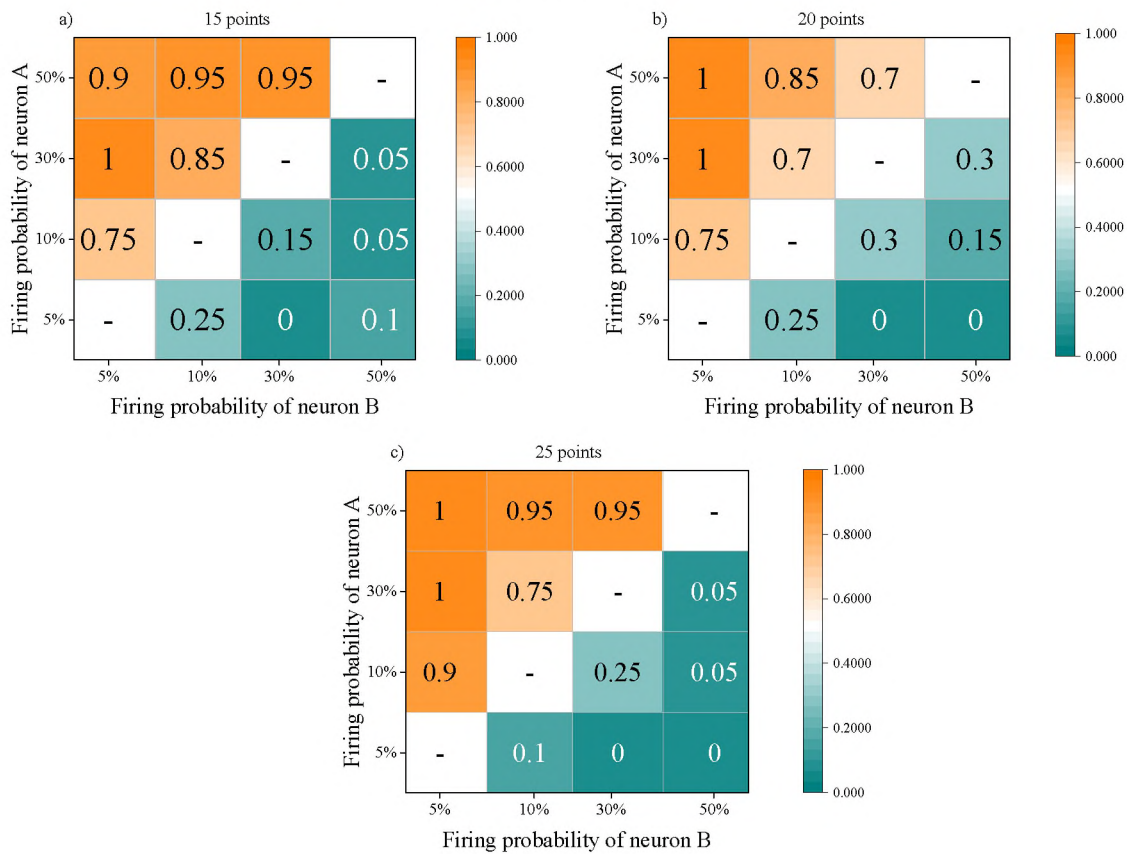
Figure 8.28. Accuracy of experimental approach to 2AFC experiment calculated based on measurement results performed for a) 15 points, b) 20 points and c) 25 points. The measurements were performed on one device for four different firing probabilities: 5%, 10%, 30% and 50% respectively in 20 series

In the case of the accuracy of the simulations' prediction, the accuracy equals 100% for high probability ratios, as shown in **Figure 8.29**. However, the accuracy calculated for ratios close to each other, for example, 50/30 for the experiment with 20 points, the probability of success equals 60%. Compared to the experimental data, which was calculated as 70%, the result of the simulation has lower accuracy. What is also worth noting is that the accuracy of the simulation is within 100% and 95% for high probability ratios, which is higher than for experimental data, and lower for a 50/30 ratio – 60% - compared to 70% in the experiment. Moreover, the results of simulations rely less on the number of points, which is shown as equal probabilities in simulations with 15 and 20 points. However, in contrary to the experimental data, the accuracy decreases for the trials consisting of 25 points, as shown in **Figure 8.29 c)**.
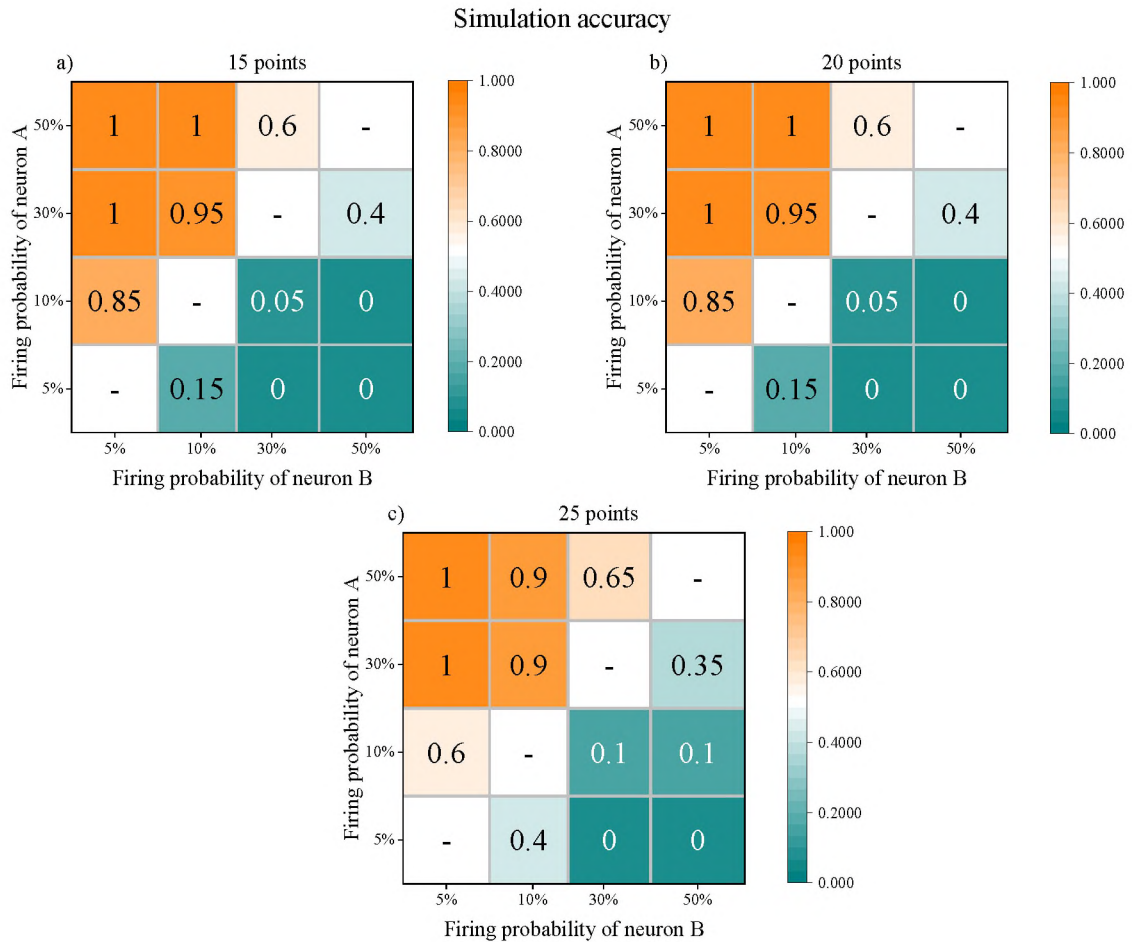
Figure 8.29. Accuracy of simulation performed using experimental parameters –memory of past events; model parameters: $\tau = 0.978$, $\eta = 1,88 \cdot 10^{-9} S/V$, $C_0 = 1.64 \cdot 10^{-6} S$

Nevertheless, the discrepancy between the accuracy of experimental and simulated results is within 10% for trials consisting of 15 and 20 points, and within 30% for trials consisting of 25 points each. This result suggests that the accuracy of the model's prediction is higher for high probability ratios and encounters problems for high firing probabilities for both excitatory and inhibitory neurons (50/30 probability ratio). On the contrary, the experimental accuracy does not encounter the same issue and results in 95%, 70% and 95% success probabilities for trials consisting of 15, 20 and 25 points respectively.

To summarize, the results of experimental data suggest the devices' higher accuracy for the 10/5 and 50/30 firing probability ratios. On the contrary, based on the simulations, the model's prediction accuracy is higher, 90% to 100%, for the high ratios of firing probabilities (50/5, 50/10, 30/5, 30/10). This suggests that the device is more sensitive to less frequent stimulation, however, performs well also in the high probability ratios. The results show that, both the device and its model, execute the 2AFC experiment with high accuracy, regardless of the accuracy differences, which might be related

to the capacity-related effects in the device. What is also worth noting is the devices' high durability, which allowed to perform over 200 experiment trials without noticeable stress-related performance drop.

8.3. Conclusions

In the first part of the Chapter, the device connections were tested to determine their responses in different settings. The results indicate that within a certain parameters range the series connection of two devices exhibits fluctuations. However, the calculated autocorrelation function excluded these to be random values, showing a strong correlation in lag = 1.

The results obtained for device connection in parallel have shown stable operation of devices within a wide parameters range. The results of devices connection in two resistor three memristor bridge supported this observation even further, showing no signal distortions propagated within the bridge.

Interesting results were obtained for two resistor two memristor bridge using memristive devices with R-P3HT contamination. The semiconductors' impurity introduced signal distortions into the bridges' current response, however, based on the calculated autocorrelation function, these instabilities were also shown to be dependent on the devices' history.

The correlation between current values measured at t_n and t_{n+1} is in line with the devices' phenomenological model differential equations. The stochasticity of memristive devices reported in literature is often attributed to the randomness of resistive switching[93]. However, the memristive character of system described in this thesis originates from interactions between consecutive material layers, which are described by differential equations. The processes occurring in the system are associated with collective ion diffusion under applied bias, which influence the conductance of semiconducting layer. It is a continuous process in which the state of the device is described by its previous state, rather than a stochastic one.

In the second part of the Chapter, the model of the device was tested in terms of its utility in Spiking Neural Networks by performing a series of experiments, including the 2-Alternative Choice Experiment.

At first, it was shown that by applying randomly generated spikes the device's conductance can be adjusted for a limited time, based on temporal spacing between

the spikes. These results proved that the devices' model could be utilized in the 2-AFC experiment. The experiment was performed in two variants, without the models' memory of the past state and with such a memory. The accuracy of the simulations revealed that there is a shift in the time of the local minimum occurrence between the variants. Moreover, the experiments with devices having memory of past events had higher prediction accuracy compared to the lack of memory from the previous trial.

In the last part of the Chapter, the 2AFC Experiment was recreated using a single device and comparing the results with respective simulation. The results reveal that both the device and the model perform well in experimental setup parameters. Moreover, the prediction accuracy of model and device are similar with a few exceptions.

To conclude, the device was proven to be an interesting alternative to previously reported in literature devices. The devices' volatile nature appears to be particularly useful as a building block of Spiking Neural Networks.

CHAPTER Nine – Conclusions

The aim of this thesis was to study a novel type of organic memristive device in terms of its' principle of operation, its response to various stimuli and its' potential applications. The thesis addressed seven different research questions. Based on the obtained results, the following conclusions can be drawn:

1. The previously observed conduction increase occurs in the studied system even when the R-P3HT and P4VP layers are separated by a thin insulating layer. This proves that the long-range interactions are an important factor causing the conduction increase in the system. It was also shown that direct molecular interactions between R-P3HT and P4VP are an important factor in conductance increase in the system.

2. The unique principle of operation of the studied system is related to the ion displacement caused by an external electric field. Ion migration causes modulation of the electric field, which is present in the system due to the dipole moment of P4VP-CoBr$_2$, resulting in dynamic changes in R-P3HT conductivity.

3. The memristive character of the system can be cancelled by cooling down the devices, which was attributed to low ion mobility at low temperatures.

4. The ion enrichment of the polymer matrix changes, to some extent, the time constants of the dynamic processes occurring in the system as well as the character of its response. Therefore, it is possible to adjust the device's response and information retention time based on the type of ion admixed to the matrix.

5. The devices' response depends both on the sampling rate and the input signal shape. It was shown that the devices' operation is slightly less stable close to its characteristic time constant. Moreover, it was shown that the device relaxes spontaneously in the time range of tens of seconds, which might be particularly useful in terms of its applications.

6. The unique character of the devices' response has been reproduced using a phenomenological model. The model was shown to reproduce the devices' key features and was further utilised in simulations to predict the system's response in Chapter Eight.

7. The results obtained for different connections between devices reveal that the system is highly stable in a wide range of parameters, however, it behaves in an unpredictable manner in certain parameter sets. The observed signal distortions were analysed and, based on the calculated autocorrelation function, it was shown that the fluctuations are not stochastic, as there are negative correlations at lag = 1.

8. Due to the systems' volatile character, it is possible to emulate Short Term Synaptic Plasticity in the system. This feature was further used in a 2-Alternative Forced Choice Experiment, showing devices' ability to recognize temporal spiking patterns, therefore proving its' utility in brain-inspired computing.

As indicated throughout the thesis, the study covered in this thesis requires further research in regard to phenomenological model improvement and extending the study into different ions. Nevertheless, one of the greatest future challenges, which was not mentioned in the thesis, will be systems' rescaling, which will allow us to extend the research into a more application-focused direction. The first rescaling attempts were successful, however, this matter requires further work and was not mentioned in the thesis.

In conclusion, the results and their discussion presented in this dissertation provide an insight into the principle of operation of the studied system, which was further utilized to formulate the devices' phenomenological model. The measurements performed on different variations of devices proved their high stability and durability. Moreover, the system proved to be a promising candidate for a building block for next-generation neuromorphic computing systems based on organic materials.

Bibliography

1. Chua, L. Memristor-The missing circuit element. *IEEE Transactions on Circuit Theory* **18**, 507–519 (1971).

2. Strukov, D. B., Snider, G. S., Stewart, D. R. & Williams, R. S. The missing memristor found. *Nature* (2008) doi:10.1038/nature06932.

3. Goswami, S. *et al.* Robust resistive memory devices using solution-processable metal-coordinated azo aromatics. *Nat Mater* **16**, 1216–1224 (2017).

4. Rao, M. *et al.* Thousands of conductance levels in memristors integrated on CMOS. *Nature* **615**, 823–829 (2023).

5. Im, I. H., Kim, S. J. & Jang, H. W. Memristive Devices for New Computing Paradigms. *Advanced Intelligent Systems* **2**, 2000105 (2020).

6. Wang, Z. *et al.* Nanoionics-Enabled Memristive Devices: Strategies and Materials for Neuromorphic Applications. *Adv Electron Mater* **3**, 1600510 (2017).

7. Li, S. *et al.* Synaptic plasticity and learning behaviours mimicked through Ag interface movement in an Ag/conducting polymer/Ta memristive system. *J Mater Chem C Mater* **1**, 5292 (2013).

8. Majcher, A. M. *et al.* Between single ion magnets and macromolecules: a polymer/transition metal-based semi-solid solution. *Chem Sci* **9**, 7277–7286 (2018).

9. Pawłowska, A. Mobile ions in the gate of organic field effect transistor. (Jagiellonian University in Kraków, 2019).

10. Dąbczyński, P. *et al.* Extraordinary conduction increase in model conjugated/insulating polymer system induced by surface located electric dipoles. *Appl Mater Today* **21**, 100880 (2020).

11. Caravelli, F., Id, † & Carbajal, J. P. Memristors for the curious outsiders. *Technologies (Basel)* **6**, 118–160 (2018).

12. Vongehr, S. & Meng, X. The missing memristor has not been found. *Sci Rep* **5**, (2015).

13. Zhang, Y. *et al.* Brain-inspired computing with memristors: Challenges in devices, circuits, and systems. *Applied Physics Reviews* vol. 7 Preprint at https://doi.org/10.1063/1.5124027 (2020).

14. Vahl, A. *et al.* Concept and modelling of memsensors as two terminal devices with enhanced capabilities in neuromorphic engineering. *Sci Rep* **9**, 4361 (2019).

15. Ryndin, E., Andreeva, N. & Luchinin, V. Compact Model for Bipolar and Multilevel Resistive Switching in Metal-Oxide Memristors. *Micromachines (Basel)* **13**, 98 (2022).

16. Chua, L. If it's pinched it's a memristor. *Semicond Sci Technol* **29**, 104001 (2014).

17. Lin, D., Chua, L. & Hui, S. Y. The first man-made memristor: Circa 1801. *Proceedings of the IEEE* **103**, 131–136 (2015).

18. Falcon, E. & Castaing, B. *Electrical conductivity in granular media and Branly's coherer: A simple experiment.* (2004).

19. Volkov, A. G. *et al.* Memristors in the Venus flytrap. *Plant Signal Behav* **9**, e29204 (2014).

20. Lim, Z. X., Sreenivasan, S., Wong, Y. H., Zhao, F. & Cheong, K. Y. Filamentary Conduction in Aloe Vera Film for Memory Application. *Procedia Eng* **184**, 655–662 (2017).

21. Pabst, O., Martinsen, Ø. G. & Chua, L. Information can be stored in the human skin memristor which has non-volatile memory. *Sci Rep* **9**, 19260 (2019).

22. Sueoka, B., Cheong, K. Y. & Zhao, F. Natural biomaterial honey-based resistive switching device for artificial synapse in neuromorphic systems. *Appl Phys Lett* **120**, 083301 (2022).

23. Volkov, A. G. *et al.* Memristors in plants. *Plant Signal Behav* **9**, e28152 (2014).

24. Gale, E., Adamatzky, A. & Costello, B. de L. Slime Mould Memristors. *Bionanoscience* **5**, 1–8 (2013).

25. Jo, S. H. *et al.* Nanoscale memristor device as synapse in neuromorphic systems. *Nano Lett* **10**, 1297–1301 (2010).

26. Pickett, M. D. & Stanley Williams, R. Sub-100fJ and sub-nanosecond thermally driven threshold switching in niobium oxide crosspoint nanodevices. *Nanotechnology* (2012) doi:10.1088/0957-4484/23/21/215202.

27. Zeng, F., Li, S., Yang, J., Pan, F. & Guo, D. Learning processes modulated by the interface effects in a Ti/conducting polymer/Ti resistive switching cell. *RSC Adv* **4**, 14822–14828 (2014).

28. Xiao, Z. & Huang, J. Energy-Efficient Hybrid Perovskite Memristors and Synaptic Devices. *Adv Electron Mater* **2**, (2016).

29. Alibart, F. *et al.* An organic nanoparticle transistor behaving as a biological spiking synapse. *Adv Funct Mater* (2010) doi:10.1002/adfm.200901335.

30. Xu, R. *et al.* Vertical MoS 2 Double-Layer Memristor with Electrochemical Metallization as an Atomic-Scale Synapse with Switching Thresholds Approaching 100 mV. *Nano Lett* **19**, 2411–2417 (2019).

31. Younis, A. *et al.* High-performance nanocomposite based memristor with controlled quantum dots as charge traps. *ACS Appl Mater Interfaces* **5**, 2249–2254 (2013).

32. Liu, G. *et al.* Organic Biomimicking Memristor for Information Storage and Processing Applications. *Adv Electron Mater* **2**, (2016).

33. Park, H. L., Kim, M. H., Kim, M. H. & Lee, S. H. Reliable organic memristors for neuromorphic computing by predefining a localized ion-migration path in crosslinkable polymer. *Nanoscale* **12**, 22502–22510 (2020).

34. Pickett, M. D. & Stanley Williams, R. Phase transitions enable computational universality in neuristor-based cellular automata. *Nanotechnology* (2013) doi:10.1088/0957-4484/24/38/384002.

35. Zhu, L. Q., Wan, C. J., Guo, L. Q., Shi, Y. & Wan, Q. Artificial synapse network on inorganic proton conductor for neuromorphic systems. *Nat Commun* **5**, 3158 (2014).

36. Lu, Q. *et al.* Biological receptor-inspired flexible artificial synapse based on ionic dynamics. *Microsyst Nanoeng* **6**, (2020).

37. Wang, R. *et al.* Recent Advances of Volatile Memristors: Devices, Mechanisms, and Applications. *Advanced Intelligent Systems* **2**, 2000055 (2020).

38. Ho, Y., Huang, G. M. & Li, P. Nonvolatile memristor memory. in 485–490 (Association for Computing Machinery (ACM), 2009). doi:10.1145/1687399.1687491.

39. Milo, V., Malavena, G., Compagnoni, C. M. & Ielmini, D. Memristive and CMOS devices for neuromorphic computing. *Materials* vol. 13 166 Preprint at https://doi.org/10.3390/ma13010166 (2020).

40. Chen, W. *et al.* Essential Characteristics of Memristors for Neuromorphic Computing. *Advanced Electronic Materials* vol. 9 Preprint at https://doi.org/10.1002/aelm.202200833 (2023).

41. McCulloch, W. S. & Pitts, W. A logical calculus of the ideas immanent in nervous activity. *Bull Math Biophys* **5**, 115–133 (1943).

42. Guo, T. *et al.* Versatile memristor for memory and neuromorphic computing. *Nanoscale Horiz* **7**, 299–310 (2022).

43. Miranda, E. & Suñé, J. Memristors for neuromorphic circuits and artificial intelligence applications. *Materials* vol. 13 Preprint at https://doi.org/10.3390/ma13040938 (2020).

44. Hendy, H. & Merkel, C. Energy-efficient and noise-tolerant neuromorphic computing based on memristors and domino logic. *Frontiers in Nanotechnology* **5**, (2023).

45. Kim, C. H., Sung, S. & Yoon, M. H. Synaptic organic transistors with a vacuum-deposited charge-Trapping nanosheet. *Sci Rep* **6**, (2016).

46. Kumar, R., Pillai, R. G., Pekas, N., Wu, Y. & McCreery, R. L. Spatially resolved raman spectroelectrochemistry of solid-state polythiophene/viologen memory devices. *J Am Chem Soc* **134**, 14869–14876 (2012).

47. Yamazaki, K., Vo-Ho, V.-K., Bulsara, D. & Le, N. Spiking Neural Networks and Their Applications: A Review. *Brain Sci* **12**, 863 (2022).

48. Brivio, S., Spiga, S. & Ielmini, D. HfO_2 -based resistive switching memory devices for neuromorphic computing. *Neuromorphic Computing and Engineering* **2**, 042001 (2022).

49. Xinyu Wu, Saxena, V. & Kehan Zhu. A CMOS spiking neuron for dense memristor-synapse connectivity for brain-inspired computing. in *2015 International Joint Conference on Neural Networks (IJCNN)* vols 2015-September 1–6 (IEEE, 2015).

50. Prezioso, M. *et al.* Training and Operation of an Integrated Neuromorphic Network Based on Metal-Oxide Memristors. *Nature* **521**, 61–64 (2014).

51. Xu, W., Wang, J. & Yan, X. Advances in Memristor-Based Neural Networks. *Frontiers in Nanotechnology* **3**, (2021).

52. *Semiconducting Polymers: Chemistry, Physics and Engineering, Tom 1.* vol. 1 (WILEY-VCH Verlag GmbH & Co. KGaA, 2007).

53. *Organic Photovoltaics: Materials, Device Physics, and Manufacturing Technologies.* (WILEY-VCH Verlag GmbH & Co. KGaA, 2008). doi:10.1002/9783527656912.

54. Brinkmann, M. Structure and morphology control in thin films of regioregular poly(3-hexylthiophene). *Journal of Polymer Science, Part B: Polymer Physics* vol. 49 1218–1233 Preprint at https://doi.org/10.1002/polb.22310 (2011).

55. Park, Y. D. *et al.* Effect of side chain length on molecular ordering and field-effect mobility in poly(3-alkylthiophene) transistors. *Org Electron* **7**, 514–520 (2006).

56. Nagai, A., Takahashi, A., Komatsu, T. & Nakagawa, T. *Complex Formation of Poly(4-vinylpyridine) with Copper(II) Ion in Mixed Solvent. Polymer Journal* vol. 20 (1988).

57. Filatova, E. O. & Konashuk, A. S. Interpretation of the Changing the Band Gap of Al_2O_3 Depending on Its Crystalline Form: Connection with

Different Local Symmetries. *Journal of Physical Chemistry C* **119**, 20755–20761 (2015).

58. Okubo, S., Horikawa, K., Kawarada, H. & Hiraiwa, A. Gate/insulator-interfacial-dipole-controlled current conduction in Al2O3 metal-insulator-semiconductor capacitors. *J Appl Phys* **126**, (2019).

59. Saha, J. K., Bukke, R. N., Mude, N. N. & Jang, J. Remarkable stability improvement of zno tft with al2o3 gate insulator by yttrium passivation with spray pyrolysis. *Nanomaterials* **10**, (2020).

60. Langereis, E., Creatore, M., Heil, S. B. S., van de Sanden, M. C. M. & Kessels, W. M. M. Plasma-assisted atomic layer deposition of Al2O3 moisture permeation barriers on polymers. *Appl Phys Lett* **89**, 081915 (2006).

61. Groner, M. D., George, S. M., McLean, R. S. & Carcia, P. F. Gas diffusion barriers on polymers using Al2O3 atomic layer deposition. *Appl Phys Lett* **88**, 051907 (2006).

62. Groenendaal, L., Jonas, F., Freitag, D., Pielartzik, H. & Reynolds, J. R. Poly(3,4-ethylenedioxythiophene) and its derivatives: past, present, and future. *Advanced Materials* **12**, 481–494 (2000).

63. Ossila S161 substrate. https://www.ossila.com/en-pl/products/interdigitated-ito-ofet-substrates?_pos=2&_sid=2946050fb&_ss=r&variant=1200244913.

64. Passeri, D., Rossi, M., Tamburri, E. & Terranova, M. L. Mechanical characterization of polymeric thin films by atomic force microscopy based techniques. *Anal Bioanal Chem* **405**, 1463–1478 (2013).

65. Parot, P. *et al.* Past, present and future of atomic force microscopy in life sciences and medicine. *Journal of Molecular Recognition* **20**, 418–431 (2007).

66. Nguyen-Tri, P. *et al.* Recent Applications of Advanced Atomic Force Microscopy in Polymer Science: A Review. *Polymers (Basel)* **12**, 1142 (2020).

67. Butt, H.-J., Cappella, B. & Kappl, M. Force measurements with the atomic force microscope: Technique, interpretation and applications. *Surf Sci Rep* **59**, 1–152 (2005).

68. Hölscher, H. *AFM, Tapping Mode. In: Bhushan, B. (eds) Encyclopedia of Nanotechnology. Encyclopedia of Nanotechnology* (Springer Netherlands, 2012). doi:10.1007/978-90-481-9751-4.

69. Motschmann, H. & Teppner, R. *Ellipsometry in Interface Science.*

70. von Hauff, E. Impedance Spectroscopy for Emerging Photovoltaics. *The Journal of Physical Chemistry C* **123**, 11329–11346 (2019).

71. Magar, H. S., Hassan, R. Y. A. & Mulchandani, A. Electrochemical Impedance Spectroscopy (EIS): Principles, Construction, and Biosensing Applications. *Sensors (Basel)* **21**, (2021).

72. Deshmukh, K. *et al.* Dielectric Spectroscopy. in *Spectroscopic Methods for Nanomaterials Characterization* 237–299 (Elsevier, 2017). doi:10.1016/B978-0-323-46140-5.00010-8.

73. Macdonald, J. R. *Impedance Spectroscopy. Annals of Biomedical Engineering* vol. 20 (1992).

74. Lawrence, C. J. The mechanics of spin coating of polymer films. *Physics of Fluids* **31**, 2786 (1988).

75. Baptista, A., Silva, F., Porteiro, J., Míguez, J. & Pinto, G. Sputtering Physical Vapour Deposition (PVD) Coatings: A Critical Review on Process Improvement and Market Trend Demands. *Coatings* **8**, 402 (2018).

76. A. Mubarak, E. Hamzah & M. R. M. Tofr. document. *Jurnal Mekanikal* **20**, 42–51 (2005).

77. Kelly, P. J. & Arnell, R. D. *Magnetron sputtering: a review of recent developments and applications.*

78. Baptista, A. *et al.* On the Physical Vapour Deposition (PVD): Evolution of Magnetron Sputtering Processes for Industrial Applications. in *Procedia Manufacturing* vol. 17 746–757 (Elsevier B.V., 2018).

79. Binnig, G., Quate' ', C. F., Gi, E. L. & Gerber, C. *Atomic Force Microscope.*

80. Brabazon, D. & Raffer, A. Advanced characterization techniques for nanostructures. in *Emerging Nanotechnologies for Manufacturing* 53–85 (Elsevier, 2015). doi:10.1016/B978-0-323-28990-0.00003-8.

81. Bogner, A., Jouneau, P.-H., Thollet, G., Basset, D. & Gauthier, C. A history of scanning electron microscopy developments: towards 'wet-STEM' imaging. *Micron* **38**, 390–401 (2007).

82. Akhtar, K., Khan, S. A., Khan, S. B. & Asiri, A. M. Scanning Electron Microscopy: Principle and Applications in Nanomaterials Characterization. in *Handbook of Materials Characterization* 113–145 (Springer International Publishing, 2018). doi:10.1007/978-3-319-92955-2_4.

83. Kim, K., Kwon, S. & Pahk, H. J. Fast Analysis of Film Thickness in Spectroscopic Reflectometry using Direct Phase Extraction. *Current Optics and Photonics* **1**, 29–33 (2017).

84. Park, J., Kim, J.-A., Ahn, H., Bae, J. & Jin, J. A Review of Thickness Measurements of Thick Transparent Layers Using Optical Interferometry.

International Journal of Precision Engineering and Manufacturing **20**, 463–477 (2019).

85. Lee, J. & Jin, J. A novel method to design and evaluate artificial neural network for thin film thickness measurement traceable to the length standard. *Sci Rep* **12**, 2212 (2022).

86. Vickerman, J. C. *ToF-SIMS-An Overview*. https://www.researchgate.net/publication/266462581.

87. Leeson, A. M., Alexander, M. R., Short, R. D., Briggs, D. & Hearn, M. J. Secondary Ion Mass Spectrometry of Polymers: a ToF SIMS Study of Monodispersed PMMA Standards. *Surface and Interface Analysis* **25**, 261–274 (1997).

88. Szakal, C., Sun, S., Wucher, A. & Winograd, N. C60 molecular depth profiling of a model polymer. *Appl Surf Sci* **231–232**, 183–185 (2004).

89. Ferrari, S. *et al.* Atomic layer deposited Al2O3 as a capping layer for polymer based transistors. *Org Electron* **8**, 407–414 (2007).

90. Cho, H., Cho, W., Kim, Y., Lee, J. G. & Kim, J. H. Influence of residual sodium ions on the structure and properties of poly(3,4-ethylenedioxythiophene):poly(styrenesulfonate). *RSC Adv* **8**, 29044–29050 (2018).

91. Klein, R. J. *et al.* Modeling electrode polarization in dielectric spectroscopy: Ion mobility and mobile ion concentration of single-ion polymer electrolytes. *J Chem Phys* **124**, 144903 (2006).

92. Habisreutinger, S. N., Noel, N. K. & Snaith, H. J. Hysteresis Index: A Figure without Merit for Quantifying Hysteresis in Perovskite Solar Cells. *ACS Energy Lett* **3**, 2472–2476 (2018).

93. Annual IEEE Computer Conference, IEEE International Symposium on Circuits and Systems 2014.06.01-05 Melbourne & ISCAS 2014.06.01-05 Melbourne. *IEEE International Symposium on Circuits and Systems (ISCAS), 2014 1-5 June 2014, Melbourne, Australia*.

94. Jiang, H. *et al.* A novel true random number generator based on a stochastic diffusive memristor. *Nat Commun* **8**, 882 (2017).

95. Ricci, S., Kappel, D., Tetzlaff, C., Ielmini, D. & Covi, E. Decision Making by a Neuromorphic Network of Volatile Resistive Switching Memories. in *2022 29th IEEE International Conference on Electronics, Circuits and Systems (ICECS)* 1–4 (IEEE, 2022). doi:10.1109/ICECS202256217.2022.9971100.

96. Wang, W. *et al.* Neuromorphic Motion Detection and Orientation Selectivity by Volatile Resistive Switching Memories. *Advanced Intelligent Systems* **3**, 2000224 (2021).

97.   Luo, L., Hu, X., Duan, S., Dong, Z. & Wang, L. Multiple memristor series-parallel connections with use in synaptic circuit design. *IET Circuits, Devices and Systems* **11**, 123–134 (2017).

98.   Barrios, G. A., Retamal, J. C., Solano, E. & Sanz, M. Analog simulator of integro-differential equations with classical memristors. *Sci Rep* **9**, (2019).

99.   Seabold, S. & Josef, P. statsmodels: Econometric and statistical modeling with python. *Proceedings of the 9th Python in Science Conference.* (2010).

100. NIST/SEMATECH e-Handbook of Statistical Methods. https://www.itl.nist.gov/div898/handbook/eda/section3/autocopl.htm doi:10.18434/M32189.

101. Pabst, O. & Schmidt, T. Frequency dependent rectifier memristor bridge used as a programmable synaptic membrane voltage generator. *J Electr Bioimpedance* **4**, 23–32 (2013).

Financial support

Polish National Agency For Academic Exchange

International Scholarship Exchange of PhD Candidates and Academic Staff Participation in 18th International Conference on Nanosciences & Nanotechnologies.

Ministry of Science and Higher Education competition "Initiative of Excellence - Research University" (IDUB)

The research has been supported by grants from SciMat Priority Research Area under the Strategic Programme Excellence Initiative at the Jagiellonian University in years:

- **2020** – Organiczne tranzystory FET z efektem pamięci
- **2021** – Badanie mechanizmu dyfuzji oraz funkcji STP i STD organicznego urządzenia memrystywnego opartego na dyfuzji jonów
- **2022** – Badanie stałych czasowych procesów relaksacyjnych zachodzących w organicznym urządzeniu memrystywnym

Excellence Initiative at the Jagiellonian University („ID.UJ") – Visibility & Mobility Module

International Scholarship Exchange of PhD Candidates. Participation in 4th International Conference on Materials: Advanced and Emerging Materials.

Excellence Initiative at the Jagiellonian University („ID.UJ") – Skills Development & Engagement Module

Scholarship for PhD Candidates. Participation in BigBrain Workshop and Young Researchers Meet.